UNIVERSIDAD Ð LA LAGUNA
Departamento de Astrofísica

Planetary systems around red dwarfs and activity of their host stars

Memoria que presenta
D. Rafael Luque Ramírez
para optar al grado de
Doctor en Ciencias Físicas.

INSTITUTO Ð ASTROFISICA Ð CANARIAS
marzo de 2021

Examination date: May, 2021
Thesis supervisors: Prof. Dr. Enric Pallé Bago and Dr. Grzegorz Nowak

ISBN: xx-xxx-xxxx-x
Depósito legal: TF-xxxx/2021
Some of the material included in this document has been already published in *Astronomy & Astrophysics*.

To my family.
A mi familia.

Agradecimientos

First of all, I would like to thank the "la Caixa" Banking Foundation for believing in me and fund this work. Thank you to all the people that make the INPhINIT program a reality and, in particular, to Gisela and Paola for taking care so lovingly of all of us. And, of course, a shout-out to all my fellow "becaris", an extraordinary generation of young researchers who will spearhead scientific and social advance in the future while enjoying life at its best.

To Enric and Grzegorz, the best supervisor duo. Grzegorz, meticulous and organized, willing to spend countless hours explaining technical details and software difficulties. Enric, a true research group leader, always available for whatever necessity I could come up with and the bigger, scientific picture in mind to guide me when I felt lost in the day-to-day routine. You are a role model to me.

I do not want to miss this opportunity to thank Trifon and Martin for the chance to visit again my beloved Heidelberg during the thesis. To be back in Königstuhl at the MPIA during the "Sommersemester" was very enriching and truly wonderful. And also, to my friends and colleagues from the CARMENES consortium, who make every bi-annual scientific meeting a memorable gathering, and the whole exoplanets group at IAC for creating the best working atmosphere I have ever been part of.

To all the "titos" and "titas" who became a true family during our years in Tenerife. Thank you for all the birthdays, nepali festivals, carnivals, beach days, mountain days, beers and wines we have shared, and being there for us even in the most difficult times. And to my CRULL teammates to make me feel that I belong and that rugby values still prevail.

Gracias a mi familia, al tito Emilio, mi padre, mi madre y mi hermana. Gracias por creer siempre en mi y haberos sacrificado tanto durante tanto tiempo con la seguridad de que este día llegaría. Gracias por todo vuestro apoyo y amor incondicional. Ahora, siendo padre, se que un hijo no necesita nada más para crecer.

And, undoubtedly, to my soon-to-be-wife who followed me in this endeavor without hesitation. For keeping my feet in the ground, being the world expert at figuring out life, transforming an ugly house in a home, and giving birth to the most extraordinary daughter a man could dream of. Thank you mero tara.

Rafael Luque Ramírez,
La Laguna, 5 de marzo de 2021.

Resumen

Uno de los campos más apasionantes de la ciencia hoy en día es el estudio de los exoplanetas, que cautivan la imaginación no sólo de la comunidad astronómica sino también de la sociedad en general. Desde el descubrimiento — merecedor del Premio Nobel de Física 2019 — de un planeta gigante alrededor de la estrella tipo solar 51 Pegasi (Mayor & Queloz, 1995), se han detectado más de 4000 planetas extrasolares, cambiando de forma irreversible el paradigma de las ciencias planetarias y situando a nuestro sistema solar en un contexto mucho más amplio. Identificar exoplanetas como la Tierra, potencialmente habitables y encontrar biomarcadores en sus atmósferas está entre los principales objetivos de la astronomía de este siglo, motivando el desarrollo y construcción de ambiciosas misiones espaciales y telescopios en tierra de enormes dimensiones. Planetas pequeños y rocosos orbitando estrellas de tipo espectral M, también conocidas como enanas rojas, son los únicos candidatos similares a la Tierra cuyas atmósferas se pueden estudiar con la tecnología actual. Además, son los mejores, si no los únicos, candidatos para detectar signos de vida en ellos con la próxima generación de instrumentos terrestres y espaciales.

Esta tesis se centra en el descubrimiento y caracterización de planetas pequeños en torno a enanas rojas. Las enanas rojas componen el 70% de las estrellas de nuestra galaxia y debido a su pequeña masa y tamaño ofrecen varias ventajas para la detección y caracterización de exoplanetas usando las dos técnicas más comunes y exitosas: el método de tránsito y el de las velocidades radiales. El objetivo principal de este trabajo es aprovechar la oportunidad que ofrecen este tipo de estrellas para descubrir y estudiar los mejores candidatos para el estudio de atmósferas exoplanetarias con instrumentos venideros usando la sinergia entre misiones espaciales que buscan planetas transitantes y espectrógrafos de alta resolución en tierra.

Dentro de este ámbito, siete nuevos planetas en cuatro sistemas extrasolares se han detectado y analizado como parte de esta tesis. El segundo capítulo describe el descubrimiento de dos supertierras orbitando las enanas rojas GJ 3779 y GJ 1265, monitoreadas por el instrumento CARMENES dentro de su búsqueda de exoplanetas

alrededor de estrellas de baja masa usando la técnica de las velocidades radiales. Los planetas poseen características muy similares y, a pesar de haberse realizado búsquedas en la fotometría obtenida por instrumentos espaciales y terrestres, no transitan sus estrellas madre. Los resultados se detallan en Luque et al. (2018). El tercer capítulo presenta el descubrimiento de un sistema multiplanetario orbitando la enana roja GJ 357. El planeta más cercano a su estrella, transitante, fue detectado por el satélite *TESS* y confirmado con velocidades radiales nuevas y de archivo obtenidas por una multitud de instrumentos en tierra. Es un planeta caliente con una densidad similar a la Tierra, ideal para el estudio de su atmósfera con el telescopio espacial *JWST* y se ha convertido en el planeta transitante más cercano al nuestro orbitando una enana roja aislada. El análisis de las velocidades radiales revelaron dos planetas adicionales de tipo supertierra en órbitas externas, estando la más alejada en la zona habitable de su estrella, es decir, en el rango de órbitas donde el agua líquida podría mantenerse en su superficie. Los resultados se detallan en Luque et al. (2019b). El cuarto capítulo anuncia el descubrimiento de dos minineptunos transitando la enana roja TOI-776. Sus masas y radios, medidos con los instrumentos HARPS y *TESS*, respectivamente, indican que ambos planetas deben haber retenido una atmósfera considerable. Esto, junto al brillo de su estrella madre, los convierten en objetivos prioritarios para el estudio de sus atmósferas con el *JWST*, el cual permitirá determinar de forma precisa la composición interna de los planetas y estimar la formación y evolución del sistema. Los resultados se detallan en Luque et al. (2021).

El número de exoplanetas pequeños con medidas precisas de su densidad orbitando enanas rojas se ha triplicado durante el transcurso de esta tesis. Las nuevas incorporaciones no sólo han permitido encontrar candidatos apropiados para estudiar sus atmósferas, especialmente con el telescopio espacial *JWST*, sino que también nos ayudan a comprender la composición, origen y evolución de esta población de una forma global. Los resultados y las técnicas desarrolladas en esta tesis contribuyen a mejorar nuestro conocimiento acerca del tipo de planeta más frecuente en el universo, los planetas rocosos orbitando enanas rojas, y su potencial para albergar condiciones propicias para la vida en su superficie.

Abstract

One of the most exciting areas of astronomical research today is the study of exoplanetary systems, engaging the imagination not only of the astronomical community but also of the general public. Since the Nobel-winning discovery of a giant planet around the Sun-like star 51 Pegasi (Mayor & Queloz, 1995), about 4000 extra-solar planets have been detected, changing the view of planetary science and placing our solar system into a much broader context. Identifying habitable Earth-like exoplanets and searching for biomarkers in their atmospheres is among the main objectives of this century's astronomy, motivating ambitious space missions and extremely large telescopes in the ground. Small, rocky planets orbiting M dwarfs are the only candidates whose atmospheric characterization is feasible with available technology. Besides, they will be the best, if not the only, candidates to detect life signatures with the next generation of ground- and space-based instruments.

This thesis focuses on the discovery and characterization of small planets around M dwarfs. M dwarfs constitute 70% of the stars in our Galaxy and given their small size and mass they offer several advantages for the detection and characterization of exoplanets using the two most successful and popular methods, namely the transit and radial velocity techniques. The main goal of this work is to tackle the so-called "M-dwarf opportunity": to find and study the best planet candidates for atmospheric characterization using upcoming facilities based on the synergy between space-based transit searches around bright stars and ground-based high-resolution spectrographs.

In this context, seven new planets in four planetary systems are detected and characterized as part of this thesis. Chapter 2 describes the discovery of two super-Earth planets orbiting the mid-type M dwarfs GJ 3779 and GJ 1265, monitored with the CARMENES instrument as part of its radial velocity search for exoplanets around low-mass stars. The planets share very similar properties and, despite photometric searches with ground- and space-based telescopes, they do not transit their parent stars. The results are detailed in Luque et al. (2018). Chapter 3 presents the discovery of a three-planet system orbiting the mid-type M dwarf GJ 357. The innermost, transiting

planet in the system was detected by the *TESS* satellite and confirmed with archival and new radial velocity observations from several instruments. It is a hot, Earth-like density planet optimal for atmospheric studies with the upcoming *JWST* and the closest transiting planet to the Sun orbiting a single M dwarf. The analysis of the radial velocity data revealed two additional super-Earths in longer orbits, being the outermost located within the habitable zone of the host star, i.e., in the orbital range where liquid water can be stable at the planetary surface. The results are detailed in Luque et al. (2019b). Chapter 4 reports the discovery of two transiting sub-Neptune planets orbiting the early-type M dwarf TOI-776. The precise mass and radius determination of the system using HARPS and *TESS*, respectively, shows that both planets must have retained a substantial atmosphere. Combined with the brightness of their host, they are straightforward targets for atmospheric characterization with the *JWST*, which will allow to precisely determine their internal composition and study the formation and evolution of the system. The results are detailed in Luque et al. (2021).

The number of precisely characterized small planets around M dwarfs has tripled during the course of this thesis. The new additions did not only allow to find suitable candidates for atmospheric studies, particularly with the *JWST*, but also to understand the composition, origin and evolution of these planets in a demographic sense. The techniques developed and the results gathered in this thesis will contribute to a deeper understanding of the most frequent kind of planets in the Universe, the rocky worlds in orbit around red dwarfs, and of their potential to host habitable conditions on their surfaces.

Contents

1

Introduction

Se equivocó la paloma.
Se equivocaba.

Por ir al Norte fue al Sur.
Creyó que el trigo era agua.
Se equivocaba.

Creyó que el mar era el cielo;
que la noche, la mañana.
Se equivocaba.

Rafael Alberti (1941)

1.1 The exoplanet revolution

The discovery of the first *exoplanets* — planets outside the solar system — has ended a debate spanning more than two millennia: are there infinite worlds like and unlike ours (Epicurus, 341–270 BCE) or is the Earth unique (Aristotle, 384–322 BCE)? With hundreds of billions of galaxies in the observable Universe, each of them containing hundreds of billions of stars, humankind is certain, for the first time in its history, about the existence of countless planets.

The first detected exoplanet was the claim by Campbell et al. (1988) of a planetary companion with a mass two times the mass of Jupiter (M_J) and an orbital period of roughly 3 years to γ Cephei Ab using the radial velocity technique. But its detection was only tentative at the time, and it had to wait more than 15 years to be fully confirmed by Hatzes et al. (2003). Thus, the first confirmed planetary system was dis-

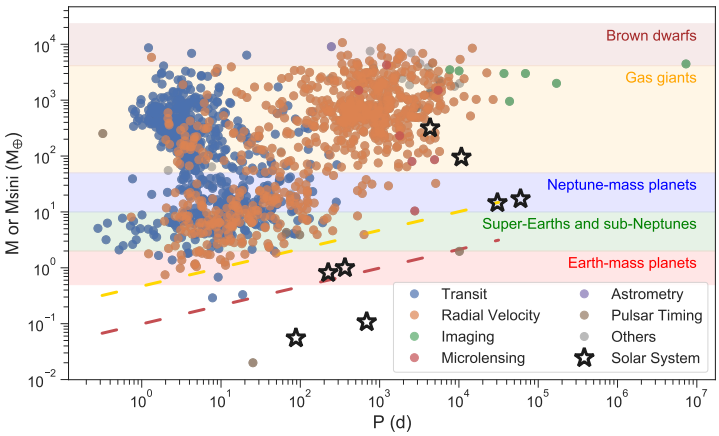

FIGURE 1.1— Mass-orbital period diagram of known exoplanets color-coded by discovery method. Only objects with mass determination better than 60% in the NASA Exoplanet Archive (as of September 1, 2020) are indicated. The dashed line indicates the minimum mass detectable with the state-of-the-art radial velocity precision instrument ESPRESSO (Pepe et al., 2010) for a planet orbiting a Sun-like star (yellow) or a mid-type M dwarf (red).

covered around a stellar remnant. In 1992, Wolszczan & Frail (1992) announced their discovery of two planets with masses of roughly four times the mass of the Earth ($M_\oplus$) with periods of 67 and 98 days, respectively, orbiting the pulsar PSR 1257+12.

Although it was not the first detected exoplanet, the discovery of a planetary companion to the Sun-like star 51 Pegasi by Mayor & Queloz (1995) launched the field of exoplanets. The Nobel-winning discovery of 51 Peg b, which has a minimum mass of roughly 0.5 M_J, but an orbital period of only about 4 days, surprised many. This is because the then-popular planet formation model predicted that such planets, so-called *hot Jupiters*, could not form in situ (e.g., Lin et al., 1996). The discovery of 51 Peg b led to the realization that at least some fraction of exoplanets undergo large-scale migration from their birthplaces and coined a fundamental principle that still holds in exoplanet science: expect the unexpected.

Today, astronomers have discovered more than 4200 exoplanets[1]. Their location

[1] According to the NASA Exoplanet Archive (https://exoplanetarchive.ipac.caltech.edu/index.html), accessed September 1, 2020.

in the mass–period diagram for confirmed planets with measured masses is shown in Fig. 1.1. Every new discovery shows a remarkable diversity, challenging the perception and understanding of our own solar system. Here, I present a description of some of the strange and unexpected worlds found.

Hot Jupiters and distant gas giants These planets, with sizes and masses like Jupiter and Saturn, have been discovered both very close (with orbital periods less than 10 days) and very far from their stars (twice the distance between Neptune and the Sun). They have changed the understanding of planet formation theories and highlight the role of evolution since the first stages of formation in the protoplanetary disk.

Super-Earths and sub-Neptunes These planets do not have enough mass to become giant, but are more massive than small rocky planets like our own. With masses between 2 and 10 $M_\oplus$ (i.e., significantly more massive than the Earth, but less massive than Uranus), depending on their bulk densities can be classified between *sub-Neptunes*, if they possess a substantial atmosphere made of hydrogen and helium, or *super-Earths*, if they are rocky and have none or a much smaller atmosphere. They remain poorly understood in terms of formation and do not have a direct solar system analogue.

Lava worlds These planets have an Earth-like compositions and a mass of order one to a few $M_\oplus$. They are located extremely close to their stars and might have a magma ocean running on their surfaces, as a result of the high temperatures on the dayside (of approximately 2000 K or more) caused by stellar irradiation. Terrestrial planets have a solid surface, and may have the same basic type of structure, comprising a central metallic core, mostly iron, with a surrounding silicate mantle. It is possible that they have secondary atmospheres, generated through outgassing or comet impacts, in contrast to the giant planets, whose atmospheres are primary, captured directly from the original solar nebula.

1.2 Discovery and characterization of exoplanets

Several methods have been developed in the past 30 years to detect exoplanets. Radial velocity, transit, direct imaging, microlensing, astrometry, and pulsar timing has been the most prolific so far (see Fig. 1.1). Figure 1.2 shows an overview of the sensitivity of each method in the mass-orbital separation diagram. The radial velocity and transit methods are particularly sensitive to massive planets in short orbital periods. On the other hand, direct imaging and astrometry preferably detect massive planets at large orbital separations. Microlensing complements the others with a sensitivity up to Earth-mass planets at orbital distances of a few au. Altogether, the different detection

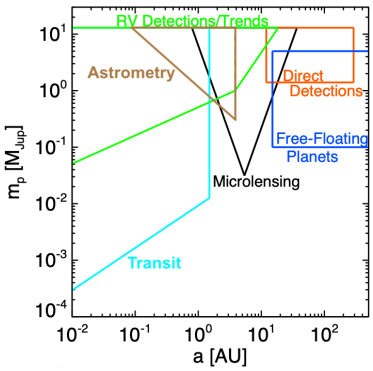

FIGURE 1.2— Sensitivity of the main exoplanet detection methods as a function of mass and orbital separation. Figure courtesy of Christian Clanton.

techniques allow us to probe a wide range of the parameter space around stars of every spectral type at distances from the closest neighbor to a few kpc, or even free-floating planets. A comprehensive review of all discovery methods can be found in Perryman (2011).

The results of this dissertation have been obtained by means of the radial velocity and transit techniques. Therefore, in the next sections I provide an overview of their formalism, application and main results.

1.2.1 Radial velocity technique

The presence of a planetary companion with mass M_p around a host star with mass $M_\star$ displaces the center-of-mass of that two-body system from the center of the star itself. Thus, a star with a sole companion exhibits a Keplerian orbit around the system's barycenter. The stellar motion along the line-of-sight of the observer is known as the radial velocity, which is the fundamental measured quantity naming this technique. Here, I derive the radial velocity equation following a similar approach as in Seager (2010).

Radial velocity signature of Keplerian motion

The equation of the ellipse described by the star around the center of mass is, in polar coordinates,

$$\mathrm{r}_\star = \frac{a_\star\left(1-e^2\right)}{1+e\cos\mathrm{f}} \tag{1.1}$$

where $r_\star$ is the distance of the star from the barycenter, e is the eccentricity, and f is true anomaly, i.e., the angle between the periastron direction and the position on the orbit measured from the center of mass. The semi-major axis of the star around the barycenter, $a_\star$, is related to the orbital semi-major axis a through

$$a_\star = \frac{M_p}{M_\star + M_p} a \quad . \tag{1.2}$$

Since the observable quantity will be the radial velocity of the star, it is necessary to obtain the relation between the position of the orbit and orbital velocity. In Cartesian coordinates, with the x-axis pointing in the periastron direction and the origin at the barycenter, the position and velocity vectors are given by

$$\mathbf{r}_\star = \begin{pmatrix} \mathrm{r}_\star\cos\mathrm{f} \\ \mathrm{r}_\star\sin\mathrm{f}\end{pmatrix} \quad , \quad \dot{\mathbf{r}}_\star = \begin{pmatrix} \dot{\mathrm{r}}_\star\cos\mathrm{f} - \mathrm{r}_\star\dot{\mathrm{f}}\sin\mathrm{f} \\ \dot{\mathrm{r}}_\star\sin\mathrm{f} + \mathrm{r}_\star\dot{\mathrm{f}}\cos\mathrm{f}\end{pmatrix} \quad . \tag{1.3}$$

Differentiating Eq. 1.1 to express the velocity as a function of the true anomaly,

$$\dot{\mathrm{r}}_\star = \frac{a_\star e\left(1-e^2\right)\dot{\mathrm{f}}\sin\mathrm{f}}{(1+e\cos\mathrm{f})^2} = \frac{e\,\mathrm{r}_\star^2\,\dot{\mathrm{f}}\sin\mathrm{f}}{a_\star\left(1-e^2\right)} \quad , \tag{1.4}$$

and replacing it into Eq. 1.3, it is obtained

$$\dot{\mathbf{r}}_\star = \frac{\mathrm{r}_\star^2\,\dot{\mathrm{f}}}{a_\star\left(1-e^2\right)}\begin{pmatrix}-\sin\mathrm{f}\\ e+\cos\mathrm{f}\end{pmatrix} = \frac{\mathrm{h}_\star}{M_\star a_\star\left(1-e^2\right)}\begin{pmatrix}-\sin\mathrm{f}\\ e+\cos\mathrm{f}\end{pmatrix} \quad , \tag{1.5}$$

where $\mathrm{h}_\star = M_\star\,\mathrm{r}_\star^2\,\dot{\mathrm{f}}$ is the angular momentum of the star, which is a constant of motion. This quantity can be expressed as a function of the ellipse parameters a and e (see Murray & Correia, 2010) as

$$\mathrm{h}_\star = \sqrt{\frac{G\,M_\star^2\,M_p^4\,a\,\left(1-e^2\right)}{\left(M_\star+M_p\right)^3}} \quad . \tag{1.6}$$

Substituting Eq. 1.2 and 1.6 in Eq. 1.5, I finally obtain

$$\dot{\mathbf{r}}_\star = \sqrt{\frac{G\,M_p^2}{\left(M_\star+M_p\right)}\frac{1}{a\left(1-e^2\right)}}\begin{pmatrix}-\sin\mathrm{f}\\ e+\cos\mathrm{f}\end{pmatrix} \quad . \tag{1.7}$$

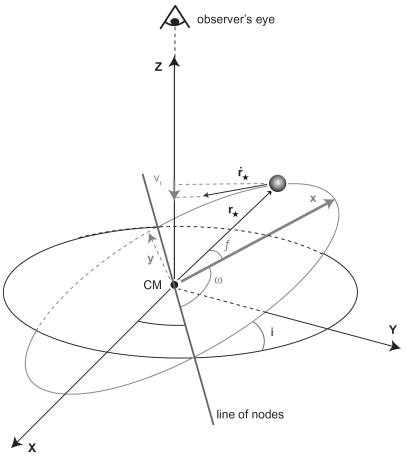

FIGURE 1.3— The relationship between the star's velocity around the center of mass, $\dot{\mathbf{r}}_\star$, and its radial component along the line of sight, $v_{r,\star}$. Adapted from Murray & Correia (2010).

The final step is to project the velocity vector onto the line of sight of the observer. The inclination angle i of the system is defined as the angle between the orbital plane and the plane of the sky (i.e., the perpendicular to the line of sight). The argument of periastron ω is defined as the angle between the line of nodes and the periastron direction (see Fig.1.3 for an overview of the geometry). The radial velocity equation is obtained by projecting the velocity vector on the line of sight unit vector $\hat{\mathbf{k}}$, with x and y axes in the orbital plane and z perpendicular to them, as

$$v_{r,\star} = \dot{\mathbf{r}}_\star \cdot \hat{\mathbf{k}} = \dot{\mathbf{r}}_\star \cdot \begin{pmatrix} \sin\omega \sin i \\ \cos\omega \sin i \\ \cos i \end{pmatrix} = \sqrt{\frac{G}{\left(M_\star + M_p\right) a \left(1 - e^2\right)}} M_p \sin i \left(\cos(\omega + \mathrm{f}) + e \cos\omega\right) \quad . \tag{1.8}$$

From here the radial velocity semi-amplitude $K = (\dot{v}_{r,\max} - \dot{v}_{r,\min})/2$ is derived, the fundamental observable quantity relating the radial velocity to the position on the orbit.

$$K = \sqrt{\frac{G}{(1 - e^2)}} M_p \sin i \left(M_\star + M_p\right)^{-1/2} a^{-1/2} \quad . \tag{1.9}$$

Replacing the semi-major axis a with the orbital period P using Kepler's third law

and expressing this formula in more practical units, I obtain

$$K = \frac{28.4329\,\mathrm{m\,s^{-1}}}{\sqrt{1-e^2}} \frac{M_p \sin i}{M_J} \left(\frac{M_\star + M_p}{M_\odot}\right)^{-2/3} \left(\frac{P}{1\,\mathrm{yr}}\right)^{-1/3} \quad . \tag{1.10}$$

From a radial velocity time series, five orbital parameters can be determined by fitting a Keplerian orbit: e, ω, P, K, and f. Prior knowledge of the stellar mass — see Schweitzer et al. (2018) for a review of the different techniques to determine the stellar physical parameters — allows to determine the mass of the planetary companion from the radial velocities using Eq. 1.10. However, the radial velocity technique, in the exoplanet case where $M_p \ll M_\star$, is only sensitive to the minimum mass $M_p \sin i$ of the companion unless there is a priori information from the system's orbital inclination i from transit or astrometric observations. The $\sin i$ factor in the companion's mass illustrates the geometric effect of the radial velocity signal when the orbit is edge-on ($i = 90$ deg) or face-on ($i = 0$ deg) from the observer's line of sight.

Equation 1.10 is applicable to any two celestial bodies. The radial velocity semi-amplitude is higher for more massive companions around low-mass objects at short orbital periods. For stellar binary systems K is on the order of $\mathrm{km\,s^{-1}}$, but for an Earth-Sun analog system the semi-amplitude is only $9\,\mathrm{cm\,s^{-1}}$, comparable with the walking speed of a snail and out of reach for state-of-the-art instrumentation. Yet.

Precise radial velocities: high-resolution spectrographs

The line-of-sight velocity component of a star induced by a planetary companion provokes a back-and-forth shift in the measured wavelength of the stellar spectral lines. This Doppler effect is detectable with cross-dispersed echelle spectrographs with typical resolving powers $R \equiv \lambda/\Delta\lambda \sim 100\,000$. However, the wavelength shift of a single pixel at such resolution corresponds to radial velocity change of $1\,\mathrm{km\,s^{-1}}$. To detect giant or Earth-mass planets one must measure shifts hundred to tens of thousands better than that. Therefore, precise radial velocities at the $\mathrm{m\,s^{-1}}$ level rely on averaging the individual velocities of many lines, high instrumental stability and accurate wavelength calibration. Still, large telescopes and long integration times are required to achieve the necessary high signal-to-noise (S/N) for sub-pixel accuracies.

On the other hand, not every star is amenable for precise radial velocity measurements. Stars with very high effective temperatures ($T_{\mathrm{eff}} > 10\,000$ K) have spectra that do not show any spectral features since all chemical elements in their photospheres are ionized. Besides, such stars are typically fast rotators, which smears out spectral lines even more via rotational broadening. For very cool dwarfs ($T_{\mathrm{eff}} < 3200$ K), the presence of complex molecular bands make the many available spectra lines packed, less

contrasted and overlapping; together with the fact that most of their bolometric flux falls into the near infrared, putting demanding constraints on instrumentation (telluric removal, cryogenic components, etc.) and achievable S/N. Thus, stars with spectral types between F5 to M5 V are the best suited for radial velocity exoplanet searches.

There are two main strategies for accurate wavelength calibration in the radial velocity technique. The first one is the iodine method (Marcy & Butler, 1992). It is based in the observation of a reference spectrum — a gas cell filled with iodine placed in the telescope beam before it enters the spectrograph — that is superimposed to the stellar spectrum. In this way, the iodine lines are used as a stable wavelength reference. If both the iodine and stellar lines shift in the same way, the reason for the apparent Doppler effect is instrumental; on the other hand, if the stellar lines shift relative to the iodine lines, the change is astrophysical and inherent to the star. This technique is used, among others, in the instruments HIRES[2] (Vogt et al., 1994), placed at the Keck-I 10-m telescope in Mauna Kea, Hawaii, covering the 364–797 nm range with a $R \sim 55\,000$ and an internal radial velocity precision of 1.5 m s^{-1}; UVES[3] (Dekker et al., 2000), placed at the UT2 Kueyen 8.2-m VLT telescope in Paranal, Chile, covering the 330–700 nm range with a $R \sim 110\,000$ and an internal radial velocity precision of 2.6 m s^{-1}; and PFS[4] (Crane et al., 2006), placed at the 6.5-m Magellan telescope in Las Campanas, Chile, covering the 390–670 nm range with a $R \sim 76\,000$ and an internal radial velocity precision of 1.2 m s^{-1}. The iodine lines track all instrumental changes, which can be calibrated and corrected, making spectrographs using this technique relatively simple and cheap. However, the wavelength range to derive precise radial velocities is very limited because most of the spectral information from the iodine's is contained in the region between 500 and 620 nm. Furthermore, light losses in the cell are of the order of 20–30% making these spectrographs inefficient.

The second strategy is to build a spectrograph where the light from a calibration unit is fed with an optical fiber to the instrument (Baranne et al., 1996). The spectrograph is enclosed in a pressure- and temperature-stabilized tank. The stellar spectrum and calibration reference are ingested in the spectrograph with fibers that follow a very similar optical path within the instrument. In this way, instrumental changes due to pressure and temperature variations inside the tank are monitored with the spectrum of the calibration reference. There are several calibration unit sources, being the most common a thorium-argon emission lamp, a Fabry-Pérot interferometer, or a laser frequency comb. This technique is used, among others, in the instruments HARPS[5] (Mayor et al., 2003), placed at the 3.6-m ESO telescope in La Silla, Chile, covering

[2] **HI**gh-**R**esolution **E**chelle **S**pectrograph.
[3] **U**ltraviolet and **V**isual **E**chelle **S**pectrograph.
[4] **P**lanet **F**inder **S**pectrograph.
[5] **H**igh **A**ccuracy **R**adial velocity **P**lanet **S**earcher.

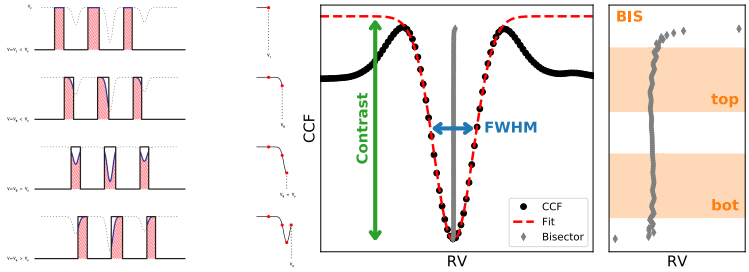

FIGURE 1.4— *Left:* Illustration of the construction of the cross-correlation function. Diagrams on the left represent the stellar spectrum (dashed lines) and the binary mask (solid lines, transmission zones depicted as hatched areas). Diagrams on the right show the result of the cross-correlation process. *Right:* Illustration of the classical activity indicators measured with the CCF method. In black is shown the typical CCF of an M dwarf and the best Gaussian fit (red dashed line) together with the FWHM, contrast and bisector (grey diamonds) derived from the fit. In the right it is shown a zoom to the central region of the CCF to show the bisector shape and the top/bottom regions used to compute it. Adapted from Eggenberger & Udry (2010) and Lafarga et al. (2020).

the 380–690 nm range with a $R \sim 115\,000$ and an internal radial velocity precision of 0.8 m s^{-1}; its northern sibling HARPS-N (Cosentino et al., 2012), placed at the 3.6-m Telescopio Nazionale Galileo at Roque de los Muchachos Observatory, Spain, covering the 380–690 nm range with a $R \sim 115\,000$ and an internal radial velocity precision of 0.8 m s^{-1}; CARMENES[6] (Quirrenbach et al., 2014), placed at the 3.5-m telescope in Calar Alto, Spain, composed by two spectrographs covering the 520–960 nm range with a $R \sim 94\,600$ and an internal radial velocity precision of 1.2 m s^{-1}, and the 960–1710 nm range with a $R \sim 80\,400$ and an internal radial velocity precision of 3.7 m s^{-1}; and ESPRESSO[7] (Pepe et al., 2010), placed at the VLT in Paranal, Chile, covering the 380–788 nm range with a $R \sim 140\,000$ and a state-of-the-art internal radial velocity precision of 26 cm s^{-1} (Suárez Mascareño et al., 2020). The gain in efficiency and precision is compensated with the complexity of the optical design and environment stabilization systems.

For the final radial velocity extraction there are two main approaches: the cross-correlation (CCF) method or the template matching technique. The first one is based on obtaining a mean-line profile of the spectrum by cross-correlating the stellar spectrum with a mask or a template of the same or similar spectral type (Fig. 1.4, left

[6]**C**alar **A**lto high-**R**esolution search for **M** dwarfs with **E**xoearths with **N**ear-infrared and optical **E**chelle **S**pectrographs.

[7]**E**chelle **SP**ectrograph for **R**ocky **E**xoplanets and **S**table **S**pectroscopic **O**bservations.

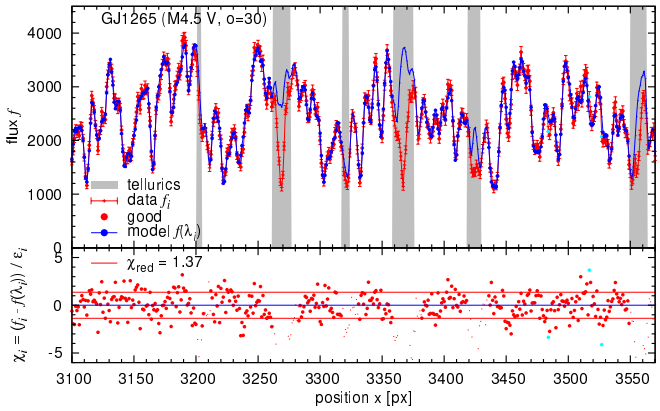

FIGURE 1.5— Illustration of the template matching algorithm to compute radial velocities. The top panel shows the least-squares radial velocity fit of one observation (red) with the CARMENES VIS spectrograph of GJ 1265 to the high S/N template (blue) created from co-adding all the observations of the star. Data points within telluric regions (grey area) are a priori excluded. The fit residuals are shown in the bottom panel. Figure from Zechmeister et al. (2018).

panel). The radial velocity measurement corresponds to the centroid of a Gaussian function fitted to the mean-line profile. This method allows to measure other spectral line indicators such as the full width at half maximum (FWHM), the line contrast or the bisector velocity span, very useful to identify spurious signals not associated to the presence of a planetary companion (Fig. 1.4, right panel).

The second method minimizes the difference between the observed stellar spectrum and a high S/N template obtained by combining all the observations of the same star (Fig. 1.5). This method has demonstrated to be more accurate and precise for cool stars than the CCF technique (Anglada-Escudé & Butler, 2012; Zechmeister et al., 2018), whose masks are incomplete due to the blending of numerous adjacent lines and complicated continuum determination. For these cases a Gaussian fit matches poorly the mean-line profile and a least-squares minimization to the high S/N template is the best approach.

Main results from radial velocity searches

The radial velocity technique has the longest time baseline of all exoplanet discovery methods. Improvements in the precision and long-term stability have allowed dedi-

cated searches in both small and large telescopes to reveal a myriad of exoplanets with diverse mass and orbital properties. Despite being able to target only one star at a time and requiring long exposure times for each measurement, the radial velocity technique has quantified the statistical occurrence of planets at short to moderate orbital distances and it has linked these results with the stellar host properties.

Here, I summarize some of the most important results achieved by radial velocity searches:

- There is a larger-than-expected population of hot Jupiters and a paucity of brown dwarfs in close-in orbits, known as the *brown dwarf desert* (e.g., Marcy & Butler, 2000; Cumming et al., 2008).
- Short-period giant planets are more commonly found orbiting metal-rich stars (e.g., Gonzalez, 1997; Fischer & Valenti, 2005). In contrast, small-planet occurrence is not a function of stellar metallicity for solar-type stars (Sousa et al., 2008; Buchhave et al., 2012).
- Warm Jupiters (loosely defined as those with orbital periods between 10 and 100 d) orbiting metal-rich stars are normally in eccentric orbits (Dawson & Murray-Clay, 2013). This observational result supports that close-in giant planets do not form in situ, but migrate to their current locations via dynamical interactions with planets that also formed in the system.
- M dwarfs have fewer giant planets with periods smaller than 1 yr than solar-type stars (e.g., Endl et al., 2006; Bonfils et al., 2013).
- Low-mass planets at short orbital periods are much more numerous than giant planets (Howard et al., 2010; Mayor et al., 2011).
- Temperate Earth-mass planets have been discovered around the closest M dwarfs. Remarkable systems include Proxima Centauri (Anglada-Escudé et al., 2016), Ross 128 (Bonfils et al., 2018), Teegarden's star (Zechmeister et al., 2019), and GJ 1061 (Dreizler et al., 2020). These planets are the best targets for follow-up studies of atmospheric and habitability characterization with current and future facilities.

1.2.2 Transit method

The transit technique is based upon the concept of an eclipse. An eclipse is the obscuration of one celestial body by another. When the size difference between the bodies is large then the passage of the smaller body in front of the larger one is called a *transit* and the passage of the smaller body behind the larger one is an *occultation*.

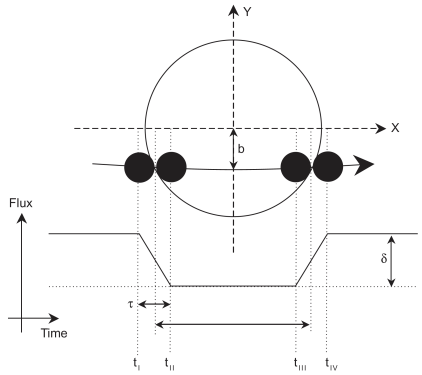

FIGURE 1.6— Illustration of a transit, using the same coordinate system than Sect. 1. Adapted from Seager (2010).

Probability of a transit and inferred quantities

Transits are only detectable by an observer in the line of sight between a star and its planet. As the planet orbits its star, its shadow describes a cone that sweeps out a band on the celestial sphere. A distant observer within the shadow band will observe transits. The angular size of the band is $\sin\theta = (R_p+R_\star)/\mathrm{r}$, where r is the instantaneous star-planet distance as in Eq. 1.1, and R_p and $R_\star$ are the radii of the planet and the star, respectively. The transit is observable if $\cos i \leq (R_p + R_\star)/a$, hence, for a randomly-placed observer the geometric probability to detect a transiting planet is

$$p_{\mathrm{transit}} = \frac{R_p + R_\star}{a}\left(\frac{1 + e\sin\omega}{1 - e^2}\right) \approx \frac{R_\star}{a}\,, \quad \text{for } R_\star \gg R_p \text{ and } e = 0\,. \tag{1.11}$$

Therefore, the probability to find a planet at 1 au distance in a circular orbit transiting a Sun-like star is just 0.5%. Assuming that all Sun-like stars have planets at 1 au then one must survey at least 200 stars before finding a transiting planet. As an example, it has been statistically inferred that one every thousand Sun-like stars have hot Jupiters (e.g., Howard et al., 2012), for which at least 10000 stars must be searched in order to find one such planet. However, in practice, many other factors such as measurement precision or time baseline influence the actual detection potential in a survey.

During a planetary transit, four observables can be measured from a photometric time series, as seen in Fig. 1.6: the orbital period P (for which at least two transits are

required), the transit depth δ, the total transit duration $t_T \equiv t_{IV} - t_I$, and the transit full duration $t_F \equiv t_{III} - t_{II}$. The total transit duration is the time between the first (*ingress*) and the last (*egress*) planet-star contact, while the transit full duration measures the time that the planet is fully in front of the stellar disk. From these observables it is possible to infer the orbital parameters related to the geometric and physical properties of the system (Seager & Mallén-Ornelas, 2003; Winn, 2010). The parameters derivable from observables are the following: the planet-star radius ratio,

$$\frac{R_p}{R_\star} = \delta \quad ; \tag{1.12}$$

the impact parameter b, defined as the projected distance between the planet and star center during midtransit in units of the stellar radius,

$$b \equiv \frac{a}{R_\star}\cos i = \left(\frac{(1-\delta)^2 - \left[\sin^2(\pi\, t_F/P)/\sin^2(\pi\, t_T/P)\right](1+\delta)^2}{1 - \left[\sin^2(\pi\, t_F/P)/\sin^2(\pi\, t_T/P)\right]} \right)^{1/2} \quad ; \tag{1.13}$$

the scaled semi-major axis of the orbit,

$$\frac{a}{R_\star} = \left(\frac{(1+\delta)^2 - b^2\left[1 - \sin^2(\pi\, t_T/P)\right]}{\sin^2(\pi\, t_T/P)} \right)^{1/2} \quad ; \tag{1.14}$$

and the stellar density $\rho_\star$, which can be derived from Eq. 1.14 and Kepler's third law for $M_p \ll M_\star$,

$$\rho_\star \equiv \frac{M_\star}{R_\star^3} = \left(\frac{4\pi^2}{G\,P^2}\right)\left(\frac{(1+\delta)^2 - b^2\left[1 - \sin^2(\pi\, t_T/P)\right]}{\sin^2(\pi\, t_T/P)} \right)^{3/2} \quad . \tag{1.15}$$

The orbital inclination i may be derived a posteriori using the definition of the impact parameter (Eq. 1.13).

Theoretically, the eccentricity can be derived from the different transit ingress and egress times (de Kort, 1954). However, for exoplanets, this effect is of the order of seconds or fractions of seconds and observationally very difficult to measure. On the other hand, the transit technique alone cannot measure the planetary mass, hence, complementary radial velocity data is often used to infer the absolute mass of the planet (M_p) and constrain the eccentricity (e and ω) of the orbit.

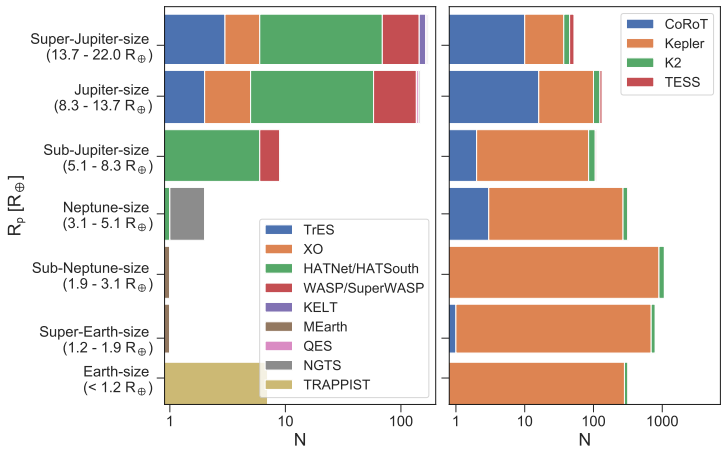

FIGURE 1.7— Histogram of the number of transiting planets by size, color-coded by discovery facility. The left panel shows the discoveries from ground-based searches, while the right panel shows the discoveries from space-based searches. Data from the NASA Exoplanet Archive as of September 1, 2020.

Relevant transit searches

The transit technique is most sensitive to short-period planets with large radii around small stars. The sensitivity decreases as a function of increasing star-planet distance, which relates also with the smaller geometric probability of these cases. Although the observation of eclipses is among the oldest methodologies in astronomy (see Briot & Schneider, 2018, for a thorough review of the history of transit searches), the first exoplanet transit detection was the partial transit of the hot Jupiter HD 209458 b, previously known from radial velocity measurements, reported by Henry et al. (1999) and later confirmed independently by Henry et al. (2000) and Charbonneau et al. (2000). The first "unknown" transiting planet was discovered and confirmed using radial velocity measurements by Konacki et al. (2003).

Since then, ground-based searches such as TrES[8] (Alonso et al., 2004), XO (McCullough et al., 2005), HATNet/HATSouth[9] (Bakos et al., 2004, 2013), WASP[10] (Pollacco et al., 2006), KELT[11] (Pepper et al., 2007), MEarth (Nutzman & Charbonneau,

[8] **Tr**ans-Atlantic **E**xoplanet **S**urvey.
[9] **H**ungarian **A**utomated **T**elescope.
[10] **W**ide **A**ngle **S**earch for **P**lanets.
[11] The **K**ilodegree **E**xtremely **L**ittle **T**elescope.

2008), QES[12] (Alsubai et al., 2013), NGTS[13] (Wheatley et al., 2013), or TRAPPIST[14] (Gillon et al., 2013), have discovered hundreds of transiting planets (Fig. 1.7, left panel). However, ground-based photometry has a limiting precision around 1 mmag due to atmospheric effects such as scintillation and variable atmospheric extinction. Thus, most of the transit searches from ground have detected hot Jupiters orbiting every stellar type and smaller planets only around M dwarfs.

Space-based transit searches, on the other hand, have made the transit method the most effective and sensitive to date. The absence of atmospheric effects together with the long, uninterrupted baseline of the observations have pushed the detection limits to the discovery of Earth-sized planets orbiting Sun-like stars and provided more than 2000 new exoplanets so far (Fig. 1.7, right panel).

The first rocky exoplanet (CoRot-7 b; Léger et al., 2009) was discovered by the *CoRoT* satellite (Baglin et al., 2006), the first space mission partially dedicated to exoplanets, which ran from 2007 to 2012 and discovered 32 planets[15]. Its successor, *Kepler* (Borucki et al., 2010), revolutionized the field of exoplanet science. Carrying out a 4-year mission to survey a single field of 170 000 stars, *Kepler* has discovered more than half of all known exoplanets[16]. After a failure of two of the four spacecraft's reaction wheels, the *Kepler* mission ended and was reinvented under the name of *K2* (Howell et al., 2014). The observing mode was adapted, due to the unreliable pointing of the spacecraft, to surveying several fields near the ecliptic plane in campaigns of 80 days each from May 2014 until October 2018, when the spacecraft ran out of fuel. The new mission allowed, for the first time, to routinely confirm and characterize transiting planetary candidates by means of precise radial velocities thanks to the newly targeted stars, 3 magnitude brighter in average than its predecessor. International collaborations such as KESPRINT[17] (e.g., Sanchis-Ojeda et al., 2015; Johnson et al., 2016; Fridlund et al., 2017) have capitalized this opportunity to conduct large campaigns of radial velocity follow-up to measure the masses and study the diversity of bulk densities and internal compositions of small exoplanets.

Currently, the *Transit Exoplanet Survey Satellite* (*TESS*; Ricker et al., 2014) is the main space mission in orbit dedicated to the discovery of transiting planets. Its primary mission, finished in July 2020, was a 2-year survey of 200 000 nearby, bright stars covering approximately 63% of the entire sky in pointings of 27 days each (Fig. 1.8). As

[12] **Q**atar **E**xoplanet **S**urvey.
[13] **N**ext **G**eneration **T**ransit **S**urvey.
[14] **TRA**nsiting **P**lanets and **P**lanetes**I**mals **S**mall **T**elescope.
[15] According to the NASA Exoplanet Archive, accessed September 1, 2020.
[16] About 2400 out of 4200 exoplanets, according to the NASA Exoplanet Archive, accessed September 1, 2020.
[17] http://kesprint.science/.

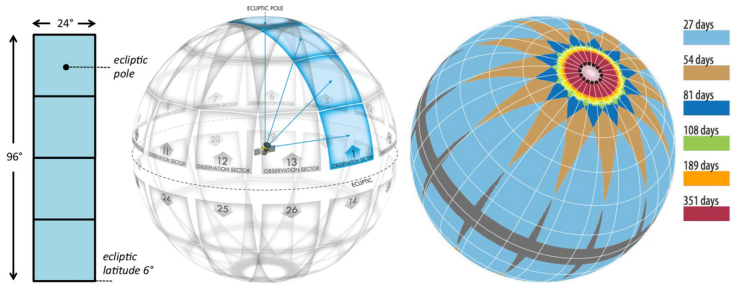

FIGURE 1.8— Illustration of *TESS* field of view and observing strategy. *TESS* consists of 4 wide-field cameras that cover a stripe of the sky of 24 by 96 deg. Each hemisphere is divided in 13 Sectors with uninterrupted photometry for 27 days, overlapping regions are monitored further. The pointings for Sectors 14-16 were shifted toward the North ecliptic pole to minimize impacts of scattered light from the Earth and Moon, loosing 12% of the expected sky coverage prior the mission. Credit: NASA.

of today, it is undergoing its first extended mission until September 2022. The stars *TESS* is studying are 30 to 100 times brighter than those the *Kepler* and *K2* missions surveyed, which enables far easier follow-up observations with both ground-based and space-based telescopes. *TESS* is expected to detect approximately 1300 exoplanets in its 2-min cadence data, including 250 smaller than $2\,R_\oplus$ (Barclay et al., 2018), but its Level One science requirement is to measure the masses and radii of at least 50 planets smaller than $4\,R_\oplus$. So far, *TESS* has confirmed 82 planets[18] and has approximately 2500 candidates pending validation and/or confirmation. The Level One science requirement is well underway, with more than 30 exoplanets with measured masses and radii published, and about 40 additional planets in advance stages of preparation (Sam Quinn, priv. comm.). The mission's legacy will be a list of the closest transiting planetary systems, which will always be the best targets for follow-up studies and, especially, atmospheric characterization.

In the near future, the ESA mission *PLATO* (*PLAnetary Transits and Oscillations of stars*; Rauer et al., 2014) will be launched into an orbit around the L2 point to perform a 4-year survey of large sky areas using 24 sensitive, small-aperture telescopes. *PLATO* is expected to discover hundreds of Earth and super-Earth planets in the habitable zone of Sun-like stars, i.e., the region where a planet with sufficient atmospheric pressure can maintain liquid water on its surface. Exquisite photometric precision and a sufficiently long baseline is necessary to achieve this goal, out of the reach of any

[18] As of December 1, 2020, according to the NASA Exoplanet Archive

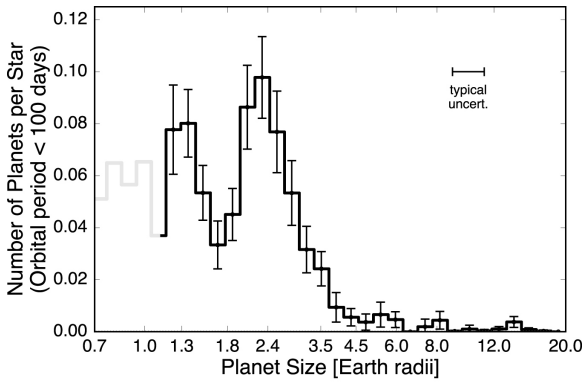

FIGURE 1.9— The frequency of planets around Sun-like stars with orbital periods smaller than 100 days as measured by *Kepler*. The bimodal distribution indicates two distinct populations of planets: those that are primarily rocky with very thin atmospheres, and those that have substantial atmospheres, which are separated by a gap. From Fulton et al. (2017).

other ground- or space-based facility nowadays.

Main results from transit searches

Due to its exquisite sensitivity, long temporal baseline and the large number of monitored stars, most of the understanding of exoplanet demographics come from the results of the *Kepler* mission. *Kepler* was able to detect Mercury-sized planets at short orbital distances and planets slightly larger than the Earth with periods shorter than one year (Fig. 1.2).

Here, I summarize some of the most important results achieved by transit searches, in particular, with the *Kepler* mission:

- Small planets ($R_p < 4\,R_\oplus$) in close-in orbits (less than 1 au) are ubiquitous in the Galaxy (e.g., Howard et al., 2012).
- The occurrence rate of small ($R < 4\,R_\oplus$), close-in ($P < 100$ d) planets features a paucity of planets with sizes between 1.7–2.0 $R_\oplus$ (Fulton et al., 2017, Fig. 1.9). The so-called radius gap is likely a result of the existence of an orbital separation-dependent transition between primarily rocky planets and non-rocky planets that host extended envelopes rich in hydrogen and helium.

- Planets in *Kepler* multiplanetary systems are regularly spaced and similar in size, also known as the "peas in a pod" pattern (Weiss et al., 2018).

- Observationally, there is a dichotomy between the planets in systems displaying two or three transits and the planets in systems displaying only one transit (Lissauer et al., 2011; Fabrycky et al., 2014). Double-transit and triple-transit systems have mostly small planets, while the single-transit systems host both small planets and an additional population of large planets. Although originally difficult to reconcile with synthetic planet population models (e.g., Lissauer et al., 2011; Johansen et al., 2012), this feature has been suggested to be simply an observational artifact (Izidoro et al., 2017).

- In addition, systems with only one detected transiting planet have a different eccentricity distribution than systems with multiple detected transiting planets. Single transiting systems have low to moderate eccentricities, while systems with multiple detected transits are almost circular (Van Eylen et al., 2019).

- There is approximately one Earth-sized, temperate planet every 5 M-dwarf stars (Dressing & Charbonneau, 2015). Extrapolating results from shorter orbital distances, there is one terrestrial habitable-zone planet every 10 Sun-like stars (Burke et al., 2015).

1.3 The M dwarf opportunity

M dwarfs account for 70% of the stars in the Milky Way (Reid & Gizis, 1997; Bochanski et al., 2010) and dominate the stellar population in the solar neighborhood — 50 out of the 63 stars within 5 pc from the Sun are M dwarfs. They are among the coolest (2300 K $< T_{\rm eff} <$ 4000 K; Cifuentes et al. 2020) and smallest (0.1 $R_\odot <$ $R_\star <$ 0.6 $R_\odot$; Cifuentes et al. 2020) stars and they are the transition between stellar and substellar objects[19]. As a spectral class, M dwarfs span an order of magnitude in mass and two orders of magnitude in luminosity. They span a larger range in mass than the next three spectral classes (FGK) combined (Boyajian et al., 2012, 2013; Cifuentes et al., 2020).

M dwarfs, given their low masses, burn their nuclear fuel at considerably slower rates compared to Sun-like or brighter stars (Iben, 1967). They are extremely long-lived, with main-sequence lifetimes of trillions of years for the lowest-mass M dwarfs (Laughlin et al., 1997). The main feature of this spectral type is the prevalence of

[19] A substellar object is an astronomical object whose mass is smaller than the smallest mass at which hydrogen fusion can be sustained (approximately 0.08 $M_\odot$). This definition includes *brown dwarfs* and also exoplanets.

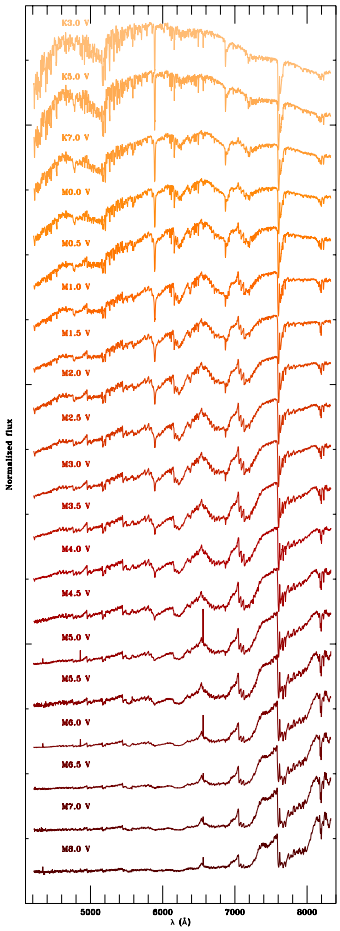

FIGURE 1.10— Low resolution spectra of prototype low-mass stars. Spectral types are indicated in steps of 0.5 subtypes for M dwarfs. M dwarfs are often refer as early-type for spectral types between M0.0 V and M2.5 V, mid-type from M3.0 V to M5.5 V, and late-type from M6.0 V to M8.0 V. From Alonso-Floriano et al. (2015).

molecular bands at optical wavelengths, especially the ones produced by titanium oxide (Fig. 1.10). Moreover, M dwarfs are cool enough to exhibit molecular bands of diatomic hydrogen, water and vanadium oxide making the spectral continuum almost impossible to determine. The determination of atmospheric parameters for these stars is more difficult than for hotter Sun-like stars (see Passegger et al., 2016, 2018, 2020, for a review of the challenges to infer the physical properties of M dwarfs).

1.3.1 Planets orbiting M-dwarf stars

Planets orbiting M dwarfs offer several detection advantages. A planet of a given mass and size will induce a larger radial velocity semi-amplitude (Eq. 1.10) and block a larger fraction of the stellar host disk during a transit (Eq. 1.12) on a M-type host star than a Sun-like star. In particular, for a typical mid-type M4 V, the radial velocity signature and the transit depth are 2.5 and 15 times larger, respectively, than for the Sun. However, the reason why M dwarfs have become the favorite targets for exoplanet studies in recent years is their low luminosities.

The habitable zone (HZ) of a star is defined as the range of orbital distances in which a planet can possibly maintain liquid water on its surface and it depends on the star bolometric luminosity (Kasting et al., 1993; Kopparapu et al., 2013, 2014). The low effective temperatures of M dwarfs move their HZs closer in, enhancing planet detectability and transit probability. The probability of a transit for a planet residing in the HZ is 1.5% (for a M4 V dwarf) and 2.7% (for a M8 V dwarf), significantly above the Earth-Sun value of 0.47% and exhibiting transits much more frequently (Charbonneau & Deming, 2007).

There has been several dedicated studies to find planets around M dwarfs with both the radial velocity and transit techniques. The most relevant radial velocity searches of planets orbiting M dwarfs are the ones by Zechmeister et al. (2009), using UVES; Bean et al. (2010), using CRIRES; and Bonfils et al. (2013), using HARPS. Ongoing surveys include those from the instruments HPF in the 10-m Hobby-Eberly Telescope (Mahadevan et al., 2012), CARMENES (Quirrenbach et al., 2014), SPIRou at the 3.6-m Canada-France-Hawaii Telescope (Artigau et al., 2014), IRD at the 8-m Subaru telescope (Kotani et al., 2014), and the Red Dots project using HARPS (e.g., Anglada-Escudé et al., 2016; Ribas et al., 2018). On the other hand, transit searches such as MEarth and *Kepler/K2* have helped to constrain the occurrence of planets around M dwarfs (η) and, in particular, the holy grail value of $\eta_\oplus$, i.e., the relative abundance of Earth-type planets in the habitable zone.

MEarth predictions from Berta et al. (2013) agreed with those of *Kepler* (Dressing & Charbonneau, 2013) claiming that there is one Earth-sized planet every two M dwarfs. The estimate of $\eta_\oplus$ by Dressing & Charbonneau (2013), $\eta_\oplus = 0.15^{+0.13}_{-0.06}$, was

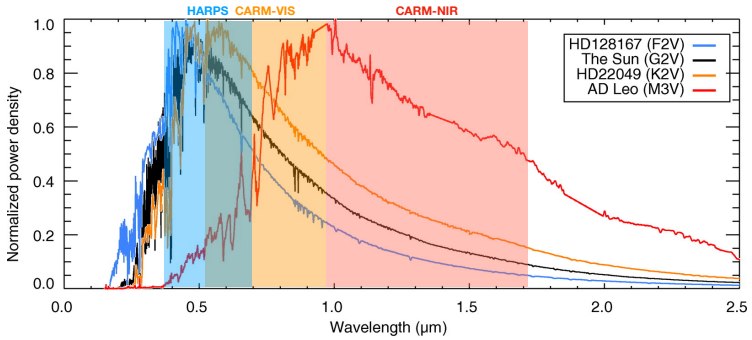

FIGURE 1.11— Spectral energy distributions for representative F-, G-, K-, and M-dwarf stars, normalized by the peak flux. The wavelength range covered by the high-resolution spectrographs HARPS (blue) and CARMENES (visible and near-infrared arms in orange and red, respectively) is indicated. Adapted from Shields et al. (2013).

later revised by Kopparapu (2013) to be $\eta_\oplus = 0.51^{+0.10}_{-0.20}$, in agreement with HARPS radial velocity results from Bonfils et al. (2013, $\eta_\oplus = 0.41^{+0.54}_{-0.13}$). Using the full *Kepler* dataset, Dressing & Charbonneau (2015) and Gaidos et al. (2016) estimated an occurrence rate for small planets with periods below 200 days of approximately $\eta = 2.3 \pm 0.3$ planets per M dwarf. Recent studies with improved stellar parameters using *Gaia* (Gaia Collaboration et al., 2018) leave the number at $\eta = 1.19^{+0.70}_{-0.49}$ for mid-type M dwarfs (Hardegree-Ullman et al., 2019). This value decreases towards earlier spectral types and solar-type stars.

The latest estimate of $\eta_\oplus$ for M dwarfs has been derived by Hsu et al. (2020) using the final Kepler DR25 catalog, with updated stellar properties from *Gaia* and 2MASS. Their value, $\eta_\oplus = 0.33^{+0.10}_{-0.12}$, is still in agreement with previous estimates, but with considerably smaller uncertainties. Occurrence rates for M dwarfs are greater than those for solar-type stars and indicate that most M dwarfs harbor planetary systems.

1.3.2 Challenges and achievements

The spectral energy distribution of M dwarfs

Despite the reasons above, M dwarfs have not been historically as well studied as other spectral types. First of all, their relatively cool temperatures cause their spectra to peak at wavelengths between 900–1200 nm rather than in the optical and, therefore, they were out of reach for most "classic" high-resolution spectrographs (Fig. 1.11).

Curiously, none of the M dwarfs in the sky are visible to the naked eye. The brightest of all, GJ 887, has a visual magnitude $V = 7.34$ mag.

To overcome this, the next generation of high-precision velocimeters are being adapted from optical instruments to near-infrared (NIR) spectrographs. Instruments like the aforementioned CARMENES, HPF, SPIRou IRD and, in the near future, NIRPS[20] (Bouchy et al., 2017) are optimized to observe M dwarfs thanks to their red-optical and NIR wavelength ranges, where the spectral energy distributions of these stars peak. Major developments in cryogenic and detector technologies have brought the precision of these instruments ($\sim$ 3–5 m s^{-1}) close to their optical counterparts, although there is still room for improvement in calibration and telluric contamination modeling techniques.

Beside the precision limits set by the instrument, radial velocity precision also depends on the S/N. Precise radial velocity measurements are therefore limited by photon noise and the amount of spectral information that is available in a certain wavelength interval and can be used to measure the Doppler shift. Reiners et al. (2018) analyzed the empirical information on the radial velocity precision from more than 6500 CARMENES observations (Fig. 1.12). They measured, for the first time, that for all M-type dwarfs, the highest radial velocity precision can be reached in the wavelength range 700–900 nm. Observations at longer wavelengths are equally precise only at the very latest spectral types (M8 and M9), where the large amount of absorption features compensates for their intrinsic faintness. In a follow-up study, Reiners & Zechmeister (2020) concluded that a HARPS-like instrument outperforms a NIR-only spectrograph for FGKM stars up to spectral type M4 V. However, a red-optical design such as the visual arm of the CARMENES spectrograph outperforms a HARPS-like design for M dwarfs of every spectral type thanks to its coverage of the 700–900 nm wavelength range. Therefore, although next generation spectrographs are moving to NIR wavelengths, reaching 1 m s^{-1} precision or below will be possible only for late-type M stars using large telescopes.

With respect to transit searches, the problem of the NIR-peaked spectral energy distribution of M dwarfs have been largely overcome by observing in the z-band ($\lambda_{\rm eff} \sim 900$ nm). Commercial charge-coupled devices are considerably cheaper and more precise than infrared detectors, although it would allow to use smaller aperture telescopes. However, the main challenges of dedicated M dwarf planet transit searches are their faintness and that they are uniformly distributed across the sky. Wide-field surveys are not a valid approach since there are few bright suitable targets in a single pointing, hence the stars must be observed sequentially. Projects like MEarth, TRAPPIST or SPECULOOS have tried to overcome this aspect by having several telescopes

[20] **N**ear-**I**nfra**R**ed **P**lanet **S**earcher.

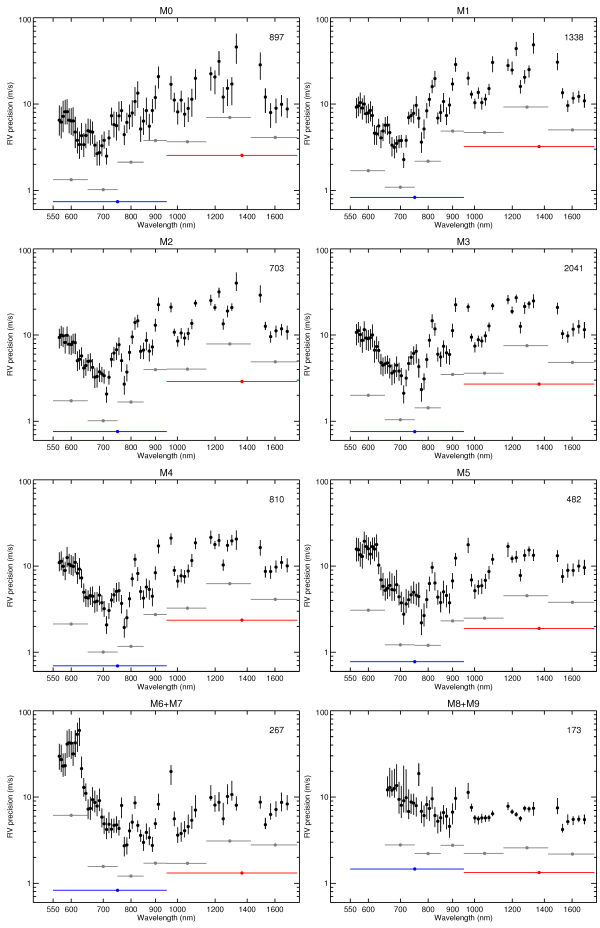

FIGURE 1.12— Empirical radial velocity precision for individual spectral orders of CARMENES observed in the sample stars. Each panel shows for each order the median value for all observations taken of stars with the indicated spectral types. Gray points show quadratically added for 100 or 200 nm wide spectral windows, as indicated by the horizontal bars. Blue and red symbols show the CARMENES VIS and NIR spectral ranges. The number of observations per spectral type is given in the upper right corner of each panel. From Reiners et al. (2018).

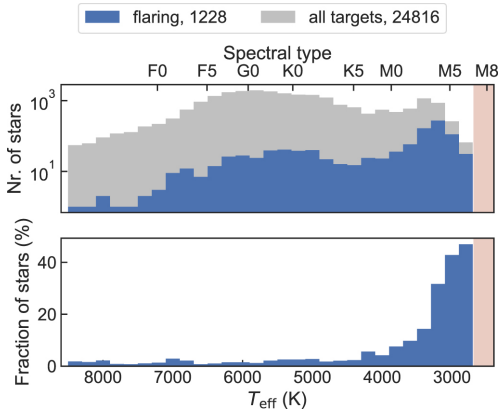

FIGURE 1.13— Histograms of the number (upper panel) and fraction (lower panel) of flaring stars (blue) compared with the total number of stars (gray) in the *TESS* short-cadence observations of Sectors 1 and 2, shown as a function of the stellar effective temperature. M dwarfs dominate the sample of flaring stars, while FGK stars rarely have detectable flares. From Günther et al. (2020a).

in both hemispheres and curated, precisely-selected stellar target lists. With the increase of high-precision Doppler instruments optimized for M dwarfs, radial velocity follow-up of transiting candidates have not been a major obstacle to discard astrophysical false positives and confirm and characterize the planet detections.

Stellar activity

Despite all the above, the main challenge of planet searches around M dwarfs are the stars themselves. M dwarf variability was first detected and reported by Hertzsprung (1924). The realization that these changes in brightness were due to short time scale flares only came in 1947, when Edwin Carpenter noted a 3 mag brightening of UV Ceti (M5.5 V) in just 12 min. However, flares are not the only physical processes at play in the photospheres and chromospheres of M dwarfs. There are several mechanisms acting with different timescales and manifestations in spectroscopic and photometric observations. Here, I summarize some of the sources of stellar magnetic activity in M dwarfs.

Flares. Stellar flares are explosive magnetic reconnection events in a star's magnetosphere, releasing bursts of isotropic radiation (Benz & Güdel, 2010). They emit energy

ranging from 10^{23} erg (*nanoflares*) to 10^{33}–10^{38} erg (*superflares*) in short timescales of minutes to a few hours. Most of the emission is in the X-ray spectrum, but large flares can be also detected with photometric instruments in the optical. Besides, large flares are often accompanied by coronal mass ejections, but both events can also appear independently. The largest study to date of stellar flares by Günther et al. (2020a) using *TESS* data shows that mid- to late-type M dwarfs are the most common flaring stars (Fig. 1.13), with an occurrence rate (40%) significantly larger than for early M dwarfs (10%). Hotter stars of type FGK seem to rarely host flaring events, although this is also partly related with *TESS* detection biases. Photometric and radial velocity measurements affected by flares can be easily identified by their characteristic brightness and line intensity spike in short timescales followed by an exponential decay. These measurements are usually neglected by planet searches (Reiners, 2009).

Stellar oscillations. Pressure waves, also known as *p-modes*, propagate at the surface of Sun-like stars contracting and dilating the stellar surface over timescales of a few minutes. These oscillations create observable pulses in brightness and in the radial velocity with amplitudes between 10 and 400 $\mathrm{cm\,s^{-1}}$, depending on the star type and evolutionary stage (Schrijver & Zwaan, 2000). This phenomenon is predominantly observed in Sun-like stars and post main sequence stars. Theoretical studies (Rodríguez-López et al., 2012, 2014) support the existence of pulsations in M dwarfs, although the predictions have not been observationally confirmed with radial velocities (Berdiñas et al., 2017). Photometric campaigns have only been able to establish an upper limit in their amplitudes of tens of μmag (Rodríguez et al., 2016).

Granulation. Surface granulation is a phenomenon that can only be directly measured on the Sun, but is expected to be present in other stars. The different phenomena of granulation are due to the convective nature of solar-type stars and can be found all over the stellar surface, except in active regions where convection is suppressed (Dravins, 1982; Gray, 1992). Convection creates time-variable asymmetries in the stellar absorption lines due to a combination of upward flowing, bright, hot, blue-shifted bubbles of plasma, known as *granules*, that eventually cool, darken, and fall back down, red-shifting, into the surrounding regions, known as *intergranular lanes* (Fig. 1.14, left). Since the granules are brighter and cover more surface area, they do not completely cancel out the intergranular lane contribution, which acts to depress the red wing of the combined line profile (Fig. 1.14, right). The larger contribution from the granules provoke an overall net blue-shift for most absorption lines.

The amplitudes of granulation phenomena are similar to the ones for p-modes (Kjeldsen et al., 2005; Kjeldsen & Bedding, 2011). The reason for this is that over the stellar disc much of the plasma upflows and downflows cancel out, although the ve-

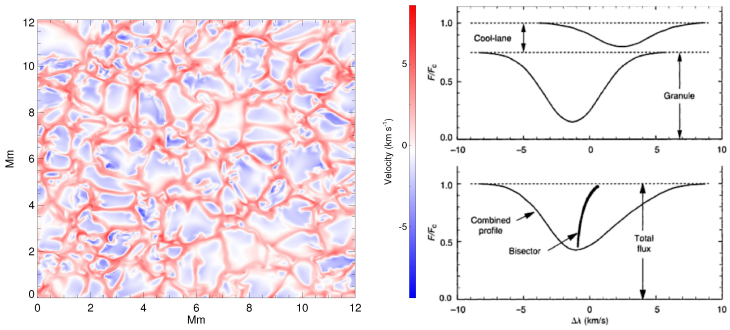

FIGURE 1.14— *Left*: Net radial velocity effect for a 3D simulation of a Sun-like star at disc center. *Right*: Illustration of the relative (top) and combined (bottom) contribution of the bright, blueshifted granules and the dark, redshifted intergranular lanes. The curvature in the line bisector displays the asymmetries in the combined profile and the convective blueshift net effect. Adapted from Cegla (2019).

locities for individual cells are between 1–4 km s^{-1}. The effect of granulation decrease toward low-mass stars, so it is not the main source of astrophysical noise in M dwarfs (Meunier et al., 2017). The effect of stellar oscillations and granulation in both photometric and radial velocity observations can be typically averaged out with sufficiently long exposure times and targeted observing strategies (e.g., Dumusque et al., 2011b; Chaplin et al., 2019).

Starspots, faculae and plages. Dark spots, hot faculae or bright plages are usually referred as *active regions* in the photospheres of stars. They exist in all the stars with outer convective zones and, in the case of M dwarfs, they are the main source of the stellar activity in photometric and spectroscopic observations.

Starspots appear as dark spots on the surface of the stars. They are created by local magnetic fields on the surface, strong enough to suppress the overturning convective motion and thus block or redirect the flow of energy from the stellar interior outwards to the surface, appearing locally cooler and darker. Their temperatures in the centers are typically 500–2000 K smaller than the surrounding photosphere. This temperature difference could give rise to a brightness variation up to 0.6 mag between the spot and the surface next to it. Faculae are bright spots that form in the intergranular lanes by concentration of magnetic field lines. Plages are bright regions near starspots also associated with concentrations of magnetic fields. They are the counterpart of faculae in the chromosphere and are best seen in Hα.

Active regions create a photometric variation, a temporally-changing radial veloc-

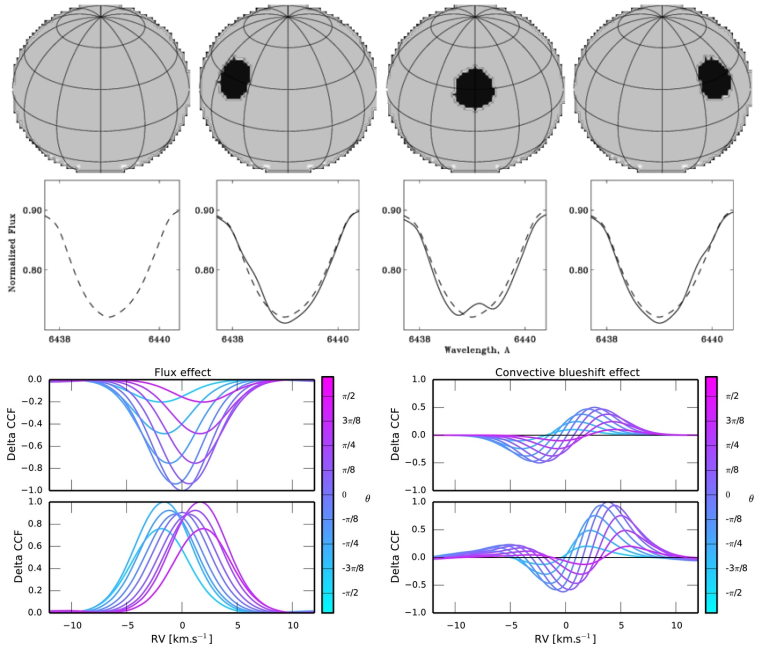

FIGURE 1.15— *Top*: Spectral line profiles for a model fast rotating star with a spot moving across the disk as the star rotates. *Bottom*: Radial velocity effect induced by an equatorial spot or plage of size 1% on a star seen equator-on as it rotates. The color indicates the phase of the stellar rotation. The left column shows the flux correction for a spot (top) or plage (bottom). The right column shows the convective blueshift correction when assuming Gaussian CCFs (top), and when assuming observed CCFs (bottom). The use of observed (non-symmetric) CCFs breaks the symmetry of the convective blueshift correction. Adapted from Berdyugina (2005) and Dumusque et al. (2014).

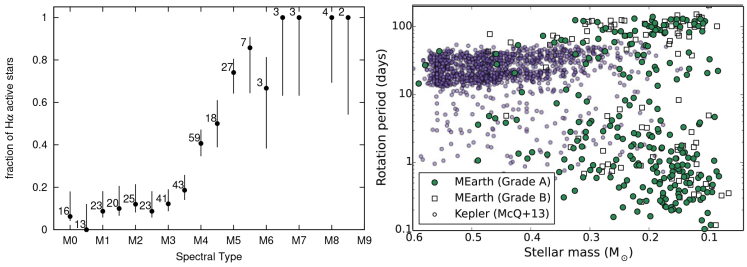

FIGURE 1.16— *Left*: Fraction of Hα active stars per spectral subtype from a sample of spectroscopic observations with CARMENES. Numbers reflect the total number of sample stars in the corresponding bin. The fraction of active stars raises steeply for spectral types later than M4 V. *Right*: Stellar rotation period as a function of stellar mass. Purple circles are photometric measurements from *Kepler* (McQuillan et al., 2013), green circles and white squares are photometric measurements from MEarth (Newton et al., 2016b). There is evidence for two populations of slow and fast rotators, and a lack of stars with intermediate rotation periods. Adapted from Schöfer et al. (2019) and Newton et al. (2016b).

ity signal, and spectral line profile distortion due to their distinct temperatures that is coupled with the star's rotation. As a star rotates, starspot groups form, are carried across the face of the star, and eventually decay because of turbulent diffusion. A single spot or spot group depresses the observable photospheric flux by an amount that depends on the spot's area, surface brightness, and limb darkening. Spectroscopically, on a rotating star, the light blocked by dark spot contains both continuum and line absorption features, Doppler shifted by an amount that depends on the stellar equatorial rotation speed, the inclination of the rotation axis to the line of sight, and the projected distance of the spot from the stellar rotation axis. The resulting distortion of the rotation profile consists of a bright bump, which migrates across the line absorption profile from blue to red as the spot traverses the visible hemisphere, producing a centroid radial velocity variation and a net convective blueshift effect (Fig. 1.15). The form of the photometric and spectroscopic modulation seen by an observer depends on the latitude of the spot, the inclination of the stellar rotation axis to the line of sight, and the ratio of the spot lifetime to the rotation period.

When a star is young, contraction and accretion mechanisms speed up its spin, while when it reaches the main sequence, it slows down. The increase in rotation period is the result of angular momentum losses via magnetized stellar winds (Hartmann & Stauffer, 1989; Barnes, 2003). The stellar spin down leads to a decrease in dynamo activity and, as a consequence, a decrease in overall magnetic activity as the star ages. For a given stellar mass, it is possible to derive a direct relation between the stellar rotation period and the age of the star, leading to an indirect method to measure stellar ages

called *gyrochronology* (Skumanich, 1972; Noyes et al., 1984; Barnes, 2007; Mamajek & Hillenbrand, 2008). M dwarfs follow this relation up to the spectral types around M4 V (Chabrier & Baraffe, 1997). At this stellar mass, M dwarfs transition from partially to fully convective (Reiners, 2009) and are expected to have a different type of dynamo mechanism than solar-type stars. However, recent studies show no evident transition in activity properties, but the appearance of two populations of slow and fast rotators, with a significant stellar activity enhancement (Fig. 1.16). Therefore, mid-type M dwarfs maintain rapid rotation, and enhanced magnetic activity, for the first several billion years and then spin-down rapidly, reaching periods of approximately 100 days by a typical age of 5 Gyr, but still with stable photometric and spectroscopic modulations.

Active regions coupled with stellar rotation influence the ability to detect and derive precise and accurate orbital parameters of a planetary system. The overlap of the planet and the active zones on the surface of a star can create anomalies inside the transit lightcurve that cause difficulties in constraining the transit depth and, as a result, the radius of the planet, the limb darkening profile of the star or even the presence of additional transiting planets (Rabus et al., 2009; Czesla et al., 2009; Oshagh et al., 2013). Particularly challenging is to study the influence of active regions that are not occulted by the planet. The flux blocked by a planet traversing an immaculate photosphere is constant. If unocculted spots are present, the ratio of flux blocked in transit to total flux out of transit is larger. More importantly, because the spot contrast is greater at blue wavelengths due to the temperature difference, the inferred planet radius can exhibit a wavelength-dependent overestimation (Pont et al., 2008). Emission from faculae is also wavelength-dependent and needs to be modeled correctly (Rackham et al., 2018). On the other hand, stellar spot anomalies can cause offsets in the transit timing measurement that can lead to a false-positive detection of a non-transiting planet by the transit-timing variation method (Sanchis-Ojeda & Winn, 2011; Sanchis-Ojeda et al., 2011; Oshagh et al., 2012).

Stable, periodic stellar signals originated from active regions can mimic radial velocity variations induced by a true planetary companion, leading to false positives (e.g., Queloz et al., 2001; Huélamo et al., 2008). Besides, stellar activity generates correlated noise in the radial velocity and prevents accurate measurements of the planetary system parameters. The amplitude of the Doppler shifts ranges between a few cm s^{-1} to hundreds of m s^{-1} and depend on the projected rotational velocity of the star, the spectrograph resolution and both the size and temperature of the spot (Saar & Donahue, 1997; Desort et al., 2007). A number of studies have shown that radial velocity variability caused by stellar spots is wavelength dependent, because the flux contrast of cold spots and hot faculae is smaller toward the infrared (Desort et al., 2007; Reiners et al., 2010). Thus, in principle, measurements obtained at different spectral bands

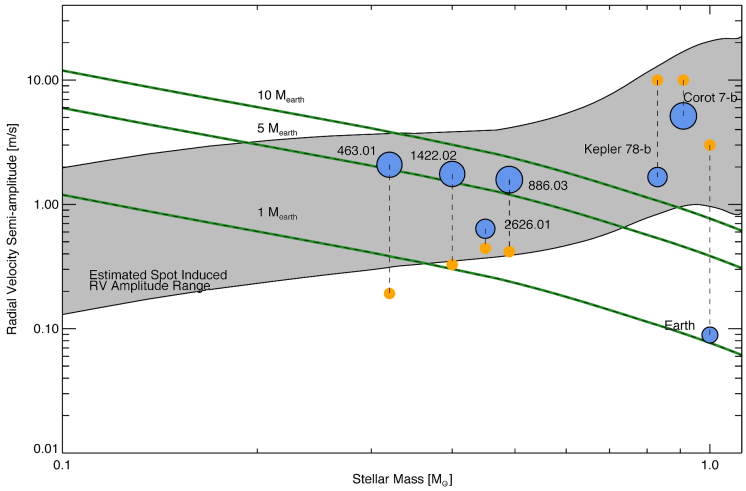

FIGURE 1.17— Estimated characteristic semi-amplitudes of radial velocity signals. The semi-amplitude of rotational modulations due to starspots as a function of stellar mass is shown in gray. The radial velocity semi-amplitude of exoplanets in the habitable zone of stars of various masses are drawn in green lines. Characteristic exoplanets are plotted in blue, with the size of the dot corresponding to the planetary radius. Each exoplanet plotted is connected by a thin dashed vertical line to an orange dot, corresponding to the predicted or observed radial velocity semi-amplitude induced by stellar rotation. Earth- and super-Earth-mass planets in the HZ of M dwarfs ($M_\star < 0.6\,M_\odot$) have radial velocity signals caused by planetary companions or active regions with the same amplitude. From Vanderburg et al. (2016).

can be used to correct for intrinsic stellar radial velocity jitter. However, the picture is much more complicated because the effects of limb darkening, convection, and magnetic field, for instance, can cause both amplitude and phase differences between radial velocities derived from spectra at different wavelengths. On the other hand, these differential wavelength-dependent effects can be used to constrain the properties of stellar active regions themselves (e.g., Herrero et al., 2016; Baroch et al., 2020).

While stellar activity presents challenges to radial velocity detection of planets around stars of every spectral type, only for M dwarfs does the characteristic rotation period coincide with the habitable zone (Newton et al., 2016a; Vanderburg et al., 2016, Fig. 1.17). Numerous approaches have been proposed to model and subtract the contribution of stellar activity from radial velocity measurements: using linear correlation models between radial velocity and spectral activity indicators (Queloz et al., 2001; Boisse et al., 2011; Meunier & Lagrange, 2013; Suárez Mascareño et al., 2015, 2017;

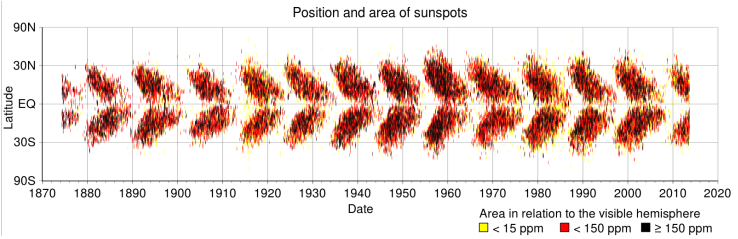

FIGURE 1.18— "Butterfly" diagram of the Sun conceived by Annie S. D. Maunder in 1904. Sunspots are typically confined to an equatorial belt between ±35 degrees latitude. At the beginning of a new solar cycle, sunspots tend to form at high latitudes, but as the cycle reaches a maximum (large numbers of sunspots) the spots form at lower latitudes. Near the minimum of the cycle, sunspots appear even closer to the equator, and as a new cycle starts again, sunspots again appear at high latitudes. From the solar gropu at NASA Marshall Space Flight Center.

Astudillo-Defru et al., 2017, e.g.,), fitting additional Keplerian signals to account for the stellar rotational period and its harmonics (e.g., Bonfils et al., 2007; Boisse et al., 2011), the floating chunk offset method (e.g., Hatzes et al., 2011; Hatzes, 2014; Dai et al., 2017), analytical surface and spot modelling (Lanza et al., 2010; Boisse et al., 2012; Herrero et al., 2016), computing the radial velocity using individual line measurements that are less affected by stellar activity (Dumusque, 2018; Cretignier et al., 2020), correlations with photometric brightness (e.g., Aigrain et al., 2012), or using Gaussian processes (Haywood et al., 2014; Grunblatt et al., 2015; Rajpaul et al., 2015), among others. This is currently one of the most active topics in the exoplanet field and, although enormous progress has been made (e.g., Dumusque, 2016; Dumusque et al., 2017), there is still much work to do in order to push the detection of radial velocity signals at the level of $10\,\mathrm{cm\,s^{-1}}$, which corresponds to the internal instrumental precision of the state-of-the-art spectrographs to date.

Magnetic cycles. The Babcock-Leighton solar dynamo cycle corresponds to an oscillatory exchange of energy between toroidal and poloidal solar magnetic fields in a timescale of 22 years (Schrijver & Zwaan, 2000). The solar cycle gives rise to a quasi-periodic 11-year cycle characterized by an increasing and decreasing number and size of active regions, coronal mass ejections, strong prominences, and levels of solar radiation (Fig. 1.18). During periods of minimum activity the solar photosphere is immaculate for months at a time, while during periods of maximum activity up to about 0.5% of the entire disc may be covered with spots and umbrae (Watson et al., 2011). These long-term magnetic cycles have been also observed in spectroscopic monitoring programs (Vaughan et al., 1981; Makarov, 2010) and several studies have

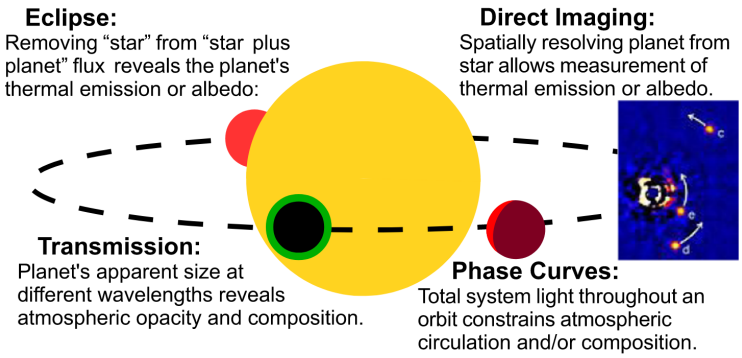

FIGURE 1.19— Observational approaches used to characterize the atmospheres of exoplanets. From Crossfield (2015).

demonstrated that the majority of Sun-like stars exhibit magnetic activity cycles with periods ranging from 7 to 30 years (Duncan et al., 1991; Baliunas et al., 1995; Santos et al., 2010). The corresponding radial velocity signal from magnetic cycles can reach tens of $m\,s^{-1}$.

Magnetic cycles have been reported around M dwarfs with photometry and spectroscopy independently (Savanov, 2012; Gomes da Silva et al., 2012; Robertson et al., 2013; Díez Alonso et al., 2019). The durations of the activity cycles appear to be independent of the rotation periods. Fortunately, when searching for planets whose orbital periods are much smaller that the timescale of the star's magnetic cycle this source of stellar activity is not often a major concern and can be characterized and corrected with a long enough baseline of observations (Kürster et al., 2003; Dumusque et al., 2011a; Toledo-Padrón et al., 2019).

1.3.3 Atmospheric characterization and habitability

The detection of an exoplanet is just the first step. Once detected it is desirable to aim for an exhaustive characterization of its properties, ranging from the most basic (e.g. mass, size, eccentricity, equilibrium temperature) to more complex ones such as the internal composition and structure, the three-dimensional geometry of the system, atmospheric constituents and their dynamics, climate or habitability. The detectability advantages of planets around M dwarfs and their closeness make them also prime targets for further characterization. Of special interest are the atmospheric studies of

Earth-type planets orbiting in the HZ and their habitability prospects.

In general, there are two primary methods of characterizing the atmospheres of exoplanets: *direct imaging* with starlight suppression, and *transit spectroscopy* of favorably aligned systems (Fig. 1.19). For direct imaging in *reflected* light, one measures a spectrum of the host star that has been filtered through the planetary atmosphere twice, whereas for direct imaging in *thermal* light, one measures the thermal emission from the planet that has been filtered through the atmosphere once. In both wavelength ranges, the constituents of the planetary atmosphere are imprinted on the spectrum. Studying the brightness of the planet as a function of phase also reveals aspects of the planetary atmosphere, and potentially can detect the presence of a surface ocean. However, direct imaging is tremendously challenging and less than a dozen planets at large orbital distances with masses below Jupiter have been discovered to date using ground-based coronagraphs. Extremely large ground-based telescopes (ELTs) equipped with extreme adaptive optics systems are needed to push the detection limits to Jupiter analogs and ambitious, space-based proposed missions equipped with starshades and/or coronagraphic instruments like HabEx (Gaudi et al., 2020) or LUVOIR (The LUVOIR Team, 2019) are needed to study Earth analogs (Fig. 1.20).

However, there is a direct imaging avenue to study the atmospheres of potentially habitable rocky planets around M dwarfs in this decade. High-dispersion spectroscopy can be used to isolate exoplanet signals from starlight (Snellen et al., 2010, 2013). This method cross-correlates an observed spectrum with a model template of the exoplanet's atmosphere. It relies on there being a large number of molecular absorption features in the exoplanet atmosphere spectrum, but combined with high-contrast imagers on large telescopes (Snellen et al., 2015; Wang et al., 2017) it could enable the detection of molecular bands in Earth-like planets orbiting the closest M dwarfs such as Proxima Centauri b (Lovis et al., 2017).

For transit spectroscopy, there are three primary methods. First, one can measure a thermal emission and/or reflection spectrum by measuring the drop in the combined planet plus star flux as the exoplanet passes behind the star, also known as *eclipse spectroscopy*. Second, when the planet passes in front of the star the absorption spectrum of the planet's atmosphere can be measured. The starlight is filtered through the intervening planetary atmosphere and absorbed at wavelengths corresponding to atomic and molecular transitions in that atmosphere, also known as *transmission spectroscopy*. Finally, one can measure the variation in the combined stellar and planetary brightness as the planet orbits its star via *phase curves*. Eclipse spectroscopy and phase curves do not necessarily require that the planet transit its host star, but it enhances detectability and the precision of the retrieved parameters. On the other hand, for a non-transiting planet to be occulted by its host star is necessary an eccentric orbit with an argument of periastron close to 270 deg.

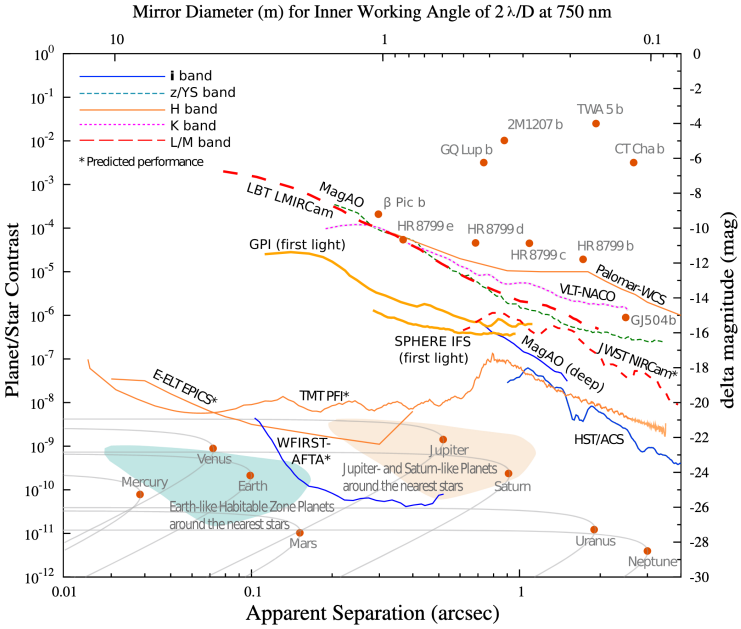

FIGURE 1.20— Planet-to-star contrast achieved via current and planned direct imaging instruments. Orange points indicate a subset of detected planets (upper right, as seen in *K*-band), and solar system planets at 10 pc (bottom, assuming reflected light). Green and orange shadowed areas indicate the parameter space of Earth-like HZ planets and Jupiter- and Saturn-like planets, respectively. Future space mission concepts like HabEx predict planet-to-start contrast sensitivities below 10^{-10} all the way to 2 arcsec apparent separations, enabling the detection of solar system analogs. From Crossfield (2015).

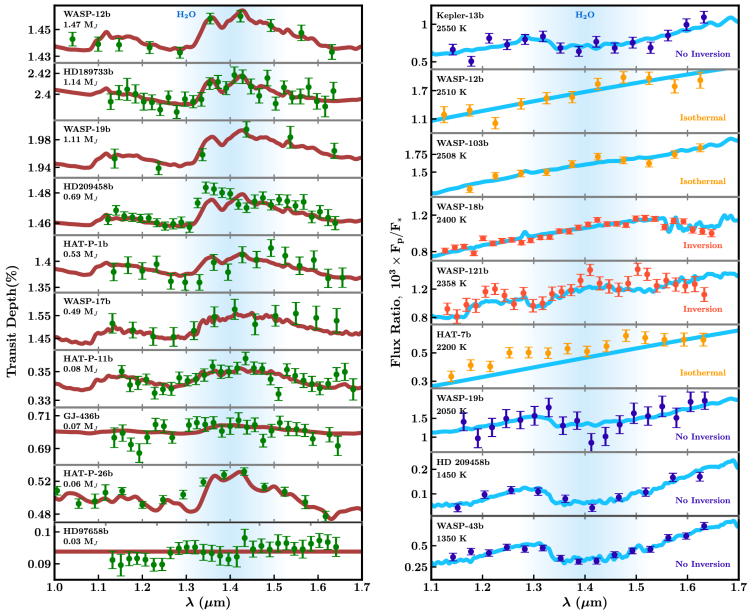

FIGURE 1.21— A panorama of observational detections of exoplanet atmospheres. *Left*: space-based primary transit observations arranged by ascending mass. The spectral range affected by water absorption is shaded in blue and water features are present in many of the spectra. *Right*: space-based secondary transit observations arranged by ascending temperature. Different temperature structures are indicated. From Madhusudhan (2019).

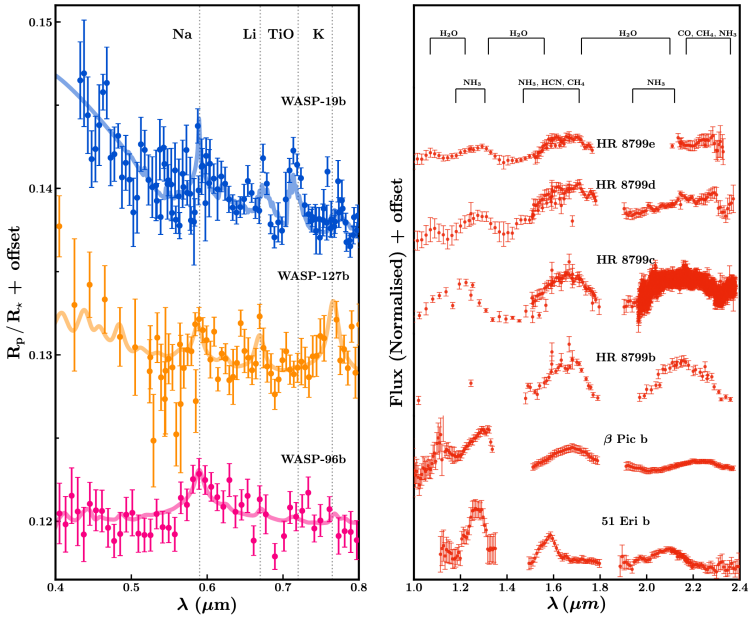

FIGURE 1.22— A panorama of observational detections of exoplanet atmospheres. High-quality spectra of transiting (left) and directly imaged (right) planets using ground-based telescopes. The locations of the spectral features from different chemical species are marked with vertical dashed lines and brackets. From Madhusudhan (2019).

HD 209458 b was the first transiting planet discovered and the first with an atmospheric detection using the *Hubble Space Telescope* (Charbonneau et al., 2002). Although the sodium detection in HD 209485 b has been recently challenged (Casasayas-Barris et al., 2020, 2021), it opened a field that has grown at a tremendous pace in the last two decades. Atmospheres of nearly a hundred exoplanets have been detected using at least one technique in at least one spectral band (see the recent review of Madhusudhan, 2019, and some representative examples in Figs. 1.21 and 1.22). Detections of H_2O, Na, K, TiO, AlO, H, He, C, O, Li, Ca, Sc, Mg, and Si with transmission spectroscopy; H_2O, CO, VO, TiO, and HCN with eclipse spectroscopy; H_2O, CO, TiO, HCN, Ti, Fe, H, He, Ca, and many rare neutral and ionized metals with high-resolution spectroscopy; and H_2O, CH_4, NH_3, and CO with direct imaging have been achieved in the last years. Most observations have employed space- or ground-based low-resolution spectroscopy or broadband photometry (e.g., Sing et al., 2016; Tsiaras et al., 2018; Garhart et al., 2020; Chen et al., 2018), but high-resolution spectroscopy has also proved very powerful to detect atmospheric features and, in some cases, their dynamics (e.g., Redfield et al., 2008; Nortmann et al., 2018; Ehrenreich et al., 2020). Hot and ultra-hot Jupiters are the golden targets for atmospheric characterization and the ones that has advanced the field the most, but detections of Neptunes and super-Earths are becoming feasible nowadays.

The *James Webb Space Telescope* (*JWST;* Gardner et al., 2006) has the potential to revolutionize the study of exoplanetary atmospheres. The key advantages of *JWST* for exoplanet transit spectroscopy are its 6.5-m aperture, and hence high sensitivity, and wide spectral range, particularly in the infrared. It will obtain atmospheric spectra of a small sample of super-Earths, a larger sample of sub-Neptunes, and improve substantially our understanding of giant planets (Beichman et al., 2014; Greene et al., 2016). But more importantly, it will be sensitive, for the first time, to the atmospheric features of Earth-like planets in the HZ of late-type M dwarfs (Fig. 1.23; Morley et al., 2017; Wunderlich et al., 2019). The requisites are an optimal target, a large amount of observing time, a deep understanding and control of systematics, and some luck. The temperate Earth-density planets of the M8 V star TRAPPIST-1 (Gillon et al., 2016, 2017) are serious candidates to become *the* target for this effort and an international community initiative to coordinate the potential *JWST* observations (several hundreds of hours) and their analysis has been set into motion (Gillon et al., 2020b).

It is conceivable that a chemical signature in the atmosphere of a habitable exoplanet may be discovered within the next decade with large facilities in space and/or ground. However, whether or not the detected chemical will be a robust signature of life is a subject of much debate.

The concept of habitability itself is heavily discussed, particularly, in the case of M dwarfs. There are many complications with respect to the habitability of planets

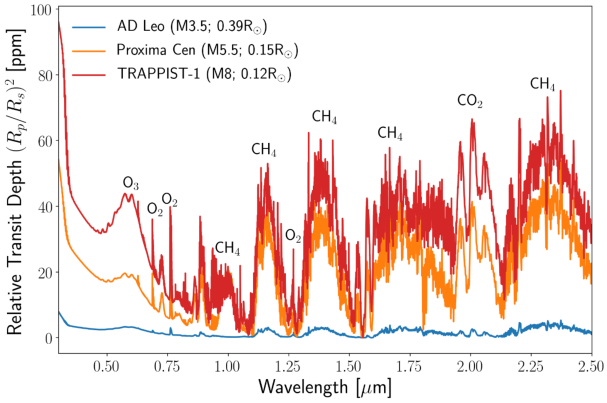

FIGURE 1.23— Simulated transmission spectra for three Earth-like planets around three M dwarfs with different radii. The relative transit depth of the prominent NIR methane bands of an Earth-like planet orbiting an M8 V is expected to be ~ 50 ppm, but only ~ 5 ppm for a M3.5 V host star. The optimistic expected floor noise of *JWST* is 10–25 ppm (Fauchez et al., 2019), conservative values range from 20–50 ppm depending on the instrument (Greene et al., 2016). From Gillon et al. (2020a).

around M dwarfs (e.g., Scalo et al., 2007; Lingam & Loeb, 2018), even if they have surface temperature and pressure conditions favorable to maintain liquid water, such as tidal locking (Heller et al., 2011; Leconte et al., 2015), run-away greenhouse effects (Kopparapu, 2013), water loss (Luger & Barnes, 2015; Tian & Ida, 2015), the influence of stellar activity (especially during the pre-main sequence phase; Tilley et al., 2019; Günther et al., 2020b), atmospheric loss (Owen & Mohanty, 2016; Dong et al., 2017), or the productivity of photosynthesis (Lehmer et al., 2018), among many others (see Shields et al., 2016, for a recent review about the prospects for the habitability of M-dwarf planets). However, through a combination of observational data for recently discovered planetary systems and complex theoretical simulations powered by the increase in computational capabilities, the latest research indicate that M dwarfs are still a good place to look for habitable planets (e.g., Tarter et al., 2007; Shields et al., 2013; Garcia-Sage et al., 2017; Mullan & Bais, 2018; Wandel, 2018; O'Malley-James & Kaltenegger, 2019; Checlair et al., 2019; Moore & Cowan, 2020).

The ideal biosignature should not be a product of non-biological processes (reliability), it should have strong enough spectral features to be detectable (detectability), and it should be long-lasting enough to be detectable (survivability). Initial studies show that the possible space of biochemical byproducts may comprise an infinite

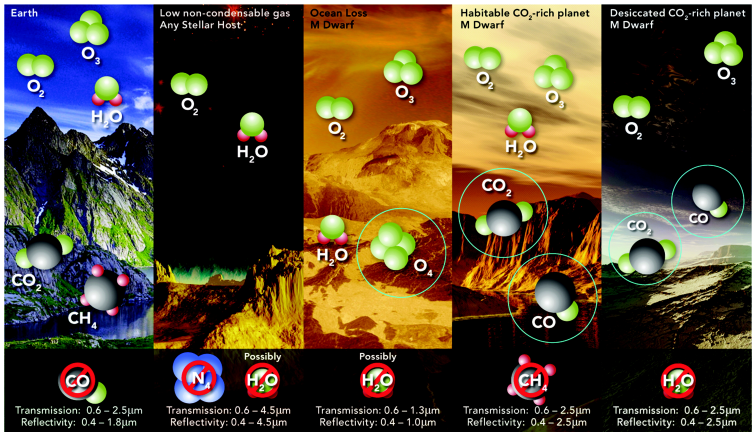

FIGURE 1.24— Discriminating false positives for different habitability environments. For a photosynthetic biosphere (Left) the simultaneous presence of O_2, O_3, CH_4, and the absence of a large abundance of CO points to a photosynthetic origin for Earth's O_2. In the remaining panels, we show the predominant molecules for various false-positive scenarios, the molecular discriminants whose presence indicates a false-positive mechanism (circled), and the missing molecules (in the bottom region) whose absence indicates a likely false-positive mechanism. The nominal wavelength ranges needed to observe these discriminants or check for their absence are given at the bottom of each panel. From Meadows (2017).

combination of chemical species (see reviews by Schwieterman et al. 2018 and Seager 2018). But, recent studies show that combinations of multiple species such as O_2 and CH_4 and/or N_2O and liquid water may be a sure sign of life after excluding all the alternative abiological scenarios able to explain a strong chemical disequilibrium (Fig. 1.24; Des Marais et al., 2002).

Reality has rarely conformed to our expectations, and exoplanetology is a vivid testimony of that. A prudent approach to searching for biosignatures in terrestrial exoplanets should be driven by observational capability rather than ideal, terracentric predictions. Atmospheric characterization of Earth-like planets around Sun-like stars are out of the reach of current and upcoming facilities, but in the coming decade life may be probed for planets around M dwarfs with the space-based *JWST* and/or the ground-based ELTs in ground. Humankind could be on the verge to answer one of its most ancient question.

1.4 Objectives and thesis overview

The main goal of this dissertation is to seize the "M-dwarf opportunity" to find the best candidates for atmospheric characterization with upcoming facilities and to increase our understanding of the formation and evolution of these planets. Despite all their detectability advantages, planets around M dwarfs amount to only 10% of all known exoplanets and there is an even smaller percentage of them with precise mass and radius determination. The most basic characterization of planets (internal structure, formation history and possible atmospheric composition) starts with a measurement of their masses and radii (Fig. 1.25). And, critically, a precise mass determination is needed to infer the internal structure of the planet (e.g., Dorn et al., 2017; Otegi et al., 2020) and to retrieve and interpret chemical abundances from transit spectroscopy observations (Batalha et al., 2019). Therefore, the results of this thesis are based on the synergy between space-based transit searches around bright stars such as *TESS* (to obtain the radius) and ground-based high-resolution spectrographs with $\sim 1\,\mathrm{m\,s^{-1}}$ radial velocity precision such as CARMENES or HARPS (to measure the mass).

Chapter 2 presents the discovery of two super-Earths orbiting the mid-type M dwarfs GJ 3779 and GJ 1265. It constitutes the first detection of planets in the super-Earth mass range with the CARMENES instrument. None of the planets transit despite their short orbital periods as confirmed with *K2* observations and follow-up transit searches with ground-based telescopes, but populate a sparse region of the period-mass space of very low mass stars.

Chapter 3 reports the discovery of a multi-planetary system orbiting the mid-type M dwarf GJ 357, the most-cited work of this thesis so far. The innermost planet was

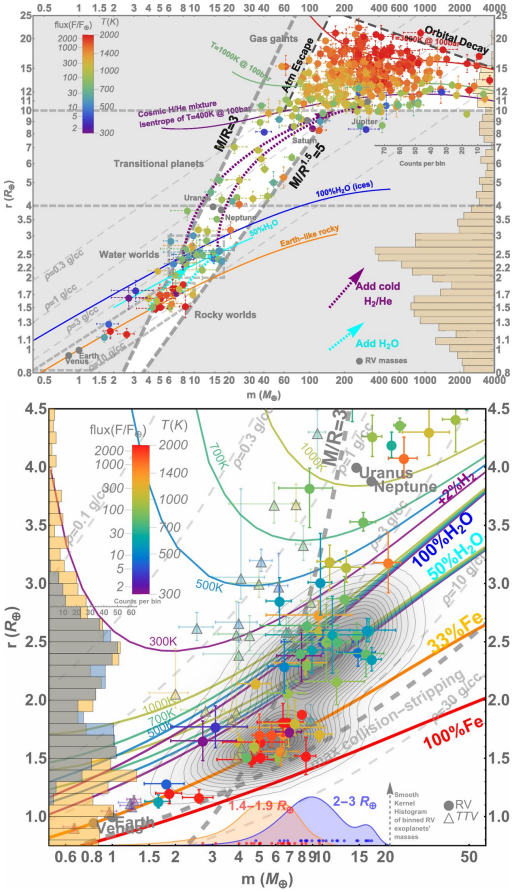

FIGURE 1.25— Mass-radius diagram of exoplanets with masses and densities constrained to better than 50%. The color of the points denotes stellar insolation receive by the planet in Earth units. *Top*: The vertical histogram on the right y axis shows the log-binned radius distribution of *Kepler* planets with radius errors less than 10%, orbiting solar-type stars. The dotted cyan and purple arrows show the growth trajectories of planets formed by continuous addition of either water ices or volatile-rich gas to a planetary core of a given mass. *Bottom*: Close-up version of the top panel. The radius gap at 2 $R_\oplus$ separates two distinctive groups of planets: super-Earths, with radii 1.4–1.9 $R_\oplus$, and sub-Neptunes, with radii 2–3 $R_\oplus$. The different curves show distinct internal composition models. From Zeng et al. (2019).

detected in transit by the *TESS* satellite and is the closest transiting planet orbiting a single M dwarf to the Sun. Archival and new radial velocity observations from several instruments confirmed the presence of the transiting planet and enabled the detection of two additional planets in longer orbits. The innermost, transiting planet is one of the best Earth-like density candidates for atmospheric studies and the outermost resides in the habitable zone of its star and has triggered transit searches with ground-based telescopes and theoretical studies of its potential atmospheric composition and habitability (Kaltenegger et al., 2019).

Chapter 4 describes the discovery of a multi-planetary system orbiting an early-type M dwarf, TOI-776. The system consists of two transiting sub-Neptune planets detected by *TESS* and followed-up with HARPS as part of the KESPRINT consortium efforts. The manuscript comprises numerous analyses and is a representative example of the articles devoted to the discovery and characterization of exoplanets nowadays. The system is an excellent laboratory to explore the mechanism(s) responsible for the radius gap emergence around M dwarfs as compared to Sun-like stars and for *JWST* observations, which could break the degeneracy in planetary interior models.

Finally, Chapter 5 discusses the results of this thesis and draws their conclusions. Future work related to the contents of this thesis and exoplanet research overall is presented in Chapter 6.

2

Two twin super-Earths orbiting GJ 3779 and GJ 1265

Cazadores extrahumanos
Están cazando luceros,
Cisnes de plata maciza
En el agua del silencio.

Federico García Lorca (1920)

The contents of this chapter refer to the article *The CARMENES search for exoplanets around M dwarfs. The warm super-Earths in twin orbits around the mid-type M dwarfs Ross 1020 (GJ 3779) and LP 819-052 (GJ 1265)*, published in the journal Astronomy & Astrophysics (Luque et al., 2018). This work makes use of observations from the Guaranteed Time Observations (GTO) program of the CARMENES consortium, which I am part of since 2017.

The stars GJ 3779 and GJ 1265 are two mid-type M dwarfs monitored by the CARMENES consortium during GTO time as part of its blind search for exoplanets around approximately 320 M dwarfs, running from January 2016 to December 2020. The work included in this chapter presents the detection of a super-Earth planet around each of the stars, the first planets in the super-Earth mass range discovered by the CARMENES consortium. The stars share similar properties, both are relatively bright, mid-type M dwarfs within 15 pc from the Sun. The planets share similar properties as well, they have orbital periods of approximately 3 days, minimum masses in the range 7–8 $M_\oplus$ and low eccentricity orbits. Their hosts do not show any significant stellar activity and, using photometric observations from MEarth for GJ 3779 and from *K2* for

GJ 1265, we were able to determine their rotational periods. In addition, we searched for transits in both light curves, but found that the planets are likely not transiting.

This first work makes use of several techniques that are applied in following studies. Radial velocities from CARMENES high-resolution spectroscopic observations are computed using SERVAL (Zechmeister et al., 2018), which is based upon template matching algorithms rather than cross-correlation techniques. Frequency analyses in order to find periodicities in the data and identify potential false positives due to stellar activity are carried out with generalized Lomb-Scargle periodograms (GLS; Zechmeister & Kürster, 2009). To obtain the orbital parameters of the planets, radial velocity data are modeled with Keplerian orbits that are optimized using the Levenberg-Marquard method (Press et al., 1992). Uncertainties are computed from the covariance matrix of the fit and also using the Markov chain Monte Carlo (MCMC) sampler `emcee` (Foreman-Mackey et al., 2013) for repeatability and robustness. The search for transits is done using a box-fitting least squares periodogram (Kovács et al., 2002) after detrending the light curves.

Finally, this work glances at a potential correlation in the period-mass space of planets around M dwarfs. Although at the time of publication there were only 18 planetary systems around M dwarfs with measured dynamical masses, it seems to exist a dearth of close-in planets with masses between 2–5 $M_\oplus$ orbiting mid- and late-type M dwarfs. Remarkably, it is found that most of the short-period planets in the Earth-mass range are mostly found in multi-planetary systems, while the super-Earths seem to appear single. Due to the small number statistics and potential detection biases, we did not delve into the physical origin of this observational insight, but proposed two explanations: i) the formation of super-Earth impedes the formation of smaller Earth-like planets in the same system, or ii) super-Earths around M dwarfs are formed by pile-up of several low-mass planets. Further detections in this parameter space from radial velocity and/or transit searches may shed some light on this trend.

A&A 620, A171 (2018)
https://doi.org/10.1051/0004-6361/201833423

Astronomy & Astrophysics

The CARMENES search for exoplanets around M dwarfs

The warm super-Earths in twin orbits around the mid-type M dwarfs Ross 1020 (GJ 3779) and LP 819-052 (GJ 1265)*

R. Luque[1,2], G. Nowak[1,2], E. Pallé[1,2], D. Kossakowski[3], T. Trifonov[3], M. Zechmeister[4], V. J. S. Béjar[1,2], C. Cardona Guillén[1,2], L. Tal-Or[4,14], D. Hidalgo[1,2], I. Ribas[5,6], A. Reiners[4], J. A. Caballero[7], P. J. Amado[8], A. Quirrenbach[9], J. Aceituno[10], M. Cortés-Contreras[7], E. Díez-Alonso[11], S. Dreizler[4], E. W. Guenther[12], T. Henning[3], S. V. Jeffers[4], A. Kaminski[9], M. Kürster[3], M. Lafarga[5,6], D. Montes[7], J. C. Morales[5,6], V. M. Passegger[13], J. H. M. M. Schmitt[13], and A. Schweitzer[13]

[1] Instituto de Astrofísica de Canarias, 38205 La Laguna, Tenerife, Spain
e-mail: rluque@iac.es
[2] Departamento de Astrofísica, Universidad de La Laguna, 38206 La Laguna, Tenerife, Spain
[3] Max-Planck-Institut für Astronomie, Königstuhl 17, 69117 Heidelberg, Germany
[4] Institut für Astrophysik, Georg-August-Universität, Friedrich-Hund-Platz 1, 37077 Göttingen, Germany
[5] Institut de Ciències de l'Espai (ICE,CSIC), Campus UAB, c/ de Can Magrans s/n, 08193 Bellaterra, Barcelona, Spain
[6] Institut d'Estudis Espacials de Catalunya (IEEC), 08034 Barcelona, Spain
[7] Centro de Astrobiología (CSIC-INTA), ESAC Campus, Camino Bajo del Castillo s/n, 28692 Villanueva de la Cañada, Madrid, Spain
[8] Instituto de Astrofísica de Andalucía (IAA-CSIC), Glorieta de la Astronomía s/n, 18008 Granada, Spain
[9] Landessternwarte, Zentrum für Astronomie der Universtät Heidelberg, Königstuhl 12, 69117 Heidelberg, Germany
[10] Centro Astronómico Hispano-Alemán (CSIC-MPG), Observatorio Astronómico de Calar Alto, Sierra de los Filabres, 04550 Gérgal, Almería, Spain
[11] Departamento de Astrofísica y Ciencias de la Atmósfera, Facultad de Ciencias Físicas, Universidad Complutense de Madrid, 28040 Madrid, Spain
[12] Thüringer Landessternwarte Tautenburg, Sternwarte 5, 07778 Tautenburg, Germany
[13] Hamburger Sternwarte, Gojenbergsweg 112, 21029 Hamburg, Germany
[14] School of Geosciences, Raymond and Beverly Sackler Faculty of Exact Sciences, Tel Aviv University, Tel Aviv 6997801, Israel

Received 14 May 2018 / Accepted 16 October 2018

ABSTRACT

We announce the discovery of two planetary companions orbiting around the low-mass stars Ross 1020 (GJ 3779, M4.0V) and LP 819-052 (GJ 1265, M4.5V). The discovery is based on the analysis of CARMENES radial velocity (RV) observations in the visual channel as part of its survey for exoplanets around M dwarfs. In the case of GJ 1265, CARMENES observations were complemented with publicly available Doppler measurements from HARPS. The datasets reveal two planetary companions, one for each star, that share very similar properties: minimum masses of $8.0 \pm 0.5\ M_\oplus$ and $7.4 \pm 0.5\ M_\oplus$ in low-eccentricity orbits with periods of 3.023 ± 0.001 d and 3.651 ± 0.001 d for GJ 3779 b and GJ 1265 b, respectively. The periodic signals around 3 d found in the RV data have no counterpart in any spectral activity indicator. Furthermore, we collected available photometric data for the two host stars, which confirm that the additional Doppler variations found at periods of approximately 95 d can be attributed to the rotation of the stars. The addition of these planets to a mass-period diagram of known planets around M dwarfs suggests a bimodal distribution with a lack of short-period low-mass planets in the range of 2–5 $M_\oplus$. It also indicates that super-Earths (>5 $M_\oplus$) currently detected by RV and transit techniques around M stars are usually found in systems dominated by a single planet.

Key words. techniques: radial velocities – stars: late-type – stars: low-mass – planetary systems

1. Introduction

The search for exoplanets has become a prominent research field in the past twenty years, particularly the detection of rocky planets in the habitable zones of their parent stars. The radial velocity (RV) technique has been successfully applied to detect such companions around M dwarfs given the relatively low mass of these stars (Marcy et al. 1998; Rivera et al. 2005; Udry et al. 2007; Bonfils et al. 2013; Anglada-Escudé et al. 2016). M stars account for three quarters of all stars known within 10 pc of our solar system (Henry et al. 2016) and show an average occurrence rate of more than two planets per host star (Dressing & Charbonneau 2015; Gaidos et al. 2016).

Despite their high potential for finding rocky planets, M dwarfs pose various observational difficulties. On the one hand, low-mass stars emit more flux in the near-infrared (NIR)

* The RV and formal uncertainties of GJ 3779 and GJ 1265 are only available at the CDS via anonymous ftp to cdsarc.u-strasbg.fr (130.79.128.5) or via http://cdsarc.u-strasbg.fr/viz-bin/qcat?J/A+A/620/A171

than in the visual (VIS). On the other hand, chromospheric variability and activity cycles may produce changes in the spectral line profiles, which mimic a Doppler shift. These periodic variations induce signals in the RV data that could be incorrectly interpreted as being of planetary origin (e.g. Queloz et al. 2001; Robertson et al. 2014; Sarkis et al. 2018). Since stellar jitter can reach amplitudes of a few metres per second, detecting low-signal companions generally requires a considerable number of observations (Barnes et al. 2011). However, since the amplitude of an activity-related signal is expected to be wavelength-dependent, a successful program searching for exoplanets around M dwarfs must tackle these difficulties by observing simultaneously in the widest possible wavelength range, especially covering the reddest optical wavelengths, and following an observing strategy that ensures numerous and steady observations covering a long time span.

The CARMENES search for exoplanets around M dwarfs accomplishes these requirements in its guaranteed time observation (GTO) M dwarf survey, which began in January 2016 (Reiners et al. 2018b). Ross 1020 (GJ 3779) and LP 819-052 (GJ 1265) are two mid-type M dwarfs monitored as part of this project. Their RVs indicate the presence of two super-Earths in short-period orbits of the order of 3 d. Section 2 summarises the basic information of the host stars. In Sect. 3, the RV observations for each star are presented. The analysis of the RV data is explained in Sect. 4, while in Sect. 5 we discuss the results from the Keplerian fit and the location of the two planets in a mass-period diagram.

2. Stellar parameters

The basic information of the host stars GJ 3779 and GJ 1265 is presented in Table 1. Both targets exhibit similar properties and their values are consistent with the literature. They are mid-type M dwarfs that kinematically belong to the Galactic thin disc (Cortés-Contreras 2016), with GJ 1265 being part of the young population. Their photospheric metallicities are compatible with solar values (Neves et al. 2014; Newton et al. 2014; Passegger et al. 2018). They are thought to be inactive, with no emission in Hα (Jeffers et al. 2018) and only very faint X-ray emission for the case of GJ 1265 (Rosen et al. 2016). The photospheric parameters of the stars were determined as in Passegger et al. (2018) using the latest grid of PHOENIX-ACES model spectra (Husser et al. 2013) and the method described in Passegger et al. (2016). We determined the radii R using Stefan–Boltzmann's law, the spectroscopic $T_{\rm eff}$ as in Passegger et al. (2018), and the luminosities L by integrating the photometric stellar energy distribution collected for the CARMENES targets (Caballero et al. 2016) with the Virtual Observatory Spectral energy distribution Analyser (Bayo et al. 2008). The stellar masses were derived from the linear M–R relation presented by Schweitzer et al. (in prep.). These values are the same using instead empirical mass–luminosity relations such as those presented by Delfosse et al. (2000) and Benedict et al. (2016). The details of the calculation of the physical parameters are described in Reiners et al. (2018a) and will be reported in further detail by Schweitzer et al. (in prep.).

The star GJ 3779 (Ross 1020, J13229+244) is a high proper motion star classified as M4.0 V by Hawley et al. (1996). It resides in the Coma Berenices constellation, located at a distance of $d = 13.748 \pm 0.011$ pc (Gaia Collaboration 2018) with an apparent magnitude in the J band of 8.728 mag (Skrutskie et al. 2006). Using CARMENES data, Reiners et al. (2018b) determined its absolute RV to be $V_r = -19.361$ km s^{-1} and a Doppler broadening upper-limit of $v \sin i < 2$ km s^{-1}.

Table 1. Stellar parameters for GJ 3779 and GJ 1265.

Parameter	GJ 3779	GJ 1265	Ref.
Main identifiers and coordinates			
Name	Ross 1020	LP 819-052	
Karmn	J13229 + 244	J22137-176	
α	13:22:56.74	22:13:42.78	2MASS
δ	+24:28:03.4	−17:41:08.2	2MASS
Spectral type and magnitudes			
SpT	M4.0 V	M4.5 V	PMSU
G [mag]	11.6266 ± 0.0008	12.0807 ± 0.0006	*Gaia* DR2
J [mag]	8.728 ± 0.02	8.955 ± 0.03	2MASS
Kinematics			
d [pc]	13.748 ± 0.011	10.255 ± 0.007	*Gaia* DR2
$\mu_\alpha \cos\delta$ [mas yr^{-1}]	−615.95 ± 0.13	856.89 ± 0.12	*Gaia* DR
μ_δ [mas yr^{-1}]	−865.13 ± 0.10	−306.30 ± 0.11	*Gaia* DR2
V_r [km s^{-1}]	−19.361	−24.297	Rei18
Photospheric parameters			
$T_{\rm eff}$ [K]	3324 ± 51	3236 ± 51	This work[a]
log g	5.05 ± 0.07	5.09 ± 0.07	This work[a]
[Fe/H]	0.00 ± 0.16	−0.04 ± 0.16	This work[a]
Derived physical parameters			
L [10^{-5} $L_\odot$]	867 ± 11	364 ± 5	This work
R [$R_\odot$]	0.281 ± 0.010	0.192 ± 0.007	This work
M [$M_\odot$]	0.27 ± 0.02	0.178 ± 0.018	This work
Stellar rotation			
$v \sin i$ [km s^{-1}]	<2.0	<2.0	Rei18
$P_{\rm rot}$ [d]	95 ± 5	>70	This work

References. 2MASS: Skrutskie et al. (2006); PMSU: Hawley et al. (1996); *Gaia* DR2: Gaia Collaboration (2018); Rei18: Reiners et al. (2018b). [(a)]Estimated as in Passegger et al. (2018).

The object GJ 1265 (LP 819-052, J22137-176) is also a high proper motion star at a distance of $d = 10.255 \pm 0.007$ pc (Gaia Collaboration 2018) in the Aquarius constellation. Its apparent magnitude in the J band is 8.955 mag (Skrutskie et al. 2006), and it is approaching the solar system with an absolute RV of $V_r = -24.297$ km s^{-1} (Reiners et al. 2018b). The star exhibits a luminosity in X-rays of $\log L_{\rm X} = 26.1 \pm 0.2$ erg s^{-1}, measured with the *XMM-Newton* observatory (Rosen et al. 2016). Therefore, we can estimate the rotational period of the star to be of the order of 100 d following the $L_{\rm X}$–$P_{\rm rot}$ relation proposed by Reiners et al. (2014).

3. Observations

The CARMENES instrument, installed at the 3.5 m Calar Alto telescope at the Calar Alto Observatory in Spain consists of a simultaneous dual-channel fibre-fed high-resolution spectrograph covering a wide wavelength range from 0.52 μm to 0.96 μm in the VIS and from 0.96 μm to 1.71 μm in the NIR, with spectral resolutions of $R = 94\,600$ and $R = 80\,400$, respectively (Quirrenbach et al. 2014). The performance of the instrument and its ability to discover exoplanets around M dwarfs using the RV technique has already been demonstrated by Trifonov et al. (2018), Reiners et al. (2018a), and Kaminski et al. (2018).

The survey contains 104 observations for GJ 3779 in the VIS channel covering a time span of 820 d, with typical exposure times of 1800 s and median internal RV precision of $\sigma_{\rm VIS} = 1.7$ m s^{-1}. In the case of GJ 1265, 87 observations were acquired in the visible, covering a timespan of 782 d, typical exposure

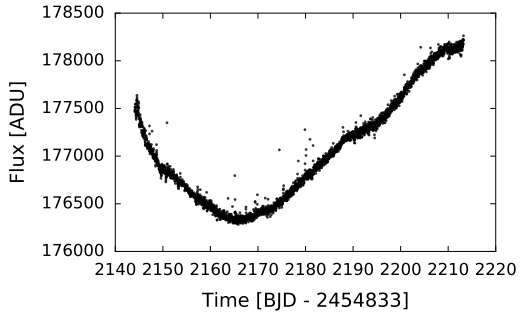

Fig. 1. *K*2 light curve of GJ 1265. The photometric variability of the star is longer than the 69 d baseline of the observations.

times of 1800 s, and median internal RV precision of σ_{VIS} = 1.8 m s^{-1}. The NIR median internal RV precisions are considerably higher: σ_{NIR} = 10.4 m s^{-1} and σ_{NIR} = 6.7 m s^{-1} for GJ 3779 and GJ 1265, respectively. As a result, we only use the RVs from the VIS channel in our analysis.

Doppler measurements, together with several spectral indicators useful to discuss the planetary hypothesis, were obtained with the SERVAL program (Zechmeister et al. 2018) using high signal-to-noise-ratio (S/N) templates created by co-adding all available spectra of each star. They are corrected for barycentric motion (Wright & Eastman 2014) as well as for secular acceleration, which is important for stars with high proper motions (Zechmeister et al. 2009). In addition, the RVs were corrected by means of an instrumental nightly zero-point (NZP), which was calculated from a subset of RV-quiet stars observed each night whose RV standard deviation is less than 10 m s^{-1}. This correction is described in Trifonov et al. (2018). For each spectrum, we also computed the cross-correlation function (CCF) using a weighted mask by co-adding the stellar observations themselves. Fitting a Gaussian function to the final CCF, we determined the RV, FWHM, contrast, and bisector velocity span. The methodology regarding how the CCF is computed for our CARMENES spectra is described in Reiners et al. (2018a).

Moreover, for our southern target, GJ 1265, we further included 11 publicly available observations from HARPS (Mayor et al. 2003) taken between July 2003 and July 2014. We used SERVAL to derive their RVs and obtained a median internal uncertainty of σ_{HARPS} = 5.6 m s^{-1}. The individual RVs for GJ 3779 and GJ 1265 are shown in Figs. 3 and 6, respectively.

In addition to the Doppler measurements, we also collected available photometry for both targets with the goal of determining the rotational period. We analysed photometric time series for GJ 3779 from The MEarth Project (Charbonneau et al. 2008; Berta et al. 2012) from January 2009 to July 2010 in the RG715 filter. For GJ 1265 (EPIC 205913009) we employed photometric time series from the *K*2 space mission during its Campaign 3 (Vanderburg & Johnson 2014) from November 2014 to February 2015. Figure 1 shows the photometric variability of GJ 1265. Assuming that the signal is close to sinusoidal we derive a rotational period of ∼95 d, which agrees with the ∼100 d rotational period estimated from the X-ray luminosity presented in Sect. 2. However, due to the mix of periodic and stochastic behaviour of stellar variability and the fact that the *K*2 time span does not cover a full phase of such a period, we can only conclude that GJ 1265 is a slowly rotating star with a period longer than 70 d.

4. Data analysis

4.1. GJ 3779 b

In Fig. 2, we show the generalized Lomb–Scargle periodograms (GLS; Zechmeister & Kürster 2009) of different data products obtained with SERVAL and our CCF analysis. For each panel, we compute the theoretical false alarm probability (FAP) as described in Zechmeister & Kürster (2009), and show the 10%, 1%, and 0.1% levels. In the CARMENES RVs (Fig. 2a), a single relevant peak with FAP = 2.2×10^{-35} at f = 0.3307 d^{-1} (P = 3.023 d) is found. The next highest peak in the RVs GLS, though above FAP = 10%, is found at f = 0.0105 d^{-1} (P = 95.24 d), which agrees with the periodic photometric variation found in the MEarth data (Fig. 2c). After subtraction of the 3.023 d periodic signal in the RV GLS, no further significant signals are found (Fig. 2b).

A strong alias[1] of the signal discussed so far is found at a frequency of 1 d^{-1} − f = 0.6693 d^{-1}. A periodogram of the data does not provide information about which of the two peaks is the true planetary signal. However, the peak at 1 d^{-1} − f, that is, P = 1.494 d, has less power and therefore appears less likely to be the true period. If the fitted signal is the one at P = 1.494 d, the 3.023 d peak in the RV GLS does not disappear, proving that the P = 1.494 d signal is indeed an alias of the ∼3 d one. Furthermore, if we choose the true Keplerian period to be the shortest one at ∼1.5 d, the goodness of the fit gets significantly worse, changing from χ^2_ν = 2.6 to χ^2_ν = 5.6, and the derived eccentricity of the orbit becomes larger, which is unlikely compared to the period and eccentricity distributions of known exoplanets.

Taking full advantage of the spectral information provided by SERVAL and the one contained in the CCF, we further investigate possible periodic signals related with chromospheric activity of the host star that may have induced RV variations. Periodograms of the chromatic index (CRX), differential line width (dLW), and Hα index as described in Zechmeister et al. (2018) are shown in panels d–f of Fig. 2, while full width half maximum (FWHM), contrast (CTR), and bisector velocity span (BVS) from the CCF are shown in panels g–i.

Only the dLW GLS shows significant peaks between 80 and 100 d, almost coincident with those found in the photometry, the radial velocities, best-fit residuals, and the CCF FWHM. We also investigated the nature of the marginal power close to ∼3 d with FAP ∼ 10% present in Fig. 2d. A significant signal in the CRX at the RV period may indicate that the measured Doppler shifts are dependent on wavelength, which would refute the planetary hypothesis. However, we checked that there is no correlation in the RV–CRX scatter plot that may call into question the nature of the periodic signal at f = 0.3307 d^{-1} (see left panel of Fig. B.1). None of the other indicators show periodicity at this frequency and therefore we conclude that the periodic signal at 3.023 d is due to a planetary origin and the signal at P ∼ 95 d is related to the rotation of the star.

To obtain the orbital parameters of the planet, we fit the RV dataset searching for the χ^2 minimum using the Levenberg–Marquardt method (Press et al. 1992) in a Keplerian scheme. The best-fit Keplerian orbital parameters and their corresponding 1σ uncertainties of the planet GJ 3779 b are listed in Table 2.

[1] For the sake of clarity, we only show the full GLS periodogram up to 1 d^{-1} in Fig. A.1.

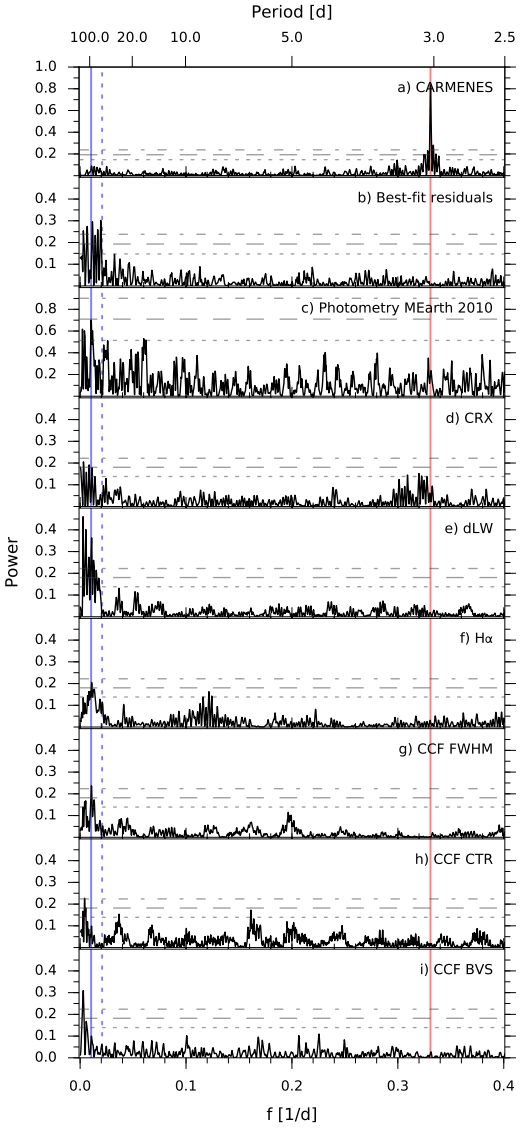

Fig. 2. GLS periodograms for GJ 3779 CARMENES RVs (*panel a*) and its residuals (*panel b*) after removing the prominent peak at f = 0.3307 d^{-1} (P = 3.023 d), marked in red. *Panel c*: periodogram of a photometric campaign of MEarth data from 2010. The highest peak at $f_{\rm rot}$ = 0.0105 d^{-1} (P = 95.2 d) associated with the star's rotation is marked with a solid blue line and its first harmonic ($2f_{\rm rot}$) with a dashed blue line. *Panels d–f*: periodograms of the chromatic index, differential line width, and Hα index, while *panels g–i* show periodograms for the cross-correlation function FWHM, contrast, and bisector velocity span. Horizontal lines show the theoretical FAP levels of 10% (short-dashed line), 1% (long-dashed line), and 0.1% (dot-dashed line) for each panel.

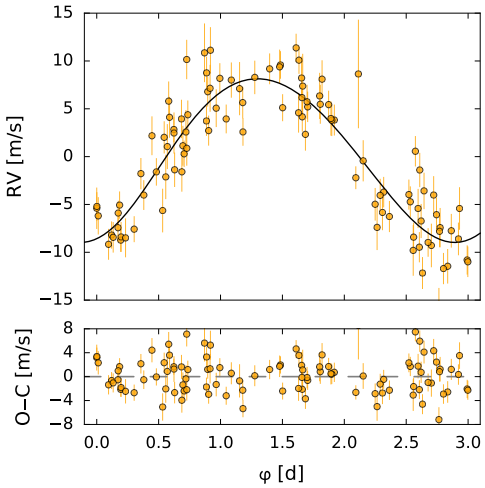

Fig. 3. CARMENES RVs and residuals phase-folded to the best Keplerian fit consistent with a 3.023 d period planet around GJ 3779.

We estimated the uncertainties of the best-fit parameters using two different approaches. First, we obtained the errors given by the covariance matrix in the Levenberg–Marquardt algorithm itself. Second, using the Markov chain Monte Carlo (MCMC) sampler `emcee` (Foreman-Mackey et al. 2013) and a Keplerian model with flat priors, we can derive median and 1 σ uncertainty values from the posterior distributions. A noise term ("jitter") is modelled simultaneously during the parameter optimisation following Baluev (2009). The posterior distributions from the MCMC analysis are shown in Fig. C.1.

The phased RVs and their residuals around the best fit are shown in Fig. 3. The abscissa values of phase-folded plot are determined by computing the difference between each Julian date and the epoch of the first RV observation, and then computing the remainder of the quotient of this difference with the orbital period. The planet candidate GJ 3779 b has a minimum mass of 8.0 ± 0.5 $M_\oplus$ orbiting at a semi-major axis of 0.026 au, much closer to the host star than the conservative habitable-zone limits (0.094–0.184 au; Kopparapu et al. 2013, 2014). The results from best-fit and MCMC analyses all agree within the uncertainties. The posterior distributions show Gaussian profiles and peak close to the best-fit values from Table 2.

Finally, using the photometric time-series data, we looked for the possibility that GJ 3779 b transits its host star. After detrending and flattening, no significant peaks were found in the box-fitting least squares (BLS) periodogram (Kovács et al. 2002). Nevertheless, we shifted the observations to the predicted secondary transit following Kane et al. (2009) and phase-folded the light curve to the 3.023 d period of the planet. We did not find any hints of transits, as shown in Fig. 4. However, since the radius of the planet could be between 1–3 $R_\oplus$ depending on the volatile content, the depth of a hypothetical transit could be between 0.1 and 1.0%. In addition, since the expected duration of the transit is approximately 1 h, the uncertainties of the transit window are large, and there are gaps in the phase-folded photometric data, there could still be a chance that the transit was

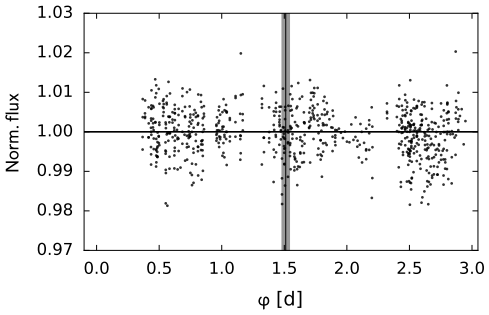

Fig. 4. Phase-folded light curve to the 3.023 d planet period of the MEarth photometric data for GJ 3779. The grey shaded area marks the expected transit duration. The central time of the expected transit is also marked with a vertical bar.

missed or hidden in the noise of the MEarth data. Therefore, we conclude that more data would be required to completely rule out the possibility that GJ 3779 b transits its host star.

4.2. GJ 1265 b

The same approach as for the previous system was applied for the RV analysis of GJ 1265. The first three panels of Fig. 5 show the GLS periodograms for the CARMENES, HARPS, and combined (CARMENES+HARPS) radial velocities. A prominent single peak at $f = 0.2739\,\mathrm{d}^{-1}$ ($P = 3.651$ d) and its corresponding alias at $1\,\mathrm{d}^{-1} - f$ (Fig. A.1, right panel) can be seen in the CARMENES dataset. Even though the HARPS measurements are not sufficient and are too spread in time to detect the short-period signal in the GLS, when combined with the CARMENES radial velocities the aforementioned peak increases in significance from FAP = 2.1×10^{-29} using only CARMENES data to FAP = 1.7×10^{-32} adding the HARPS RVs, also improving the frequency resolution. The nature of the peak at $1\,\mathrm{d}^{-1} - f$ has been analysed in the same way as in Sect. 4.1, concluding that it is an alias of the true Keplerian signal. Fitting a sinusoid at 3.651 d, the GLS of the residuals (Fig. 5d) exhibits some power at $f < 0.012\,\mathrm{d}^{-1}$ ($P > 83.3$ d), which is compatible with the stellar variability seen in the $K2$ photometry (Fig. 1) and the predicted rotational period derived in Sect. 2.

In the periodogram analysis of the activity indicators, no remarkable peaks have been found at the frequency of the RV signal or the rotational period of the star. However, following the procedure explained in Sect. 4.1, we checked the nature of the power at ∼5 d in the CRX. As in the previous case, no significant correlation was found between the RVs and the CRX in the CARMENES VIS data (Fig. B.1, right panel), either between HARPS RVs and the CCF parameters or Hα. Gathering all the evidence, we conclude that the periodic signal found in the CARMENES RVs can only be due to the star's reflex motion caused by a planetary companion. Therefore, we took the RVs GLS periodogram peak as initial period guess to fit a Keplerian orbit to the combined RV dataset using the Levenberg–Marquardt method. The best-fit Keplerian orbital parameters and 1σ uncertainties of the planet candidate GJ 1265 b are listed in Table 2, with their corresponding MCMC analysis as explained in Sect. 4.1 shown in Fig. C.2.

Combined phase-folded RVs together with their best-fit are depicted in Fig. 6. The rms around the best-fit is of 3.0 m s^{-1}

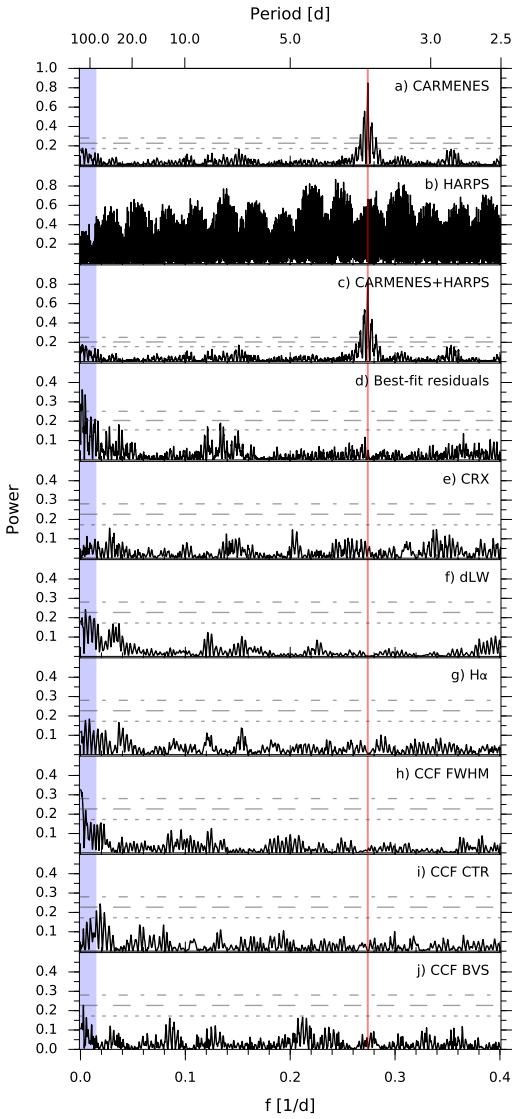

Fig. 5. GLS periodograms for GJ 1265 CARMENES (*panel a*), HARPS (*panel b*), and combined CARMENES+HARPS (*panel c*) data. *Panel d*: residuals after removing the prominent peak at $f = 0.2739\,\mathrm{d}^{-1}$ ($P = 3.651$ d) marked in red. The blue shaded area depicts the excluded planetary region due to stellar variability as discussed in Sect. 3. *Panels e–j* and horizontal lines are the same as in Fig. 2.

and 8.3 m s^{-1} for the CARMENES and HARPS RVs, respectively, which corresponds to 1.5σ and 1.2σ given their internal RV uncertainties. The planet orbiting around the M dwarf star GJ 1265 shows similar properties to the one presented in Sect. 4.1, with a minimum mass of $7.4 \pm 0.5\,M_\oplus$ in a 3.651 d

Table 2. Keplerian orbital parameters and 1σ uncertainties of the planet candidates.

Parameter	Best-fit	MCMC
	GJ 3779 b	
K [m s^{-1}]	8.61 ± 0.40	$8.62^{+0.39}_{-0.39}$
P [d]	3.0232 ± 0.0013	$3.0232^{+0.0004}_{-0.0004}$
e	0.07 ± 0.05	$0.06^{+0.05}_{-0.06}$
ω [deg]	225 ± 42	231^{+42}_{-54}
M [deg]^a	339 ± 41	333^{+52}_{-41}
$\gamma_{\rm VIS}$ [m s^{-1}]	0.85 ± 0.52	$0.86^{+0.30}_{-0.29}$
$\sigma_{\rm jitt,VIS}$ [m s^{-1}]	2.2 (fixed)	$2.19^{+0.29}_{-0.29}$
$m_p \sin i$ [$M_\oplus$]	8.0 ± 0.5	
a [au]	0.026 ± 0.001	
	GJ 1265 b	
K [m s^{-1}]	9.89 ± 0.47	$9.82^{+0.51}_{-0.52}$
P [d]	3.6511 ± 0.0012	$3.6511^{+0.0001}_{-0.0001}$
e	0.04 ± 0.04	$0.06^{+0.04}_{-0.06}$
ω [deg]	282 ± 72	293^{+24}_{-25}
M [deg]^a	19 ± 74	9^{+30}_{-27}
$\gamma_{\rm VIS}$ [m s^{-1}]	1.28 ± 0.57	$1.25^{+0.37}_{-0.38}$
$\gamma_{\rm HARPS}$ [m s^{-1}]	4.74 ± 1.80	$4.96^{+1.63}_{-1.46}$
$\sigma_{\rm jitt,VIS}$ [m s^{-1}]	2.4 (fixed)	$2.40^{+0.37}_{-0.35}$
$\sigma_{\rm jitt,HARPS}$ [m s^{-1}]	3.2 (fixed)	$3.23^{+2.39}_{-2.10}$
$m_p \sin i$ [$M_\oplus$]	7.4 ± 0.5	
a [au]	0.026 ± 0.001	

Notes. $^{(a)}$Mean anomaly valid for the first epoch of observation, JD = 2457489.5644 in the case of GJ 3779, and JD = 2453203.8148 in the case of GJ 1265.

low-eccentricity orbit at a semi-major axis of 0.026 au. The MCMC analysis agrees with the best-fit results within the errors.

As mentioned in Sect. 3, GJ 1265 was observed by the *K*2 space mission during its Campaign 3. Using this photometry information, we analysed the light curve to look not only for periodic signals associated with the rotation of the star, but also for planetary transits. After removing the photometric variation caused by the rotation of the star, no further signals were found in the BLS periodogram. Nonetheless, we phase-folded the photometric data to the RV signal at 3.651 d to look for possible transits but found none at the period of the planet, as shown in Fig. 7.

5. Discussion and summary

The results from the RV analysis reveal two very similar planets orbiting very similar M dwarfs. Not only do the stars exhibit comparable photospheric and physical parameters but they also show long rotational periods. Mid-type slow-rotators are considered to be less magnetically active than their late-type or rapid-rotator counterparts (West et al. 2015), which agrees with the absence of periodic signals in the photospheric spectral indicators (Figs. 2 and 5). The planetary candidates are both orbiting at a semi-major axes of 0.026 au with periods of the order of 3 d and super-Earth-like minimum masses of 7–8 $M_\oplus$. The MCMC analyses reveal that the derived eccentricities of GJ 3779 b and

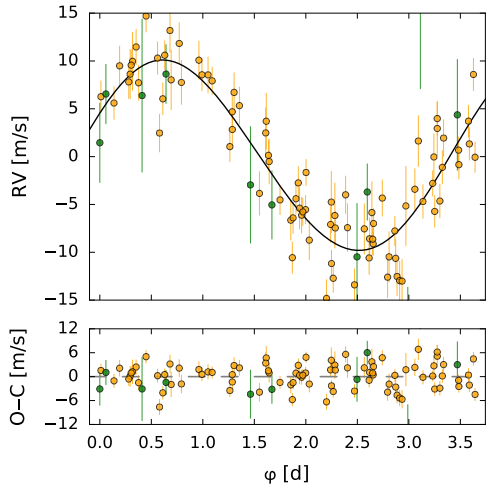

Fig. 6. CARMENES (orange) and HARPS (green) radial velocities and residuals phase-folded to the best Keplerian fit consistent with a planet around GJ 1265 with a period of 3.651 d.

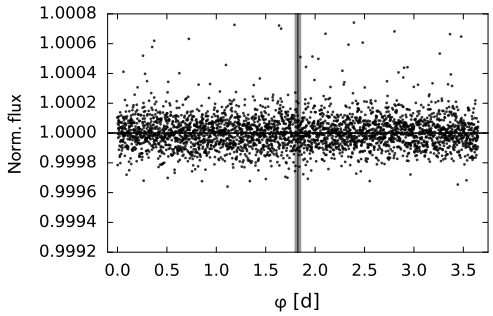

Fig. 7. Phase-folded light curve to the 3.651 d planet period of the *K*2 photometric data for GJ 1265. The grey shaded area marks the expected transit duration. The central time of the expected transit is also marked with a vertical bar.

GJ 1265 b are compatible with circular orbits, which is predicted by orbital evolution models for such short-period planets.

Mass determination for Earth-size and super-Earth planets around M dwarfs is very challenging, and there is a limited number of systems similar to the ones presented here. Only 18 planetary systems have masses derived from RV measurements: GJ 54.1 (Astudillo-Defru et al. 2017b), GJ 1132 (Berta-Thompson et al. 2015), GJ 1214 (Charbonneau et al. 2009), GJ 176 (Forveille et al. 2009), GJ 273 (Astudillo-Defru et al. 2017a), GJ 3138 (Astudillo-Defru et al. 2017a), GJ 3323 (Astudillo-Defru et al. 2017a), GJ 3634 (Bonfils et al. 2011), GJ 3942 (Perger et al. 2017), GJ 3998 (Affer et al. 2016), GJ 433 (Bonfils et al. 2013), GJ 447 (Bonfils et al. 2018), GJ 536 (Suárez Mascareño et al. 2017), GJ 581 (Bonfils et al. 2005), GJ 628 (Wright et al. 2016), GJ 676 A (Anglada-Escudé & Tuomi 2012), GJ 667 C (Bonfils et al. 2013), and GJ 876 (Rivera et al. 2005). Furthermore, the TRAPPIST-1 system was detected by transit

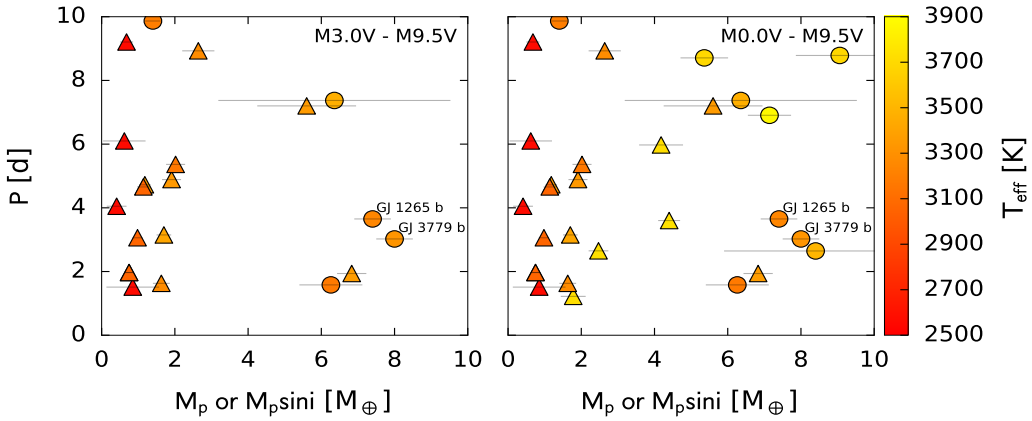

Fig. 8. Mass-period diagram of all super-Earth planets, with masses determined from RVs or TTVs, orbiting mid- and late-type M dwarfs (*left panel*) and for all M dwarfs (*right panel*) taken from the NASA Exoplanet Archive from May 2018 (`https://exoplanetarchive.ipac.caltech.edu`). Single- and multi-planet systems are drawn with circles and triangles, respectively. The colorbar indicates the effective temperature of the host star.

search and the planet's dynamical masses have been inferred from transit timing variations (Gillon et al. 2017; Grimm et al. 2018).

Figure 8 shows the mass-period parameter space of all known M dwarf planets for which both parameters are well-determined. The left panel shows the planets orbiting mid- and late-type M stars, while the right panel also includes those around early-type M dwarfs. The diagrams exhibit a bimodal distribution that resembles the one found in planetary radius using *Kepler* data mainly for solar-like stars (Fulton et al. 2017; Fulton & Petigura 2018) but also confirmed for validated and well-characterised transiting planets around M dwarfs (Hirano et al. 2018).

We also note the fact that short-period Earth-like planets in the range of 0.5–2 $M_\oplus$ are mostly found in multiple systems (triangle symbols), while regarding those in the range of 5–8 $M_\oplus$, eight out of ten planets were not found to have further planetary companions. Also striking is the lack of planets in the range of 2–5 $M_\oplus$ with orbital periods shorter than 10 d around mid- and late-type M stars. This raises questions about their formation process. Is it possible that super-Earth planets around M dwarfs prevent the formation of smaller counterparts, or are they formed by aggregation of smaller, Earth-size planets? Is the formation of a smaller counterpart dependent on the mass of the host star?

The sample of known planets with accurate mass and radius determinations around M dwarfs is still too small to address the validity of such a distribution, and its connection with planet multiplicity, with any statistical confidence. Ground-based searches, such as the CARMENES GTO program among others, together with planet detections around M dwarfs over the next few years from TESS (Ricker et al. 2014), may provide insight into this issue.

In summary, we report on the discovery of two short-period super-Earth-like planets orbiting the low-mass stars GJ 3779 and GJ 1265. They are the least massive planets discovered by the CARMENES search for exoplanets around M dwarfs to date. The CARMENES visible Doppler measurements reveal a planetary companion with a minimum mass of 8.0 $M_\oplus$ on a 3.023 d orbit around GJ 3779, and a planet of 7.4 $M_\oplus$ on a 3.651 d orbit around GJ 1265. Besides the periodic signals at around 95 d associated with rotation, the host stars do not show any evidence of RV-induced variations due to activity at the planet periods. The planets do not transit their parent stars, and they seem to belong to a population of short-period single planets around M stars with masses between 5 and 8 $M_\oplus$.

Acknowledgements. CARMENES is an instrument for the Centro Astronómico Hispano-Alemán de Calar Alto (CAHA, Almería, Spain). CARMENES is funded by the German Max-Planck-Gesellschaft (MPG), the Spanish Consejo Superior de Investigaciones Científicas (CSIC), the European Union through FEDER/ERF FICTS-2011-02 funds, and the members of the CARMENES Consortium (Max-Planck-Institut für Astronomie, Instituto de Astrofísica de Andalucía, Landessternwarte Königstuhl, Institut de Ciències de l'Espai, Insitut für Astrophysik Göttingen, Universidad Complutense de Madrid, Thüringer Landessternwarte Tautenburg, Instituto de Astrofísica de Canarias, Hamburger Sternwarte, Centro de Astrobiología and Centro Astronómico Hispano-Alemán), with additional contributions by the Spanish Ministry of Economy, the German Science Foundation through the Major Research Instrumentation Programme and DFG Research Unit FOR2544 "Blue Planets around Red Stars", the Klaus Tschira Stiftung, the states of Baden-Württemberg and Niedersachsen, and by the Junta de Andalucía. Based on observations collected at the European Organisation for Astronomical Research in the Southern Hemisphere under ESO programme(s) 072.C-0488(E) and 183.C-0437(A). R. L. has received funding from the European Union's Horizon 2020 research and innovation program under the Marie Skłodowska-Curie grant agreement No. 713673 and financial support through the "la Caixa" INPhINIT Fellowship Grant for Doctoral studies at Spanish Research Centres of Excellence, "la Caixa" Banking Foundation, Barcelona, Spain. This work is partly financed by the Spanish Ministry of Economy and Competitiveness through grants ESP2013-48391-C4-2-R, ESP2016-80435-C2-1/2-R, and AYA2016-79425–C3–1/2/3–P.

References

Affer, L., Micela, G., Damasso, M., et al. 2016, A&A, 593, A117
Anglada-Escudé, G., & Tuomi, M. 2012, A&A, 548, A58
Anglada-Escudé, G., Amado, P. J., Barnes, J., et al. 2016, Nature, 536, 437
Astudillo-Defru, N., Forveille, T., Bonfils, X., et al. 2017a, A&A, 602, A88
Astudillo-Defru, N., Díaz, R. F., Bonfils, X., et al. 2017b, A&A, 605, L11
Baluev, R. V. 2009, MNRAS, 393, 969
Barnes, J. R., Jeffers, S. V., & Jones, H. R. A. 2011, MNRAS, 412, 1599
Bayo, A., Rodrigo, C., Barrado Y., Navascués, D., et al. 2008, A&A, 492, 277
Benedict, G. F., Henry, T. J., Franz, O. G., et al. 2016, AJ, 152, 141
Berta, Z. K., Irwin, J., Charbonneau, D., Burke, C. J., & Falco, E. E. 2012, AJ, 144, 145

Berta-Thompson, Z. K., Irwin, J., Charbonneau, D., et al. 2015, Nature, 527, 204
Bonfils, X., Forveille, T., Delfosse, X., et al. 2005, A&A, 443, L15
Bonfils, X., Gillon, M., Forveille, T., et al. 2011, A&A, 528, A111
Bonfils, X., Delfosse, X., Udry, S., et al. 2013, A&A, 549, A109
Bonfils, X., Astudillo-Defru, N., Díaz, R., et al. 2018, A&A, 613, A25
Caballero, J. A., Cortés-Contreras, M., Alonso-Floriano, F. J., et al. 2016, 19th Cambridge Workshop on Cool Stars, Stellar Systems, and the Sun (CS19), 148
Charbonneau, D., Irwin, J., Nutzman, P., & Falco, E. E. 2008, AAS Meeting Abstracts, 212, 44.02
Charbonneau, D., Berta, Z. K., Irwin, J., et al. 2009, Nature, 462, 891
Cortés-Contreras, M. 2016, Ph.D. Thesis, Universidad Complutense de Madrid, Spain
Delfosse, X., Forveille, T., Ségransan, D., et al. 2000, A&A, 364, 217
Dressing, C. D., & Charbonneau, D. 2015, ApJ, 807, 45
Foreman-Mackey, D., Hogg, D. W., Lang, D., & Goodman, J. 2013, PASP, 125, 306
Forveille, T., Bonfils, X., Delfosse, X., et al. 2009, A&A, 493, 645
Fulton, B. J., & Petigura, E. A. 2018, AJ, 156, 264
Fulton, B. J., Petigura, E. A., Howard, A. W., et al. 2017, AJ, 154, 109
Gaia Collaboration (Brown, A. G. A., et al.) 2018, A&A, 616, A1
Gaidos, E., Mann, A. W., Kraus, A. L., & Ireland, M. 2016, MNRAS, 457, 2877
Gillon, M., Triaud, A. H. M. J., Demory, B.-O., et al. 2017, Nature, 542, 456
Grimm, S. L., Demory, B.-O., Gillon, M., et al. 2018, A&A, 613, A68
Hawley, S. L., Gizis, J. E., & Reid, I. N. 1996, AJ, 112, 2799
Henry, T. J., Jao, W.-C., Winters, J. G., et al. 2016, AAS Meeting Abstracts, 227, 142.01
Hirano, T., Dai, F., Gandolfi, D., et al. 2018, AJ, 155, 127
Husser, T.-O., Wende-von Berg, S., Dreizler, S., et al. 2013, A&A, 553, A6
Jeffers, S. V., Schöfer, P., Lamert, A., et al. 2018, A&A, 614, A76
Kaminski, A., Trifonov, T., Caballero, J. A., et al. 2018, A&A, 618, A115
Kane, S. R., Mahadevan, S., von Braun, K., Laughlin, G., & Ciardi, D. R. 2009, PASP, 121, 1386
Kopparapu, R. K., Ramirez, R., Kasting, J. F., et al. 2013, ApJ, 765, 131
Kopparapu, R. K., Ramirez, R. M., SchottelKotte, J., et al. 2014, ApJ, 787, L29
Kovács, G., Zucker, S., & Mazeh, T. 2002, A&A, 391, 369
Marcy, G. W., Butler, R. P., Vogt, S. S., Fischer, D., & Lissauer, J. J. 1998, ApJ, 505, L147
Mayor, M., Pepe, F., Queloz, D., et al. 2003, The Messenger, 114, 20
Neves, V., Bonfils, X., Santos, N. C., et al. 2014, A&A, 568, A121
Newton, E. R., Charbonneau, D., Irwin, J., et al. 2014, AJ, 147, 20
Passegger, V. M., Wende-von Berg, S., & Reiners, A. 2016, A&A, 587, A19
Passegger, V. M., Reiners, A., Jeffers, S. V., et al. 2018, A&A, 615, A6
Perger, M., Ribas, I., Damasso, M., et al. 2017, A&A, 608, A63
Press, W. H., Teukolsky, S. A., Vetterling, W. T., & Flannery, B. P. 1992, Numerical Recipes in FORTRAN. The Art of Scientific Computing (Cambridge: University Press)
Queloz, D., Henry, G. W., Sivan, J. P., et al. 2001, A&A, 379, 279
Quirrenbach, A., Amado, P. J., Caballero, J. A., et al. 2014, in Ground-based and Airborne Instrumentation for Astronomy V, Proc. SPIE, 9147, 91471F
Reiners, A., Schüssler, M., & Passegger, V. M. 2014, ApJ, 794, 144
Reiners, A., Ribas, I., Zechmeister, M., et al. 2018a, A&A, 609, L5
Reiners, A., Zechmeister, M., Caballero, J. A., et al. 2018b, A&A, 612, A49
Ricker, G. R., Winn, J. N., Vanderspek, R., et al. 2014, in Space Telescopes and Instrumentation 2014: Optical, Infrared, and Millimeter Wave, Proc. SPIE, 9143, 914320
Rivera, E. J., Lissauer, J. J., Butler, R. P., et al. 2005, ApJ, 634, 625
Robertson, P., Mahadevan, S., Endl, M., & Roy, A. 2014, Science, 345, 440
Rosen, S. R., Webb, N. A., Watson, M. G., et al. 2016, A&A, 590, A1
Sarkis, P., Henning, T., Kürster, M., et al. 2018, AJ, 155, 257
Skrutskie, M. F., Cutri, R. M., Stiening, R., et al. 2006, AJ, 131, 1163
Suárez Mascareño, A., González Hernández, J. I., Rebolo, R., et al. 2017, A&A, 597, A108
Tal-Or, L., Zechmeister, M., Reiners, A., et al. 2018, A&A, 614, A122
Trifonov, T., Kürster, M., Zechmeister, M., et al. 2018, A&A, 609, A117
Udry, S., Bonfils, X., Delfosse, X., et al. 2007, A&A, 469, L43
Vanderburg, A., & Johnson, J. A. 2014, PASP, 126, 948
West, A. A., Weisenburger, K. L., Irwin, J., et al. 2015, ApJ, 812, 3
Wright, J. T., & Eastman, J. D. 2014, PASP, 126, 838
Wright, D. J., Wittenmyer, R. A., Tinney, C. G., Bentley, J. S., & Zhao, J. 2016, ApJ, 817, L20
Zechmeister, M., & Kürster, M. 2009, A&A, 496, 577
Zechmeister, M., Kürster, M., & Endl, M. 2009, A&A, 505, 859
Zechmeister, M., Reiners, A., Amado, P. J., et al. 2018, A&A, 609, A12

Appendix A: Frequency-extended periodogram analysis

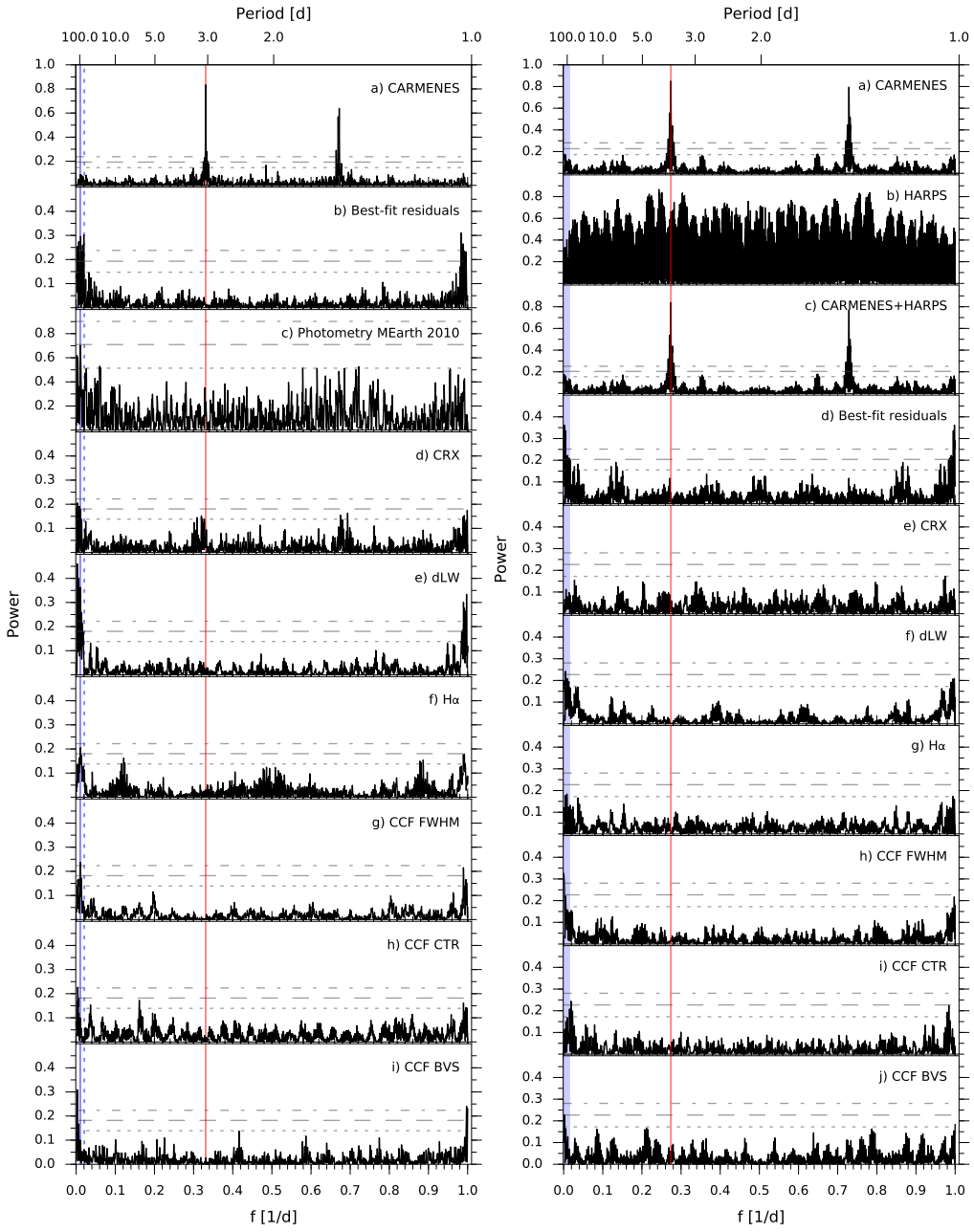

Fig. A.1. Extended GLS periodograms for GJ 3779 (*left panels*) and GJ 1265 (*right panels*) covering the full frequency range. The magnitudes and the format represented are the same as in Figs. 2 and 5.

Appendix B: Correlation between radial velocities and chromatic index

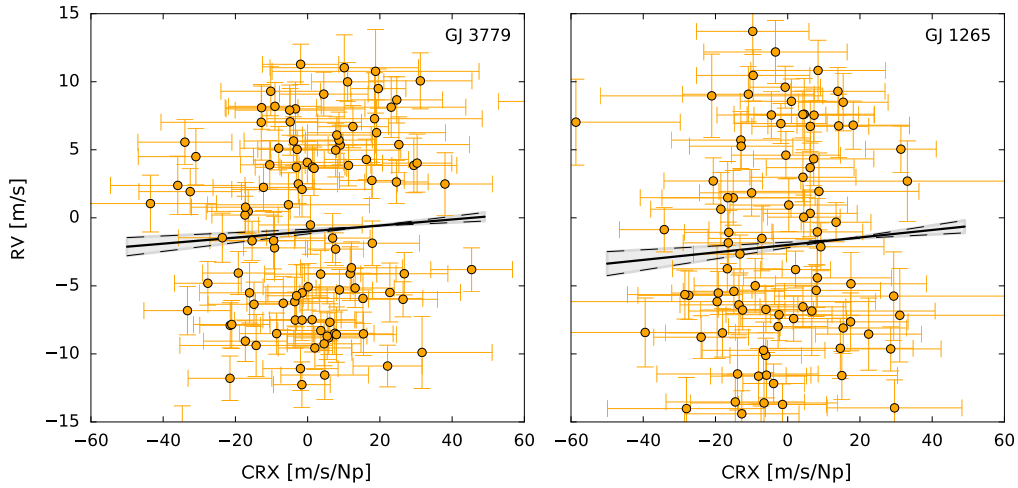

Fig. B.1. CARMENES VIS radial velocities against the chromatic index (CRX) for GJ 3779 (*left panel*) and GJ 1265 (*right panel*). The slopes of each linear fit are consistent with zero within the errors; activity-induced correlation is usually associated with a negative slope (Tal-Or et al. 2018).

Appendix C: MCMC analysis

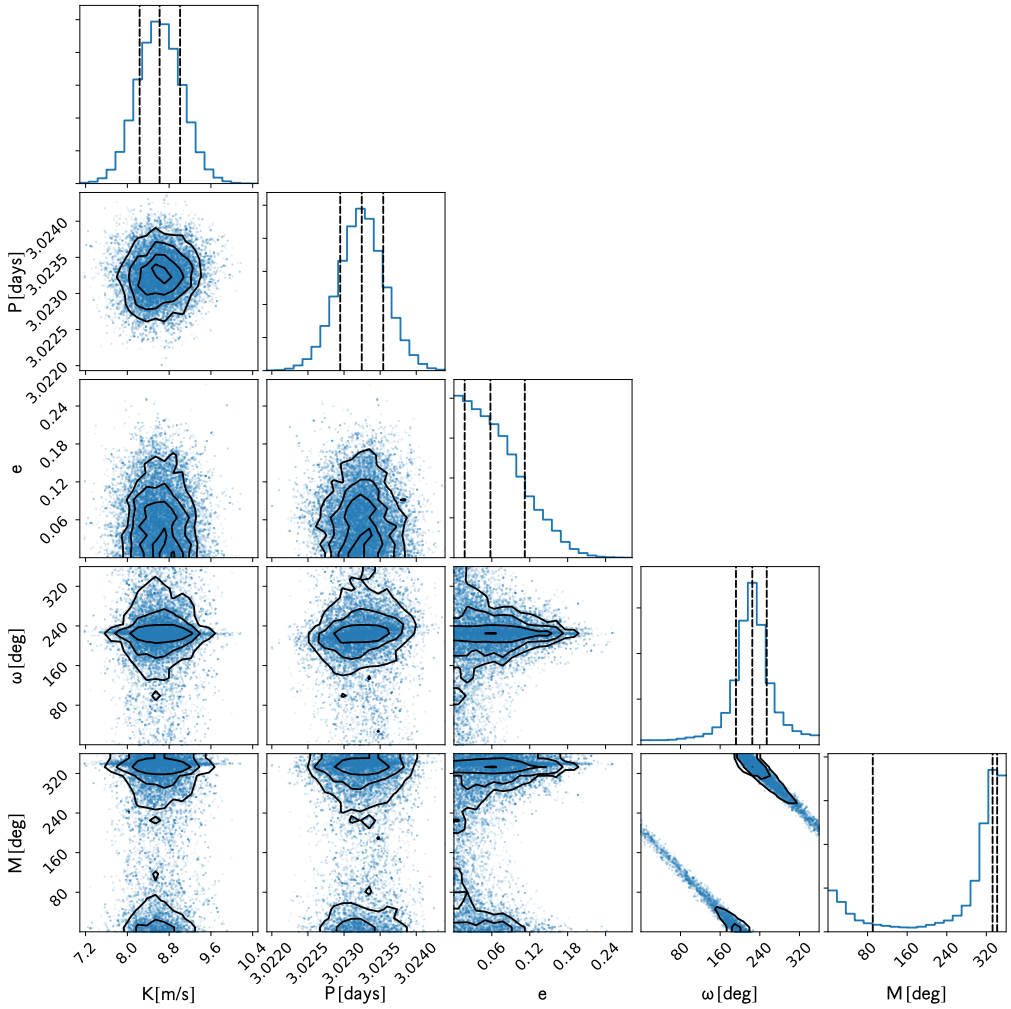

Fig. C.1. MCMC results using the CARMENES RVs obtained for GJ 3779. Each panel contains approximately 40 000 Keplerian samples. The *upper panels* of the corner plot show the probability density distributions of each orbital parameter. The vertical dashed lines indicate the mean and 1σ uncertainties of the fitted parameters. The *rest of the panels* show the dependencies between all the orbital elements in the parameter space. Black contours are drawn to improve the visualisation of the two-dimensional histograms. The distributions agree within the errors with the best-fit values from Table 2.

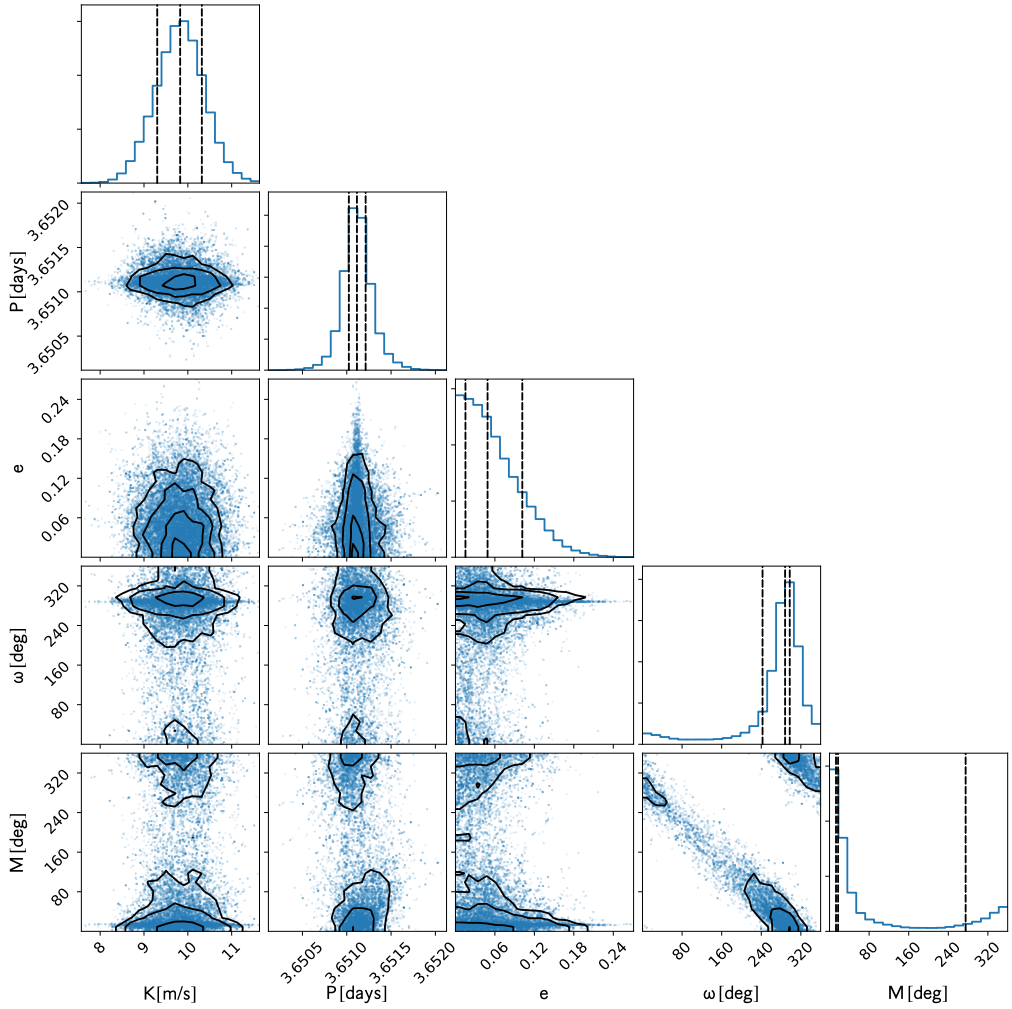

Fig. C.2. MCMC results using CARMENES and HARPS datasets obtained for GJ 1265. Each panel contains approximately 40 000 Keplerian samples. The quantities represented and the format of the plot are the same as in Fig. C.1. The distributions agree within the errors with the best-fit values from Table 2.

3

Multi-planetary system around the nearby GJ 357

The contents of this chapter refer to the article *Planetary system around the nearby GJ 357 including a transiting, hot, Earth-sized planet optimal for atmospheric characterization*, published in the journal Astronomy & Astrophysics (Luque et al., 2019b). The article was written during a four-month stay in the Max Planck Institute for Astronomy in Heidelberg, Germany, working with Prof. Dr. Martin Kürster and Dr. Trifon Trifonov. This work makes use of observations from *TESS*, archival data from HIRES, UVES, and HARPS; and unpublished radial velocities from CARMENES and PFS. The article is part of the efforts from the CARMENES-TESS project, a working group within the CARMENES consortium devoted to follow-up observations of planet candidates transiting M dwarfs detected by *TESS* in collaboration with the official *TESS* Follow-up Observing Program (TFOP). The author list comprises members from the CARMENES-TESS working group, the Magellan-TESS Survey using PFS, key investigators of the *TESS* mission and contributing members from TFOP with either analyses or ground-based follow-up observations such as transit follow-up, photometric monitoring, and high-resolution imaging. A total of 75 researchers from 39 different institutions co-sign the article.

The star GJ 357 was observed in February 2019 by the *TESS* mission, detecting a transiting Earth-sized planet that was announced in the *TESS* alerts public website on April 13, 2019. Two weeks later, we submitted an article describing the confirmation and mass determination of the alerted transiting planet and the detection of two additional planets in longer orbits. The rapid discovery and characterization was possible

thanks to the 145 readily available radial velocity observations from HIRES, UVES, HARPS, PFS, and CARMENES. Due to the precise ephemeris from transit observations and using the combined radial velocity dataset, it was possible to quickly confirm the *TESS* detection, to measure the absolute mass of the transiting planet, and to discover additional signals in the RV data that otherwise would have passed unnoticed due to their low statistical significance.

The host of this multi-planetary system is a M2.5 V star in the Hydra constellation, the closest single M dwarf with a transiting planet and the third overall. GJ 357 b, the candidate alerted by *TESS*, has an orbital period of 4 days and a bulk density like the Earth. Thanks to the brightness of its host, it is one of the best Earth-sized planets for atmospheric characterization. In this work, we simulate the planet's atmosphere assuming an Earth-like composition and assess its detectability if it were observed with the *JWST*. Our results show that methane and carbon dioxide spectral features would be detectable in just one transit in the absence of clouds or hazes.

The other two planets in the system are super-Earths with orbital periods of 9 and 55 days, respectively. Planet c would have been detected in the *TESS* photometry, which implies that its orbit is tilted more than 1 degree with respect to planet b, causing it not to transit. On the other hand, due to the 27 day baseline of *TESS* observations, the transiting window of the outermost planet was missed. If GJ 357 d transits it would become the closest transiting planet in the habitable zone of its star. Transit searches from the ground have been triggered, but so far unsuccessful — which is not surprising given that the transit probability is just $2.7 \pm 0.4\%$ (Espinoza, 2019).

This work comprises numerous analyses, but of particular importance are the stellar rotation period determination and the radial velocity modeling. For the stellar rotation period we analyzed a large dataset of ground-based photometric monitoring of the star spanning several years from the automated surveys ASAS, NSVS, ASAS-SN, and WASP-South. We modeled the photometry using Gaussian Processes, in particular a quasi-periodic kernel that is flexible enough to account for the diversity of cadence, precision and passband of the different instruments, while still being able to model a common periodicity to the complete dataset. On the other hand, the light curve and radial velocity modeling is done using the code `juliet` (Espinoza et al., 2019), which uses nested sampling algorithms to sample the parameter space. Nested sampling can efficiently compute the Bayesian evidence, which allows to perform rigorous statistical model comparison. We take advantage of this new code and carry out detailed model comparison analyses to asses the veracity of the different signals in the radial velocity data and to distinguish between true planetary companions and stellar variability.

A&A 628, A39 (2019)
https://doi.org/10.1051/0004-6361/201935801

Astronomy & Astrophysics

Planetary system around the nearby M dwarf GJ 357 including a transiting, hot, Earth-sized planet optimal for atmospheric characterization*

R. Luque[1,2], E. Pallé[1,2], D. Kossakowski[3], S. Dreizler[4], J. Kemmer[5], N. Espinoza[3], J. Burt[6,**], G. Anglada-Escudé[7,8], V. J. S. Béjar[1,2], J. A. Caballero[9], K. A. Collins[10], K. I. Collins[11], M. Cortés-Contreras[9], E. Díez-Alonso[12,13], F. Feng[14], A. Hatzes[15], C. Hellier[16], T. Henning[3], S. V. Jeffers[4], L. Kaltenegger[17], M. Kürster[3], J. Madden[17], K. Molaverdikhani[3], D. Montes[12], N. Narita[1,18,19,20], G. Nowak[1,2], A. Ofir[21], M. Oshagh[4], H. Parviainen[1,2], A. Quirrenbach[5], S. Reffert[5], A. Reiners[4], C. Rodríguez-López[8], M. Schlecker[3], S. Stock[5], T. Trifonov[3], J. N. Winn[22], M. R. Zapatero Osorio[23], M. Zechmeister[4], P. J. Amado[8], D. R. Anderson[16], N. E. Batalha[24], F. F. Bauer[8], P. Bluhm[5], C. J. Burke[6], R. P. Butler[14], D. A. Caldwell[25,26], G. Chen[27], J. D. Crane[28], D. Dragomir[6,***], C. D. Dressing[29], S. Dynes[6], J. M. Jenkins[26], A. Kaminski[5], H. Klahr[3], T. Kotani[18,20], M. Lafarga[30,31], D. W. Latham[10], P. Lewin[32], S. McDermott[33], P. Montañés-Rodríguez[1,2], J. C. Morales[30,31], F. Murgas[1,2], E. Nagel[34], S. Pedraz[35], I. Ribas[30,31], G. R. Ricker[6], P. Rowden[36], S. Seager[6,37,38], S. A. Shectman[28], M. Tamura[18,20,39], J. Teske[28,***], J. D. Twicken[25,26], R. Vanderspeck[6], S. X. Wang[14], and B. Wohler[25,26]

(Affiliations can be found after the references)

Received 29 April 2019 / Accepted 27 June 2019

ABSTRACT

We report the detection of a transiting Earth-size planet around GJ 357, a nearby M2.5 V star, using data from the Transiting Exoplanet Survey Satellite (TESS). GJ 357 b (TOI-562.01) is a transiting, hot, Earth-sized planet ($T_{eq} = 525 \pm 11$ K) with a radius of $R_b = 1.217 \pm 0.084\,R_\oplus$ and an orbital period of $P_b = 3.93$ d. Precise stellar radial velocities from CARMENES and PFS, as well as archival data from HIRES, UVES, and HARPS also display a 3.93-day periodicity, confirming the planetary nature and leading to a planetary mass of $M_b = 1.84 \pm 0.31\,M_\oplus$. In addition to the radial velocity signal for GJ 357 b, more periodicities are present in the data indicating the presence of two further planets in the system: GJ 357 c, with a minimum mass of $M_c = 3.40 \pm 0.46\,M_\oplus$ in a 9.12 d orbit, and GJ 357 d, with a minimum mass of $M_d = 6.1 \pm 1.0\,M_\oplus$ in a 55.7 d orbit inside the habitable zone. The host is relatively inactive and exhibits a photometric rotation period of $P_{rot} = 78 \pm 2$ d. GJ 357 b is to date the second closest transiting planet to the Sun, making it a prime target for further investigations such as transmission spectroscopy. Therefore, GJ 357 b represents one of the best terrestrial planets suitable for atmospheric characterization with the upcoming JWST and ground-based ELTs.

Key words. planetary systems – techniques: photometric – techniques: radial velocities – stars: individual: Gl 357 – stars: late-type

1. Introduction

To date nearly 200 exoplanets have been discovered orbiting approximately 100 M dwarfs in the solar neighborhood (e.g., Bonfils et al. 2013; Rowe et al. 2014; Trifonov et al. 2018; Ribas et al. 2018). Some of these orbit near to or in the habitable zone (e.g., Udry et al. 2007; Anglada-Escudé et al. 2013, 2016; Tuomi & Anglada-Escudé 2013; Dittmann et al. 2017; Reiners et al. 2018). However, only 11 M dwarf planet systems have been detected with both the transit as well as the radial velocity (RV) method, which allows us to derive their density from their measured radius and mass, informing us about its bulk properties. When transit timing variation (TTV) mass measurements are included, TRAPPIST-1 (2MUCD 12171, Gillon et al. 2017) represents the 12th M dwarf planet system with mass and radius measurements.

Only six of the abovementioned eleven systems contain planets with masses below $10\,M_\oplus$: LHS 1140 b and c (GJ 3053, Dittmann et al. 2017; Ment et al. 2019), K2-3 b and c (PM J11293–0127, Almenara et al. 2015; Sinukoff et al. 2016), K2-18 b (PM J11302+0735, Cloutier et al. 2017; Sarkis et al. 2018), GJ 1214 b (LHS 3275 b, Harpsøe et al. 2013), GJ 1132 (Berta-Thompson et al. 2015; Bonfils et al. 2018), and b–g planets of TRAPPIST-1 (Gillon et al. 2016, 2017). However, only three planets with masses similar to Earth orbit M dwarfs of moderate brightness ($J = 9.2$–9.8 mag): GJ 1132 b ($1.66 \pm 0.23\,M_\oplus$), LHS 1140 c ($1.81 \pm 0.39\,M_\oplus$), and K2-18 b ($2.1^{+2.1}_{-1.3}\,M_\oplus$). Systems hosting small terrestrial exoplanets orbiting bright stars are ideal not only from the perspective of precise mass measurements with ground-based instruments, but also for further orbital (e.g., obliquity determination) and atmospheric characterization using current and future observatories (see, e.g., Batalha et al. 2018).

The Transiting Exoplanet Survey Satellite (TESS, Ricker et al. 2015) mission is an observatory that was launched to find small planets transiting small, bright stars. Indeed, since the start of scientific operations in July 2018, TESS has already

* RV data are only available at the CDS via anonymous ftp to cdsarc.u-strasbg.fr (130.79.128.5) or via http://cdsarc.u-strasbg.fr/viz-bin/qcat?J/A+A/628/A39
** Torres Fellow.
*** NASA Hubble Fellow.

uncovered over 600 new planet candidates, and is quickly increasing the sample of known Earths and super-Earths around small M-type stars (Vanderspek et al. 2019; Günther et al. 2019; Kostov et al. 2019). In this paper, we present the discovery of three small planets around a bright M dwarf, one of which, GJ 357 b, is an Earth-sized transiting exoplanet discovered using photometry from the TESS mission. To date, GJ 357 b is the second nearest ($d = 9.44$ pc) transiting planet to the Sun after HD 219134 b (Motalebi et al. 2015, $d = 6.53$ pc), and the closest around an M dwarf. Besides, it is amenable to future detailed atmospheric characterization, opening the door to new studies for atmospheric characterization of Earth-like planet atmospheres (Pallé et al. 2009).

The paper is structured as follows. Section 2 presents the TESS photometry used for the discovery of GJ 357 b. Section 3 presents ground-based observations of the star including seeing-limited photometric monitoring, high-resolution imaging, and precise RVs. Section 4 presents a detailed analysis of the stellar properties of GJ 357. Section 5 presents an analysis of the available data in order to constrain the planetary properties of the system, including precise mass constraints on GJ 357 b along with a detection and characterization of two additional planets in the system, GJ 357 c and GJ 357 d. Section 6 presents a discussion of our results and, finally, Sect. 7 presents our conclusions.

2. TESS photometry

Planet GJ 357 (TIC 413248763) was observed by TESS in 2-min short-cadence integrations in Sector 8 (Camera #2, CCD #3) from February 2, 2019 until February 27, 2019 (see Fig. 1), and will not be observed again during the primary mission. At BJD = 2 458 531.74, an interruption in communications between the instrument and spacecraft occurred, resulting in an instrument turn-off until BJD = 2 458 535.00. Together with the satellite repointing for data downlink between BJD = 2 458 529.06 and BJD = 2 458 530.44, a gap of approximately 6 d is present in the photometry. In our analysis, the datapoints between BJD = 2 458 530.44 and BJD = 2 458 531.74 were masked out.

2.1. Transit searches

TESS objects of interest (TOIs) are announced regularly via the TESS data alerts public website[1]. TOI-562.01 was announced on April 13, 2019 and its corresponding light curve produced by the Science Processing Operations Center (SPOC; Jenkins et al. 2016) at the NASA Ames Research Center was uploaded to the Mikulski Archive for Space Telescopes (MAST)[2] on April 17, 2019. SPOC provided for this target simple aperture photometry (SAP) and systematics-corrected photometry, a procedure consisting of an adaptation of the Kepler Presearch Data Conditioning algorithm (PDC, Smith et al. 2012; Stumpe et al. 2012, 2014) to TESS. The light curves generated by both methods are shown in Fig. 1. We use the latter one (PDC-corrected SAP, Fig. 1 bottom panel) for the remainder of this work.

A signal with a period of 3.93 d and a transit depth of 1164 ± 66 ppm, corresponding to a planet radius of approximately $1.3 \pm 0.3\,R_\oplus$ was detected in the TESS photometry. The Earth-sized planet candidate passed all the tests from the Alerts Data Validation Report[3] (DVR; Twicken et al. 2018; Li et al. 2019), for example, even-odd transits comparison, eclipsing binary discrimination tests, ghost diagnostic tests to help rule out scattered light, or background eclipsing binaries, among others. The report indicates that the dimming events are associated with significant image motion, which is usually indicative of a background eclipsing binary. However, in this case, the reported information is meaningless because the star is saturated. On the other hand, the transit source is coincident with the core of the stellar point spread function (PSF), so the transit events happen on the target and not, for example, on a nearby bright star.

We also performed an independent analysis of the TESS light curve in order to confirm the DVR analysis and search for additional transit signals. An iterative approach was employed: in each iteration the same raw data were detrended and outliers-rejected, a signal was identified and then modeled, and that model was temporarily divided-out during the detrending of the next iteration to produce a succession of improving models, until the χ^2 converges. The raw photometry was detrended by fitting a truncated Fourier series, starting from the natural period of twice the data span, and all of its harmonics, down to some "protected" time span to make sure the filter does not modify the shape of the transit itself. We used a protected time span of 0.5 d, and this series was iteratively fitted with 4σ rejection. Finally, `OptimalBLS` (Ofir 2014) is used to identify the transit signal, which is then modeled using the Mandel & Agol (2002) model and the differential evolution Markov chain Monte Carlo algorithm (ter Braak & Vrugt 2008). The final model has $\chi^2_\nu = 1.017$ and the resultant transit parameters are consistent with the TESS DVR. We also checked for odd-even differences between the transits, additional transit signals, and parabolic TTVs (Ofir et al. 2018) – all with null results.

2.2. Limits on photometric contamination

Given the large TESS pixel size of 21″, it is essential to verify that no visually close-by targets are present that could affect the depth of the transit. There are two bright objects within one TESS pixel of GJ 357: (i) *Gaia* DR2 5664813824769090944 at 15.19″ and $G_{R_P} = 15.57$ mag; and (ii) *Gaia* DR2 5664814202726212224 at 18.31″ and $G_{R_P} = 5.50$ mag. However, they are much fainter than GJ 357 (TOI-562, *Gaia* DR2 5664814198431308288, $G_{R_P} = 8.79$ mag) and their angular separations actually increased between the epochs of observation of *Gaia* (J2015.5) and TESS (J2019.1–J2019.2) due to the high proper motion of this star.

These two sources are by far the brightest ones apart from our target in the digitizations of red photographic plates taken in 1984 and 1996 with the UK Schmidt telescope. The *Gaia* G_{R_P}-band (630–1050 nm) and the TESS band (600–1000 nm) are very much alike, allowing us to estimate the dilution factor for TESS using Eq. (2) in Espinoza et al. (2018) to be $D_{\rm TESS} = 0.996$, which is consistent with 1.00, therefore compatible with no flux contamination.

3. Ground-based observations

3.1. Transit follow-up

We acquired ground-based time-series follow-up photometry of a full transit of TOI-562.01 on UTC April 26, 2019 from a Las Cumbres Observatory (LCO) 1.0 m telescope (Brown et al. 2013) at Cerro Tololo Inter-American Observatory (CTIO) as part of the TESS follow-up program (TFOP) SG1 Group. We used the `TESS Transit Finder`, which is a customized version of the `Tapir` software package (Jensen 2013), to schedule

[1] https://tess.mit.edu/alerts/
[2] https://mast.stsci.edu
[3] The complete DVR of TOI-562.01 can be downloaded from https://tev.mit.edu/vet/spoc-s08-b01/413248763/dl/pdf/

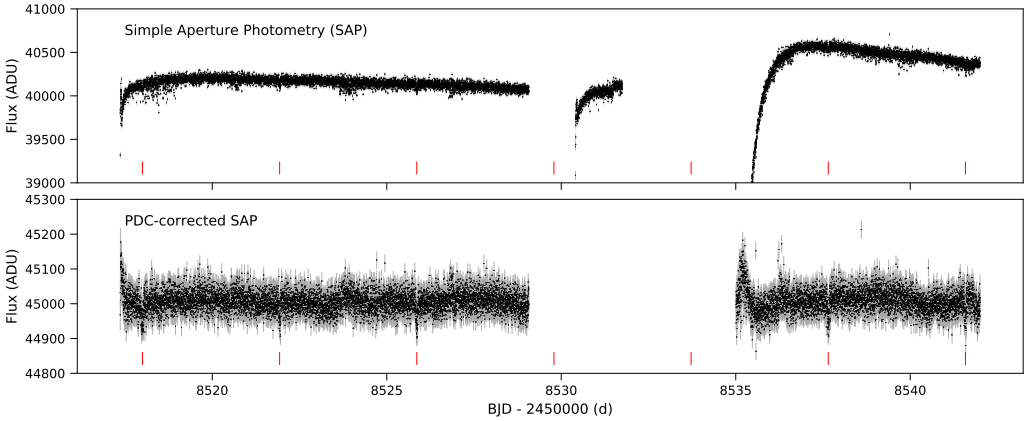

Fig. 1. TESS light curves of GJ 357 provided by SPOC. *Top panel*: simple aperture photometry. *Bottom panel*: PDC-corrected photometry. Transits of the planet candidate TOI-562.01 are marked in red.

photometric time-series follow-up observations. The 4096 × 4096 LCO SINISTRO camera has an image scale of 0.″389 pix^{-1} resulting in a 26′ × 26′ field of view. The 227 min observation in z_s band used 30 s exposure times which, in combination with the 26 s readout time, resulted in 244 images. The images were calibrated by the standard LCO `BANZAI` pipeline and the photometric data were extracted using the `AstroImageJ` software package (Collins et al. 2017). The target star light curve shows a clear transit detection in a 7.78″ radius aperture (see middle right panel of Fig. 5). The full width half maximum (FWHM) of the target and nearby stars is ∼4″, so the follow-up aperture is only marginally contaminated by neighboring faint *Gaia* DR2 stars. The transit signal can be reliably detected with apertures that have a radius as small as 4.28″, after which systematic effects start to dominate the light curve. We note that the detection of an ∼1200 ppm transit with a 1 m ground-based telescope in a single transit is remarkable. A similar performance has been achieved only with the 1.2 m *Euler*-Swiss telescope combining two transits of HD 106315 c (Lendl et al. 2017), and highlights the importance of ground-based facilities to maintain and refine ephemeris of TESS planet candidates even in the Earth-sized regime.

3.2. Seeing-limited photometric monitoring

We made a compilation of photometric series obtained by long-time baseline, automated surveys exactly as in Díez Alonso et al. (2019). In particular we retrieved data from the following public surveys: All-Sky Automated Survey (ASAS; Pojmanski 2002), Northern Sky Variability Survey (NSVS; Woźniak et al. 2004), and All-Sky Automated Survey for Supernovae (ASAS-SN; Kochanek et al. 2017). The telescope location, instrument configurations, and photometric bands of each public survey were summarized by Díez Alonso et al. (2019). We did not find GJ 357 data in other public catalogs, such as The MEarth Project (Charbonneau et al. 2008), the Catalina surveys (Drake et al. 2014), or the Hungarian Automated Telescope Network (Bakos et al. 2004).

WASP-South, the southern station of the Wide Angle Search for Planets (Pollacco et al. 2006), is an array of eight cameras using 200-mm f/1.8 lenses backed by 2048 × 2048 CCDs, each camera covering 7.8° × 7.8°. It rasters a set of different pointings with a typical 10-min cadence. WASP-South observed fields containing GJ 357 every year from 2007 to 2012, obtaining data over a span of typically 120 d each season, acquiring a total of 48 000 photometric observations.

3.3. High-resolution imaging

FastCam. Although we discuss in Sect. 2.2 that there are no visually close companions that could affect the depth of the transit of GJ 357, we obtained high-resolution observations at different epochs to exclude the possibility of a physically-bound eclipsing binary that may produce the transits detected in the TESS light curve. First, we observed GJ 357 with the FastCam instrument (Oscoz et al. 2008) mounted on the 1.5 m Telescopio *Carlos Sánchez* at the Teide Observatory on January 14, 2013. These observations were part of our high-resolution imaging campaign of M dwarfs to characterize stellar multiplicity and select the most appropriate targets for the CARMENES survey (Cortés-Contreras et al. 2017). FastCam is a lucky imaging camera with a high readout speed, employing the subelectron noise L3CCD Andor 512 × 512 detector, which provides a pixel size of 0.0425″ and a field of view of 21.2″ × 21.2″. We obtained ten blocks of a thousand individual frames with 50 ms exposure time in the I band. Data were bias subtracted, aligned, and combined using the brightest pixel as a reference as described in Labadie et al. (2010) and Jódar et al. (2013). We selected the best 10% of the frames to produce the final image and determined that there are no background contaminating sources with $\delta I < 3$ mag down to 0.5″ and with $\delta I < 6$ mag down to 3.0″ and up to 8.5″ (given by the detector size).

IRD. We also observed GJ 357 with the InfraRed Doppler (IRD, Kotani et al. 2018) instrument on the Subaru 8.2 m telescope on April 18, 2019. IRD is a fibre-fed instrument through a fibre injection module behind an adaptive optics (AO) system (AO188, Hayano et al. 2010). A fibre injection module camera (FIMC) monitors images around targets to enable fibre injection of stellar light and guiding, and can take AO-corrected images of observing targets. The FIMC employs a CCD with pixel scale of 0.067″ per pixel and observes in 970–1050 nm. Figure 2 is the

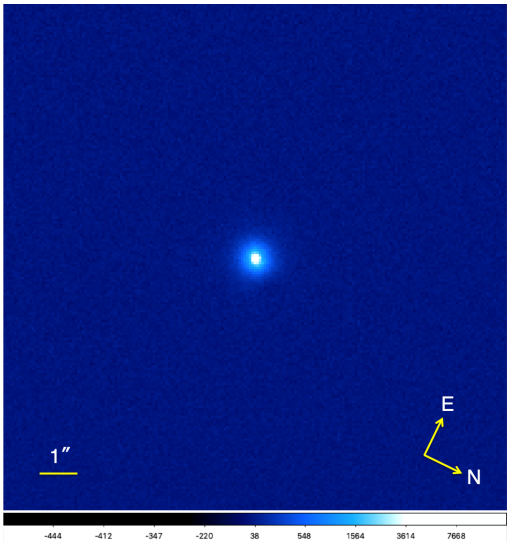

Fig. 2. Adaptive-optics-corrected image taken with the fiber injection module camera of IRD mounted on the Subaru 8.2 m telescope on April 18, 2019. The field of view is 13.4″ × 13.4″ (200 × 200 pix). Color coding is assigned in logarithmic scale. North is 116° turned clockwise from the upper direction.

FIMC image of GJ 357. The image shows a 200 × 200 pixel region around GJ 357, revealing no nearby point source.

We note that GJ 357 is a high proper motion star with 0.139″ per year in RA and −0.990″ per year in Dec based on the *Gaia* Data Release 2 (DR2) data (Gaia Collaboration 2018). It means that the star was about 0.8″ to the west and about 6″ to the north at the time of the FastCam observation. The FastCam and IRD FIMC non-detection of any nearby companion excludes any background object at the original position of the FastCam observation. We exclude any false positive scenario and conclude there is no flux contamination from visually close-by targets in the GJ 357 transit data, and we fix the dilution factor for TESS to one in all of our model fits.

3.4. Precise radial velocities

3.4.1. HIRES

The high-resolution spectrograph HIRES (Vogt et al. 1994) mounted on the 10-m Keck-I telescope has been extensively used to search for exoplanets around bright dwarf stars using the RV technique (e.g., Vogt et al. 2000; Cumming et al. 2008). As part of this effort, Butler et al. (2017) published 64 480 observations of a sample of 1699 stars collected with HIRES between 1996 and 2014. These data have been recently reanalyzed by Tal-Or et al. (2019) using a sample of RV-quiet stars (i.e., whose RV scatter is <10 m s^{-1}), who found small, but significant systematic effects in the RVs: a discontinuous jump caused by major modifications of the instrument in August 2004, a long-term drift, and a small intra-night drift. We use a total of 36 measurements for GJ 357 taken between January 26, 1998 and February 20, 2013. The RVs show a median internal uncertainty of 2.4 m s^{-1} and a rms of 4.0 m s^{-1} around the mean value.

3.4.2. UVES

Zechmeister et al. (2009) published 70 RV measurements of GJ 357 taken between November 15, 2000 and March 25, 2007 as part of the M dwarf planet search for terrestrial planets in the habitable zone with UVES at the ESO Very Large Telescope. RVs were obtained with the AUSTRAL code (Endl et al. 2000) and combined into nightly averages following Kürster et al. (2003). The 30 nightly binned RVs show a median internal uncertainty of 2.5 m s^{-1} and a rms of 5.3 m s^{-1} around the mean value.

3.4.3. HARPS

The High Accuracy Radial velocity Planet Searcher (HARPS, Mayor et al. 2003) is an ultra-precise Échelle spectrograph in the optical regime installed at the ESO 3.6 m telescope at La Silla Observatory in Chile, with a sub-m s^{-1} precision. We retrieved 53 high-resolution spectra from the ESO public archive collected between December 13, 2003 and February 13, 2013. We extracted the FWHM and bisector span (BIS) of the cross-correlation function from the FITS headers as computed by the DRS ESO HARPS pipeline (Lovis & Pepe 2007), but to obtain the RVs we used SERVAL (Zechmeister et al. 2018), based on least-squares fitting with a high signal-to-noise (S/N) template created by co-adding all available spectra of the star. The RVs have a median internal uncertainty of 1 m s^{-1} and a rms of 3.3 m s^{-1} around the mean value.

3.4.4. PFS

The Planet Finder Spectrograph (Crane et al. 2010) is an iodine-cell, high-precision RV instrument mounted on the 6.5 m *Magellan* II telescope at Las Campanas Observatory in Chile. RVs are measured by placing a cell of gaseous I_2 in the converging beam of the telescope. This imprints the 5000–6200 Å region of incoming stellar spectra with a dense forest of I_2 lines that act as a wavelength calibrator, and provide a proxy for the PSF of the instrument. GJ 357 was observed a total of nine times as part of the long-term *Magellan* Planet Search Program between March 2016 and January 2019. After TESS' identification of transits in GJ 357, the star was then observed at higher precision during the April and May 2019 runs, which added an additional seven RVs to the dataset. The iodine data prior to February 2018 (PFSpre) were taken through a 0.5″ slit resulting in $R \sim 80\,000$, and those after (PFSpost) were taken through a 0.3″ slit, resulting in $R \sim 130\,000$. A different offset must be accounted for the RVs taken before and after this intervention. All PFS data are reduced with a custom IDL pipeline that flat fields, removes cosmic rays, and subtracts scattered light. Additional details about the iodine-cell RV extraction method can be found in Butler et al. (1996). The RVs have a median internal uncertainty of 1.3 (0.7) m s^{-1} and an rms of 3.1 (2.3) m s^{-1} around the mean value for PFSpre (PFSpost).

3.4.5. CARMENES

The star GJ 357 (Karmn J09360-216) is one of the 342 stars monitored in the CARMENES Guaranteed Time Observation program to search for exoplanets around M dwarfs, which began in January 2016 (Reiners et al. 2018). The CARMENES instrument is mounted at the 3.5 m telescope at the Calar Alto Observatory in Spain and has two channels: the visual (VIS) covers the spectral range 0.52–0.96 μm and the near-infrared (NIR) covers the 0.96–1.71 μm range (Quirrenbach et al. 2014, 2018). GJ 357 was observed ten times between December 13,

2016 and March 16, 2019, and the VIS RVs – extracted with SERVAL and corrected for barycentric motion, secular acceleration, instrumental drift, and nightly zero-points (see Trifonov et al. 2018; Luque et al. 2018, for details) – show a median internal uncertainty of 1.3 m s^{-1} and a rms of 2.8 m s^{-1} around the mean value.

4. Stellar properties

4.1. Stellar parameters

The star GJ 357 (L 678-39, Karmn J09360-216, TIC 413248763) is a high proper motion star in the Hydra constellation classified as M2.5 V by Hawley et al. (1996). Located at a distance of $d \approx 9.4$ pc (Gaia Collaboration 2018), it is one of the brightest single M dwarfs in the sky, with an apparent magnitude in the J band of 7.337 mag (Skrutskie et al. 2006) and no evidence for multiplicity, either at short or wide separations (Cortés-Contreras et al. 2017). Accurate stellar parameters of GJ 357 were presented in Schweitzer et al. (2019), who determined radii, masses, and updated photospheric parameters for 293 bright M dwarfs from the CARMENES survey using various methods. In summary, Schweitzer et al. (2019) derived the radii from Stefan–Boltzmann's law, effective temperatures from a spectral analysis using the latest grid of PHOENIX-ACES models, luminosities from integrating broadband photometry together with *Gaia* DR2 parallaxes, and masses from an updated mass-radius relation derived from eclipsing binaries.

According to this analysis, GJ 357 has an effective temperature of 3505 ± 51 K and a mass of $0.342 \pm 0.011\ M_\odot$. Furthermore, with the *Gaia* DR2 equatorial coordinates, proper motions, and parallax, and absolute RV measured from CARMENES spectra, we compute galactocentric space velocities UVW as in Montes et al. (2001) and Cortés Contreras (2016) that kinematically put GJ 357 in the thin disk of the Galaxy. A summary of all stellar properties can be found in Table 1.

4.2. Activity and rotation period

Using CARMENES data, Reiners et al. (2018) determined a Doppler broadening upper limit of $v \sin i < 2$ km s^{-1} for GJ 357. This slow rotational velocity is consistent with its low level of magnetic activity. An analysis of the Hα activity in the CARMENES spectra shows that it is an inactive star and that the rotational variations in Hα and other spectral indicators are consistent with other inactive stars (Schöfer et al. 2019). GJ 357 has a $\log R'_{\rm HK}$ value of –5.37, and is one of the least active stars in the Boro Saikia et al. (2018) catalog of chromospheric activity of nearly 4500 stars, consistent with our kinematic analysis. In addition, this is in agreement with the upper limit set by Stelzer et al. (2013) in its X-ray flux ($\log F_{\rm X} < -13.09$ mW m^{-2}) and the fact that Moutou et al. (2017) were not able to measure its magnetic field strength based on optical high-resolution spectra obtained with ESPaDOnS at the Canada–France–Hawai'i Telescope.

From spectroscopic determinations, the small value of $\log R'_{\rm HK}$ indicates a long rotation period of between 70 and 120 d (Suárez Mascareno et al. 2015; Astudillo-Defru et al. 2017; Boro Saikia et al. 2018). Therefore, we searched the WASP data for rotational modulations, treating each season of data in a given camera as a separate dataset, using the methods presented in Maxted et al. (2011). The results are tabulated in Table 2. We find a significant 70–90 d periodicity across all seasons with more than 2000 datapoints. Since this timescale is not much shorter than the coverage in each year, the period error in each dataset is ∼10 d. The amplitude of the modulation ranges from 2 to 9 mmag, and the false-alarm probability is less than 10^{-4}.

Then, we use a more sophisticated model to determine precisely the empirical rotational period of the star by fitting the full photometric dataset described in Sect. 3.2 (i.e., the ASAS, NSVS, ASAS-SN – with observations both in g and V bands – and WASP datasets) with a quasi-periodic (QP) Gaussian process (GP). In particular, we use the GP kernel introduced in Foreman-Mackey et al. (2017) of the form

$$k_{i,j}(\tau) = \frac{B}{2+C} e^{-\tau/L} \left[\cos\left(\frac{2\pi\tau}{P_{\rm rot}}\right) + (1+C) \right], \quad (1)$$

where $\tau = |t_i - t_j|$ is the time-lag, B and C define the amplitude of the GP, L is a timescale for the amplitude-modulation of the GP, and $P_{\rm rot}$ is the rotational period of the QP modulations. For the fit, we consider that each of the five datasets can have different values of B and C in order to account for the possibility

Table 1. Stellar parameters of GJ 357.

Parameter	Value	Reference
	Name and identifiers	
Name	L 678-39	Luyten (1942)
GJ	357	Gliese (1957)
Karmn	J09360-216	AF15
TOI	562	TESS Alerts
TIC	413248763	Stassun et al. (2018)
	Coordinates and spectral type	
α	09:36:01.64	*Gaia* DR2
δ	–21:39:38.9	*Gaia* DR2
SpT	M2.5 V	Hawley et al. (1996)
	Magnitudes	
B (mag)	12.52 ± 0.02	UCAC4
V (mag)	10.92 ± 0.03	UCAC4
g (mag)	11.70 ± 0.02	UCAC4
G (mag)	9.8804 ± 0.0014	*Gaia* DR2
r (mag)	10.34 ± 0.09	UCAC4
i (mag)	9.35 ± 0.27	UCAC4
J (mag)	7.337 ± 0.034	2MASS
H (mag)	6.740 ± 0.033	2MASS
$K_{\rm s}$ (mag)	6.475 ± 0.017	2MASS
	Parallax and kinematics	
π (mas)	105.88 ± 0.06	*Gaia* DR2
d (pc)	9.444 ± 0.005	*Gaia* DR2
$\mu_\alpha \cos\delta$ (mas yr^{-1})	$+138.694 \pm 0.100$	*Gaia* DR2
μ_δ (mas yr^{-1})	-990.311 ± 0.083	*Gaia* DR2
V_r (km s^{-1})	-34.70 ± 0.50	This work
U (km s^{-1})	41.11 ± 0.13	This work
V (km s^{-1})	11.37 ± 0.45	This work
W (km s^{-1})	-37.25 ± 0.19	This work
	Photospheric parameters	
$T_{\rm eff}$ (K)	3505 ± 51	Schweitzer et al. (2019)
$\log g$	4.94 ± 0.07	Schweitzer et al. (2019)
[Fe/H]	-0.12 ± 0.16	Schweitzer et al. (2019)
$v \sin i_\star$ (km s^{-1})	<2.0	Reiners et al. (2018)
	Physical parameters	
M ($M_\odot$)	0.342 ± 0.011	Schweitzer et al. (2019)
R ($R_\odot$)	0.337 ± 0.015	Schweitzer et al. (2019)
L ($10^{-4}\ L_\odot$)	159.1 ± 3.6	Schweitzer et al. (2019)

References. AF15: Alonso-Floriano et al. (2015); *Gaia* DR2: Gaia Collaboration (2018); UCAC4: Zacharias et al. (2013); 2MASS: Skrutskie et al. (2006).

Table 2. Rotation-modulation search of WASP-South data.

Year (camera)	N_{pts}	P (d)	Ampl. (mag)	FAP	A_{95} [(a)] (mag)
2007 (226)	7225	74	0.002	0.0099	0.0011
2008 (226)	8947	79	0.002	0.0083	0.0013
2009 (228)	5785	91	0.005	0.0000	0.0015
2010 (227)	2291	84	0.006	0.0001	0.0036
2010 (228)	4745	84	0.009	0.0000	0.0038
2011 (222)	5272	72	0.004	0.0000	0.0019
2012 (222)	5085	74	0.007	0.0000	0.0026
2012 (227)	2605	71	0.006	0.0000	0.0030

Notes. [(a)]Amplitude corresponding to a 95% probability of a false alarm.

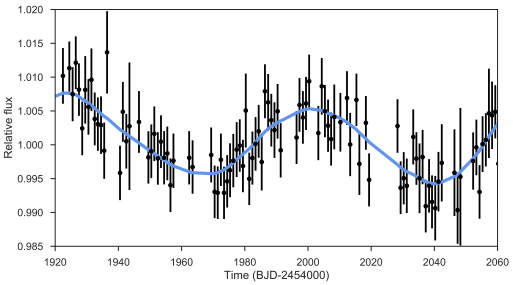

Fig. 3. Close-up of the GP fit to all the photometric datasets used to estimate the stellar rotation period of the star. Black points show the WASP data, where a QP modulation can be clearly seen. Our best-fit GP fit (blue) reveals a rotational period of $P_{rot} = 77.8^{+2.1}_{-2.0}$ d.

that different bands could have different GP amplitudes, while the timescale of the modulation as well as the rotational period is left as a common parameter between the datasets. In addition, we fit for a flux offset between the photometric datasets, as well as for extra jitter terms added in quadrature to the diagonal of the resulting covariance matrix implied by this QP GP. We consider wide priors for B, C (log-uniform between 10^{-5} ppm and 10^5 ppm), L (log-uniform between 10^{-5} and 10^5 d), rotation period (uniform between 0 and 100 d), flux offsets (Gaussian centered on 0 and standard deviation of 10^5 ppm), and jitters (log-uniform between 1 and 10^5 ppm). The fit is performed using `juliet` (Espinoza et al. 2018, see next section for a full description of the algorithm) and a close-up of the resulting fit is presented in Fig. 3 for illustration on how large the QP variations are in the WASP photometry, where the flux variability can be readily seen by eye.

The resulting rotational period from this analysis is of $P_{rot} = 77.8^{+2.1}_{-2.0}$ d, consistent with the expectation from the small value of $\log R'_{HK}$.

5. Analysis and results

5.1. Period analysis of the RV data

We performed a signal search in the RV data using generalized Lomb–Scargle (GLS) periodograms (Zechmeister & Kürster 2009). Figure 4 presents a series of GLS periodograms of the residual RVs after subtracting an increasing number of periodic signals. For each panel, we computed the theoretical false alarm probability (FAP) as described in Zechmeister & Kürster (2009), and show the 10, 1, and 0.1% levels. After subtracting a model that fits only the instrumental offsets μ_{instr} and jitters σ_{instr} (Fig. 4a), we find that the periodogram is dominated by a periodic signal at $P \sim 56$ d and its aliases around periods of one day due to the sampling of the data.

After fitting a sinusoid to this signal, a GLS periodogram of the residuals shows many signals with FAP < 1%. One of those signals is at 3.93 d, corresponding to the transiting planet detected in the TESS data. In this case, however, we want to know what is the probability that noise can produce a peak higher than what is seen exactly at the known frequency of the transiting planet, the spectral FAP. Following Zechmeister & Kürster (2009), we use a bootstrapping randomization method over a narrow frequency range centered on the planet orbital frequency to determine it. The analysis yields spectral FAP = 0.00075. We thus estimate a FAP ~ 0.08% for the 3.93 d signal.

The residuals after the modeling of the 56 and 3.93 d signals support a further periodicity of $P = 9.1$ d with a FAP < 0.1% (Fig. 4c). This signal is persistent throughout the complete analysis and therefore cannot be explained by any of the other two known sources. Including this periodicity in the model as an extra sinusoid (Fig. 4d), the GLS of the residuals reveals a single relevant periodicity at 87 d. When including a fourth sinusoid in the analysis at 87 d, different peaks with FAP ≈ 10% populate the 1 d region. We discuss in depth the nature of the four signals detected in the GLS in the next section, using more sophisticated models to fit the numerous periodicities in the RV dataset.

5.2. Modeling results

We used the recently published algorithm `juliet` (Espinoza et al. 2018) to model jointly the photometric and Doppler data. The algorithm is built on many publicly available tools for the modeling of transits (`batman`, Kreidberg 2015), RVs (`radvel`, Fulton et al. 2018), and GP (`george`, Ambikasaran et al. 2015; `celerite`, Foreman-Mackey et al. 2017). In order to compare different models, `juliet` efficiently computes the Bayesian model log evidence ($\ln Z$) using either MultiNest (Feroz et al. 2009) via the `PyMultiNest` package (Buchner et al. 2014) or the `dynesty` package (Speagle 2019). Nested sampling algorithms sample directly from the given priors instead of starting off with an initial parameter vector around a likelihood maximum found via optimization techniques, as done in common sampling methods. The trade-off between its versatility and completeness in the parameter space search is the computation time. For this reason, our prior choices have been selected to be the ideal balance between being informed, yet wide enough to fully acquire the posterior distribution map. We consider a model to be moderately favored over another if the difference in its Bayesian log evidence is greater than two, and strongly favored if it is greater than five (Trotta 2008). If $\Delta \ln Z \lesssim 2$, then the models are indistinguishable so the simpler model with less degrees of freedom would be chosen.

5.2.1. Photometry only

In order to constrain the orbital period and time of transit center, we performed an analysis with `juliet` using only the TESS photometry. We chose the priors in the orbital parameters from the TESS DVR and our independent optimal BLS analysis. We adopted a few parametrization modifications when dealing with the transit photometry. Namely, we assigned a quadratic limb-darkening law for TESS, as shown to be appropriate for

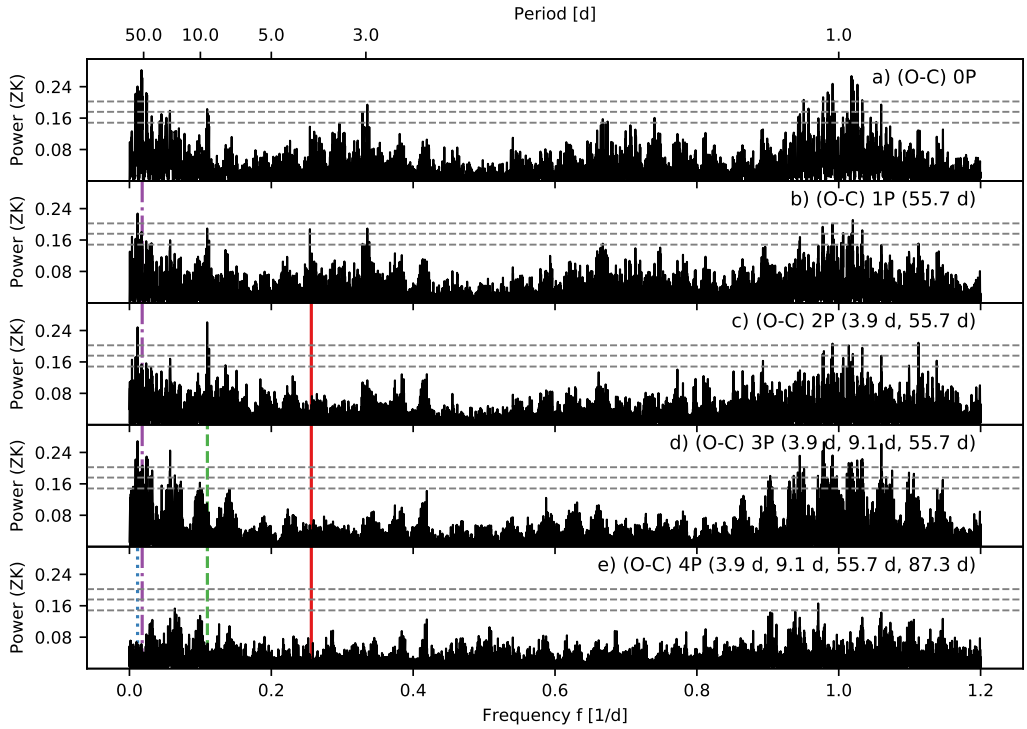

Fig. 4. Generalized Lomb–Scargle periodograms of the residual RVs after subtraction of different models. *Panel a*: no signal subtracted, only instrumental offsets and jitter fitted. *Panel b*: periodogram of the RV residuals after the subtraction of one sinusoidal signal with $P = 55.7$ d (vertical purple dashed-dotted line). *Panel c*: periodogram of the RV residuals after the simultaneous modeling of two signals with periods at 3.93 d (red solid line) and 55.7 d. *Panel d*: periodogram of the RV residuals after the simultaneous modeling of three periodic signals with $P = 55.7$ d, $P = 3.93$ d, and $P = 9.1$ d (green dashed line). *Panel e*: periodogram of the RV residuals after the simultaneous modeling of four periodic signals with $P = 55.7$ d, $P = 3.93$ d, $P = 9.1$ d, and $P \sim 87$ d (blue dotted line). The gray dashed lines indicate from bottom to top the analytic 10, 1, and 0.1% FAP levels, respectively.

space-based missions (Espinoza & Jordán 2015), which then was parametrized with the uniform sampling scheme (q_1, q_2), introduced by Kipping (2013). Additionally, rather than fitting directly for the planet-to-star radius ratio ($p = R_p/R_*$) and the impact parameter of the orbit (b), we instead used the parametrization introduced in Espinoza (2018) and fit for the parameters r_1 and r_2 to guarantee full exploration of physically plausible values in the (p, b) plane. Lastly, we applied the classical parametrization of $(e,\ \omega)$ into $(\mathcal{S}_1 = \sqrt{e}\sin\omega$, $\mathcal{S}_2 = \sqrt{e}\cos\omega)$, always ensuring that $e = \mathcal{S}_1^2 + \mathcal{S}_2^2 \leq 1$. We fixed the TESS dilution factor to one based on our analysis from Sects. 2.2 and 3.3, but accounted for any residual time-correlated noise in the light curve with an exponential GP kernel of the form $k_{i,j} = \sigma^2_{\rm GP,TESS} \exp(-|t_i - t_j|/T_{\rm GP,TESS})$, where $T_{\rm GP,TESS}$ is a characteristic timescale and $\sigma_{\rm GP,TESS}$ is the amplitude of this GP modulation. Furthermore, we added in quadrature a jitter term $\sigma_{\rm TESS}$ to the TESS photometric uncertainties, which might be underestimated due to additional systematics in the space-based photometry. The details of the priors and the description for each parameter are presented in Table A.1.

The results from the photometry-only analysis with `juliet` are completely consistent with those provided by the TESS DVR and our independent transit search, but with improved precision in the transit parameters after accounting for extra systematics with the jitter term and the GP. We also searched for an additional transiting planet in the system by modeling a two-planet fit where we use the same priors in Table A.1 for the first planet, and then allow the period and time of transit center to vary for the second. The transiting model for the hypothetical second planet is totally flat and we find no strong evidence ($\Delta \ln Z = \ln Z_{\rm 1pl} - \ln Z_{\rm 2pl} = 5.16$) for any additional transiting planets in the light curve, in agreement with our findings in Sect. 2.1.

5.2.2. RV only

In Sect. 5.1, we have shown that several signals are present in the RV data. We tested several models using `juliet` on the RV dataset independently to understand the nature of those signals and their significance when doing a simultaneous multi-planetary fit. We discuss three sets of models, each exploring possible system architectures covering the four interesting periodicities from Sect. 5.1 of 3.93, 9.1, 55.7, and 87.3 d. The details regarding the priors and Bayesian log evidence of all the runs are listed in Table 3. We included an instrumental jitter term for each

Table 3. Model comparison of RV-only fits with `juliet`.

Model	Prior $P_{\rm planet}$	GP kernel	$\Delta \ln Z$
1pl	$\mathcal{N}_{\rm b}(55.7, 0.5^2)$	...	19.93
2pl	$\mathcal{N}_{\rm b}(3.931, 0.001^2)$ $\mathcal{N}_{\rm c}(55.7, 0.5^2)$	...	15.51
3pl	$\mathcal{N}_{\rm b}(3.931, 0.001^2)$ $\mathcal{N}_{\rm c}(9.1, 0.1^2)$ $\mathcal{N}_{\rm d}(55.7, 0.5^2)$	...	9.03
4pl	$\mathcal{N}_{\rm b}(3.931, 0.001^2)$ $\mathcal{N}_{\rm c}(9.1, 0.1^2)$ $\mathcal{N}_{\rm d}(55.7, 0.5^2)$ $\mathcal{N}_{\rm e}(87.3, 0.5^2)$	...	−2.15
1pl+GPexp	$\mathcal{N}_{\rm b}(3.931, 0.001^2)$	Exp [(a)]	19.51
2pl+GPexp	$\mathcal{N}_{\rm b}(3.931, 0.001^2)$ $\mathcal{N}_{\rm c}(9.1, 0.1^2)$	Exp [(a)]	9.29
3pl+GPexp	$\mathcal{N}_{\rm b}(3.931, 0.001^2)$ $\mathcal{N}_{\rm c}(9.1, 0.1^2)$ $\mathcal{N}_{\rm d}(55.7, 0.5^2)$	Exp [(a)]	**0.00**
4pl+GPexp	$\mathcal{N}_{\rm b}(3.931, 0.001^2)$ $\mathcal{N}_{\rm c}(9.1, 0.1^2)$ $\mathcal{N}_{\rm d}(55.7, 0.5^2)$ $\mathcal{N}_{\rm e}(87.3, 0.5^2)$	Exp [(a)]	−0.95
1pl+GPess	$\mathcal{N}_{\rm b}(3.931, 0.001^2)$	ExpSinSq [(b)]	18.06
2pl+GPess	$\mathcal{N}_{\rm b}(3.931, 0.001^2)$ $\mathcal{N}_{\rm c}(9.1, 0.1^2)$	ExpSinSq [(b)]	6.32
3pl+GPess	$\mathcal{N}_{\rm b}(3.931, 0.001^2)$ $\mathcal{N}_{\rm c}(9.1, 0.1^2)$ $\mathcal{N}_{\rm d}(55.7, 0.5^2)$	ExpSinSq [(b)]	−1.59
4pl+GPess	$\mathcal{N}_{\rm b}(3.931, 0.001^2)$ $\mathcal{N}_{\rm c}(9.1, 0.1^2)$ $\mathcal{N}_{\rm d}(55.7, 0.5^2)$ $\mathcal{N}_{\rm e}(87.3, 0.5^2)$	ExpSinSq [(b)]	3.11

Notes. The prior label $\mathcal{N}$ represents a normal distribution. The final model used for the joint fit is marked in boldface (see Sect. 5.2.2 for details about the selection of the final model). [(a)]Simple exponential kernel of the form $k_{i,j} = \sigma^2_{\rm GP,RV} \exp(-|t_i - t_j|/T_{\rm GP,RV})$. [(b)]Exponential-sine-squared kernel of the form $k_{i,j} = \sigma^2_{\rm GP,RV} \exp\left(-\alpha_{\rm GP,RV}(t_i - t_j)^2 - \Gamma_{\rm GP,RV} \sin^2\left[\frac{\pi|t_i - t_j|}{P_{\rm rot;GP,RV}}\right]\right)$ with a uniform prior in $P_{\rm rot;GP,RV}$ ranging from 30 to 100 d.

of the six individual RV datasets and assumed circular orbits. We also considered eccentric orbits but found the circular model fits to have comparable log evidence and be computationally less expensive.

The first set of models (1pl, 2pl, 3pl, 4pl) treats the signals found in the periodogram analysis as Keplerian circular orbits. The preferred model is clearly the four-planet one, with a minimum $\Delta \ln Z > 11$ with respect to the others. This model is also the one with the highest evidence in our analysis. The three signals at 3.93, 9.1, and 55.7 d have eccentricities compatible with zero. However, the derived eccentricity for the 87.3 d signal is substantially high ($e \sim 0.4$). We notice that the RV phase-folded curve to the 87.3 d signal is not homogeneously sampled, with very few RV points covering both quadratures, which could explain the relatively high eccentric behavior derived for the 87.3 d signal.

To test the planetary nature of the signals, we also tried more complex models using GP regression to account for correlated noise. The explicit mathematical form of the GP kernels can be found in the notes to Table 3. We first employed a quasi-periodic exponential-sine-squared kernel (GPess) using a wide prior for the period term. In doing this, we can evaluate the preference for Keplerian signals over correlated periodic noise in the data, especially focusing on modeling the dubious 87.3 d periodicity. Even though the posterior distribution does not show any interesting signals, a periodogram of the GP component of the 3pl+GPess model – obtained by substracting the median Keplerian model to our full median 3pl+GPess model – reveals that the 87.3 d periodicity is the main component. However, if we consider the 87.3 d as a Keplerian along with the other three periodicities and a GPess kernel to account for the residual noise seen in Fig. 4e, it yields worse results in terms of model log evidence. Besides, a simpler exponential kernel (GPexp) for the GP with a three-Keplerian model gives comparable results to the 3pl+GPess model. This indicates that the exponential kernel is sufficient in accounting for the stochastic behavior of the data. Additionally, we tried a GPess kernel with a normal prior in $P_{\rm rot;GP,RV}$ centered at the 77.8 d rotational period of the star derived in Sect. 4.2. In that case, the results are worse or equivalent to the GPexp kernel case, meaning that the GP model did not catch any clear periodicity. This suggests also that the stellar spots do not imprint any modulation in the RVs, which is in line with the absence of peaks around 78 d in the periodograms of Fig. 4.

Given the log evidence of the different models in Table 3, 4pl, 3pl+GPexp, and 3pl+GPess are statistically equivalent. Although 4pl is weakly favored in terms of $\ln Z$, the fact that the derived orbit of the 87.3 d signal is much more eccentric than the others and the phase is not well covered by our measurements withdraw us from firmly claiming the signal as of planetary nature. Further observations of GJ 357 will help shed light on the true nature of this signal and further potential candidates. Therefore, for the final joint fit we consider the model with three Keplerians and an exponential GP to be the simplest model that best explains the current data present.

5.2.3. Joint fit

To obtain the most precise parameters of the GJ 357 system, we performed a joint analysis of the TESS and LCO photometry and Doppler data using `juliet`, of the model 3pl+GPexp from our RV-only analysis in Sect. 5.2.2. In this way, we simultaneously constrain all the parameters for the transiting planet GJ 357 b, the planet candidates at 9.12 d and 55.7 d, and the correlated noise seen in the RV data with an exponential GP kernel. To optimize the computational time, we narrowed down our priors based on the analyses from the sections above, but we kept them wide enough to fully sample the posterior distribution of the quantities of interest. Our choice of the priors for each parameter in the joint analysis of the 3pl+GPexp model can be found in Table A.1.

The posterior distribution of the parameters of our best-fit joint model are presented in Table 4. We also ran an eccentric version of the joint 3pl+GPexp model, but the circular fit model was strongly favored ($\Delta \ln Z > 8$) and thus we only show the circular results in Table 4. The corresponding modeling of the data based on these posteriors is shown in Fig. 5 and the derived

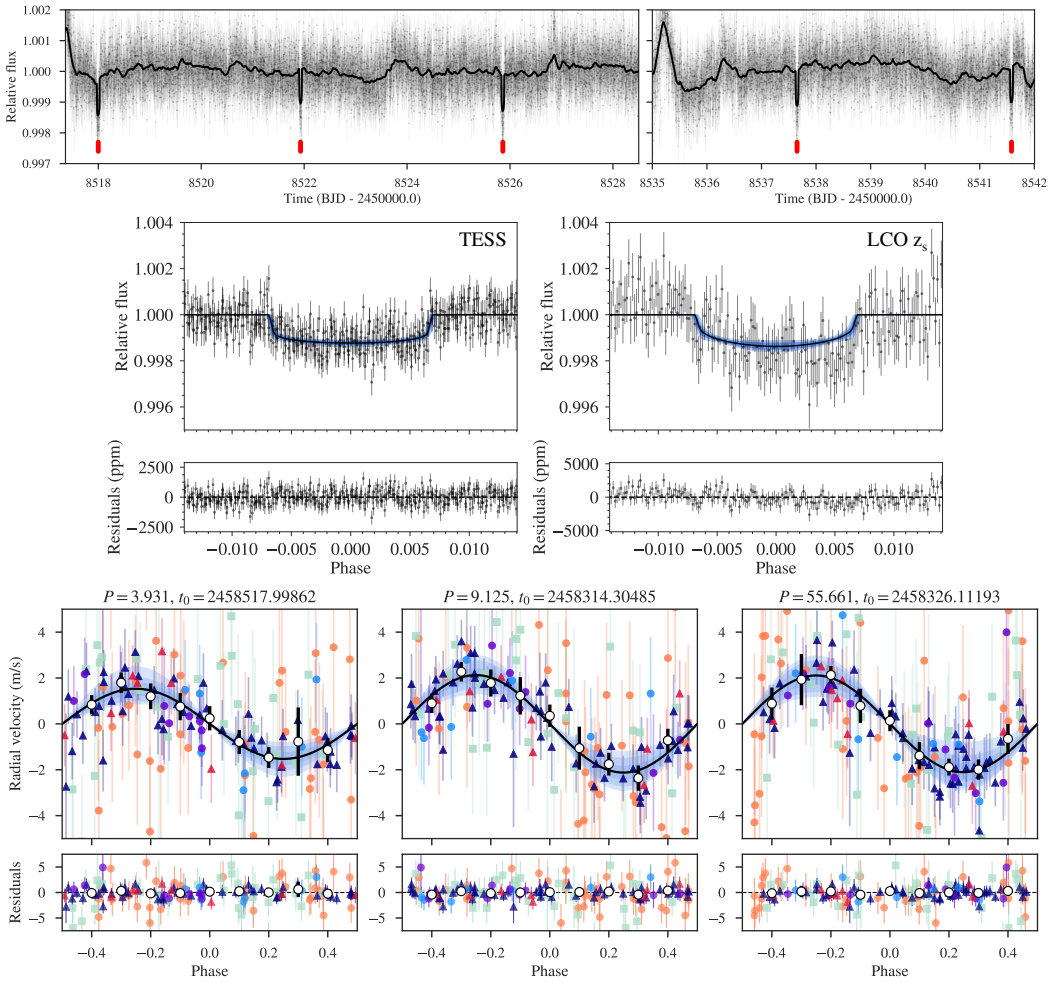

Fig. 5. Results from the joint fit of the best model 3pl+GPexp. *Top panel*: TESS photometry time series (gray points with error bars) along with the best-fit model (solid black line) from our joint modeling. This best-fit model includes an exponential GP used to account for the evident trends as well as for a transit model. Individual transits of GJ 357 b are indicated with red ticks. *Middle panel*: TESS photometry (*left*) and LCO photometry (*right*) phase-folded to the 3.93 d period of GJ 357 b along with best-fit transit model from the joint fit. The GP fitted to the photometry has been removed. *Bottom panel*: RVs phase-folded to the period of the three confirmed planets (GJ 357 b, left; GJ 357 c, center; GJ 357 d, right). RV data come from HIRES (orange circles), UVES (light green squares), HARPS (navy blue triangles), PFSpre (light blue circles), PFSpost (red triangles), and CARMENES (purple circles). The GP fitted to the RV dataset has been removed. White circles show binned datapoints in phase for visualisation. The error bars of both photometry and RV data include their corresponding jitter.

physical parameters of the system are presented in Table 5. The RV time series is shown for completeness in Fig. B.1.

6. Discussion

The GJ 357 system consists of one transiting Earth-sized planet in a 3.93 d orbit, namely GJ 357 b, with a radius of $R_b = 1.217 \pm 0.084\,R_\oplus$, a mass of $M_b = 1.84 \pm 0.31 M_\oplus$, and a density of $\rho_b = 5.6^{+1.7}_{-1.3}$ g cm^{-3}; and two additional planets, namely GJ 357 c, with a minimum mass of $M_c = 3.40 \pm 0.46\,M_\oplus$ in a 9.12 d orbit, and GJ 357 d, with a minimum mass of $M_c = 6.1 \pm 1.0\,M_\oplus$ in a 55.7 d orbit. The modulations from the GP model have an amplitude of 2.66 m s^{-1} and account for the short timescale of the stochastic variations and the dubious 87.3 d signal.

6.1. Searching for transits of planets c and d

Although in Sects. 2.1 and 5.2.1 we looked for additional transit features in the TESS light curve, but could not find any,

Table 4. Posterior parameters of the final joint fit obtained for GJ 357 b, c, and d, using `juliet`.

Parameter [a]	GJ 357 b	GJ 357 c	GJ 357 d
Stellar parameters			
$\rho_\star$ (kg m^{-3})	$13\,600.0^{+1400}_{-1600}$		
Planet parameters			
P (d)	$3.93072^{+0.00008}_{-0.00006}$	$9.1247^{+0.0011}_{-0.0010}$	$55.661^{+0.055}_{-0.055}$
t_0 [b]	$8517.99862^{+0.00039}_{-0.00038}$	$8314.30^{+0.42}_{-0.38}$	$8326.1^{+3.9}_{-3.8}$
r_1	$0.56^{+0.07}_{-0.09}$	...	...
r_2	$0.0331^{+0.0009}_{-0.0009}$	...	...
K (m s^{-1})	$1.52^{+0.25}_{-0.25}$	$2.13^{+0.28}_{-0.28}$	$2.09^{+0.34}_{-0.35}$
Photometry parameters			
$M_{\rm TESS}$ (ppm)	-47^{+65}_{-69}		
$M_{\rm LCO}$ (ppm)	173^{+65}_{-64}		
$\sigma_{\rm TESS}$ (ppm)	127^{+15}_{-16}		
$\sigma_{\rm LCO}$ (ppm)	928^{+50}_{-48}		
$q_{1,\rm TESS}$	$0.20^{+0.21}_{-0.13}$		
$q_{2,\rm TESS}$	$0.32^{+0.34}_{-0.21}$		
$q_{1,\rm LCO}$	$0.72^{+0.18}_{-0.28}$		
RV parameters			
$\mu_{\rm HIRES}$ (m s^{-1})	$0.96^{+0.60}_{-0.62}$		
$\sigma_{\rm HIRES}$ (m s^{-1})	$1.99^{+0.78}_{-0.85}$		
$\mu_{\rm UVES}$ (m s^{-1})	$1.06^{+0.64}_{-0.66}$		
$\sigma_{\rm UVES}$ (m s^{-1})	$1.68^{+0.89}_{-0.90}$		
$\mu_{\rm HARPS}$ (m s^{-1})	$-5.15^{+0.41}_{-0.40}$		
$\sigma_{\rm HARPS}$ (m s^{-1})	$0.61^{+0.41}_{-0.37}$		
$\mu_{\rm PFSpre}$ (m s^{-1})	$-2.31^{+1.17}_{-1.19}$		
$\sigma_{\rm PFSpre}$ (m s^{-1})	$1.71^{+1.39}_{-1.04}$		
$\mu_{\rm PFSpost}$ (m s^{-1})	$-0.97^{+0.99}_{-0.99}$		
$\sigma_{\rm PFSpost}$ (m s^{-1})	$1.20^{+0.99}_{-0.74}$		
$\mu_{\rm CARM}$ (m s^{-1})	$-1.61^{+0.93}_{-0.92}$		
$\sigma_{\rm CARM}$ (m s^{-1})	$0.98^{+0.99}_{-0.64}$		
GP hyperparameters			
$\sigma_{\rm GP,TESS}$ (ppm)	$0.10^{+0.04}_{-0.02}$		
$T_{\rm GP,TESS}$ (d)	$0.38^{+0.17}_{-0.09}$		
$\sigma_{\rm GP,RV}$ (m s^{-1})	$2.66^{+1.02}_{-0.76}$		
$T_{\rm GP,RV}$ (d)	$0.12^{+0.12}_{-0.06}$		

Notes. Priors and descriptions for each parameter can be found in Table A.1. [a]Error bars denote the 68% posterior credibility intervals. [b]Units are BJD – 2 450 000.

Table 5. Derived planetary parameters obtained for GJ 357 b, c, and d using the posterior values from Table 4.

Parameter [a]	GJ 357 b	GJ 357 c	GJ 357 d
Derived transit parameters			
$p = R_{\rm p}/R_\star$	$0.0331^{+0.0009}_{-0.0009}$	...	...
$b = (a/R_\star)\cos i_{\rm p}$	$0.34^{+0.10}_{-0.14}$	...	...
$a/R_\star$	$22.31^{+0.76}_{-0.90}$	...	...
i_p (deg)	$89.12^{+0.37}_{-0.31}$	...	...
u_1 [b]	$0.27^{+0.24}_{-0.17}$	...	...
u_2 [b]	$0.14^{+0.29}_{-0.24}$	...	...
t_T (h)	$1.53^{+0.12}_{-0.11}$	...	...
Derived physical parameters			
$M_{\rm p}$ ($M_\oplus$) [c]	$1.84^{+0.31}_{-0.31}$	$>3.40^{+0.46}_{-0.46}$	$>6.1^{+1.0}_{-1.0}$
$R_{\rm p}$ ($R_\oplus$)	$1.217^{+0.084}_{-0.083}$	...	...
$\rho_{\rm p}$ (g cm^{-3})	$5.6^{+1.7}_{-1.3}$	...	...
$g_{\rm p}$ (m s^{-2})	$12.1^{+2.9}_{-2.5}$	...	...
$a_{\rm p}$ (au)	$0.035^{+0.002}_{-0.002}$	$0.061^{+0.004}_{-0.004}$	$0.204^{+0.015}_{-0.015}$
$T_{\rm eq}$ (K) [d]	525^{+11}_{-9}	$401.2^{+10.8}_{-10.7}$	$219.6^{+5.9}_{-5.9}$
S ($S_\oplus$)	$12.6^{+1.1}_{-0.8}$	$4.45^{+0.14}_{-0.14}$	$0.38^{+0.01}_{-0.01}$

Notes. [a]Error bars denote the 68% posterior credibility intervals. [b]Derived only from the TESS light curve. [c]The masses for GJ 357 c and GJ 357 d are a lower limit ($M_{\rm p} \sin i$) since they are detected in the RV data only. [d]Equilibrium temperatures were calculated assuming zero Bond albedo.

we performed a last run with `juliet` to rule out the possibility that GJ 357 c transits. To do so, we took the period and time of transit center from Table 4 as priors and added $r_{1,\rm c}$ and $r_{2,\rm c}$ as free parameters assuming an eccentricity equal to zero. In agreement with previous analyses, the log evidence shows that the non-transiting model for GJ 357 c is slightly preferred ($\Delta \ln Z \sim 3$).

Therefore, we can conclude that GJ 357 c, although firmly detected in the RV dataset, does not transit. On the other hand, any possible transit of GJ 357 d would have been missed by TESS observations, according to the predicted transit epoch from the RVs fits. With the current data the uncertainty in the ephemeris is on the order of days, however, additional RVs could improve the precision on the period and phase determination enough to allow a transit search. The a priori transit probability is only 0.8%, but this transit search is doable by *CHEOPS* (Broeg et al. 2013) since the star will fall in its 50 d observability window.

As in other planetary systems recently revealed by TESS (e.g., Espinoza et al. 2019) or *Kepler*/K2 (e.g., Quinn et al. 2015; Buchhave et al. 2016; Otor et al. 2016; Christiansen et al. 2017; Gandolfi et al. 2017; Cloutier et al. 2017), non-transiting planets in these transit-detected systems expand our understanding of the system architecture. In those works, after the modeling of the transiting planet detected in the space-based photometry, further signals appear in the RV data that would not have been significant otherwise. This emphasizes the importance of long, systematic, and precise ground-based searches for planets around bright stars and the relevance of archival public data.

6.2. System architecture

We determine that the transiting planet GJ 357 b has a mass of $M_{\rm b} = 1.84 \pm 0.31\,M_\oplus$ and a radius of $R_{\rm b} = 1.217 \pm 0.084\,R_\oplus$, which corresponds to a bulk density of $\rho_{\rm b} = 5.6^{+1.7}_{-1.3}$ g cm^{-3}. Figure 6 shows masses and radii of all confirmed planets whose precision in both parameters is better than 30%. GJ 357 b joins the very small group of Earth-sized and Earth-mass planets orbiting M dwarfs discussed in the introduction. The bulk

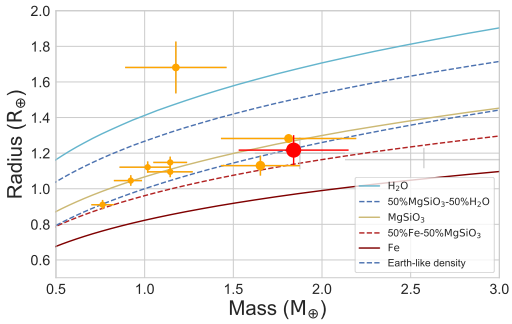

Fig. 6. Mass-radius diagram for all known transiting planets with masses between 0.5–3 $M_\oplus$ and radii 0.5–2 $R_\oplus$ determined with a precision better than 30%. GJ 357 b is shown in red. Planets orbiting around late-type stars ($T_{\rm eff}$ < 4000 K) are shown in orange, otherwise gray. The size of the orange datapoints is inversely proportional to the magnitude of their host star in the J-band. Data are taken from the TEPCat database of well-characterized planets (Southworth 2011). Theoretical models for the planet's internal composition are taken from Zeng et al. (2016).

density we measure for GJ 357 b overlaps with the 30% Fe and 70% $MgSiO_3$ mass-radius curve as calculated by Zeng et al. (2016).

We derive a minimum mass for GJ 357 c of $M_{\rm c} \sin i_{\rm c} = 3.40 \pm 0.46\,M_\oplus$, which falls between the vaguely defined mass range for Earth- and super-Earth-like planets. Since we determine only a lower limit for $M_{\rm c}$, it is possible that this planet falls into the super-Earth category joining the group of planets that make up the lower radius bump in the bimodal distribution of small planets found with *Kepler* (Fulton et al. 2017; Van Eylen et al. 2018).

The derived minimum mass of GJ 357 d is $M_{\rm d} \sin i_{\rm d} = 6.1 \pm 1.0\,M_\oplus$. However, a prediction of its bulk composition is not straightforward since both super-Earth ($1 < R < 2\,R_\oplus$) and mini-Neptune ($2 < R < 4\,R_\oplus$) exoplanets encompass this range of masses. As an example of this dichotomy, Kepler-68 b (Gilliland et al. 2013, $R = 2.33 \pm 0.02\,R_\oplus$) and Kepler-406 b (Marcy et al. 2014, $R = 1.43 \pm 0.03\,R_\oplus$) have similar masses of $M \sim 6.0\,M_\oplus$ and $M \sim 6.3\,M_\oplus$, respectively, but their compositions differ significantly (between rocky and gaseous for Kepler-68 b, and purely rocky for Kepler-406 b).

We note that the planetary system of GJ 357 is quite similar to that of GJ 1132 (Berta-Thompson et al. 2015; Bonfils et al. 2018). In both cases we find a similar bulk density of the inner planet of ~6 g cm^{-3} (see orange datapoint down left of GJ 357 b in Fig. 6) and a second non-transiting planet with an orbital period around 9 d. Furthermore, the long-term trends found with GJ 1132 could indicate the presence of one or more outer, more massive planets, which would then be comparable to the existence of planet d in GJ 357.

6.3. Dynamics and TTV analysis

While a detailed characterization of the dynamical properties of the potential planetary system is beyond the scope of this paper, we nevertheless started to investigate its properties using *Systemic* (Meschiari et al. 2009). Given the fact that TESS could only cover five transits, the detection of transit timing variations (TTV) would only be possible in a system with more massive planets or in a first order resonance like, for example, in Kepler-87 (Ofir et al. 2014). The inner pair of planets is, however, close to a 7:3 period commensurability. The dynamical interactions are small but, depending on the initial eccentricities, the system may undergo significant exchange of angular momentum, but on very long timescales of ~500 yr, which are clearly too long to be detectable in the currently available RV measurements.

Since we cannot detect a transit for planet c, its orbit could be inclined with respect to planet b. The inclination of planet c only needs to be <88.5 ± 0.1 deg for a non-detection, meaning a very gentle tilt with respect to planet b ($i_{\rm b} = 89.12^{+0.37}_{-0.31}$ deg) would be enough to miss it. For planet d to transit, doing this same exercise implies one would need inclinations larger than about 89.55 + −0.04 deg, which is a 1 deg difference in mutual inclination with planet c, and a 0.4 deg difference with the transiting planet b. Since multi-planet systems in general have mutual inclinations within ~2 deg from each other (Dai et al. 2018), there is still room for planet d to be a transiting planet. For initially low eccentric configurations, the inclination probably cannot be constrained from dynamics, because preliminary tests show that the system is stable even for a low inclination for planet c of $i_{\rm c} = 10$ deg. At large mutual inclinations (30 deg), the mutual torque is significant and planet b would drift slowly out of a transiting configuration. This effect, however, reduces significantly with a lower mutual inclination, when small mutual tilts result in torques that could bring planet c or d into transit or planet b out of transit. A long-term monitoring of planet b could show or constraint inclination changes from transit duration or depth variations (TDVs).

We carried out a more in-depth search for TTVs using PyTransit (Parviainen 2015). The approach models the near vicinity of each transit (4.8 h around the expected transit center based on the linear ephemeris) as a product of a transit model and a flux baseline made of $n_{\rm L}$ Legendre polynomials. The transits are modeled jointly, and parametrized by the stellar density, impact parameter, planet-star area ratio, two quadratic limb darkening coefficients, an independent transit center for each transit, and $n_{\rm L}$ Legendre polynomial coefficients for each transit (modeling the baseline as a sum of polynomials rather than, for example, a Gaussian process, is still feasible given the small number of transits). The analysis results in an estimate of the model posterior distribution, where the independent parameter estimates are based on their marginal posterior distributions. The uncertainty in the transit center estimates – calculated as $0.5 \times (t_{84} - t_{16})$, where t_{16} and t_{84} are the 16th and 84th transit center posterior percentiles – varies from 1.5 to 4 min, and no significant deviations from the linear ephemeris can be detected, in agreement with our previous estimate.

6.4. Formation history

The predominant formation channel to build terrestrial planets is the core accretion scenario, where a solid core is formed before the accretion of an atmosphere sets in (Mordasini et al. 2012). This scenario involves several stages: first, dust grows into larger particles that experience vertical settling and radial drift, commonly referred to as "pebbles" (Birnstiel et al. 2012). They can undergo gravitational collapse into ~100 km sized planetesimals wherever a local concentration exceeds a level set by the disk turbulence (Johansen et al. 2007; Lenz et al. 2019). These planetesimals can form planetary embryos of roughly Moon size via mutual collisions (Levison et al. 2015), at which point an accretion of further planetesimals and, even more importantly, of drifting pebbles can lead to further growth

(Ormel & Klahr 2010). Pebble accretion is thus very powerful in quickly forming the cores of gas giants (Klahr & Bodenheimer 2006; Lambrechts et al. 2014), but usually fails to produce terrestrial planets akin to the inner solar system due to its high efficiency. To explain the low final mass of such planets, a mechanism that stops further accretion of solids is needed.

One way to inhibit pebble accretion is to cut the supply of solid material by another planet that forms further out earlier than or concurrently with the inner planets. Such a companion would act as a sink for the influx of material that would otherwise be available to build inner planets. This is achieved when the outer planet reaches a critical mass where the fraction of the pebble flux accreted by the planet

$$\epsilon_{\rm PA} \approx 0.1 \times \left(\frac{q}{10^{-5}}\right)^{\frac{2}{3}}, \quad \text{with } q = \frac{M_{\rm Planet}}{M_\star}, \tag{2}$$

approaches unity (Ormel et al. 2017). With $q = 3 \times 10^{-5}$ and $\epsilon_{\rm PA} \approx 0.2$, GJ 357 c could have efficiently absorbed pebbles that would otherwise have reached GJ 357 b. Likewise, GJ 357 d reached a pebble accretion efficiency of $\epsilon_{\rm PA} \approx 0.3$ and could have starved the inner two planets of further accretion of pebbles. In this scenario, the planets must have formed outside-in and one would expect one or several additional planets of at least the mass of GJ 357 d further out. Such a hypothetical GJ 357 e again should have reached high pebble accretion efficiencies before its inner siblings. This is quite feasible, since the conditions for fast embryo formation are very favorable just outside the ice line of the protoplanetary disk, where the recondensation of vapor leads to a large abundance of planetesimals (Stevenson & Lunine 1988; Cuzzi & Zahnle 2004; Ciesla & Cuzzi 2006; Schoonenberg & Ormel 2017). We used the minimum masses of GJ 357 c and GJ 357 d for these estimates. Thus, the efficiencies we calculated should be considered conservative, making this mechanism even more robust.

However, timing is key in order to stop the supply of solid material at the right time. The window is only open for $\sim 10^5$ yr, which corresponds to the timescale for growing from a roughly Earth-sized planet to a super-Earth (e.g., Bitsch et al. 2019).

A scenario with less stringent assumptions is one where an inner planet grows to its own pebble isolation mass, which can be approximated as

$$M_{\rm iso} \approx h^3 M_\star \tag{3}$$

with the local disk aspect ratio h (Ormel et al. 2017). Reaching $M_{\rm iso}$, the planet locally modifies the radial gas pressure gradient such that the inward drift of pebble-sized particles stops, starving itself and the inner system of solid material. Assuming the current orbit of GJ 357 b and an $M_{\rm iso}$ equal to the planetary mass inferred in our study, Eq. (3) yields a local disk aspect ratio of 0.025, which is a reasonable value in the inner disk. Similarly, the minimum masses of GJ 357 c and GJ 357 d give $h \approx 0.031$ and $h \approx 0.038$, respectively, which is again consistent with estimated disk scale heights in the literature (e.g., Chiang & Goldreich 1997; Ormel et al. 2017).

Given the significant assumptions needed to explain the emergence of both planets by a cut-off of pebble flux in the system, the second scenario is favored. If pebble accretion is the dominating mechanism to form planetary embryos in the system, then GJ 357 b–d stopped growing when they reached their respective pebble isolation masses. However, a hypothetical future discovery of a more massive planet further out might shift the balance again towards shielding by this outer planet.

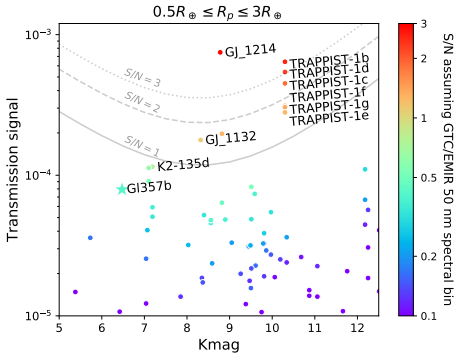

Fig. 7. Expected primary transit transmission signal per scale height plotted against the K-band magnitude of GJ 357 b (star) and all know planets (dots) with mass measurements and with radius between 0.5 and 3 $R_\oplus$. The color scale provides the expected S/N for a single transit assuming the use of a ten-meter telescope and 50 nm wavelength integration bins. The gray lines indicate the pattern of the S/N assuming a single transit duration of 3 h. The relative S/N is maintained when extrapolated to other instrumentation. A few benchmark targets for JWST transmission spectroscopy studies are labeled.

6.5. Atmospheric characterization and habitability

The integrated stellar flux that hits the top of an Earth-like planet's atmosphere from a cool red star warms the planet more efficiently than the same integrated flux from a hot blue star. This is partly due to the effectiveness of the Rayleigh scattering in an atmosphere mostly composed of N_2-H_2O-CO_2, which decreases at longer wavelengths, together with the increased near-IR absorption by H_2O and CO_2.

Planets GJ 357 b and GJ 357 c receive about 13 times and 4.4 times the Earth's irradiation ($S_\oplus$), respectively. Venus in comparison receives about 1.7 $S_\oplus$. Thus, both planets should have undergone a runaway greenhouse stage as proposed for Venus' evolution. Due to its incident flux level, GJ 357 c is located closer to the star than the inner edge of the empirical habitable zone as defined in Kasting et al. (1993) and Kopparapu et al. (2014). On the other hand, GJ 357 d receives an irradiation of 0.38 $S_\oplus$, which places it inside the habitable zone (as defined above), in a location comparable to Mars in the solar sytem, making it a very interesting target for further atmospheric observations.

Atmospheric characterization of exoplanets is difficult because of the high contrast ratio between a planet and its host star. While atmospheres of Earth and super-Earth planets are still outside our technical capabilities, upcoming space missions such as the *James Webb* Space Telescope (JWST) and the extremely large ground-based telescopes (ELTs) will open this possibility for a selected group of rocky planets offering the most favorable conditions.

The star GJ 357 is one of the brightest M dwarfs in the sky, and as such, planets orbiting it are interesting targets for follow-up characterization. To illustrate this fact, in Fig. 7 we plot the expected transmission signal reachable in a single transit with a ground-based 10 m telescope for all known planets with mass measurements and with radius between 0.5 and 3 $R_\oplus$. The transmission signal per scale height is defined as

$$\mathrm{TS} = 2H_{\rm s}\frac{R_{\rm p}}{R_{\rm s}^2}, \tag{4}$$

where R_p and R_s are the radii of planet and star, respectively, and H is the scale height

$$H_s = \frac{k_B T_{eq}}{\mu g_p}, \quad (5)$$

where k_B is the Boltzmann constant, T_{eq} and g_p are the equilibrium temperature and surface gravity of the planet, respectively, and $\mu = 2.3\,\mathrm{g\,mol^{-1}}$ is the mean molecular weight. The signal is calculated then as $1.8 \times \mathrm{TS}$ where a spectral modulation of $1.8\,H_s$ is adopted (Iyer et al. 2016). This signal is an optimistic estimate, because terrestrial planets are unlikely to host an atmosphere of mean molecular weight at $2.3\,\mathrm{g\,mol^{-1}}$. The most favorable planets for atmospheric characterization offer a combination of a large scale height (puffiness of the atmospheres) and host star brightness, and are labeled in the figure together with GJ 357 b.

Kempton et al. (2018) proposed a metric to select TESS (and other missions) planet candidates according to their suitability for atmospheric characterization studies. Using the mass and radius determined in this work ($1.84\,M_\oplus$, $1.217\,R_\oplus$), we obtained a transmission metric value of 23.4 for GJ 357 b. For comparison, two of the most well-known planets around bright M-type stars with favorable metrics, LHS 1140 b and TRAPPIST-1 f, have metric values of 9.13 and 13.7, respectively. It is worth noting that out of the simulated yield of TESS terrestrial planets with $R < 2\,R_\oplus$ used in Kempton et al. (2018), in turn based on Sullivan et al. (2015) and assuming an Earth-like composition, only one had a larger metric value (28.2). Using the same reference, the emission spectroscopy metric for GJ 357 b is 4.1, a modest number compared to the simulated yield of TESS planets suitable for these types of studies.

In order to assess an estimation of GJ 357 b's atmospheric signal through transmission spectroscopy, we simulated a simplified atmospheric photochemistry model for a rocky planet basing it on early Earth's temperature structure, increasing the surface temperature to be consistent with $T_{eff} = 525\,\mathrm{K}$ and removing water from the atmosphere using `ChemKM` (Molaverdikhani, in prep.). The temperature and pressure structures of GJ 357 b's atmosphere are not modeled self consistently, as this only shows sample spectra.

Geometric mean spectra of GJ 667 C ($T_{eff} = 3327\,\mathrm{K}$) and GJ 832 ($T_{eff} = 3816\,\mathrm{K}$) were considered as an estimation of GJ 357's flux in the range of X-ray to optical wavelengths. The data were obtained from the MUSCLES database (France et al. 2016). We modeled three different metallicities, 1×, 10×, and 100× solar metallicity to explore a wider range of possibilities (Wakeford et al. 2017) and selected a temperature and atmosphere profile based on an anoxic Earth atmosphere. We selected three geological epochs, namely 2.0 Gyr (after the Great Oxygenation Event), 0.8 Gyr (after the Neoproterozoic Oxygenation Event, when multicellular life began to emerge), and the modern Earth (Kawashima & Rugheimer 2019), to consider three different atmospheric conditions with different temperature structures. To set up the models, we used Venot et al. (2012)'s full kinetic network and an updated version of Hébrard et al. (2012)'s UV absorption cross sections and branching yields.

Synthetic sample transmission spectra for GJ 357 b are calculated using `petitRADTRANS` (Mollière et al. 2019), shown in Fig. 8. The major opacity source in the atmosphere is mostly methane, and as expected CH_4 and CO_2 contribute more significantly at higher temperatures and metallicities in this class of planets (Molaverdikhani et al. 2019). Such spectral features are expected to be above JWST's noise floor; 20 ppm, 30 ppm, and 50 ppm, for NIRISS SOSS, NIRCam grism, and MIRI LRS,

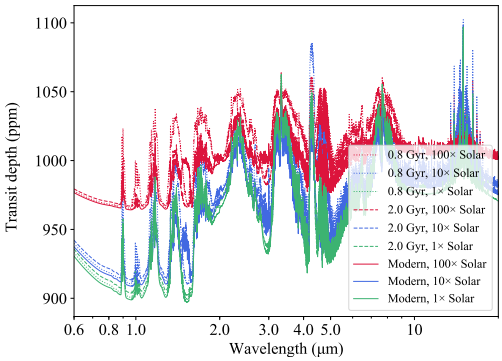

Fig. 8. Synthetic spectra of GJ 357 b in the JWST wavelength range. Nine transmission spectra, including three atmospheric metallicities and three temperature structures from three different Earth epochs are shown. The assumed temperature profile is the Earth's one adapted for $T_{eff} = 525\,\mathrm{K}$ to resemble a hot-terminator scenario.

respectively (Greene et al. 2016). Ground-based, high-resolution spectroscopy can potentially access these strong absorption lines too. We must emphasize that these synthetic spectra are calculated under the assumption of cloud-free atmospheres. If clouds were present, the spectral features could be obscured or completely muted, resulting in a flattened transmission spectrum (Kreidberg et al. 2014).

As a final note on the atmospheric characterization of GJ 357 b, the star may be too bright in some of the JWST's observing modes, which demands careful observational planning for transmission spectroscopy. Such bright objects, however, are excellent for ground-based facilities. Louie et al. (2018) pointed out that only a few TESS planets of terrestrial size are expected to be as good or better targets for atmospheric characterization than the currently known planets. GJ 357 b is one of them and, although it is not in the habitable zone, in fact it could be so far the best terrestrial planet for atmospheric characterization with the upcoming JWST and ground-based ELTs.

For GJ 357 d, a rocky Earth-like composition corresponds to a $1.75\,R_\oplus$ planet, while an ice composition would correspond to a planet radius of $2.4\,R_\oplus$. We still do not know whether GJ 357 d transits its host star, however, if it did, the atmospheric signal (assuming an Earth-like composition and atmosphere) would become detectable by JWST for both NIRISS/NIRSpec (Fig. 9) and MIRI. Self-consistent models of the planet, as well as an expected atmospheric signal for GJ 357 d, assuming a range of different compositions and atmospheres, show cool surface temperatures for Earth-like models and warm conditions for early Earth-like models. The models as well as the observable spectral features have been generated using EXO-Prime (see, e.g., Kaltenegger & Sasselov 2010) and are discussed in detail in Kaltenegger et al. (in prep.). The code incorporates a 1D climate, 1D photochemistry, and 1D radiative transfer model that simulates both the effects of stellar radiation on a planetary environment and the planet's outgoing spectrum.

7. Conclusions

We report the discovery and confirmation of a planetary system around the bright M dwarf GJ 357. Data from the TESS mission revealed the first clue of this discovery by detecting the

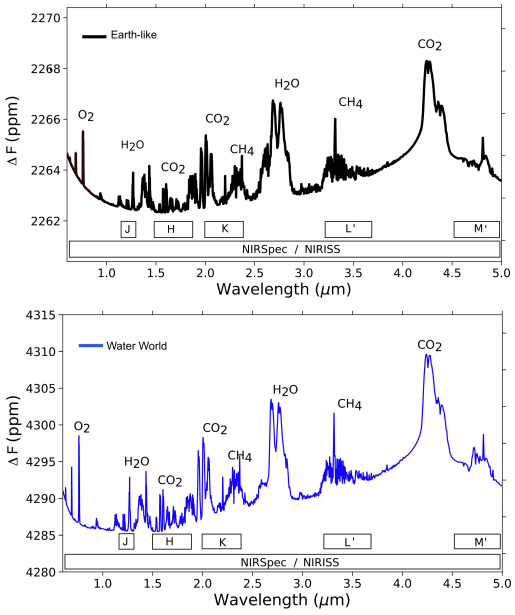

Fig. 9. Synthetic spectra for GJ 357 d in the JWST NIRISS/NIRSpec wavelength range for two models: Earth-like composition and atmosphere (assuming a radius of 1.75 $R_\oplus$, black) and water world composition with Earth-like atmosphere (assuming a radius of 2.4 $R_\oplus$,blue) as an example for detectable features.

transit signals of GJ 357 b through the TESS Alerts website. The availability of archival and new high-precision RV data made possible the quick confirmation of GJ 357 b, and a search for further planet candidates in the system.

Planet GJ 357 b is a hot Earth-sized transiting planet with a mass of $1.84 \pm 0.31\,M_\oplus$ in a 3.93 d orbit. The brightness of the planet's host star makes GJ 357 b one of the prime targets for future atmospheric characterization, and arguably one of the best future opportunities to characterize a terrestrial planet atmosphere with JWST and ELTs. To date, GJ 357 b is the nearest transiting planet to the Sun around an M dwarf and contributes to the TESS Level One Science Requirement of delivering 50 transiting small planets (with radii smaller than $4\,R_\oplus$) with measured masses to the community.

Finally, there is evidence for at least two more planets, namely GJ 357 c, with a minimum mass of $3.4 \pm 0.46\,M_\oplus$ in a 9.12 d orbit, and GJ 357 d, an interesting super-Earth or sub-Neptune with a minimum mass of $6.1 \pm 1.0\,M_\oplus$ in a 55.7 d orbit inside the habitable zone. Thus, GJ 357 adds to the growing list of TESS discoveries deserving more in-depth studies, as these systems can provide relevant information for our understanding of planet formation and evolution.

Acknowledgements. This paper includes data collected by the TESS mission. Funding for the TESS mission is provided by the NASA Explorer Program. We acknowledge the use of TESS Alert data, which is currently in a beta test phase, from pipelines at the TESS Science Office and at the TESS Science Processing Operations Center. Resources supporting this work were provided by the NASA High-End Computing (HEC) Program through the NASA Advanced Supercomputing (NAS) Division at Ames Research Center for the production of the SPOC data products. This research has made use of the Exoplanet Follow-up Observation Program website, which is operated by the California Institute of Technology, under contract with the National Aeronautics and Space Administration under the Exoplanet Exploration Program. This work has made use of data from the European Space Agency (ESA) mission *Gaia* (https://www.cosmos.esa.int/gaia), processed by the *Gaia* Data Processing and Analysis Consortium (DPAC, https://www.cosmos.esa.int/web/gaia/dpac/consortium). Funding for the DPAC has been provided by national institutions, in particular the institutions participating in the *Gaia* Multilateral Agreement. CARMENES is an instrument for the Centro Astronómico Hispano-Alemán de Calar Alto (CAHA, Almería, Spain) funded by the German Max-Planck-Gesellschaft (MPG), the Spanish Consejo Superior de Investigaciones Científicas (CSIC), the European Union through FEDER/ERF FICTS-2011-02 funds, and the members of the CARMENES Consortium. R. L. has received funding from the European Union's Horizon 2020 research and innovation program under the Marie Skłodowska-Curie grant agreement No. 713673 and financial support through the "la Caixa" INPhINIT Fellowship Grant LCF/BQ/IN17/11620033 for Doctoral studies at Spanish Research Centers of Excellence from "la Caixa" Banking Foundation, Barcelona, Spain. This work is partly financed by the Spanish Ministry of Economics and Competitiveness through projects ESP2016-80435-C2-2-R and ESP2016-80435-C2-1-R. We acknowledge support from the Deutsche Forschungsgemeinschaft under DFG Research Unit FOR2544 "Blue Planets around Red Stars", project no. QU 113/4-1, QU 113/5-1, RE 1664/14-1, DR 281/32-1, JE 701/3-1, RE 2694/4-1, the Klaus Tschira Foundation, and the Heising Simons Foundation. This work is partly supported by JSPS KAKENHI Grant Numbers JP15H02063, JP18H01265, JP18H05439, JP18H05442, and JST PRESTO Grant Number JPMJPR1775. This research has made use of the services of the ESO Science Archive Facility. Based on observations collected at the European Southern Observatory under ESO programs 072.C-0488(E), 183.C-0437(A), 072.C-0495, 078.C-0829, and 173.C-0606. IRD is operated by the Astrobiology Center of the National Institutes of Natural Sciences. M.S. thanks Bertram Bitsch for stimulating discussions about pebble accretion.

References

Almenara, J. M., Astudillo-Defru, N., Bonfils, X., et al. 2015, A&A, 581, L7
Alonso-Floriano, F. J., Morales, J. C., Caballero, J. A., et al. 2015, A&A, 577, A128
Ambikasaran, S., Foreman-Mackey, D., Greengard, L., Hogg, D. W., & O'Neil, M. 2015, IEEE Trans. Pattern Anal. Mach. Intell., 38, 252
Anglada-Escudé, G., Tuomi, M., Gerlach, E., et al. 2013, A&A, 556, A126
Anglada-Escudé, G., Amado, P. J., Barnes, J., et al. 2016, Nature, 536, 437
Astudillo-Defru, N., Delfosse, X., Bonfils, X., et al. 2017, A&A, 600, A13
Bakos, G., Noyes, R. W., Kovács, G., et al. 2004, PASP, 116, 266
Batalha, N. E., Lewis, N. K., Line, M. R., Valenti, J., & Stevenson, K. 2018, ApJ, 856, L34
Berta-Thompson, Z. K., Irwin, J., Charbonneau, D., et al. 2015, Nature, 527, 204
Birnstiel, T., Klahr, H., & Ercolano, B. 2012, A&A, 539, A148
Bitsch, B., Izidoro, A., Johansen, A., et al. 2019, A&A, 623, A88
Bonfils, X., Delfosse, X., Udry, S., et al. 2013, A&A, 549, A109
Bonfils, X., Almenara, J. M., Cloutier, R., et al. 2018, A&A, 618, A142
Boro Saikia, S., Marvin, C. J., Jeffers, S. V., et al. 2018, A&A, 616, A108
Broeg, C., Fortier, A., Ehrenreich, D., et al. 2013, Eur. Phys. J. Web Conf., 47, 03005
Brown, T. M., Baliber, N., Bianco, F. B., et al. 2013, PASP, 125, 1031
Buchhave, L. A., Dressing, C. D., Dumusque, X., et al. 2016, AJ, 152, 160
Buchner, J., Georgakakis, A., Nandra, K., et al. 2014, A&A, 564, A125
Butler, R. P., Marcy, G. W., Williams, E., et al. 1996, PASP, 108, 500
Butler, R. P., Vogt, S. S., Laughlin, G., et al. 2017, AJ, 153, 208
Charbonneau, D., Irwin, J., Nutzman, P., & Falco, E. E. 2008, BAAS, 40, 242
Chiang, E. I., & Goldreich, P. 1997, ApJ, 490, 368
Christiansen, J. L., Vanderburg, A., Burt, J., et al. 2017, AJ, 154, 122
Ciesla, F. J., & Cuzzi, J. N. 2006, Icarus, 181, 178
Cloutier, R., Astudillo-Defru, N., Doyon, R., et al. 2017, A&A, 608, A35
Collins, K. A., Kielkopf, J. F., Stassun, K. G., & Hessman, F. V. 2017, AJ, 153, 77
Cortés Contreras, M. 2016, PhD Thesis, Universidad Complutense de Madrid, Madrid, Spain
Cortés-Contreras, M., Béjar, V. J. S., Caballero, J. A., et al. 2017, A&A, 597, A47
Crane, J. D., Shectman, S. A., Butler, R. P., et al. 2010, in Ground-based and Airborne Instrumentation for Astronomy III, Proc. SPIE, 7735, 773553
Cumming, A., Butler, R. P., Marcy, G. W., et al. 2008, PASP, 120, 531
Cuzzi, J. N., & Zahnle, K. J. 2004, ApJ, 614, 490
Dai, F., Masuda, K., & Winn, J. N. 2018, ApJ, 864, L38
Díez Alonso, E., Caballero, J. A., Montes, D., et al. 2019, A&A, 621, A126
Dittmann, J. A., Irwin, J. M., Charbonneau, D., et al. 2017, Nature, 544, 333

Drake, A. J., Graham, M. J., Djorgovski, S. G., et al. 2014, ApJS, 213, 9
Endl, M., Kürster, M., & Els, S. 2000, A&A, 362, 585
Espinoza, N. 2018, Res. Notes AAS, 2, 209
Espinoza, N., & Jordán, A. 2015, MNRAS, 450, 1879
Espinoza, N., Kossakowski, D., & Brahm, R. 2018, MNRAS, submitted [arXiv:1812.08549]
Espinoza, N., Brahm, R., Henning, T., et al. 2019, MNRAS, submitted [arXiv:1903.07694]
Feroz, F., Hobson, M. P., & Bridges, M. 2009, MNRAS, 398, 1601
Foreman-Mackey, D., Agol, E., Ambikasaran, S., & Angus, R. 2017, celerite: Scalable 1D Gaussian Processes in C++, Python, and Julia
France, K., Loyd, R. P., Youngblood, A., et al. 2016, ApJ, 820, 89
Fulton, B. J., Petigura, E. A., Blunt, S., & Sinukoff, E. 2018, PASP, 130, 044504
Fulton, B. J., Petigura, E. A., Howard, A. W., et al. 2017, AJ, 154, 109
Gaia Collaboration (Brown, A. G. A., et al.) 2018, A&A, 616, A1
Gandolfi, D., Barragán, O., Hatzes, A. P., et al. 2017, AJ, 154, 123
Gilliland, R. L., Marcy, G. W., Rowe, J. F., et al. 2013, ApJ, 766, 40
Gillon, M., Jehin, E., Lederer, S. M., et al. 2016, Nature, 533, 221
Gillon, M., Triaud, A. H. M. J., Demory, B.-O., et al. 2017, Nature, 542, 456
Gliese, W. 1957, Astronomisches Rechen-Institut Heidelberg Mitteilungen Serie A, 8, 1
Greene, T. P., Line, M. R., Montero, C., et al. 2016, ApJ, 817, 17
Günther, M. N., Pozuelos, F. J., Dittmann, J. A., et al. 2019, ArXiv e-prints [arXiv:1903.06107]
Harpsøe, K. B. W., Hardis, S., Hinse, T. C., et al. 2013, A&A, 549, A10
Hawley, S. L., Gizis, J. E., & Reid, I. N. 1996, AJ, 112, 2799
Hayano, Y., Takami, H., Oya, S., et al. 2010, in Adaptive Optics Systems II, Proc. SPIE, 7736, 77360N
Hébrard, E., Dobrijevic, M., Loison, J.-C., Bergeat, A., & Hickson, K. 2012, A&A, 541, A21
Iyer, A. R., Swain, M. R., Zellem, R. T., et al. 2016, ApJ, 823, 109
Jenkins, J. M., Twicken, J. D., McCauliff, S., et al. 2016, in Software and Cyberinfrastructure for Astronomy IV, Proc. SPIE, 9913, 99133E
Jensen, E. 2013, Tapir: A web interface for transit/eclipse observability, Astrophysics Source Code Library [record ascl:1306.007]
Jódar, E., Pérez-Garrido, A., Díaz-Sánchez, A., et al. 2013, MNRAS, 429, 859
Johansen, A., Oishi, J. S., Mac Low, M.-M., et al. 2007, Nature, 448, 1022
Kaltenegger, L., & Sasselov, D. 2010, ApJ, 708, 1162
Kasting, J. F., Whitmire, D. P., & Reynolds, R. T. 1993, Icarus, 101, 108
Kawashima, Y., & Rugheimer, S. 2019, AJ, 157, 213
Kempton, E. M.-R., Bean, J. L., Louie, D. R., et al. 2018, PASP, 130, 114401
Kipping, D. M. 2013, MNRAS, 435, 2152
Klahr, H., & Bodenheimer, P. 2006, ApJ, 639, 432
Kochanek, C. S., Shappee, B. J., Stanek, K. Z., et al. 2017, PASP, 129, 104502
Kopparapu, R. K., Ramirez, R. M., SchottelKotte, J., et al. 2014, ApJ, 787, L29
Kostov, V. B., Schlieder, J. E., Barclay, T., et al. 2019, AJ, 158, 32
Kotani, T., Tamura, M., Nishikawa, J., et al. 2018, in Ground-based and Airborne Instrumentation for Astronomy VII, SPIE Conf. Ser., 10702, 107021
Kreidberg, L. 2015, PASP, 127, 1161
Kreidberg, L., Bean, J. L., Désert, J.-M., et al. 2014, Nature, 505, 69
Kürster, M., Endl, M., Rouesnel, F., et al. 2003, A&A, 403, 1077
Labadie, L., Rebolo, R., Femenía, B., et al. 2010, in Ground-based and Airborne Instrumentation for Astronomy III, Proc. SPIE, 7735, 77350X
Lambrechts, M., Johansen, A., & Morbidelli, A. 2014, A&A, 572, A35
Lendl, M., Ehrenreich, D., Turner, O. D., et al. 2017, A&A, 603, L5
Lenz, C. T., Klahr, H., & Birnstiel, T. 2019, ApJ, 874, 36
Levison, H. F., Kretke, K. A., & Duncan, M. J. 2015, Nature, 524, 322
Li, J., Tenenbaum, P., Twicken, J. D., et al. 2019, PASP, 131, 024506
Louie, D. R., Deming, D., Albert, L., et al. 2018, PASP, 130, 044401
Lovis, C., & Pepe, F. 2007, A&A, 468, 1115
Luque, R., Nowak, G., Pallé, E., et al. 2018, A&A, 620, A171
Luyten, W. J. 1942, Publications of the Astronomical Observatory University of Minnesota (Minnesota, US: University of Minnesota Press), 2, 242
Mandel, K., & Agol, E. 2002, ApJ, 580, L171
Marcy, G. W., Isaacson, H., Howard, A. W., et al. 2014, ApJS, 210, 20
Maxted, P. F. L., Anderson, D. R., Collier Cameron, A., et al. 2011, PASP, 123, 547
Mayor, M., Pepe, F., Queloz, D., et al. 2003, The Messenger, 114, 20
Ment, K., Dittmann, J. A., Astudillo-Defru, N., et al. 2019, AJ, 157, 32
Meschiari, S., Wolf, A. S., Rivera, E., et al. 2009, PASP, 121, 1016
Molaverdikhani, K., Henning, T., & Mollière, P. 2019, ApJ, 873, 32
Mollière, P., Wardenier, J. P., van Boekel, R., et al. 2019, A&A, 627, A67
Montes, D., López-Santiago, J., Gálvez, M. C., et al. 2001, MNRAS, 328, 45
Mordasini, C., Alibert, Y., Klahr, H., & Henning, T. 2012, A&A, 547, A111
Motalebi, F., Udry, S., Gillon, M., et al. 2015, A&A, 584, A72
Moutou, C., Hébrard, E. M., Morin, J., et al. 2017, MNRAS, 472, 4563
Ofir, A. 2014, A&A, 561, A138
Ofir, A., Dreizler, S., Zechmeister, M., & Husser, T.-O. 2014, A&A, 561, A103
Ofir, A., Xie, J.-W., Jiang, C.-F., Sari, R., & Aharonson, O. 2018, ApJS, 234, 9
Ormel, C. W., & Klahr, H. H. 2010, A&A, 520, A43
Ormel, C. W., Liu, B., & Schoonenberg, D. 2017, A&A, 604, A1
Oscoz, A., Rebolo, R., López, R., et al. 2008, in Ground-based and Airborne Instrumentation for Astronomy II, Proc. SPIE, 7014, 701447
Otor, O. J., Montet, B. T., Johnson, J. A., et al. 2016, AJ, 152, 165
Pallé, E., Zapatero Osorio, M. R., Barrena, R., Montañés-Rodríguez, P., & Martín, E. L. 2009, Nature, 459, 814
Parviainen, H. 2015, MNRAS, 450, 3233
Pojmanski, G. 2002, Acta Astron., 52, 397
Pollacco, D. L., Skillen, I., Collier Cameron, A., et al. 2006, PASP, 118, 1407
Quinn, S. N., White, T. R., Latham, D. W., et al. 2015, ApJ, 803, 49
Quirrenbach, A., Amado, P. J., Caballero, J. A., et al. 2014, in Ground-based and Airborne Instrumentation for Astronomy V, Proc. SPIE, 9147, 91471F
Quirrenbach, A., Amado, P. J., Ribas, I., et al. 2018, in Ground-based and Airborne Instrumentation for Astronomy VII, SPIE Conf.Ser., 10702, 107020W
Reiners, A., Zechmeister, M., Caballero, J. A., et al. 2018, A&A, 612, A49
Ribas, I., Tuomi, M., Reiners, A., et al. 2018, Nature, 563, 365
Ricker, G. R., Winn, J. N., Vanderspek, R., et al. 2015, J. Astron. Telesc. Instrum. Syst., 1, 014003
Rowe, J. F., Bryson, S. T., Marcy, G. W., et al. 2014, ApJ, 784, 45
Sarkis, P., Henning, T., Kürster, M., et al. 2018, AJ, 155, 257
Schöfer, P., Jeffers, S. V., Reiners, A., et al. 2019, A&A, 623, A44
Schoonenberg, D., & Ormel, C. W. 2017, A&A, 602, A21
Schweitzer, A., Passegger, V. M., Cifuentes, C., et al. 2019, A&A, 625, A68
Sinukoff, E., Howard, A. W., Petigura, E. A., et al. 2016, ApJ, 827, 78
Skrutskie, M. F., Cutri, R. M., Stiening, R., et al. 2006, AJ, 131, 1163
Smith, J. C., Stumpe, M. C., Van Cleve, J. E., et al. 2012, PASP, 124, 1000
Southworth, J. 2011, MNRAS, 417, 2166
Speagle, J. S. 2019, MNRAS, submitted [arXiv:1904.02180]
Stassun, K. G., Oelkers, R. J., Pepper, J., et al. 2018, AJ, 156, 102
Stelzer, B., Marino, A., Micela, G., López-Santiago, J., & Liefke, C. 2013, MNRAS, 431, 2063
Stevenson, D. J., & Lunine, J. I. 1988, Icarus, 75, 146
Stumpe, M. C., Smith, J. C., Van Cleve, J. E., et al. 2012, PASP, 124, 985
Stumpe, M. C., Smith, J. C., Catanzarite, J. H., et al. 2014, PASP, 126, 100
Suárez Mascare no, A., Rebolo, R., González Hernández, J. I., & Esposito, M. 2015, MNRAS, 452, 2745
Sullivan, P. W., Winn, J. N., Berta-Thompson, Z. K., et al. 2015, ApJ, 809, 77
Tal-Or, L., Trifonov, T., Zucker, S., Mazeh, T., & Zechmeister, M. 2019, MNRAS, 484, L8
ter Braak, C. J. F., & Vrugt, J. A. 2008, Stat. Comput., 18, 435
Trifonov, T., Kürster, M., Zechmeister, M., et al. 2018, A&A, 609, A117
Trotta, R. 2008, Contemp. Phys., 49, 71
Tuomi, M., & Anglada-Escudé, G. 2013, A&A, 556, A111
Twicken, J. D., Catanzarite, J. H., Clarke, B. D., et al. 2018, PASP, 130, 064502
Udry, S., Bonfils, X., Delfosse, X., et al. 2007, A&A, 469, L43
Van Eylen, V., Agentoft, C., Lundkvist, M. S., et al. 2018, MNRAS, 479, 4786
Vanderspek, R., Huang, C. X., Vanderburg, A., et al. 2019, ApJ, 871, L24
Venot, O., Hébrard, E., Agúndez, M., et al. 2012, A&A, 546, A43
Vogt, S. S., Allen, S. L., Bigelow, B. C., et al. 1994, in Instrumentation in Astronomy VIII, eds. D. L. Crawford & E. R. Craine, Proc. SPIE, 2198, 362
Vogt, S. S., Marcy, G. W., Butler, R. P., & Apps, K. 2000, ApJ, 536, 902
Wakeford, H. R., Sing, D. K., Kataria, T., et al. 2017, Science, 356, 628
Woźniak, P. R., Vestrand, W. T., Akerlof, C. W., et al. 2004, AJ, 127, 2436
Zacharias, N., Finch, C. T., Girard, T. M., et al. 2013, AJ, 145, 44
Zechmeister, M., & Kürster, M. 2009, A&A, 496, 577
Zechmeister, M., Kürster, M., & Endl, M. 2009, A&A, 505, 859
Zechmeister, M., Reiners, A., Amado, P. J., et al. 2018, A&A, 609, A12
Zeng, L., Sasselov, D. D., & Jacobsen, S. B. 2016, ApJ, 819, 127

[1] Instituto de Astrofísica de Canarias (IAC), 38205 La Laguna, Tenerife, Spain
e-mail: rluque@iac.es
[2] Departamento de Astrofísica, Universidad de La Laguna (ULL), 38206 La Laguna, Tenerife, Spain
[3] Max-Planck-Institut für Astronomie, Königstuhl 17, 69117 Heidelberg, Germany
[4] Institut für Astrophysik, Georg-August-Universität, Friedrich-Hund-Platz 1, 37077 Göttingen, Germany
[5] Landessternwarte, Zentrum für Astronomie der Universität Heidelberg, Königstuhl 12, 69117 Heidelberg, Germany

[6] Kavli Institute for Astrophysics and Space Research, Massachusetts Institute of Technology, Cambridge, MA 02139, USA
[7] School of Physics and Astronomy, Queen Mary University of London, 327 Mile End Road, London, E1 4NS, UK
[8] Instituto de Astrofísica de Andalucía (IAA-CSIC), Glorieta de la Astronomía s/n, 18008 Granada, Spain
[9] Centro de Astrobiología (CSIC-INTA), ESAC, Camino bajo del castillo s/n, 28692 Villanueva de la Cañada, Madrid, Spain
[10] Harvard-Smithsonian Center for Astrophysics, 60 Garden St, Cambridge, MA 02138, USA
[11] Department of Physics and Astronomy, Vanderbilt University, Nashville, TN 37235, USA
[12] Departamento de Física de la Tierra y Astrofísica & IPARCOS-UCM (Instituto de Física de Partículas y del Cosmos de la UCM), Facultad de Ciencias Físicas, Universidad Complutense de Madrid, 28040 Madrid, Spain
[13] Department of Exploitation and Exploration of Mines, University of Oviedo, Oviedo, Spain
[14] Department of Terrestrial Magnetism, Carnegie Institution for Science, 5241 Broad Branch Road, NW, Washington, DC 20015, USA
[15] Thüringer Landessternwarte Tautenburg, Sternwarte 5, 07778 Tautenburg, Germany
[16] Astrophysics Group, Keele University, Staffordshire, ST5 5BG, UK
[17] Carl Sagan Institute, Cornell University, Ithaca, NY 14853, USA
[18] Astrobiology Center, 2-21-1 Osawa, Mitaka, Tokyo 181-8588, Japan
[19] JST, PRESTO, 2-21-1 Osawa, Mitaka, Tokyo 181-8588, Japan
[20] National Astronomical Observatory of Japan, 2-21-1 Osawa, Mitaka, Tokyo 181-8588, Japan
[21] Weizmann Institute of Science, 234 Herzl Street, Rehovot 761001, Israel
[22] Department of Astrophysical Sciences, Princeton University, 4 Ivy Lane, Princeton, NJ 08544, USA
[23] Centro de Astrobiología (CSIC-INTA), Carretera de Ajalvir km 4, 28850 Torrejón de Ardoz, Madrid, Spain
[24] Department of Astronomy and Astrophysics, University of California, Santa Cruz, CA 95064, USA
[25] SETI Institute, Mountain View, CA 94043, USA
[26] NASA Ames Research Center, Moffett Field, CA 94035, USA
[27] Key Laboratory of Planetary Sciences, Purple Mountain Observatory, Chinese Academy of Sciences, Nanjing 210008, PR China
[28] Observatories of the Carnegie Institution for Science, 813 Santa Barbara Street, Pasadena, CA 91101, USA
[29] Department of Astronomy, The University of California, Berkeley, CA 94720, USA
[30] Institut de Ciències de l'Espai (ICE, CSIC), Campus UAB, C/Can Magrans s/n, 08193 Bellaterra, Spain
[31] Institut d'Estudis Espacials de Catalunya (IEEC), 08034 Barcelona, Spain
[32] The Maury Lewin Astronomical Observatory, Glendora, California 91741, USA
[33] Proto-Logic LLC, 1718 Euclid Street NW, Washington, DC 20009, USA
[34] Hamburger Sternwarte, Universität Hamburg, Gojenbergsweg 112, 21029 Hamburg, Germany
[35] Centro Astronómico Hispano-Alemán (CSIC-MPG), Observatorio Astronómico de Calar Alto, Sierra de los Filabres-04550 Gérgal, Almería, Spain
[36] School of Physical Sciences, The Open University, Milton Keynes MK7 6AA, UK
[37] Department of Earth, Atmospheric and Planetary Sciences, Massachusetts Institute of Technology, Cambridge, MA 02139, USA
[38] Department of Aeronautics and Astronautics, MIT, 77 Massachusetts Avenue, Cambridge, MA 02139, USA
[39] Department of Astronomy, The University of Tokyo, 7-3-1 Hongo, Bunkyo-ku, Tokyo 113-0033, Japan

Appendix A: Joint fit priors

Table A.1. Priors used for the joint fit model 3pl+GPexp presented in Sect. 5.2.3 using `juliet`.

Parameter name	Prior	Units	Description
	Stellar parameters		
$\rho_\star$	$\mathcal{N}(13\,600, 1700^2)$	kg m^{-3}	Stellar density
	Planet parameters		
P_b	$\mathcal{N}(3.93079, 0.001^2)$	d	Period of planet b
P_c	$\mathcal{N}(9.1, 0.1^2)$	d	Period of planet c
P_d	$\mathcal{N}(55.7, 0.5^2)$	d	Period of planet d
$t_{0,b} - 24\,50\,000$	$\mathcal{N}(8517.99, 0.1^2)$	d	Time of transit-center of planet b
$t_{0,c} - 24\,50\,000$	$\mathcal{U}(8312, 8318)$	d	Time of transit-center of planet c
$t_{0,d} - 24\,50\,000$	$\mathcal{U}(8310, 8340)$	d	Time of transit-center of planet d
$r_{1,b}$	$\mathcal{U}(0, 1)$	...	Parametrization for p and b
$r_{2,b}$	$\mathcal{U}(0, 1)$	...	Parametrization for p and b
K_b	$\mathcal{U}(0, 10)$	m s^{-1}	RV semi-amplitude of planet b
K_c	$\mathcal{U}(0, 10)$	m s^{-1}	RV semi-amplitude of planet c
K_d	$\mathcal{U}(0, 10)$	m s^{-1}	RV semi-amplitude of planet d
$\mathcal{S}_{1,b,c,d} = \sqrt{e_{b,c,d}} \sin \omega_{b,c,d}$	0.0 (fixed)	...	Parametrization for e and ω
$\mathcal{S}_{2,b,c,d} = \sqrt{e_{b,c,d}} \cos \omega_{b,c,d}$	0.0 (fixed)	...	Parametrization for e and ω
	Photometry parameters		
D_TESS	1.0 (fixed)	...	Dilution factor
M_TESS	$\mathcal{N}(0, 0.1^2)$	ppm	Relative flux offset for TESS
σ_TESS	$\mathcal{U}(1, 500)$	ppm	Extra jitter term for TESS
$q_\mathrm{1,TESS}$	$\mathcal{U}(0, 1)$	...	Quadratic limb-darkening parametrization for TESS
$q_\mathrm{2,TESS}$	$\mathcal{U}(0, 1)$	...	Quadratic limb-darkening parametrization for TESS
M_LCO	$\mathcal{N}(0, 0.1^2)$	ppm	Relative flux offset for LCO
σ_LCO	$\mathcal{U}(1, 2000)$	ppm	Extra jitter term for LCO
$q_\mathrm{1,LCO}$	$\mathcal{U}(0, 1)$	...	Linear limb-darkening parametrization for LCO
	RV parameters		
μ_HIRES	$\mathcal{U}(-10, 10)$	m s^{-1}	Systemic velocity for HIRES
σ_HIRES	$\mathcal{U}(0, 10)$	m s^{-1}	Extra jitter term for HIRES
μ_UVES	$\mathcal{U}(-10, 10)$	m s^{-1}	Systemic velocity for UVES
σ_UVES	$\mathcal{U}(0, 10)$	m s^{-1}	Extra jitter term for UVES
μ_HARPS	$\mathcal{U}(-10, 10)$	m s^{-1}	Systemic velocity for HARPS
σ_HARPS	$\mathcal{U}(0, 10)$	m s^{-1}	Extra jitter term for HARPS
μ_PFSpre	$\mathcal{U}(-10, 10)$	m s^{-1}	Systemic velocity for PFSpre
σ_PFSpre	$\mathcal{U}(0, 10)$	m s^{-1}	Extra jitter term for PFSpre
μ_PFSpost	$\mathcal{U}(-10, 10)$	m s^{-1}	Systemic velocity for PFSpost
σ_PFSpost	$\mathcal{U}(0, 10)$	m s^{-1}	Extra jitter term for PFSpost
μ_CARMENES	$\mathcal{U}(-10, 10)$	m s^{-1}	Systemic velocity for CARMENES
σ_CARMENES	$\mathcal{U}(0, 10)$	m s^{-1}	Extra jitter term for CARMENES
	GP hyperparameters		
$\sigma_\mathrm{GP,TESS}$	$\mathcal{J}(10^{-2}, 500)$	ppm	Amplitude of GP component for TESS
$T_\mathrm{GP,TESS}$	$\mathcal{J}(10^{-2}, 1000)$	d	Length scale of GP component for TESS
$\sigma_\mathrm{GP,RV}$	$\mathcal{J}(0.1, 10)$	m s^{-1}	Amplitude of GP component for the RVs
$T_\mathrm{GP,RV}$	$\mathcal{J}(10^{-4}, 10)$	d	Length scale of GP component for the RVs

Notes. The prior labels of $\mathcal{N}$, $\mathcal{U}$, and $\mathcal{J}$ represent normal, uniform, and Jeffrey's distributions. The parametrization for (p, b) using (r_1, r_2) (Espinoza 2018) and the linear (q_1) and quadratic (q_1, q_2) limb-darkening parametrization (Kipping 2013) are both described in Sect. 5.2.1.

Appendix B: RV time series of best joint fit

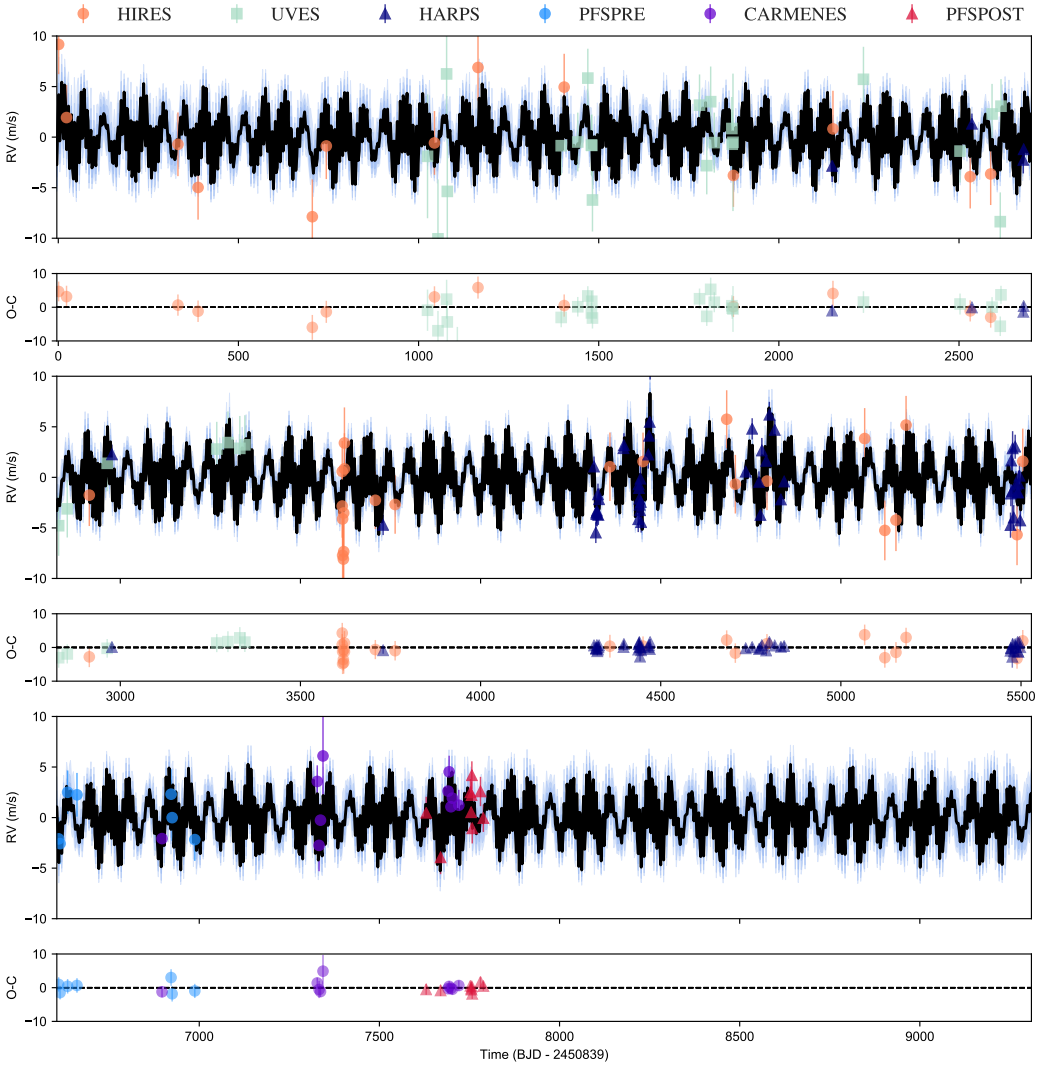

Fig. B.1. RV measurements as a function of time along with the residuals obtained from subtracting our median best joint fit model (black line) and the 68, 95, and 99% posterior bands (shown in blue). The color coding of the datapoints for each instrument is shown at the top.

4

Pair of sub-Neptunes transiting the bright TOI-776

Se cayeron las estatuas
al abrirse la gran puerta.
Federico García Lorca (1929)

The contents of this chapter refer to the article *A planetary system with two transiting mini-Neptunes near the radius valley transition around the bright M dwarf TOI-776*, published in the journal Astronomy & Astrophysics (Luque et al., 2021). This work makes use of observations from *TESS* and HARPS. The article is part of the efforts from KESPRINT, an international consortium devoted to the characterization and research of exoplanets discovered with space-based missions. The author list comprises members from KESPRINT, key investigators of the *TESS* mission and contributing members from TFOP with either analyses or ground-based follow-up observations such as transit follow-up, photometric monitoring, and high-resolution imaging. A total of 65 researchers from 41 different institutions co-sign the article.

This work describes the discovery and characterization of two transiting planets detected by the *TESS* mission orbiting the M1 V star TOI-776. Due to their alerted radii, inside the gap of the bimodal distribution of close-in small planet sizes (Fulton et al., 2017), the star was included in the target list of the HARPS large program awarded to the KESPRINT consortium to carry out radial velocity follow-up of *TESS* candidates. A year after the beginning of the HARPS observations, they were interrupted due to the COVID-19 pandemic situation in Chile. However, the collected spectra were enough for the confirmation and mass determination of the two transiting

planets and we published this work in the second half of 2020.

The manuscript is a comprehensive and thorough example of exoplanet characterization, which includes ground-based transit confirmation, high-resolution imaging and radial velocity follow-up, precise stellar parameters determination, stellar activity modeling, frequency analyses, joint fit of transit and radial velocity observations, dynamical and stability analyses, planetary composition and internal structure modeling, an insight of the formation and evolution of the system, and prospects for atmospheric characterization, including simulated transmission spectra as seen by the *JWST*.

The planets in the TOI-776 system have periods of 8.2 and 15.7 days, with radii 1.8–2.0 $R_\oplus$ and masses 4–5 $M_\oplus$. The star is moderately active, with a period of 34 days evident in the radial velocity observations and in the ground-based monitoring carried out with photometric facilities over the last 15 years. Our analyses show that the planets must posses an atmosphere, since their bulk densities are incompatible with being made only out of iron and rock. The location of the planets in the radius-period diagram make them very valuable to test models of planet formation and evolution in low-mass stars. On the other hand, the brightness of their host make them easy targets for atmospheric characterization with the *JWST*, which could help to break the degeneracies in planetary composition models and study the origin and evolution of the system.

A&A 645, A41 (2021)
https://doi.org/10.1051/0004-6361/202039455

Astronomy & Astrophysics

A planetary system with two transiting mini-Neptunes near the radius valley transition around the bright M dwarf TOI-776⋆

R. Luque[1,2], L. M. Serrano[3], K. Molaverdikhani[4,5], M. C. Nixon[6], J. H. Livingston[7], E. W. Guenther[8], E. Pallé[1,2], N. Madhusudhan[6], G. Nowak[1,2], J. Korth[9], W. D. Cochran[10], T. Hirano[11], P. Chaturvedi[8], E. Goffo[3], S. Albrecht[12], O. Barragán[13], C. Briceño[14], J. Cabrera[15], D. Charbonneau[16], R. Cloutier[16], K. A. Collins[16], K. I. Collins[17], K. D. Colón[18], I. J. M. Crossfield[19], Sz. Csizmadia[15], F. Dai[20], H. J. Deeg[1,2], M. Esposito[8], M. Fridlund[21,22], D. Gandolfi[3], I. Georgieva[22], A. Glidden[23,24], R. F. Goeke[23], S. Grziwa[9], A. P. Hatzes[8], C. E. Henze[25], S. B. Howell[25], J. Irwin[16], J. M. Jenkins[25], E. L. N. Jensen[26], P. Kábath[27], R. C. Kidwell Jr.[28], J. F. Kielkopf[29], E. Knudstrup[12], K. W. F. Lam[30], D. W. Latham[16], J. J. Lissauer[25], A. W. Mann[31], E. C. Matthews[24], I. Mireles[24], N. Narita[32,33,34,1], M. Paegert[16], C. M. Persson[22], S. Redfield[35], G. R. Ricker[24], F. Rodler[36], J. E. Schlieder[18], N. J. Scott[25], S. Seager[24,23,37], J. Šubjak[27], T. G. Tan[38], E. B. Ting[25], R. Vanderspek[24], V. Van Eylen[39], J. N. Winn[40], and C. Ziegler[41]

(Affiliations can be found after the references)

Received 16 September 2020 / Accepted 30 November 2020

ABSTRACT

We report the discovery and characterization of two transiting planets around the bright M1 V star LP 961-53 (TOI-776, $J = 8.5$ mag, $M = 0.54 \pm 0.03\,M_{\odot}$) detected during Sector 10 observations of the Transiting Exoplanet Survey Satellite (TESS). Combining the TESS photometry with HARPS radial velocities, as well as ground-based follow-up transit observations from the MEarth and LCOGT telescopes, for the inner planet, TOI-776 b, we measured a period of $P_b = 8.25$ d, a radius of $R_b = 1.85 \pm 0.13\,R_{\oplus}$, and a mass of $M_b = 4.0 \pm 0.9\,M_{\oplus}$; and for the outer planet, TOI-776 c, a period of $P_c = 15.66$ d, a radius of $R_c = 2.02 \pm 0.14\,R_{\oplus}$, and a mass of $M_c = 5.3 \pm 1.8\,M_{\oplus}$. The Doppler data shows one additional signal, with a period of ~34 d, associated with the rotational period of the star. The analysis of fifteen years of ground-based photometric monitoring data and the inspection of different spectral line indicators confirm this assumption. The bulk densities of TOI-776 b and c allow for a wide range of possible interior and atmospheric compositions. However, both planets have retained a significant atmosphere, with slightly different envelope mass fractions. Thanks to their location near the radius gap for M dwarfs, we can start to explore the mechanism(s) responsible for the radius valley emergence around low-mass stars as compared to solar-like stars. While a larger sample of well-characterized planets in this parameter space is still needed to draw firm conclusions, we tentatively estimate that the stellar mass below which thermally-driven mass loss is no longer the main formation pathway for sculpting the radius valley is between 0.63 and 0.54 $M_{\odot}$. Due to the brightness of the star, the TOI-776 system is also an excellent target for the *James Webb* Space Telescope, providing a remarkable laboratory in which to break the degeneracy in planetary interior models and to test formation and evolution theories of small planets around low-mass stars.

Key words. planetary systems – techniques: photometric – techniques: radial velocities – stars: individual: LP 961-53 – stars: low-mass

1. Introduction

Exoplanets with masses between those of Earth and Uranus are characterized by a broad range of measured bulk densities (e.g., Hatzes & Rauer 2015). A low density suggests the presence of an extended H/He-envelope around a solid core. On the contrary, if the density is high, the exoplanet is considered to be fully rocky or enriched in light elements (e.g., water, methane, ammonia). The absence of an envelope might be the result of two opposite scenarios: the planet is born without it, or the planet loses it over time. In the first case, the planet forms in a gas-poor inner protoplanetary disk without a thick H/He-envelope (e.g., Lee et al. 2014; Lee & Chiang 2016). For the second case, different mechanisms have been proposed in the last years, such as slow atmospheric escape powered by the planetary core's primordial energy reservoir from formation (Ginzburg et al. 2018; Gupta & Schlichting 2019, 2020), impact erosion by planetesimals (Shuvalov 2009; Schlichting et al. 2015; Wyatt et al. 2020), or erosion processes driven by the stellar X-ray+EUV (XUV) radiation (e.g., Murray-Clay et al. 2009; Lammer et al. 2012; Owen & Jackson 2012; Owen & Wu 2013; Kislyakova et al. 2013, 2014; Lopez & Fortney 2014; Jin et al. 2014; Chen & Rogers 2016; Osborn et al. 2017; Jin & Mordasini 2018; Lopez & Rice 2018; Wu 2019; Mordasini 2020).

For the latter, the erosion rate increases if the planetary surface gravity decreases and the amount of XUV radiation that the planet receives increases. In addition, the intensity of XUV-radiation depends on the orbital semi-major axis and on the stellar activity level. The XUV-radiation is particularly high at young ages, and then it declines as a result of age, mass, and stellar rotation (Walter et al. 1988; Briceno et al. 1997; Tu et al. 2015). A star that begins its life rapidly rotating will suffer a more rapid decline in rotation than a star that was initially a slow rotator. Thus, for a star of several Gyr, understanding its

⋆ Based on observations made with ESO Telescopes at the La Silla Observatory under programs ID 1102.C-0923 and 60.A-9709.

original activity level is challenging. The presence, or absence, of a hydrogen-rich envelope in a system containing just one planet can thus equally be explained by assuming that the host star was either a slow or rapid rotator when it was young. Systems containing more than one planet are necessary to test the theory of atmospheric erosion, because the origin of all the planets of a system should be explained with a unique evolutionary history of the host's XUV radiation (Owen & Campos Estrada 2020).

On the other hand, the amount of XUV radiation also depends on the stellar type. The XUV luminosities of young G and M stars are similar to each other. The average X-ray luminosity of G stars is 10^{29} erg s^{-1}, while in the case of M dwarfs, the 50 Myr stars in α-Per, for example, have luminosities of 10^{28} erg s^{-1} (France et al. 2016). The main difference is that M dwarfs remain in the high activity phase for up to 2 Gyr (Johnstone et al. 2015), a much longer amount of time compared to the 300 Myr of G-stars (Güdel et al. 2004). This makes M dwarfs preferred targets to study planetary systems that have experienced significant stellar XUV irradiation. Another advantage of M dwarfs is their small size, which makes it easier to detect smaller transiting planets. The paucity of close-in planets around mid-K to mid-M dwarfs between approximately 1.4 and 1.7 $R_\oplus$ (Cloutier et al. 2020), known as the radius valley, marks the transition between rocky planets and sub-Neptunes orbiting low-mass stars. As such, M dwarfs' multi-planetary systems, which include sub-Neptunes and/or rocky planets, represent an ideal benchmark for testing the theory of atmospheric erosion.

Gas-poor formation provides an alternative to explain the absence of H/He envelopes in some low-mass planets, since the erosion scenario presents some issues. For instance, if a close-in 10 $M_\oplus$ rocky planet forms while there is still a gaseous disk, its mass is high enough to undergo runaway accretion and become a Jupiter-type planet. The detection of close-in Jupiter-mass planets, at least in A stars, shows that it is hard to reconstruct a mechanism that transforms a Jupiter into a rocky super-Earth, since any working physical process should be able to completely strip off the H/He atmosphere. On the other hand, stars hosting hot Jupiters have high metallicities, while rocky planets are equally distributed between metal-poor and metal-rich stars (Winn et al. 2017). Thus, there are two alternative scenarios within gas-poor formation models that could explain the existence of rocky super-Earths. Either the dust-to-gas ratio of the inner disk is 20-times higher than solar, or the gas accretion is delayed until just before the disk disperses (Lee et al. 2014; Lee & Chiang 2016).

Lopez & Rice (2018) proposed a statistical test that could allow us to understand the most likely formation history for super-Earths. If a high percentage of rocky planets are the evaporated cores of sub-Neptunes, the transition radius from rocky to sub-Neptune planets should decrease for longer orbital periods. On the contrary, if the gas-poor formation scenario is correct, the transition radius should increase with orbital period. Another methodology to test the formation theory of super-Earths requires studying the position of the radius valley for stars with different masses, thus of different stellar types. If the photoevaporation scenario is correct, the radius valley shifts toward planets of smaller radii for stars of lower masses. If, on the contrary, the gas-poor formation scenario is at work, the valley position is not affected by the stellar mass (Cloutier & Menou 2020). However, since the radius valley represents the range of radii in which the transition between rocky planets and sub-Neptunes occurs, it is necessary to accurately determine the mass and radius of the planets to calculate the mass-fraction of their envelope and unveil their nature. Therefore, the ideal test to understand which model is more realistic between the gas-poor formation and the photoevaporation consists of measuring the masses and radii of the planets close to, or inside, the radius valley, preferably in a multi-planetary system around low-mass stars. Therefore, we can also constrain these models in a much better way than through the radius distribution alone.

As of today, there is a limited number of known multi-planetary systems that orbit M dwarfs (3000 K < $T_{\rm eff}$ < 4000 K; as a proxy of M0 V–M5 V, Cifuentes et al. 2020) and respect the condition ($M_{\rm p}$ < 10 $M_\oplus$) required to test the two mentioned formation theories. There are only two systems with three transiting planets with measured dynamical masses, Kepler-138 (Almenara et al. 2018) and L 98-59 (Cloutier et al. 2019), and four systems with two transiting planets: LHS 1140 (Lillo-Box et al. 2020), LTT 3780 (Nowak et al. 2020; Cloutier et al. 2020), K2-146 (Lam et al. 2020; Hamann et al. 2019), and Kepler-26 (Jontof-Hutter et al. 2016). This paucity of systems is inadequate for understanding the formation and evolution of planetary systems around M dwarfs. The discovery of each new system is thus important, especially if the host star is bright and the planets are close to the radius valley.

In this paper, we present the discovery of two transiting planets orbiting an M1 V star. The inner one has a period of 8.2 d and a radius of ∼1.8 $R_\oplus$; thus, it is close to the radius valley. The outer planet has a period of 15.7 d and a radius of 2.0 $R_\oplus$ in the sub-Neptune regime. By measuring their masses, we explore whether these new planets are characterized by extended H/He envelopes. Since they orbit a relatively bright, nearby M dwarf, these new objects represent ideal targets for follow-up atmospheric studies.

2. TESS photometry

The star LP 961-53 (TIC 306996324) was observed with TESS in Sector 10 (Camera #2, CCD #4) from March 26, 2019 until April 22, 2019, with 2-min cadence exposures, and it will be observed again in Sector 37 from April 2 to 28, 2021. Data collection was paused for 0.98 d during perigee passage, while downloading data. The Science Processing Operations Center (SPOC; Jenkins et al. 2016) at the NASA Ames Research Center made the data available at the Mikulski Archive for Space Telescopes (MAST)[1] on June 1, 2019. SPOC provided simple aperture photometry (SAP) for this target as well as systematics-corrected photometry, a procedure consisting of an adaptation of the Kepler Presearch Data Conditioning algorithm (PDC; Smith et al. 2012; Stumpe et al. 2012, 2014) to TESS. Figure 1 shows the TESS pixels included in the computation of the SAP and PDC-corrected SAP data. For the remainder of this work, we make use of the latter photometric data, shown in Fig. 2.

On June 11, 2019, two transiting candidates orbiting LP 961-53 were announced in the TESS data public website[2] under the TESS Object of Interest (TOI) number 776. TOI-776.01 is a planet candidate with a period of 15.65 d, a transit depth of 1484 ± 127 ppm, and an estimated planet radius of 2.2 ± 0.6 $R_\oplus$; while TOI-776.02 is a planet candidate with a period of 8.24 d, a transit depth of 1063 ± 104 ppm, and an estimated planet radius of 1.8 ± 1.4 $R_\oplus$. Both candidates passed all the tests from the threshold crossing event (TCE) Data Validation Report (DVR; Twicken et al. 2018; Li et al. 2019): even-odd transits comparison, eclipsing binary (EB) discrimination tests, ghost diagnostic tests to help rule out scattered light, or background EB, among

[1] https://mast.stsci.edu
[2] https://tev.mit.edu/data/

Table 1. TESS follow-up program transit observations.

Observatory	Date (UTC)	Filter	Exposure (s)	Total (h)	Aperture (m)	Pixel scale (arcsec)	FOV (arcmin)
TOI-776.01 = TOI-776 c							
MEarth-South, CTIO, Chile	Jul. 1, 2019	RG715	10	4.2	7×0.4	0.84	29×29
LCOGT, CTIO, Chile	Jul. 1, 2019	i'	20	3.4	1.0	0.39	26.5×26.5
TOI-776.02 = TOI-776 b							
LCOGT, SAAO, South Africa	Feb. 29, 2020	z_s	45	4.7	1.0	0.39	26.5×26.5
LCOGT, SSO, Australia	Mar. 17, 2020	z_s	45	4.1	1.0	0.39	26.5×26.5
PEST, Australia	May 22, 2020	R_C	60	3.6	0.3	1.23	31×21

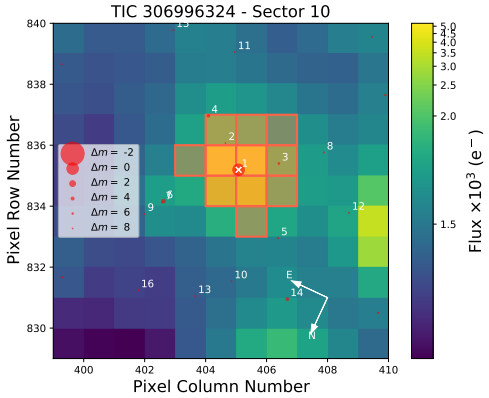

Fig. 1. TESS target pixel file image of LP 961-53 in Sector 10 (created with `tpfplotter`, Aller et al. 2020). The electron counts are color-coded. The red bordered pixels are used in the simple aperture photometry. The size of the red circles indicates the TESS magnitudes of all nearby stars and LP 961-53 (label #1 with the "×"). Positions are corrected for proper motions between the *Gaia* DR2 epoch (2015.5) and the TESS Sector 10 epoch (2019.2). The TESS pixel scale is approximately 21″.

others. However, the vetting team at the TESS Science Office proposed the possibility that TOI-776.01 could be an EB, where the secondary transit is the primary transit of TOI-776.02 candidate. The ground-based follow-up observations discussed in the next section refuted this scenario and confirmed the two announced candidates as bona-fide planets.

3. Ground-based observations

3.1. Transit follow-up

We observed the TOI-776 candidates as part of the *TESS* Follow-up Observing Program (TFOP)[3]. The goals of these ground-based photometric follow-up observations were to verify that the transits observed by TESS are on target, and to refine the transit ephemeris and depth measurements. We used the `TESS Transit Finder`, a customized version of the `Tapir` software package (Jensen 2013), to schedule photometric time-series follow-up observations. We observed two transits of TOI-776.01 and three transits of TOI-776.02, as summarized in Table 1 and discussed further below.

3.1.1. MEarth-South

A single transit of TOI-776.01 was observed with the 40 cm MEarth-South telescope array (Irwin et al. 2015) at Cerro Tololo Inter-American Observatory (CTIO), Chile on June 1, 2019. Seven telescopes observed continuously from evening twilight until the target star set below airmass 2, using an exposure time of 10 s, with all telescopes in focus. The target star was west of the meridian throughout the observation to avoid meridian flips.

Data were reduced following the standard procedures in Irwin et al. (2007) and Berta et al. (2012) with a photometric extraction aperture radius of $r = 6$ pix (5″ on sky given the pixel scale of $0\farcs84\,\mathrm{pix}^{-1}$). The light curve is shown in the lower right of Fig. 3. Due to the large variation in airmass and relatively red target star compared to the available field comparison stars, we found the light curve exhibited a small amount of residual second-order (color-dependent) atmospheric extinction, so the transit model was fit including an extinction term (linear decorrelation against airmass).

3.1.2. LCOGT

One transit of TOI-776.01 and two transits of TOI-776.02 were observed with the 1.0 m telescopes in the Las Cumbres Observatory (LCOGT) telescope network (Brown et al. 2013). The 4096×4096 pix LCOGT SINISTRO cameras have an image scale of $0\farcs389\,\mathrm{pix}^{-1}$, resulting in a $26'\times26'$ field of view. The images were calibrated using the standard LCOGT `BANZAI` pipeline, and photometric data were extracted with `AstroImageJ` (Collins et al. 2017).

An ingress of TOI-776.01 was observed from the LCOGT node at CTIO on July 1, 2019 in the i' filter, simultaneous with the MEarth-South observations mentioned above (Fig. 3, middle right). Transits of TOI-776.02 were observed from the LCOGT nodes at the South African Astronomical Observatory (SAAO) on February 29, 2020 (Fig. 3, middle left) and from the Siding Spring Observatory (SSO) on March 17, 2020, (Fig. 3, lower left). Both observations were made in the z_s filter, with the telescopes defocused.

3.1.3. PEST

A full transit of TOI-776.02 was observed with the 30 cm Perth Exoplanet Survey Telescope[4] (PEST) on May 22, 2020. These

[3] https://tess.mit.edu/followup

[4] http://pestobservatory.com/

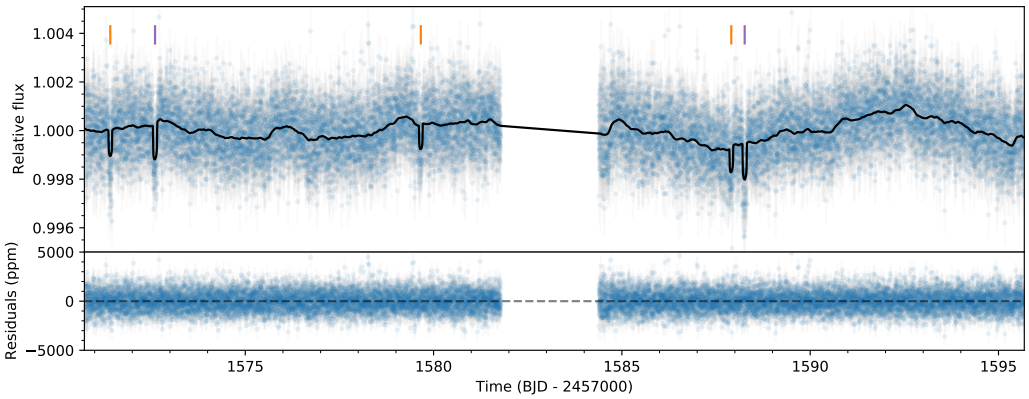

Fig. 2. TESS PDC-corrected SAP transit photometry from SPOC pipeline with the best-fit `juliet` model (black line; see Sect. 5.2.1 for details on the modeling). Purple and orange ticks above the light curve mark the transits of the candidates TOI-776.01 (purple) and TOI-732.02 (orange).

data have a scatter that is too large to reliably detect the transit. For this reason, we did not include them in the global fit.

3.2. Long-term photometric monitoring

We compiled ground-based, long baseline photometric series from automated surveys. The following public surveys observed TOI-776: the All-Sky Automated Survey for Supernovae (ASAS-SN; Kochanek et al. 2017), All-Sky Automated Survey (ASAS; Pojmanski 2002), Northern Sky Variability Survey (NSVS; Woźniak et al. 2004), and the Catalina surveys (Drake et al. 2014). The telescope location, instrument configurations, and photometric bands of each public survey were summarized in Table 1 of Díez Alonso et al. (2019). All together, the measurements span a period of 15 yr.

Additionally, TOI-776 is a candidate of the Super-Wide Angle Search for Planets (SuperWASP; Pollacco et al. 2006). SuperWASP acquired more than 11 000 photometric observations, using a broad-band optical filter spanning three consecutive seasons from May to July 2006, January to June 2007, and January to June 2008. In order to detect long-term photometric modulations associated with the stellar rotation, we binned the data into one day intervals, resulting in 201 epochs.

3.3. High spatial resolution imaging

The large pixel size of TESS increase the possibility of contamination by nearby sources that are not detected in the seeing-limited photometry or in *Gaia* DR2. Close companions can dilute the transit depth and thus alter the measured planet radius, or lead to false positives if the companion is itself an EB (e.g., Ciardi et al. 2015). We thus searched for companions by collecting adaptive optics (AO) and speckle images of TOI-776 using 4 m and 8 m class telescopes, providing robust limits on the presence of companions and the level of photometric dilution.

3.3.1. Adaptive optics imaging with Gemini/NIRI and VLT/NaCo

On June 15, 2019, TOI-776 was observed using the adaptive optics near-infrared imager (NIRI) mounted on the 8.1 m Gemini North telescope at Mauna Kea, Hawai'i. We collected a total of 9×1.4 s images in the Brγ filter centered on 2.166 μm. We dithered the telescope between exposures, so that the sky background could be constructed from the science frames themselves. After removing bad pixels, flat-fielding, and subtracting the sky background, we aligned the stellar position between frames and co-added the images. The sensitivity of our observations was calculated as a function of radius by injecting fake companions, and scaling their brightness, such that they could be detected at 5σ. The contrast curve and image are shown in Fig. 4. Only the central $4'' \times 4''$ are shown, but no companions are seen anywhere in the field, which has a field of view of $\sim 13'' \times 13''$.

On July 4, 2019, TOI-776 was observed in Brγ using the NAOS-CONICA AO instrument (NaCo), mounted at the Nasmyth A port of the 8 m UT1 Very Large Telescope (VLT) in Paranal, Chile. We collected a total of 9×10 s Brγ images. Data were reduced and analyzed using the same procedures as described above for the NIRI data, and no companions were found in the reduced image. The NaCo contrast curve is shown in Fig. 4.

3.3.2. Speckle imaging with SOAR/HRCam and Gemini/Zorro

On December 12, 2019, TOI-776 was observed in the *I* band with a pixel scale of 0.01575″ pix^{-1} using the HRCam imager, mounted on the 4.1 m Southern Astrophysical Research (SOAR) telescope at Cerro Tololo Inter-American Observatory, Chile. The data were acquired and reduced following the procedures described in Tokovinin (2018) and Ziegler et al. (2020). The resulting reconstructed image achieved a contrast of Δmag = 7.1 at a separation of 3″ (see top panel of Fig. 5).

On March 15, 2020, TOI-776 was observed using the Zorro speckle imager (Scott 2019), mounted on the 8.1 m Gemini South telescope in Cerro Pachón, Chile. Zorro uses high speed electron-multiplying CCDs (EMCCDs) to simultaneously acquire data in two bands centered at 562 and 832 nm. The data were collected and reduced following the procedures described in Howell et al. (2011). The resulting reconstructed image achieved a contrast of Δmag = 7.8 at a separation of 1″ in the 832 nm band (see bottom panel of Fig. 5). We note that at the distance of TOI-776, our Zorro speckle images cover a spatial

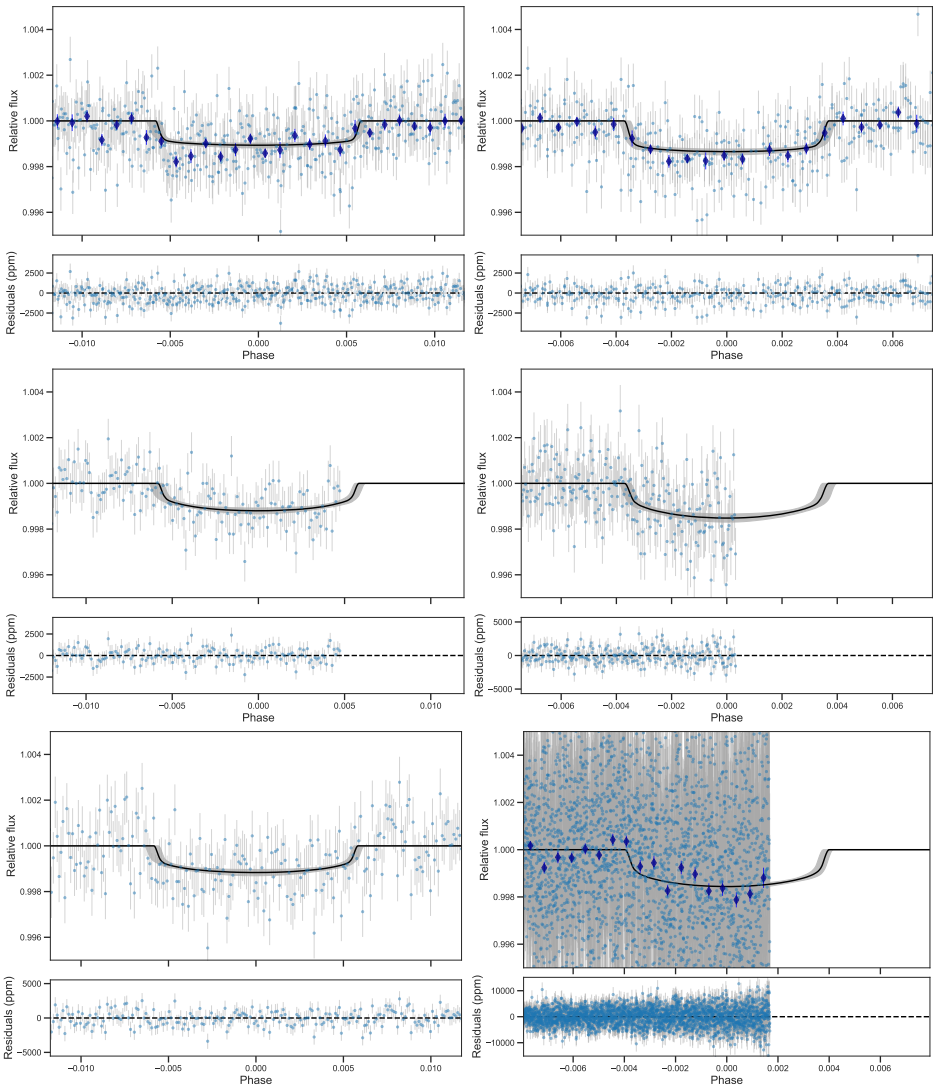

Fig. 3. Phase-folded light curves of TOI-776 b and c. *First column*: transits of TOI-776 b observed with TESS (*top*) in Sector 10, LCO-SAAO (*middle*) on Feb 29, 2020, and LCO-SSO (*bottom*) on May 22, 2020. *Second column*: transits of TOI-776 c observed with TESS (*top*) in Sector 10, and LCO-CTIO (*middle*) and MEarth-South (*bottom*) on July 2, 2020. TESS and MEarth-South photometry binned every 10 min are marked with blue diamonds to improve visualization. In all panels, the black lines and shaded areas indicate the detrended best fit model from Sect. 5.2.3 and its 1σ confidence interval. Below each panel, the residuals after the subtraction of the median best fit model are represented.

range of 0.46–32 au around the star with contrasts between 5 and 8 mag.

3.4. Radial velocity observations

We obtained 29 high-resolution ($R \approx 115\,000$) spectra of TOI-776 using the High Accuracy Radial velocity Planet Searcher (HARPS) spectrograph mounted at the ESO 3.6 m telescope of La Silla Observatory, Chile (Mayor et al. 2003). The observations were carried out as part of our large observing program 1102.C-0923 (PI: Gandolfi) starting on February 5 and ending on March 23, 2020, when ESO observatories stopped the operations due to the COVID-19 pandemic. One spectrum was acquired under the program 60.A-9709. We used the second

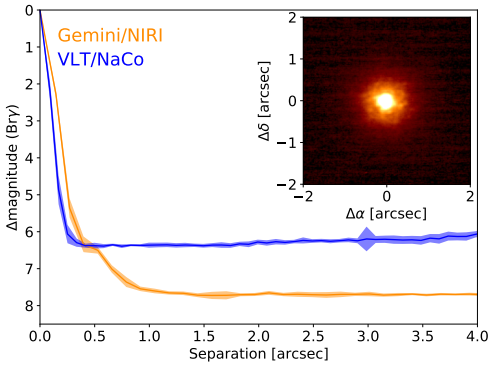

Fig. 4. Contrast curves from NIRI (orange) and NaCo (blue), and the central $4'' \times 4''$ of the NIRI image (inset). We rule out companions 6 mag fainter than TOI-776 beyond 250 mas, and 7.5 mag fainter beyond 900 mas. The NaCo observations have a slightly tighter inner working angle, while the NIRI observations reach a deeper sensitivity beyond $0.5''$.

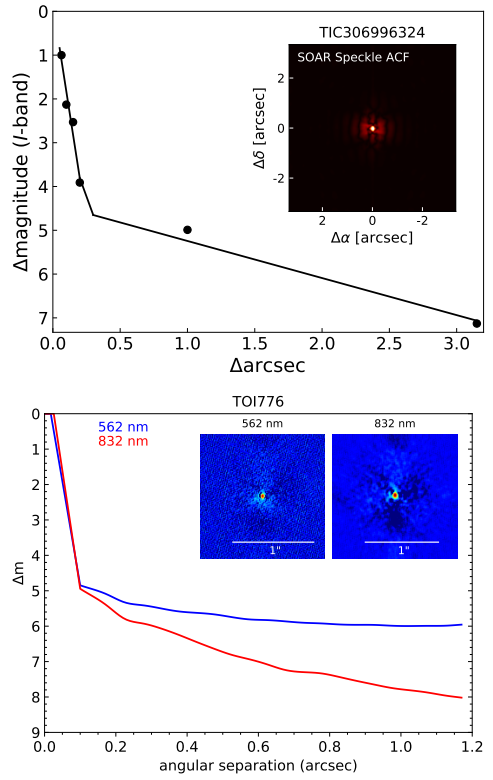

Fig. 5. *Top*: SOAR contrast curve and $6'' \times 6''$ reconstructed image (inset). *Bottom*: Gemini/Zorro contrast curves and $1.2'' \times 1.2''$ reconstructed images (inset).

fiber of the instrument to monitor the sky background and we reduced the data with the HARPS data reduction software (DRS; Lovis & Pepe 2007). To compute precise radial velocities and spectral diagnostics, we applied the codes `serval` (Zechmeister et al. 2018) and `TERRA` (Anglada-Escudé & Butler 2012) to the reduced data. Both programs employ a template-matching algorithm that is better suited to derive precise radial velocities for M dwarfs if compared to the cross-correlation function (CCF) technique implemented in the DRS. In the CCF technique, the line lists of M dwarfs used to define the binary mask are incomplete and they thus produce a CCF that is often a poor match for cool stars. The RVs have a median internal uncertainty of 1.5 m s^{-1} (1.5 m s^{-1}) and a root mean square of 5.2 m s^{-1} (3.5 m s^{-1}) around the mean value for the `serval` (`TERRA`) extractions, respectively. We report in Tables B.1 and B.2 the HARPS measurements; the extracted RVs and the associated uncertainties; Na I D, Na II D and Hα line indices from both programs together with the chromatic index (CRX) and differential line width (dLW) computed by `serval`; and the Mount Wilson S-index computed by `TERRA`.

4. Stellar properties

4.1. Stellar parameters

The star TOI-776 belongs to the Catalog Of Nearby Cool Host-Stars for Habitable ExopLanets and Life (CONCH-SHELL) compiled by Gaidos et al. (2014). For an all-sky sample of approximately 3000 M- or late K-type stars, the authors provide spectroscopically determined values of the spectral type, effective temperature, and metallicity; which, combined with empirical relations for cool stars, make it possible to estimate stellar radius, luminosity, and mass. In particular, they measure that TOI-776 is a relatively inactive M1 V dwarf star with the stellar properties shown in Table 2.

We carried out an independent analysis to improve the photospheric and fundamental parameters of TOI-776. We used `SpecMatch-Emp` (Yee et al. 2017) to empirically estimate the effective temperature, metallicity, and stellar radius by comparing the co-added HARPS high-resolution spectrum with a spectroscopic library of well-characterized stars. The results of this analysis are in agreement with the values of Gaidos et al. (2014) within the errors. Then, we derived the stellar radius and luminosity combining *Gaia* G, $G_{\rm BP}$, $G_{\rm RP}$ photometry and 2MASS J, H, $K_{\rm s}$ magnitudes with the spectroscopic parameters from the `SpecMatch-Emp` analysis and the *Gaia* parallax. We corrected the Gaia G photometry for the magnitude-dependent offset using Eq. (3) from Casagrande & VandenBerg (2018) and adopted a minimum uncertainty of 0.01 mag for the *Gaia* magnitudes to account for additional systematic uncertainties. We added 0.06 mas to the nominal *Gaia* parallax to account for the systematic offset found by Stassun & Torres (2018); Riess et al. (2018), and Zinn et al. (2019). Our best estimate of the stellar radius is consistent with the value from Gaidos et al. (2014) and in agreement with each of the radius estimates obtained independently using only one of the magnitudes. Finally, we computed the mass using the mass-radius relations for M dwarfs from Schweitzer et al. (2019).

We also applied the methods of Reddy et al. (2006) to *Gaia* DR2 astrometry for TOI-776 to compute galactic U, V, W velocities in the local standard of rest and the probabilities of kinematic membership in galactic stellar populations. We found that TOI-776 has a 96.3% probability of belonging to the thin disk population, which is in excellent agreement with the galactic

Table 2. Stellar parameters of TOI-776.

Parameter	Value	Reference
Name and identifiers		
Name	LP 961-53	Luyten (1974)
TOI	776	TESS Science Office
TIC	306 996 324	Stassun et al. (2018)
Coordinates and spectral type		
α	11:54:18.39	*Gaia* DR2
δ	−37:33:09.8	*Gaia* DR2
SpT	M1 V	Gaidos et al. (2014)
Magnitudes		
V (mag)	11.54 ± 0.04	UCAC4
g (mag)	12.35 ± 0.12	UCAC4
G (mag)	10.7409 ± 0.0005	*Gaia* DR2
r (mag)	10.92 ± 0.03	UCAC4
i (mag)	10.05 ± 0.09	UCAC4
J (mag)	8.483 ± 0.018	2MASS
H (mag)	7.877 ± 0.040	2MASS
K_s (mag)	7.615 ± 0.020	2MASS
Parallax and kinematics		
π (mas)	36.78 ± 0.04	*Gaia* DR2
d (pc)	27.19 ± 0.03	*Gaia* DR2
$\mu_\alpha \cos\delta$ (mas yr^{-1})	$+251.112 \pm 0.051$	*Gaia* DR2
μ_δ (mas yr^{-1})	-145.059 ± 0.083	*Gaia* DR2
V_r (km s^{-1})	49.34 ± 0.22	*Gaia* DR2
U (km s^{-1})	60.71 ± 0.08	This work [a]
V (km s^{-1})	-28.27 ± 0.17	This work [a]
W (km s^{-1})	18.73 ± 0.09	This work [a]
Photospheric parameters		
$T_{\rm eff}$ (K)	3709 ± 70	This work
	3766 ± 100	Gaidos et al. (2014)
log g	4.727 ± 0.025	This work
(Fe/H)	-0.20 ± 0.12	This work
Physical parameters		
R ($R_\odot$)	$0.538^{+0.024}_{-0.024}$	This work
	0.53 ± 0.05	Gaidos et al. (2014)
L ($L_\odot$)	0.049 ± 0.002	This work
	0.050 ± 0.013	Gaidos et al. (2014)
M ($M_\odot$)	$0.544^{+0.028}_{-0.028}$	This work
	0.56 ± 0.07	Gaidos et al. (2014)
Age (Gyr)	$7.8^{+3.9}_{-6.3}$	This work

Notes. [a] Computed in the local standard of rest.

References. *Gaia* DR2: Gaia Collaboration (2018); UCAC4: Zacharias et al. (2013); 2MASS: Skrutskie et al. (2006).

population probabilities for this star in the recent catalog of Carrillo et al. (2020). Additionally, using the code `isochrones` (Morton 2015), we estimated the age of TOI-776 to be loosely constrained between 2 and 10 Gyr. From the metallicity, age, and kinematics given in Table 2, we can conclude that TOI-776 is a relatively old member of the galactic thin disk population.

4.2. Stellar rotation period

To determine the rotational period of the star, we used the publicly available photometric data for TOI-776. Using `juliet`

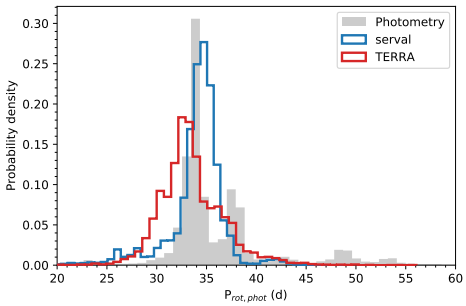

Fig. 6. Probability density of the samples of the $P_{\rm rot}$ parameter from the GP fit of the ground-based, long-term photometric monitoring (gray) from Sect. 4.2 and of the period of the additional sinusoidal signal from the RV fit from Sect. 5.2.2 using `serval` (blue) or `TERRA` (red) reductions.

(see more details about the algorithm in Sect. 5.2), we modeled the ASAS-SN, ASAS, NSVS, Catalina, and daily binned SuperWASP data with Gaussian processes (GPs). In particular, we adopted the quasi-periodic GP kernel introduced in Foreman-Mackey et al. (2017) of the form

$$k_{i,j}(\tau) = \frac{B}{2+C} e^{-\tau/L} \left[\cos\left(\frac{2\pi\tau}{P_{\rm rot}}\right) + (1+C) \right],$$

where $\tau = |t_i - t_j|$ is the time-lag, B and C define the amplitude of the GP, L is a timescale for the amplitude-modulation of the GP, and $P_{\rm rot}$ is the rotational period of the modulations. As in Luque et al. (2019), we considered each of the five data sets to have different values of B and C, in order to account for the possibility that different bands could have different GP amplitudes, while we imposed the timescale of the modulation and the rotational period as common parameters for all the data sets. In addition, we fit an extra jitter term for each photometric time series. We considered wide uninformative priors for the jitter, B, C, L, and a uniform rotation period prior between 10 and 100 d.

Figure 6 shows the posterior samples of the GP hyperparameter $P_{\rm rot}$ after fitting all the long-term monitoring ground-based photometry. The distribution is bimodal with peaks at 33 ± 1 d and 38 ± 1 d, where the samples from the first peak have the highest likelihood. From this we can estimate that the stellar rotation of TOI-776 is between 30 and 40 d over the course of 15 yr. The 38 d peak may be an alias of the true 33 d rotation due to 1 yr window function in the photometry. Alternatively, the bimodal distribution of the $P_{\rm rot}$ can be explained as a consequence of the stellar differential rotation coupled with the activity cycle (Rüdiger et al. 2014; Küker et al. 2019). For early M dwarfs with rotational periods similar to TOI-776, the expected dynamo cycle time is between 3 and 6 yr (Küker et al. 2019), thus detectable in our data. Additionally, assuming that this star is a solar-like rotator, the rotational velocity of the star decreases as the latitude increases. The two peaks correspond to two different groups of activity features, a bigger one, closer to the equator, which generates the first peak of the posterior distribution, and a smaller one, at a higher latitude, which produces the second peak. The opposite situation, with an antisolar-like rotator, is less likely, considering that TOI-776 is an adult star, still belonging to the main sequence.

5. Analysis

5.1. Frequency analysis of the HARPS data

We performed a frequency analysis of the HARPS `serval`/`TERRA` extracted measurements to search for the Doppler reflex motion induced by the two transiting planets discovered in the TESS light curve and to unveil the presence of additional signals associated with the star and/or other orbiting planets. Figure 7 shows the generalized Lomb Scargle (GLS; Zechmeister et al. 2009) periodograms of the HARPS RVs and activity indicators extracted with `serval` (blue lines) and with `TERRA` (red lines). The horizontal dashed lines mark the GLS powers corresponding to the 0.1, 1, and 5% false alarm probability (FAP)[5]. The vertical dashed lines mark the orbital frequencies of the two transiting planets detected in the TESS light curve ($f_b = 0.121\,d^{-1}$ and $f_c = 0.064\,d^{-1}$) and the stellar signal at $\sim 0.03\,d^{-1}$ (see below).

The upper panel of Fig. 7 displays the GLS periodogram of the HARPS RVs in the $0-0.42\,d^{-1}$ frequency range. The highest peak is found at $0.055\,d^{-1}$ (FAP $\approx 0.3\%$), which is close to the orbital frequency of TOI-776 c ($f_c = 0.064\,d^{-1}$). Taking into account our frequency resolution[6] of $0.021\,d^{-1}$, the two frequencies are indistinguishable. This suggests that the highest peak seen in the periodogram of the HARPS RVs is the stellar reflex motion induced by the outer transiting planet TOI-776 c. The second highest peak is found at $0.129\,d^{-1}$ (Fig. 7, upper panel), which is close to the orbital frequency of TOI-776 b. However, this signal is an alias of the signal at $0.055\,d^{-1}$. The periodogram of the window function indeed shows a peak at $0.074\,d^{-1}$ (highlighted with an arrow in the bottom panel of Fig. 7), which is equal to the frequency spacing between the two highest peaks seen in the periodogram of the HARPS RVs.

We used the code `pyaneti` (Barragán et al. 2019, see also Sect. 5.2.3) to subtract the Doppler signal of TOI-776 c from the HARPS RVs. We assumed a circular model (see also Sect. 5.2.2), fixing period and time of first transit to the TESS ephemeris, while allowing for the systemic velocity and RV semi-amplitude to vary. The periodogram of the RV residuals shows a broad peak centered around $\sim 0.04\,d^{-1}$ with a FAP of about 10%. Although the Doppler signal is not significant, the GLS periodograms of the CRX, dLW, Hα, and S-index activity indicators show also peaks at $\sim 0.04\,d^{-1}$, suggesting that this signal is caused by the presence of active regions appearing and disappearing from the visible stellar disk as the star rotates around its axis. It is worth noting that the peak at $0.130\,d^{-1}$ is not observed in the GLS periodogram of the RV residuals, corroborating the interpretation that this peak is an alias of the dominant frequency detected in the periodogram of the HARPS data.

We removed the Doppler reflex motion of TOI-776 c and the activity-induced RV signal by jointly modeling the HARPS measurements with a circular Keplerian orbit and a sine curve. For TOI-776 c, we followed the same procedure described in the previous paragraph. For the stellar signal, we fit for the phase, amplitude, and frequency. The latter was allowed to vary within a wide uniform prior centered around $0.04\,d^{-1}$. The GLS

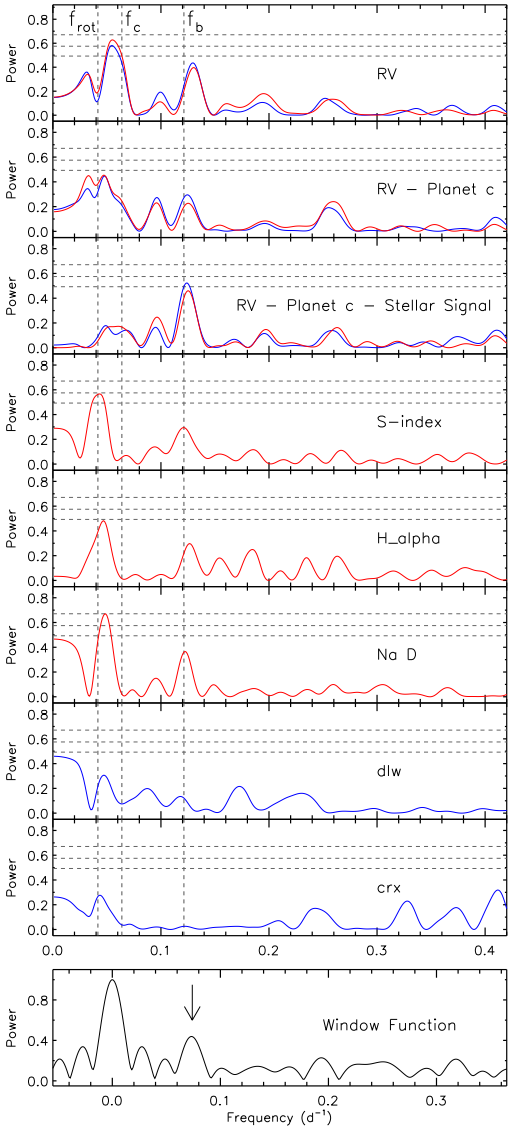

Fig. 7. Generalized Lomb-Scargle periodograms of the HARPS RVs and spectral activity indicators from `serval` (blue) and `TERRA` (red). The horizontal dashed lines mark, from bottom to top, the 5, 1, and 0.1% FAP levels, respectively. The vertical dashed lines mark the orbital frequencies of the two transiting planets ($f_b = 0.121\,d^{-1}$ and $f_c = 0.064\,d^{-1}$) and of the stellar signal at $\sim 0.03\,d^{-1}$. *Upper panel*: HARPS RVs. *Second panel*: RV residuals following the subtraction of the signal of TOI-776 c. *Third panel*: RV residuals following the subtraction of the reflex motion of TOI-776 c and of the activity-induced stellar signal. *Fourth panel*: S-index. *Fifth panel*: Hα line. *Sixth panel*: Na D lines. *Seventh panel*: differential line width (dLW). *Eighth panel*: chromatic index (CRX). *Bottom panel*: window function. The arrow in the bottom panel indicates the peak at $0.07\,d^{-1}$ referred to in the discussion of Sect. 5.1.

[5] Following the bootstrap method described, for example, in Murdoch et al. (1993) and Hatzes (2016), we estimated the FAP by computing the GLS periodogram of 10^6 time series obtained by randomly shuffling the measurements and their uncertainties, while keeping the time stamps fixed.

[6] The frequency resolution is defined as the inverse of the time baseline. The baseline of our HARPS observations is about 47 days, corresponding to a frequency resolution of about $1/47 = 0.021\,d^{-1}$.

periodogram of the RV residuals displays a peak at $0.125\,\mathrm{d}^{-1}$ (FAP $\approx 11\%$), which is very close to the frequency of the inner transiting planet TOI-776 b ($f_\mathrm{b} = 0.121\,\mathrm{d}^{-1}$). We note that the activity indicators also show peaks close to the orbital frequency of TOI-776 b. Yet, those peaks are separated by $0.074\,\mathrm{d}^{-1}$ from the stellar signal at $\sim 0.04\,\mathrm{d}^{-1}$. As such they are very likely aliases of the latter.

5.2. Modeling results

In this section, we describe our use of `juliet` (Espinoza et al. 2019) to model the photometric and Doppler data, both separately and jointly. The algorithm is built on several publicly available tools that model transits (`batman`, Kreidberg 2015), RVs (`radvel`, Fulton et al. 2018), and GPs (`george`, Ambikasaran et al. 2015; `celerite`, Foreman-Mackey et al. 2017).

5.2.1. Photometry

First, to constrain the properties of the transiting planets and use them for further analyses, we modeled the TESS, LCO, and MEarth photometry with `juliet`. We adopted a quadratic limb darkening law for TESS, since Espinoza & Jordán (2015) showed it was equally appropriate for space-based missions. The limb darkening parameters were then parameterized with a uniform sampling prior (q_1, q_2), introduced by Kipping (2013). For LCO and MEarth transits, we used a more simple linear limb darkening law, because the lower data precision with respect to TESS prevents us from adopting a more complex law. Additionally, we followed the parameterization introduced in Espinoza (2018). In particular, for each transiting planet, rather than fitting for the planet-to-star radius ratio $p = R_\mathrm{p}/R_*$ and the impact parameter of the orbit b, we sampled from the uniform priors assigned to two parameters, r_1 and r_2, which are connected to p and b with Eqs. (1)–(4) in Espinoza (2018). r_1 and r_2 were shown in Espinoza (2018) to guarantee a full exploration of the physically plausible values in the (p, b) plane. We also assumed circular orbits and fixed the TESS dilution factor to 1, based on our analysis from Sect. 3.3. Finally, we added a jitter term σ in quadrature to the TESS, LCO, and MEarth photometric uncertainties. The details of the priors and the description for each parameter are presented in Table A.1.

To account for the time-correlated noise in the light curve in Fig. 2, even using the PDC-corrected SAP, we modeled the TESS photometry with the exponential GP kernel

$$k_{i,j} = \sigma^2_\mathrm{GP,TESS} \exp\left(-|t_i - t_j|/T_\mathrm{GP,TESS}\right),$$

where $T_\mathrm{GP,TESS}$ is a characteristic timescale, and $\sigma_\mathrm{GP,TESS}$ is the amplitude of this GP modulation. For the LCO photometry, on the other hand, we used a linear model to detrend the data from airmass correlations.

Our photometry-only analysis significantly increases the precision of the planet parameters with respect to the TESS DVR. The uncertainties in the period decreases by two orders of magnitudes, which eases up future ground- and space-based follow-up efforts. The radii of the planets are determined to a precision better than 5%. Finally, we searched for an additional planet in the system by modeling a three-planet fit with the same priors as in Table A.1 for the transiting planets, and by varying the period and mid-transit time of the third hypothetical planet. Our result notably excludes the presence of any additional transits in the light curve ($\Delta \ln Z = \ln Z_\mathrm{2pl} - \ln Z_\mathrm{3pl} > 7$).

Table 3. Model comparison of RV-only fits with `juliet`.

Model	Prior P_planet	GP	$\ln Z_\mathrm{serval}$	$\ln Z_\mathrm{TERRA}$
0pl	...	...	−84.3	−85.4
2pl	$\mathcal{N}_\mathrm{b}(8.24, 0.05^2)$ $\mathcal{N}_\mathrm{c}(15.65, 0.05^2)$	...	−81.3	−81.8
2pl+GP1	$\mathcal{N}_\mathrm{b}(8.24, 0.05^2)$ $\mathcal{N}_\mathrm{c}(15.65, 0.05^2)$	EXP [(a)]	−80.7	−81.7
2pl+GP2	$\mathcal{N}_\mathrm{b}(8.24, 0.05^2)$ $\mathcal{N}_\mathrm{c}(15.65, 0.05^2)$	ESS [(b)]	−80.6	−81.8
2pl+sinusoid	$\mathcal{N}_\mathrm{b}(8.24, 0.05^2)$ $\mathcal{N}_\mathrm{c}(15.65, 0.05^2)$ $\mathcal{N}_\mathrm{d}(35.0, 10.0^2)$	...	**−78.9**	−79.4

Notes. The prior label $\mathcal{N}$ represents a normal distribution. The final model used for the joint fit is marked in boldface (see Sect. 5.2.2 for details about the selection of the final model). [(a)]Simple exponential kernel (EXP) of the form $k_{i,j} = \sigma^2_\mathrm{GP,RV} \exp\left(-|t_i - t_j|/T_\mathrm{GP,RV}\right)$. [(b)]Exponential-sine-squared kernel (ESS) of the form $k_{i,j} = \sigma^2_\mathrm{GP,RV} \exp\left(-\alpha_\mathrm{GP,RV}(t_i - t_j)^2 - \Gamma_\mathrm{GP,RV} \sin^2\left[\frac{\pi|t_i - t_j|}{P_\mathrm{rot;GP,RV}}\right]\right)$ with a uniform prior in $P_\mathrm{rot;GP,RV}$ ranging from 5 to 50 d.

5.2.2. RV

Even though the results of the RV's extraction slightly change depending on whether we used `serval` or `TERRA`, the GLS analyses in both cases show evidence of a stellar signal together with the RV trends associated with the transiting planets. To adequately describe the data, we considered several RV-only models and carried out a model comparison scheme as in Luque et al. (2019). We used `juliet`, a code that efficiently computes the Bayesian log-evidence of each tested model and explores the parameter space using the importance nested sampling included in MultiNest (Feroz et al. 2009) via the `PyMultiNest` package (Buchner et al. 2014). As discussed in Nelson et al. (2020), this method outperforms other samplers in robustly choosing the best model for those with three or fewer planets. We considered a model to be moderately favored over another if the difference in its Bayesian log-evidence $\Delta \ln Z$ is greater than two, while it is strongly favored if it is greater than five (Trotta 2008). If $\Delta \ln Z \lesssim 2$, then the models are indistinguishable. In this case, the model with fewer degrees of freedom would be chosen.

Due to the sampling and the scarce number of RV measurements, if we model the eccentricity with a wide, uninformative prior, we derive nonphysically high eccentricities for both planets that would make the system unstable in fewer than one hundred orbits. The eccentricity of systems with multiple transiting planets is low but not necessarily zero (Van Eylen & Albrecht 2015; Xie et al. 2016; Hadden & Lithwick 2017). Therefore, instead of assuming circular orbits, we placed a prior on the orbital eccentricity of a beta distribution with $\alpha = 1.52$ and $\beta = 29$ following Van Eylen et al. (2019). Table 3 summarizes the results of our analysis on both `serval`- or `TERRA`-extracted RVs. As seen in Table 3, including the two transiting planets in the model is favored over the fiducial model (0pl). On the other hand, we tested different types of two-planet models. First, we considered just the two transiting planets (2pl), without accounting for additional noise sources. Then, we accounted for the stellar noise, modeling it in three different ways: with an exponential GP kernel (2pl+GP1), with an exponential sine-squared

GP kernel (2pl+GP2) and with a simple sinusoid (2pl+sinusoid). All the tested two-planet models are statistically indistinguishable, with their Bayesian log-evidences within $\Delta \ln Z < 2$.

However, for both `serval` and `TERRA`-extracted RVs, the nominal best model accounts for two circular orbits and an additional sinusoidal curve, whose period is equal to the stellar period of rotation we estimated through the long-term ground-based photometric data. For this test, we imposed a normal prior on $P_{\rm rot}$, with a wide standard deviation (10). We additionally tried wide, uninformative priors for the period of the sinusoidal signal, and we retrieved the same posterior distributions and log evidence (Fig. 6) as for the test with a Gaussian prior. With the RV analysis, we estimated a stellar period of rotation $P_{\rm rot} = 34.4^{+1.4}_{-2.0}$ d, consistent with the rotational period estimated from the ground-based long-term photometry in Sect. 4.2. Additionally, all models presented in Table 3 derive the same RV semi-amplitude for TOI-776 b and TOI-776 c, well within their 1σ uncertainties. This proves the robustness of the mass determination for the transiting planets, independently of the stellar noise distribution.

Leveraging the prior information on the stellar rotation from photometry discussed in Sect. 4.2 with the presence of a significant periodicity in the RV residuals of a two-planet model (Fig. 7b), we decided to choose the 2pl+sinusoid as our final model for the joint fit. With respect to the RV extraction, we preferred to use the `serval` extracted RVs in the final joint fit due to their nominal highest log-evidence and lower jitter compared to `TERRA`.

5.2.3. Joint fit

We performed a joint fit using `juliet` of the TESS, LCO, and MEarth photometry and HARPS `serval` extracted RVs, using the 2pl+sinusoid model we selected after the RV-only analysis in Sect. 5.2.2. Tables A.1 and 4 show the priors and posteriors of all the fit parameters, respectively. Figure C.1 shows a corner plot of the orbital parameters of planets b and c. The data, residuals, and joint fit of the preferred model are shown in Figs. 3 and 8 for the photometry and the RVs, respectively. Table 5 lists the transit and physical parameters derived using the stellar parameters in Table 2.

As a sanity check, we performed an independent joint analysis of the transit photometry and Doppler measurements using the `pyaneti` code (Barragán et al. 2019), which estimates the parameters of planetary systems in a Bayesian framework, combined with an MCMC sampling. We imposed uniform priors for all the fit parameters. Following Winn (2010), we sampled for the mean stellar density $\rho_\star$ and recovered the scaled semi-major axis ($R_{\rm p}/R_\star$) for each planet using Kepler's third law. We found that the modeling of the transit light curves provides a mean stellar density of $\rho_\star = 5203^{+1782}_{-1228}$ kg m^{-3}, which agrees with the density of 4834^{+651}_{-559} kg m^{-3} derived from the stellar mass and radius presented in Sect. 4. As for the remaining parameters, the analysis provides parameter estimates consistent with those derived with `juliet`, thus corroborating our results.

6. Results and discussion

The TOI-776 system consists of two transiting planets. The inner planet, TOI-776 b, has a period of 8.25 d, a radius of $1.85 \pm 0.13\,R_\oplus$, a mass of $4.0 \pm 0.9\,M_\oplus$, and a bulk density of $3.4^{+1.1}_{-0.9}$ g cm^{-3}. The outer planet, TOI-776 c, has a period of 15.66 d, a radius of $2.02 \pm 0.14\,R_\oplus$, a mass of $5.3 \pm 1.8\,M_\oplus$, and a

Table 4. Median and 68% credibility intervals of the posterior distributions for each fit parameter of the final joint model obtained for the TOI-776 system using `juliet`.

Parameter	TOI-776 b	TOI-776 c
Stellar parameters		
$\rho_\star$ (kg m^{-3})	6024^{+650}_{-640}	
Planet parameters		
P (d)	$8.24661^{+0.00005}_{-0.00004}$	$15.6653^{+0.0004}_{-0.0003}$
t_0 [(a)]	$8571.4167^{+0.0010}_{-0.0011}$	$8572.5999^{+0.0018}_{-0.0016}$
r_1	$0.43^{+0.10}_{-0.07}$	$0.51^{+0.08}_{-0.07}$
r_2	$0.0316^{+0.0008}_{-0.0011}$	$0.03437^{+0.0009}_{-0.0008}$
e [(b)]	$0.06^{+0.03}_{-0.02}$ (<0.18)	$0.04^{+0.02}_{-0.01}$ (<0.18)
ω	-67^{+117}_{-73}	-11^{+55}_{-79}
K (m s^{-1})	$1.88^{+0.40}_{-0.44}$	$2.05^{+0.67}_{-0.68}$
Photometry parameters		
$\sigma_{\rm TESS}$ (ppm)	$1.1^{+8.0}_{-1.0}$	
$q_{1,\rm TESS}$	$0.26^{+0.29}_{-0.17}$	
$q_{2,\rm TESS}$	$0.36^{+0.21}_{-0.20}$	
$\sigma_{\rm LCO\text{-}CTIO}$ (ppm)	1000^{+36}_{-34}	
$M_{\rm LCO\text{-}CTIO}$ (ppm)	890^{+395}_{-468}	
$\theta_{\rm LCO\text{-}CTIO}$	$0.0011^{+0.0003}_{-0.0004}$	
$q_{1,\rm LCO\text{-}CTIO}$	$0.76^{+0.13}_{-0.14}$	
$\sigma_{\rm LCO\text{-}SAAO}$ (ppm)	471^{+60}_{-60}	
$M_{\rm LCO\text{-}SAAO}$ (ppm)	-810^{+250}_{-260}	
$\theta_{\rm LCO\text{-}SAAO}$	-0.0004 ± 0.0002	
$q_{1,\rm LCO\text{-}SAAO}$	$0.73^{+0.14}_{-0.15}$	
$\sigma_{\rm LCO\text{-}SSO}$ (ppm)	885^{+45}_{-40}	
$M_{\rm LCO\text{-}SSO}$ (ppm)	-4057^{+386}_{-413}	
$\theta_{\rm LCO\text{-}SSO}$	-0.0031 ± 0.0003	
$q_{1,\rm LCO\text{-}SSO}$	$0.46^{+0.16}_{-0.18}$	
$\sigma_{\rm MEarth}$ (ppm)	1734^{+52}_{-47}	
$M_{\rm MEarth}$ (ppm)	-2^{+47}_{-44}	
$q_{1,\rm MEarth}$	$0.73^{+0.13}_{-0.14}$	
RV parameters		
$\mu_{\rm HARPS}$ (m s^{-1})	$4.33^{+0.51}_{-0.58}$	
$\sigma_{\rm HARPS}$ (m s^{-1})	$1.66^{+0.35}_{-0.30}$	
GP hyperparameters and additional sinusoid		
$\sigma_{\rm GP,TESS}$ (ppm)	$0.17^{+0.06}_{-0.04}$	
$T_{\rm GP,TESS}$ (d)	$0.56^{+0.19}_{-0.15}$	
K (m s^{-1})	$2.71^{+0.53}_{-0.60}$	
t_0 [(b)]	$8607.0^{+11.6}_{-12.1}$	
P (d)	$34.4^{+1.4}_{-2.0}$	

Notes. Priors and descriptions for each parameter can be found in Table A.1. [(a)]Units are BJD – 2 450 000. [(b)]3σ upper limit in parenthesis.

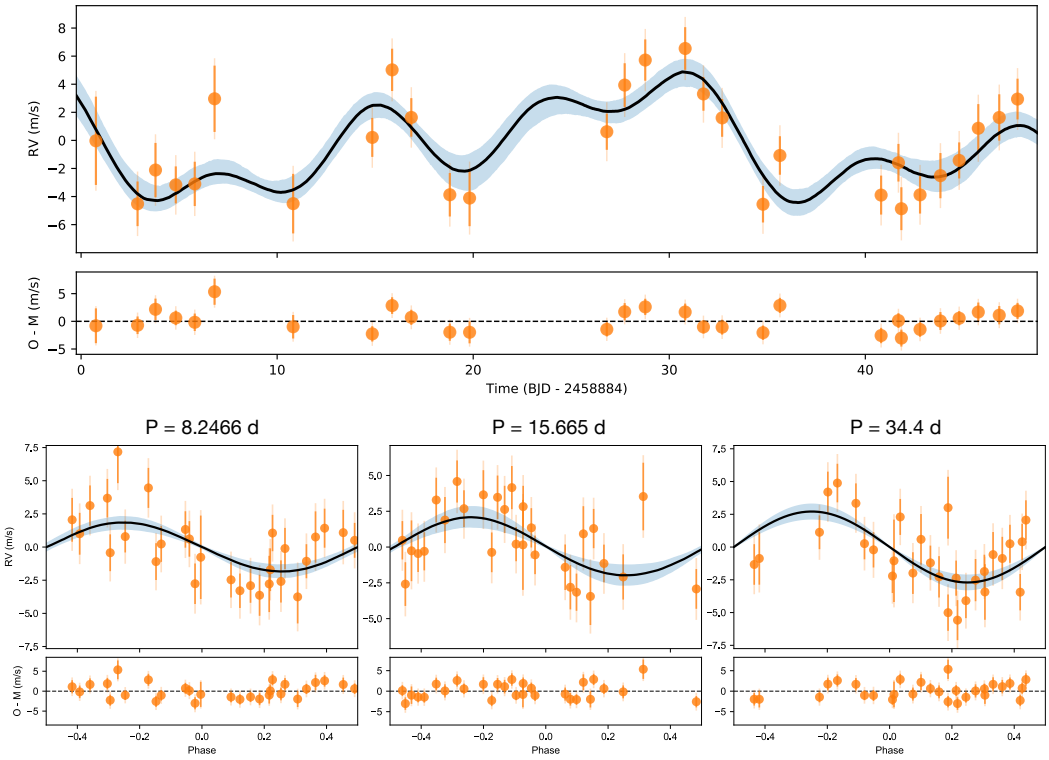

Fig. 8. *Top panel*: time series of the HARPS `serval` RVs and the best model discussed in Sect. 5.2.2 and the residuals from the fit below. The blue shaded area corresponds to the 1σ confidence interval of the model. *Bottom panel*: RVs phase-folded to the period (shown above each panel) of the two confirmed planets (TOI-776 b, *left*; TOI-776 c, *center*) and the additional sinusoid associated with the stellar variability. In both panels, the error bars of the RV data have the extra jitter term added in quadrature and plotted in a lighter orange for visualization.

bulk density of $3.5^{+1.4}_{-1.3}$ g cm^{-3}. The RV data show only one additional signal, with a semi-amplitude of ∼2.7 m s^{-1} and a period of 34 d, associated with the stellar rotation, as suggested by our analyses of the photometry and spectral line indicators.

6.1. System architecture

While the occurrence rate of planets around early M dwarfs (3500 K < $T_{\rm eff}$ < 4000 K) has been investigated in detail with *Kepler* and *K2* samples (see e.g., Dressing & Charbonneau 2013, 2015; Montet et al. 2015; Hirano et al. 2018), the number of currently known planets transiting low-mass stars is still much smaller with respect to those discovered around solar-type stars. While none of these surveys were optimized for M dwarfs, we expect more statistically significant results from the TESS mission for these stars. Figure 9 shows the confirmed transiting planets around M dwarfs as a function of the orbital period and the effective temperature of the host star. However, very few of these systems have precise determinations of the planetary masses (i.e., densities), eccentricities, and orbital architectures that would be required to link the statistical properties of this population with planet formation and evolution models in the low stellar mass regime.

There are several validated transiting multi-planetary systems orbiting early M dwarfs similar to TOI-776 in terms of planetary architecture. Kepler-225, Kepler-236, and Kepler-231 are two-planet transiting systems composed of super-Earth- and/or mini-Neptune-sized companions with similar periods and semi-major axes, all validated by Rowe et al. (2014). However, these systems are on average 5 mag fainter than TOI-776 and the planets do not have a mass determination nor precise stellar parameters. Similarly, K2-240 (Díez Alonso et al. 2018) has two transiting super-Earths with periods of 6 and 20.5 d, although they do not have mass determination, and they orbit an active star that is 2 mag fainter with a clear photometric rotational period of 10.8 d. The two outermost planets of the four-planet system, K2-133, have periods and sizes similar to TOI-776 b and c, but the star is at the faint end for RV follow-up and does not exhibit transit timing variations (TTVs).

If compared to systems with mass determination, TOI-776 shows some similarities with Kepler-26 (Steffen et al. 2012), Kepler-138 (Rowe et al. 2014), TOI-1266 (Demory et al. 2020), and K2-3 (Montet et al. 2015; Crossfield et al. 2015). Kepler-26 b and c have periods of 12.3 and 17.2 d, respectively, and bulk densities compatible with those of sub-Neptunes determined from TTVs. However, the system has two more planets without mass

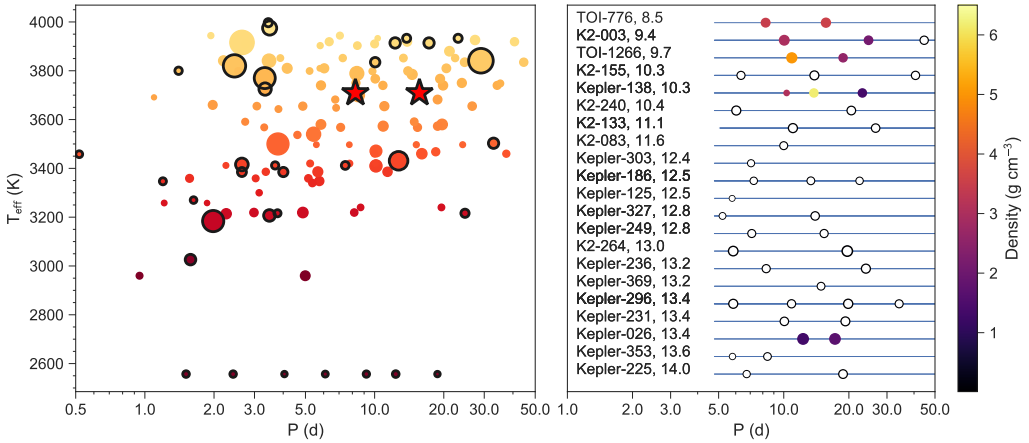

Fig. 9. *Left*: confirmed transiting planets from the TEPCat database (Southworth 2011) around M dwarfs as a function of period. Black circled points indicate planets with a mass determination better than 30%. Circles are color-coded by the host effective temperature, and their sizes are proportional to the planet radius. The red stars mark the two planets in the TOI-776 system. *Right*: transiting multi-planetary systems around early-type M dwarfs (3500 K < $T_{\rm eff}$ < 4000 K) with similar architectures to the TOI-776 system. Sizes are proportional to the planet radius, and colors indicate their bulk densities. Planets with no mass determination are marked in white. The brightness of the host star in the *J* band is indicated next to the system's name.

Table 5. Derived planetary parameters obtained for the TOI-776 system using the posterior values from Table 4 and stellar parameters from Table 2.

Parameter[a]	TOI-776 b	TOI-776 c
Derived transit parameters		
$p = R_{\rm p}/R_\star$	$0.0316^{+0.0008}_{-0.0011}$	$0.0344^{+0.0009}_{-0.0008}$
$b = (a/R_\star)\cos i_{\rm p}$	$0.25^{+0.10}_{-0.14}$	$0.27^{+0.12}_{-0.11}$
$a/R_\star$	$27.87^{+0.97}_{-1.02}$	$42.75^{+1.49}_{-1.57}$
$i_{\rm p}$ (deg)	$89.65^{+0.22}_{-0.37}$	$89.51^{+0.25}_{-0.21}$
$t_{\rm T}$ (h)	$2.41^{+0.11}_{-0.10}$	$2.99^{+0.16}_{-0.13}$
Derived physical parameters		
$M_{\rm p}$ ($M_\oplus$)	4.0 ± 0.9	5.3 ± 1.8
$R_{\rm p}$ ($R_\oplus$)	1.85 ± 0.13	2.02 ± 0.14
$\rho_{\rm p}$ (g cm^{-3})	$3.4^{+1.1}_{-0.9}$	$3.5^{+1.4}_{-1.3}$
$g_{\rm p}$ (m s^{-2})	$11.2^{+3.1}_{-2.8}$	$12.8^{+4.9}_{-4.4}$
$a_{\rm p}$ (au)	0.0652 ± 0.0015	0.1000 ± 0.0024
$T_{\rm eq}$ (K)[b]	514 ± 17	415 ± 14
S ($S_\oplus$)	11.5 ± 0.6	4.9 ± 0.2

Notes. [a]Error bars denote the 68% posterior credibility intervals. [b]Equilibrium temperatures were calculated assuming zero Bond albedo and uniform surface temperatures across the entire planet.

determination: an inner Earth-sized planet and an outer mini-Neptune-sized planet. Kepler-138 is a very interesting system of three small planets, whose densities were estimated through photodynamical modeling (Almenara et al. 2018). The most similar to the TOI-776 planets in terms of orbital period, Kepler-138 b (10.3 d) and c (13.8 d), are very different in composition, the former being a Mars analog and the latter a prototypical rocky super-Earth. The third, outermost planet seems to have retained a substantial volatile-rich envelope. TOI-1266 is the system that resembles TOI-776 the most. The two planets of the system have tentative dynamical masses determined from TTVs, although RVs are likely to become available in the future. The planets straddle the radius valley and, interestingly, the innermost one is larger and more massive than the outer one. K2-3, the brightest of all four systems, has three small transiting planets and only the two inner ones (with periods of 10 and 24.6 d) have a mass determination using HARPS-N, HARPS, HIRES and PFS RVs (Almenara et al. 2015; Damasso et al. 2018; Kosiarek et al. 2019), only an upper limit is measured for the third (with a period of 44.5 d). The planets have similar compositions, compatible with those of water worlds or water-poor planets with gaseous envelopes; however, the poor bulk density estimations of planets c and d impede further conclusions. The right panel of Fig. 9 shows all of the aforementioned systems, color-coded by bulk density and with the *J*-band magnitude of their host stars indicated.

Therefore, we conclude that, although multi-planetary systems of super-Earths and/or sub-Neptunes are common around early-type M dwarfs, only TOI-776 has all of its planets well characterized, bulk density uncertainties better than 30%, precise stellar parameters, and a host star bright enough for atmospheric follow-up observations with current and planned facilities.

6.2. Dynamics and TTV analysis

We investigated possible TTVs through a three-body simulation using the Python Tool for Transit Variations (`PyTTV`; Korth 2020). We simulated the estimated TTVs and RVs using the stellar and planetary parameters reported in Tables 2, 4, and 5 and found an expected TTV signal with a period of ~ 150 d and a maximum amplitude of ~2 min for the inner planet. Thus, the

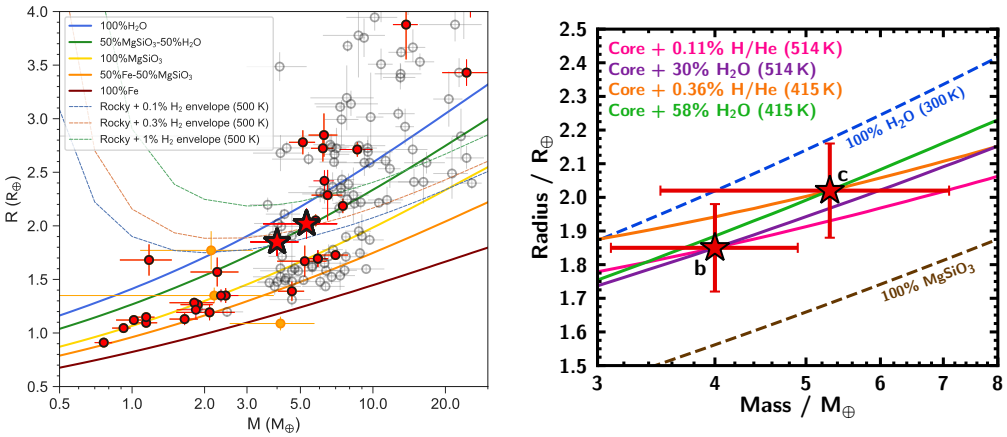

Fig. 10. Mass-radius diagrams in Earth units. In the *left panel*, open circles are transiting planets around F-, G-, and K-type stars with mass and radius measurements better than 30% from the TEPCat database of well-characterized planets (Southworth 2011); red circles are planets around M dwarfs with mass and radius measurements; orange filled circles are planets around M dwarfs with mass determinations worse than 30%; and the red stars are TOI-776 b and c, which have masses determined with accuracies of 23 and 34%, respectively. In the *left panel*, the color lines are the theoretical *R-M* models of Zeng et al. (2016, 2019). In the *right panel*, the solid pink and purple lines show the models from Sect. 6.3 that are consistent with the mass and radius of TOI-776 b, and the orange and green lines show compositions consistent with the mass and radius of TOI-776 c, assuming an Earth-like core (1/3 iron, 2/3 silicates).

time span of the photometric observations, their cadence, and signal-to-noise would prevent the detection of TTVs with the currently available data.

Additionally, we carried out a set of dynamical simulations to study the long-term stability of the system. We used the parameters in Tables 4 and 5 and randomly drew 1000 samples from the posterior distributions as initial parameters for the dynamical simulations. We integrated each parameter set for 10^6 orbits of the inner planet using the `REBOUND` (Rein & Liu 2012) tool with the standard IAS15 integrator (Rein & Spiegel 2015). We also explored the stability using the MEGNO criteria as implemented in `REBOUND`. In the cases of close encounters between the bodies or a one-body ejection, the system would be flagged as unstable for the specific set of parameters. We found that the system is dynamically stable over the entire integration time and for the whole parameter posterior space.

6.3. Planetary composition and interior structure

Figure 10 shows the location of the TOI-776 system in a mass-radius diagram. Both planets occupy a scarcely populated region, characterized by a lack of planets around M dwarfs and with precise bulk density measurements. A comparison with the theoretical models by Zeng et al. (2016), reported in the left panel of Fig. 10, shows that TOI-776 b and c are consistent with mixtures of silicates and water in a 50–50 proportion. We adopted the three-layer models from Zeng & Sasselov (2013) and Zeng et al. (2016) to infer the interior structure of the planets. However, given the mass and radius input, the solution of the model is degenerate. As a consequence, the same mass-radius pair can lead to a broad range of combinations of iron, silicate, and water-mass fractions. On the other hand, when we applied the latest models by Zeng et al. (2019), assuming a 1 mbar surface pressure level and an equilibrium temperature of 500 K (from Table 5), we found that an Earth-like rocky core with a 0.1 and 0.3% molecular hydrogen atmosphere is consistent with the bulk densities of TOI-776 b and c, respectively. Nonetheless, it is clear that both of the planets in the system have an internal composition ranging from water worlds to rocky planets that have retained a significant atmosphere.

For a better understanding of the nature of the two exoplanets, we performed a more detailed modeling of their interior compositions, using their masses, radii, and surface temperatures. Our model considers a canonical four-layer structure consisting of a two-component iron and silicate core, a layer of H_2O, and a H/He envelope. We assume that the core is Earth-like in composition (1/3 iron, 2/3 silicates by mass), meaning the core, water, and H/He envelope mass fractions ($x_{\rm core}$, $x_{\rm H_2O}$, $x_{\rm H/He}$) are free parameters that sum to unity. The model solves the planetary structure equations of mass continuity and hydrostatic equilibrium assuming spherical symmetry. Further detail regarding the internal structure model can be found in Madhusudhan et al. (2020) and Nixon & Madhusudhan (2020).

The equation of state (EOS) prescriptions for the iron and silicate layers are adopted from Seager et al. (2007), who used a Vinet EOS of the ϵ phase of Fe (Vinet et al. 1989; Anderson et al. 2001) and a Birch-Murnaghan EOS of $MgSiO_3$ perovskite (Birch 1952; Karki et al. 2000). Thermal effects in these layers are ignored, since they have a small effect on the planetary radius (Howe et al. 2014). However, thermal effects in the outer envelope can alter the mass-radius relation significantly (Thomas & Madhusudhan 2016). For this reason, the model uses a temperature-dependent EOS for the outer H_2O and H/He layers. For H_2O, we used a patchwork EOS in order to cover all possible phases of H_2O that might be present in the interior, compiled from Salpeter & Zapolsky (1967); Fei et al. (1993); Wagner & Pruß (2002); Feistel & Wagner (2006); Seager et al. (2007); French et al. (2009); Klotz et al. (2017), and Journaux et al. (2020). For H/He, we used the EOS in Chabrier et al. (2019), which assumes a solar helium fraction ($Y = 0.275$). The

temperature profile in the envelope is isothermal from the surface down to some radiative-convective boundary, where it becomes adiabatic. The pressure at the radiative-convective boundary $P_{\rm rc}$ is a free parameter in the model. For this study, we considered values of $P_{\rm rc}$ ranging from 1–100 bar.

We explored the parameter space of possible compositions in ($x_{\rm core}$, $x_{\rm H_2O}$, $x_{\rm H/He}$) space. For each composition, we considered a range of masses that agree with the observed mass of the planet to within 1σ. For a given mass $\hat{M}$, the model radius $\hat{R}$ is computed, and the χ^2 statistic is calculated:

$$\chi^2 = \frac{(M_{\rm p} - \hat{M})^2}{\sigma_M^2} + \frac{(R_{\rm p} - \hat{R})^2}{\sigma_R^2}, \quad (1)$$

where (σ_M, σ_R) are the observed uncertainties on the mass and radius of each planet.

The bulk densities of TOI-776 b and c ($3.4^{+1.1}_{-0.9}$ g cm^{-3} and $3.5^{+1.5}_{-1.3}$ g cm^{-3}, respectively) are too low for either planet to have a purely terrestrial (iron plus rock) composition. Therefore, the planets must possess an envelope with some amount of H_2O and/or H/He, in order to explain their masses and radii. The right panel of Fig. 10 shows limiting cases for each planet in which the envelope composition is either purely H_2O or purely H/He. The mass and radius of TOI-776 b can be explained to within 1σ ($\chi^2 \leq 1$) with a pure H_2O envelope of 12–73% by mass or a pure H/He envelope with a mass fraction of 1.1×10^{-4}–5.2×10^{-3}. Best-fit solutions (those which minimize χ^2) for pure envelopes are found at $x_{\rm H_2O} = 0.3$ and $x_{\rm H/He} = 1.1 \times 10^{-3}$. TOI-776 c might have larger envelopes; within 1σ, it is consistent with a pure H_2O layer of ≥18% or a pure H/He envelope with a mass fraction of 5.4×10^{-4}–1.2×10^{-2}. The best-fit pure-envelope solutions for TOI-776 c are $x_{\rm H_2O} = 0.58$ and $x_{\rm H/He} = 3.6 \times 10^{-3}$. Each of the best-fit models, shown in the right panel of Fig. 10, have a radiative-convective boundary at $P_{\rm rc} = 10$ bar.

It is also possible that the planets in this system have both H_2O and H/He components, as well as an iron/rock core. For the three components, we explored the full range of plausible values ($x_{\rm core}$, $x_{\rm H_2O}$, and $x_{\rm H/He}$) that could explain the interior compositions of each planet. We considered two different temperature profiles for each planet, with $P_{\rm rc} = 1$ and 100 bar. Figure 11 shows the mass fractions of water and H/He compatible to within 1σ ($\chi^2 \leq 1$) with the masses and radii of TOI-776 b and c. We obtained upper limits on the total H_2O and H/He mass fractions for TOI-776 b: $x_{\rm H_2O} \leq 73\%$ and $x_{\rm H/He} \leq 0.52\%$. These correspond to cases with pure H_2O or H/He envelopes, as previously discussed. For TOI-776 c, we find that $x_{\rm H/He} \leq 1.2\%$. A 100% H_2O planet would theoretically be consistent with the mass and radius of TOI-776 c, but this would be unrealistic from a planet formation perspective, as some rocky material is needed for further accretion of ice and gas (Lee & Chiang 2016). Figure 11 also shows a significant overlap between the best-fit shaded regions for the two planets, meaning that the planets could also share the same composition.

The masses and radii of TOI-776 b and c allow for a wide range of possible solutions, from water worlds with steam atmospheres to mostly rocky planets with hydrogen-rich envelopes; however, they are inconsistent with bare rocks without atmospheres. Our models assume a surface pressure of 0.1 bar, meaning a water-world solution for either planet yields a steam atmosphere. On the other hand, a higher surface pressure could result in liquid H_2O at the surface. A rocky planet with an outgassed secondary atmosphere which includes carbon compounds is unlikely: Elkins-Tanton & Seager (2008) placed an upper limit on the mass fraction for this type of atmosphere at 5%. The lower mass limits in the case of pure H_2O envelopes are 8 and 18% for TOI-776 b and c, respectively. On the other hand, in a carbon-rich atmosphere, the dominant species, CO_2, has a higher mean molecular weight than H_2O, leading to a lower atmospheric scale height. All things considered, we can infer that a 5% carbon-rich atmosphere is less than what would be needed to explain the planet radii. However, determining whether the two planets have H_2O- or H/He-rich atmospheres is impossible with the present data. Atmospheric observations of the planets would be required in order to break this degeneracy.

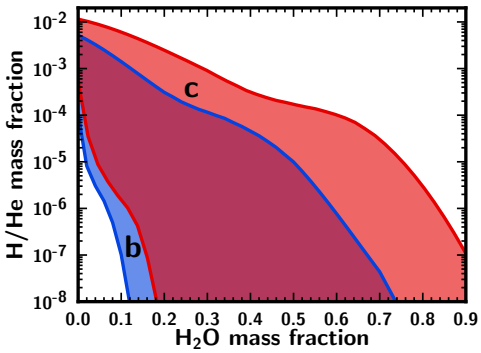

Fig. 11. H/He vs. H_2O mass fractions for the best-fit interior compositions (≤1σ) permitted by the masses and radii of TOI-776 b and c, assuming an Earth-like core, for two different pressure-temperature profiles with radiative-convective boundaries at 1 and 100 bar. The blue shaded region indicates possible compositions for TOI-776 b, and the red shaded region shows compositions for TOI-776 c. The darker red shaded area between the two corresponds to the range of possible compositions that could explain both planets. For TOI-776 b, the H_2O mass fraction is constrained to be ≤73% and the H/He mass fraction is ≤0.52%. For TOI-776 c the upper limit for H/He is 1.2%. A purely H_2O planet would be consistent with this mass and radius, but we only show H_2O mass fractions up to 90%.

6.4. Radius gap in M dwarfs

The occurrence rate distribution of close-in planets exhibits a paucity of planets from 1.7–2.0 $R_\oplus$ (Fulton et al. 2017; Fulton & Petigura 2018; Hardegree-Ullman et al. 2020) around FGK stars ($T_{\rm eff} > 4700$ K), and from 1.4–1.7 $R_\oplus$ (Hirano et al. 2018; Cloutier & Menou 2020) around mid-K to mid-M dwarfs ($T_{\rm eff} < 4700$ K). This feature is pointed out as the result of the transition from small rocky planets to larger non-rocky planets with envelopes rich in volatiles (Weiss & Marcy 2014; Dressing & Charbonneau 2015). Recent studies showed that the location of the radius gap depends on the orbital period, or, alternatively, on the planet's insolation (Van Eylen et al. 2018; Martinez et al. 2019; Cloutier & Menou 2020). Additionally, the width and center of the radius gap also depends on whether the host star is single or part of a multiple star system (Teske et al. 2018).

According to the above discussion, if we consider the radius axis in Fig. 10, TOI-776 b and c belong, within the uncertainties, to the radius gap in the case of FGK stars. On the other hand, they are well above the radius gap if we account for mid-K to mid-M dwarfs. Similarly, when looking at the distribution of transiting planets in a radius-insulation diagram (Fig. 12, left panel), the TOI-776 planets lie above the radius valley – the 2D view of

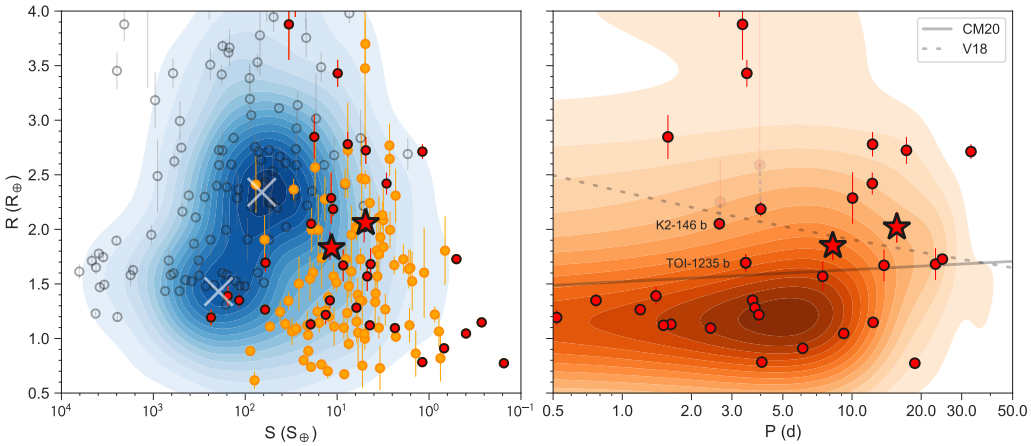

Fig. 12. Insolation-radius (*left*) and period-radius (*right*) diagrams in Earth units. In both panels, the different circles represent the same planets as in Fig. 10 from the TEPCat database (Southworth 2011). In the *left panel*, we plot in blue the *R-S* point density of all the known confirmed transiting planets with contours, and sub-Neptune and super-Earths' density maxima with white crosses. In the *right panel*, the orange contours represent the density of planets around M dwarfs with mass determinations worse than 30% or without mass constraints at all (orange circles in the *left panel*). The dashed line represents the location of the radius valley for F-, G-, and K-type stars from Van Eylen et al. (2018), consistent with the predictions from photoevaporation and core-powered mass-loss models, while the solid line represents the location of the radius valley for mid-K and mid-M dwarfs from Cloutier & Menou (2020), consistent with gas-poor formation scenarios. Together with TOI-776 b, the other two systems that are within both lines are K2-146 (solid, Hamann et al. 2019; Lam et al. 2020, translucent) and TOI-1235 (Bluhm et al. 2020; Cloutier et al. 2020).

the radius gap – that separates rocky super-Earths from gaseous sub-Neptunes around FGK stars.

The right panel of Fig. 12 shows the period-radius diagram of all known exoplanets with precise bulk density measurements that orbit M dwarfs. The dashed line marks the empirical location of the radius valley for FGK stars, following Van Eylen et al. (2018), while the solid line indicates the location of mid-K to mid-M dwarfs as in Cloutier & Menou (2020). The change in slope as a function of stellar type is the result of a change in the dominant mechanism responsible for sculpting the radius valley. For instance, the thermally driven mass loss, caused by photoevaporation or core-powered mechanisms, becomes less efficient toward low-mass stars. The measured slope for mid-K to mid-M dwarfs suggests that gas-poor formation (Lee et al. 2014; Lee & Chiang 2016; Lopez & Rice 2018) might be the main process by which small planets form. However, thousands of small planets around low-mass stars with precise radii are needed in order to robustly state if the radius valley is the result of the erosion or the gas-poor formation scenarios (Cloutier et al. 2020). Although enriching the sample of exoplanet systems orbiting M dwarfs is nowadays possible thanks to TESS and future space-based missions such as PLATO, an alternative is to obtain precise bulk density measurements of exoplanets lying in the region of discrepancy between models.

Planet TOI-776 b joins TOI-1235 b (Bluhm et al. 2020; Cloutier et al. 2020) and K2-146 b (Lam et al. 2020; Hamann et al. 2019) inside the period-radius region, where thermally driven mass-loss models disagree with the predictions from gas-poor formation. However, K2-146 b belongs to this region if we refer to the parameters reported in Hamann et al. (2019), because the radius estimated by Lam et al. (2020) (see translucent points in Fig. 12) is more than 2σ higher, causing the planet to be placed outside the radius valley. Our previous analyses show that both TOI-776 b and c are likely to have retained a significant atmosphere, with slightly different envelope mass fractions. This result, given their periods and radii, would be consistent with the predictions from gas-poor formation models.

On the other hand, the system's composition may be reconciled with thermally driven mass loss because the inner, most irradiated planet has a smaller envelope mass fraction compared to its outer companion. Unlike other known systems whose planets straddle both sides of the radius gap (e.g., Dumusque et al. 2014; Niraula et al. 2017; Nowak et al. 2020), TOI-776 is an interesting case where photo-evaporation could have stopped or become inefficient early in the planet's history. However, it is possible that the planets are currently undergoing mass loss under the core-powered mechanism, which erodes sub-Neptune planets into rocky super-Earths on Gyr timescales (Ginzburg et al. 2018), contrary to the few Myr timescale during which photoevaporation is effective (Sanz-Forcada et al. 2011). As reported in Table 2, the age of TOI-776 is between 2 and 10 Gyr. However, the current data precision and limited number of known planets in this specific regime hamper any further investigation in favor of one or the other mechanism of formation. New studies on the dependence of the radius valley with other stellar parameters such as the age or metallicity, together with a larger sample of well-characterized planets in or near the radius valley, will help to discern between them in a demographic sense (Hardegree-Ullman et al. 2020; Berger et al. 2020; Gupta & Schlichting 2020).

However, for the first time, we can compare planets that belong to this region of the parameter space where formation models make opposing predictions. TOI-1235 b has a rocky composition with a 90% confidence upper limit in the envelope mass fraction of 0.5%, thus incompatible with a gas-poor formation scenario. We reach the opposite conclusion for TOI-776 b

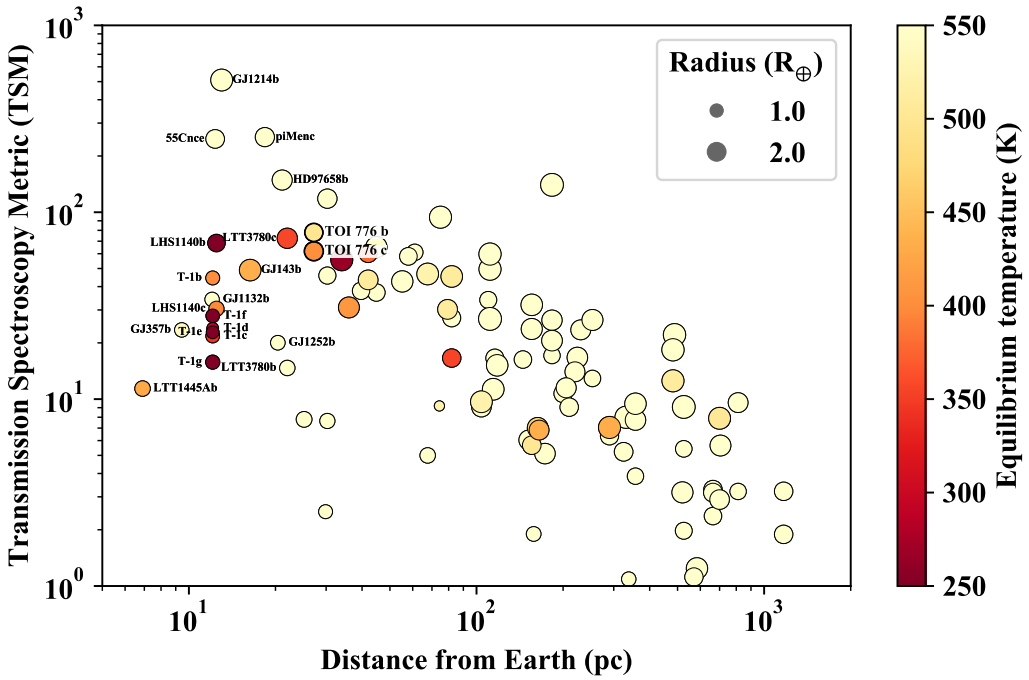

Fig. 13. Transmission spectroscopy metric (TSM) for exoplanets from the Exoplanet Encyclopedia with a radius below $3\,R_\oplus$ and a mass determination by RVs or TTVs. TOI-776 b and c are labeled and marked with thicker black borderlines.

and c, whose bulk densities imply the presence of a volatile envelope making them compatible with the predictions from gas-poor formation mechanisms, given their periods and radii. Therefore, although other stellar parameters might need to be taken into account, we can tentatively predict that the stellar mass below which thermally driven mass loss is no longer the main formation pathway for sculpting the radius valley is probably between 0.63 and 0.54 $M_\odot$, which corresponds to the host stellar masses of TOI-1235 and TOI-776, respectively. More planets in this interesting region of the parameter space with precise bulk density measurements are key to revealing the mechanisms responsible for the radius valley emergence around low-mass stars with respect to solar-like stars.

6.5. Atmospheric characterization

6.5.1. Transmission spectroscopy metric

We used the proposed metric by Kempton et al. (2018) to evaluate the suitability of the TOI-776 planets for atmospheric characterization studies. Figure 13 shows the transmission spectroscopy metric (TSM) for all exoplanets in the Exoplanet Encyclopedia[7] with a radius below $3\,R_\oplus$. We used the scale factors listed in Table 1 from Kempton et al. (2018) as opposed to the suggested value for temperate planets, 0.167, to compute the TSM values in Fig. 13. The estimated TSM of TOI-776 b and c are 77.9 and 61.8, respectively, which places them among the top priority targets for atmospheric follow-ups of small planets around nearby stars. This is not surprising, because TOI-776 is one of the brightest M dwarfs with known transiting planets. However, most of the planets shown in Fig. 13 are well below the radius gap, which makes the TOI-776 system a valuable target for atmospheric characterization in order to trace the formation and evolution of multi-planetary systems orbiting low-mass stars and break the degeneracy of internal composition models.

6.5.2. Synthetic spectra

In order to quantitatively assess the possibility of TOI-776 b and c's atmospheric characterization with the *James Webb* Space Telescope (JWST), we investigated a suite of atmospheric scenarios and calculated their JWST synthetic spectra using the photochemical model `ChemKM` (Molaverdikhani et al. 2019a) and petitRADTRANS (Mollière et al. 2019). We based the temperature structure of these planets on modern Earth's temperature structure, and we increased the surface temperature for it to be consistent with the equilibrium temperature of TOI-776 b and c (Kawashima & Rugheimer 2019). We followed a similar approach as in Luque et al. (2019): we estimated TOI-776's ($T_{\rm eff}$ = 3709 K) flux in the range between X-rays and optical wavelengths, using GJ 832's geometric mean spectra ($T_{\rm eff}$ = 3816 K) as a reference. The stellar data were obtained from the MUSCLES database (France et al. 2016). To set up the models, we used the chemical network of Hébrard et al. (2012) with 135 species and 788 reactions, and UV absorption

[7] `www.exoplanet.eu`

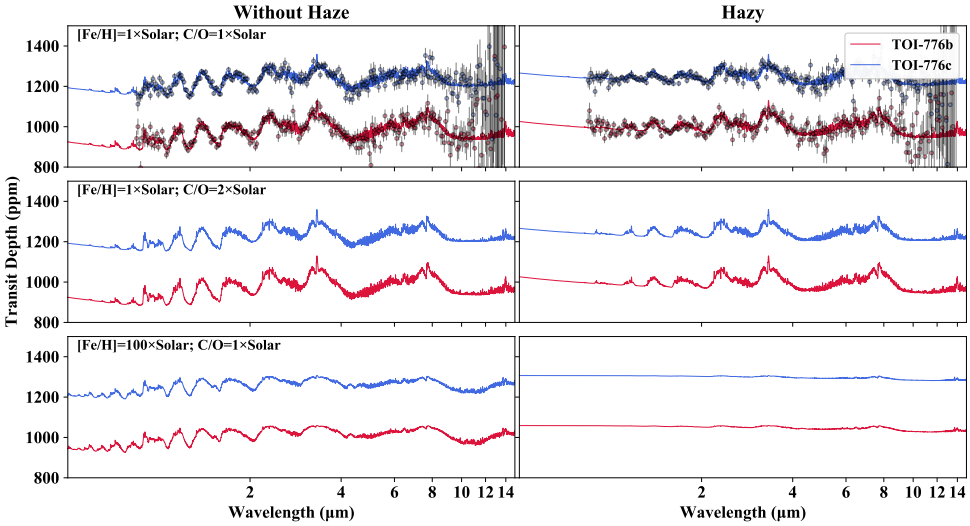

Fig. 14. Synthetic atmospheric spectra of TOI-776 b (red) and c (blue). *Top*: fiducial models with solar abundance (solid lines). Estimated uncertainties are shown for JWST NIRISS-SOSS, NIRSpec-G395M, and MIRI-LRS configurations, assuming two transits and binned for $R = 50$. *Middle*: enhanced carbon-to-oxygen ratio by a factor of two. *Bottom*: enhanced metallicity by a factor of 100. The left column represents spectra without haze opacity, and the right column with haze opacity.

cross-sections and branching yields from an updated version of Hébrard et al. (2012).

Figure 14 shows the synthetic transmission spectra of TOI-776 b and c assuming different metallicities, carbon-to-oxygen ratios, and haze opacities. For our fiducial model (top-left panel of Fig. 14), we assume solar abundances. Such spectra predominantly consist of water and methane features, as expected for this type of planet (Molaverdikhani et al. 2019b). The significance of these features are of the order of 100 ppm, well above the conservative JWST expected noise floor (20 ppm for NIRISS and 50 ppm for MIRI, Greene et al. 2016). We calculated the NIRISS-SOSS, NIRSpec-G395M, and MIRI-LRS uncertainties with PandExo (Batalha et al. 2017), assuming two transits and binned for $R = 50$, supporting the previous statement. In this scenario, the contribution from haze opacity partially obscures molecular features below 2 μm, but it is almost ineffective at longer wavelengths (see left and right upper panels of Fig. 14). We note, however, that the radiative feedback of haze particles might significantly affect the temperature structure and the composition of atmosphere (Molaverdikhani et al. 2020). We did not take this effect into account in this work in order to keep the temperature profiles consistent with the Earth's profile.

Smaller planets are expected to have enhanced metallicities (e.g. Wakeford et al. 2017). Therefore, we investigated two deviations from our solar abundance fiducial model: (1) an enhanced carbon-to-oxygen ratio (C/O) two-times the solar value; and (2) an enhanced metallicity one-hundred-times higher than solar. C/O enhancement alone does not affect the composition and spectral features substantially, as seen in the middle panels of Fig. 14. On the other hand, one might expect a higher metallicity to result in more pronounced spectral features, due to higher species abundances. However, the bottom panels of Fig. 14 discard this possibility. On the contrary, an enhanced metallicity causes a higher mean molecular weight, which in turn shrinks the spectral significance (bottom-left panel of Fig. 14), and, simultaneously, it results in a higher haze production, which also obscures the spectra significantly (bottom-right panel of Fig. 14). Therefore, a flat transmission spectrum may indicate a hazy atmosphere with a high metallicity (Kreidberg et al. 2014) as opposed to a nonexistent atmosphere (Kreidberg et al. 2019). Complementary observations, such as ground-based high-resolution spectroscopy or spectroscopy of the reflected light, are required to reveal the true nature of these flat spectra.

7. Summary

We present the discovery and characterization of the two-planet system transiting the bright ($V = 11.54$ mag, $J = 8.48$ mag) M1 V star TOI-776. Both planets were detected by the TESS mission, confirmed from ground-based transit follow-up observations and have had their dynamical masses determined with precise RV measurements using HARPS. In addition, fifteen years of ground-based photometric monitoring by ASAS-SN, ASAS, NSVS, Catalina, and SuperWASP helped us to measure a rotational period between 30 and 40 d, typical of inactive early-type M dwarfs. Our findings are summarized below:

– A joint fit of all the available transit photometry from TESS, MEarth, and LCOGT, and the precise RVs from HARPS reveal that the TOI-776 system consists of two transiting planets, namely TOI-776 b, which has a period of 8.25 d, a radius of $1.85 \pm 0.13\,R_\oplus$, a mass of $4.0 \pm 0.9\,M_\oplus$, bulk density of $3.4^{+1.1}_{-0.9}$ g cm^{-3}, and an equilibrium temperature of 514 ± 17 K; and TOI-776 c, which has a period of 15.66 d, a radius of $2.02 \pm 0.14\,R_\oplus$, a mass of $5.3 \pm 1.8\,M_\oplus$, a bulk density of $3.5^{+1.4}_{-1.3}$ g cm^{-3}, and an equilibrium temperature of 415 ± 14 K. The RV data show one additional signal, with a period of 34 d, associated with the star's rotation, in

agreement with our analyses of the photometry and spectral line indicators.
- The bulk densities of TOI-776 b and c allow for a wide range of possible interior compositions, from water worlds to rocky planets with H/He-rich atmospheres, but they are too low for either planet to have a purely terrestrial (iron plus rock) composition. Thus, an atmosphere is expected for both planets.
- From its location in a period-radius diagram, TOI-776 b lies in the transition region where formation and evolution models make different predictions for planetary systems orbiting M dwarfs. For the TOI-776 system, the planets lie above the radius valley carved by gas-poor formation mechanisms, in agreement with their bulk densities being incompatible with the absence of an atmosphere. Still, it is possible that the planets are still undergoing slow thermally driven mass loss under the core-powered scenario.

The TOI-776 system is an excellent target for the JWST. It is the only known multi-planetary system with planets inside and near the radius valley for which all planets: (1) have a bulk density determination with at least 30% relative uncertainties; and (2) are perfect candidates for atmospheric characterization. Thanks to the brightness of its host star, it is a remarkable laboratory in which to break the degeneracy in planetary interior models and to test formation and evolution theories of small planets around low-mass stars.

Acknowledgements. This work was supported by the KESPRINT[8] collaboration, an international consortium devoted to the characterization and research of exoplanets discovered with space-based missions. We are very grateful to the ESO staff members for their precious support during the observations. We warmly thank Xavier Dumusque and François Bouchy for coordinating the shared observations with HARPS and Jaime Alvarado Montes, Xavier Delfosse, Guillaume Gaisné, Melissa Hobson, and Felipe Murgas who helped collecting the data. This paper includes data collected by the TESS mission. Funding for the TESS mission is provided by the NASA Explorer Program. We acknowledge the use of TESS Alert data, which is currently in a beta test phase, from pipelines at the TESS Science Office and at the TESS Science Processing Operations Center. Resources supporting this work were provided by the NASA High-End Computing (HEC) Program through the NASA Advanced Supercomputing (NAS) Division at Ames Research Center for the production of the SPOC data products. This research has made use of the Exoplanet Follow-up Observation Program website, which is operated by the California Institute of Technology, under contract with the National Aeronautics and Space Administration under the Exoplanet Exploration Program. This work has made use of data from the European Space Agency (ESA) mission *Gaia* (https://www.cosmos.esa.int/gaia), processed by the *Gaia* Data Processing and Analysis Consortium (DPAC, https://www.cosmos.esa.int/web/gaia/dpac/consortium). Funding for the DPAC has been provided by national institutions, in particular the institutions participating in the *Gaia* Multilateral Agreement. The MEarth Team gratefully acknowledges funding from the David and Lucile Packard Fellowship for Science and Engineering (awarded to D.C.). This material is based upon work supported by the National Science Foundation under grants AST-0807690, AST-1109468, AST-1004488 (Alan T. Waterman Award), and AST-1616624, and upon work supported by the National Aeronautics and Space Administration under Grant No. 80NSSC18K0476 issued through the XRP Program. This work is made possible by a grant from the John Templeton Foundation. The opinions expressed in this publication are those of the authors and do not necessarily reflect the views of the John Templeton Foundation. This work makes use of observations from the LCOGT network. Some of the Observations in the paper made use of the High-Resolution Imaging instrument Zorro. Zorro was funded by the NASA Exoplanet Exploration Program and built at the NASA Ames Research Center by Steve B. Howell, Nic Scott, Elliott P. Horch, and Emmett Quigley. Data were reduced using a software pipeline originally written by Elliott Horch and Mark Everett. Zorro was mounted on the Gemini South telescope, and NIRI was mounted on the Gemini North telescope, of the international Gemini Observatory, a program of NSF's OIR Lab, which is managed by the Association of Universities for Research in Astronomy (AURA) under a cooperative agreement with the National Science Foundation on behalf of the Gemini partnership: the National Science Foundation (United States), National Research Council (Canada), Agencia Nacional de Investigación y Desarrollo (Chile), Ministerio de Ciencia, Tecnología e Innovación (Argentina), Ministério da Ciência, Tecnologia, Inovações e Comunicações (Brazil), and Korea Astronomy and Space Science Institute (Republic of Korea). Data collected under program GN-2019A-LP-101. Based in part on observations obtained at the Southern Astrophysical Research (SOAR) telescope, which is a joint project of the Ministério da Ciência, Tecnologia e Inovações (MCTI/LNA) do Brasil, the US National Science Foundation's NOIRLab, the University of North Carolina at Chapel Hill (UNC), and Michigan State University (MSU). This work was enabled by observations made from the Gemini North telescope, located within the Maunakea Science Reserve and adjacent to the summit of Maunakea. We are grateful for the privilege of observing the Universe from a place that is unique in both its astronomical quality and its cultural significance. Based on observations collected at the European Organization for Astronomical Research in the Southern Hemisphere under ESO programme 0103.C-0449(A). R.L. has received funding from the European Union's Horizon 2020 research and innovation program under the Marie Skłodowska-Curie grant agreement No. 713673 and financial support through the "la Caixa" INPhINIT Fellowship Grant LCF/BQ/IN17/11620033 for Doctoral studies at Spanish Research Centers of Excellence from "la Caixa" Banking Foundation, Barcelona, Spain. This work is partly financed by the Spanish Ministry of Economics and Competitiveness through projects ESP2016-80435-C2-2-R and ESP2016-80435-C2-1-R. L.M.S. and D.G. gratefully acknowledge financial support from the CRT foundation under Grant No. 2018.2323 "Gaseous or rocky? Unveiling the nature of small worlds". This work is supported by JSPS KAKENHI Grant Numbers JP19K14783, JP18H01265 and JP18H05439, and JST PRESTO Grant Number JPMJPR1775. I.J.M.C. acknowledges support from the NSF through grant AST-1824644. J.K., Sz.Cs., M.E., A.P.H., K.W.F.L., S.G. acknowledge support by DFG grants PA525/ 18-1, PA525/ 19-1, PA525/ 20-1, HA3279/ 12-1 and RA714/ 14-1 within the DFG Schwerpunkt SPP 1992, Exploring the Diversity of Extrasolar Planets. M.F, I.G. and C.M.P. gratefully acknowledge the support of the Swedish National Space Agency (DNR 65/19 and 174/18). P.K. and J.S. acknowledge the grant INTER-TRANSFER number LTT20015. S.A. knowledges support from the Danish Council for Independent Research, through a DFF Sapere Aude Starting Grant no. 4181-00487B. Funding for the Stellar Astrophysics Centre is provided by The Danish National Research Foundation (Grant agreement no.: DNRF106). H.J.D. acknowledges support by grant ESP2017-87676-C5-4-R of the Spanish Secretary of State for R&D&i (MINECO). D.G. warmly thanks Javier Alarcón, Pablo Arias, Duncan Castex, Mónica Castillo, Cecilia Farias, Mario Herrera, Francisco Labraña, Angélica León, and Ariel Sánchez (ESO La Silla) for the inspiring conversations.

[8] www.kesprint.science

References

Aller, A., Lillo-Box, J., Jones, D., Miranda, L. F., & Barceló Forteza, S. 2020, A&A, 635, A128
Almenara, J. M., Astudillo-Defru, N., Bonfils, X., et al. 2015, A&A, 581, L7
Almenara, J. M., Díaz, R. F., Dorn, C., Bonfils, X., & Udry, S. 2018, MNRAS, 478, 460
Ambikasaran, S., Foreman-Mackey, D., Greengard, L., Hogg, D. W., & O'Neil, M. 2015, IEEE Trans. Pattern Anal. Mach. Intell., 38, 252
Anderson, O. L., Dubrovinsky, L., Saxena, S. K., & LeBihan, T. 2001, Geophys. Res. Lett., 28, 399
Anglada-Escudé, G., & Butler, R. P. 2012, ApJS, 200, 15
Barragán, O., Gandolfi, D., & Antoniciello, G. 2019, MNRAS, 482, 1017
Batalha, N. E., Mandell, A., Pontoppidan, K., et al. 2017, PASP, 129, 064501
Berger, T. A., Huber, D., Gaidos, E., van Saders, J. L., & Weiss, L. M. 2020, AJ, 160, 108
Berta, Z. K., Irwin, J., Charbonneau, D., Burke, C. J., & Falco, E. E. 2012, AJ, 144, 145
Birch, F. 1952, J. Geophys. Res., 57, 227
Bluhm, P., Luque, R., Espinoza, N., et al. 2020, A&A, 639, A132
Briceno, C., Hartmann, L. W., Stauffer, J. R., et al. 1997, AJ, 113, 740
Brown, T. M., Baliber, N., Bianco, F. B., et al. 2013, PASP, 125, 1031
Buchner, J., Georgakakis, A., Nandra, K., et al. 2014, A&A, 564, A125
Carrillo, A., Hawkins, K., Bowler, B. P., Cochran, W., & Vanderburg, A. 2020, MNRAS, 491, 4365
Casagrande, L., & VandenBerg, D. A. 2018, MNRAS, 479, L102
Chabrier, G., Mazevet, S., & Soubiran, F. 2019, ApJ, 872, 51
Chen, H., & Rogers, L. A. 2016, ApJ, 831, 180
Ciardi, D. R., Beichman, C. A., Horch, E. P., & Howell, S. B. 2015, ApJ, 805, 16
Cifuentes, C., Caballero, J. A., Cortés-Contreras, M., et al. 2020, A&A, 642, A115
Cloutier, R., & Menou, K. 2020, AJ, 159, 211
Cloutier, R., Astudillo-Defru, N., Bonfils, X., et al. 2019, A&A, 629, A111
Cloutier, R., Rodriguez, J. E., Irwin, J., et al. 2020, AJ, 160, 22

Collins, K. A., Kielkopf, J. F., Stassun, K. G., & Hessman, F. V. 2017, AJ, 153, 77
Crossfield, I. J. M., Petigura, E., Schlieder, J. E., et al. 2015, ApJ, 804, 10
Damasso, M., Bonomo, A. S., Astudillo-Defru, N., et al. 2018, A&A, 615, A69
Demory, B. O., Pozuelos, F. J., Gómez Maqueo Chew, Y., et al. 2020, A&A, 642, A49
Díez Alonso, E., González Hernández, J. I., Suárez Gómez, S. L., et al. 2018, MNRAS, 480, L1
Díez Alonso, E., Caballero, J. A., Montes, D., et al. 2019, A&A, 621, A126
Drake, A. J., Graham, M. J., Djorgovski, S. G., et al. 2014, ApJS, 213, 9
Dressing, C. D., & Charbonneau, D. 2013, ApJ, 767, 95
Dressing, C. D., & Charbonneau, D. 2015, ApJ, 807, 45
Dumusque, X., Bonomo, A. S., Haywood, R. D., et al. 2014, ApJ, 789, 154
Elkins-Tanton, L. T., & Seager, S. 2008, ApJ, 685, 1237
Espinoza, N. 2018, Res. Notes Amer. Astron. Soc., 2, 209
Espinoza, N., & Jordán, A. 2015, MNRAS, 450, 1879
Espinoza, N., Kossakowski, D., & Brahm, R. 2019, MNRAS, 490, 2262
Fei, Y., Mao, H., & Hemley, R. J. 1993, J. Chem. Phys., 99, 5369
Feistel, R., & Wagner, W. 2006, J. Phys. Chem. Ref. Data, 35, 1021
Feroz, F., Hobson, M. P., & Bridges, M. 2009, MNRAS, 398, 1601
Foreman-Mackey, D., Agol, E., Ambikasaran, S., & Angus, R. 2017, celerite: Scalable 1D Gaussian Processes in C++, Python, and Julia
France, K., Loyd, R. O. P., Youngblood, A., et al. 2016, ApJ, 820, 89
French, M., Mattsson, T. R., Nettelmann, N., & Redmer, R. 2009, Phys. Rev. B, 79, 054107
Fulton, B. J., & Petigura, E. A. 2018, AJ, 156, 264
Fulton, B. J., Petigura, E. A., Howard, A. W., et al. 2017, AJ, 154, 109
Fulton, B. J., Petigura, E. A., Blunt, S., & Sinukoff, E. 2018, PASP, 130, 044504
Gaia Collaboration (Brown, A. G. A., et al.) 2018, A&A, 616, A1
Gaidos, E., Mann, A. W., Lépine, S., et al. 2014, MNRAS, 443, 2561
Ginzburg, S., Schlichting, H. E., & Sari, R. 2018, MNRAS, 476, 759
Greene, T. P., Line, M. R., Montero, C., et al. 2016, ApJ, 817, 17
Güdel, M., Audard, M., Reale, F., Skinner, S. L., & Linsky, J. L. 2004, A&A, 416, 713
Gupta, A., & Schlichting, H. E. 2019, MNRAS, 487, 24
Gupta, A., & Schlichting, H. E. 2020, MNRAS, 493, 792
Hadden, S., & Lithwick, Y. 2017, AJ, 154, 5
Hamann, A., Montet, B. T., Fabrycky, D. C., Agol, E., & Kruse, E. 2019, AJ, 158, 133
Hardegree-Ullman, K. K., Zink, J. K., Christiansen, J. L., et al. 2020, ApJS, 247, 28
Hatzes, A. P. 2016, Astrophys. Space Sci. Lib., 428, 3
Hatzes, A. P., & Rauer, H. 2015, ApJ, 810, L25
Hébrard, E., Dobrijevic, M., Loison, J.-C., Bergeat, A., & Hickson, K. 2012, A&A, 541, A21
Hirano, T., Dai, F., Gandolfi, D., et al. 2018, AJ, 155, 127
Howe, A. R., Burrows, A., & Verne, W. 2014, ApJ, 787, 173
Howell, S. B., Everett, M. E., Sherry, W., Horch, E., & Ciardi, D. R. 2011, AJ, 142, 19
Irwin, J., Irwin, M., Aigrain, S., et al. 2007, MNRAS, 375, 1449
Irwin, J. M., Berta-Thompson, Z. K., Charbonneau, D., et al. 2015, in Cambridge Workshop on Cool Stars, Stellar Systems, and the Sun (San Francisco: ASP Books), 18, 767
Jenkins, J. M., Twicken, J. D., McCauliff, S., et al. 2016, Proc. SPIE, 9913, 99133E
Jensen, E. 2013, Astrophys. Source Code Libr. [record ascl:1306.007]
Jin, S., & Mordasini, C. 2018, ApJ, 853, 163
Jin, S., Mordasini, C., Parmentier, V., et al. 2014, ApJ, 795, 65
Johnstone, C. P., Güdel, M., Brott, I., & Lüftinger, T. 2015, A&A, 577, A28
Jontof-Hutter, D., Ford, E. B., Rowe, J. F., et al. 2016, ApJ, 820, 39
Journaux, B., Brown, J. M., Pakhomova, A., et al. 2020, J. Geophys. Res. Planets, 125, e06176
Karki, B. B., Wentzcovitch, R. M., de Gironcoli, S., & Baroni, S. 2000, Phys. Rev. B, 62, 14750
Kawashima, Y., & Rugheimer, S. 2019, AJ, 157, 213
Kempton, E. M.-R., Bean, J. L., Louie, D. R., et al. 2018, PASP, 130, 114401
Kipping, D. M. 2013, MNRAS, 435, 2152
Kislyakova, K. G., Lammer, H., Holmström, M., et al. 2013, Astrobiology, 13, 1030
Kislyakova, K. G., Johnstone, C. P., Odert, P., et al. 2014, A&A, 562, A116
Klotz, S., Komatsu, K., Kagi, H., et al. 2017, Phys. Rev. B, 95, 174111
Kochanek, C. S., Shappee, B. J., Stanek, K. Z., et al. 2017, PASP, 129, 104502
Korth, J. 2020, PhD thesis, Universität zu Köln, Germany
Kosiarek, M. R., Crossfield, I. J. M., Hardegree-Ullman, K. K., et al. 2019, AJ, 157, 97
Kreidberg, L. 2015, PASP, 127, 1161
Kreidberg, L., Bean, J. L., Désert, J.-M., et al. 2014, Nature, 505, 69
Kreidberg, L., Koll, D. D., Morley, C., et al. 2019, Nature, 573, 87
Küker, M., Rüdiger, G., Olah, K., & Strassmeier, K. G. 2019, A&A, 622, A40
Lam, K. W. F., Korth, J., Masuda, K., et al. 2020, AJ, 159, 120
Lammer, H., Güdel, M., Kulikov, Y., et al. 2012, Earth Planets Space, 64, 179
Lee, E. J., & Chiang, E. 2016, ApJ, 817, 90
Lee, E. J., Chiang, E., & Ormel, C. W. 2014, ApJ, 797, 95
Li, J., Tenenbaum, P., Twicken, J. D., et al. 2019, PASP, 131, 024506
Lillo-Box, J., Figueira, P., Leleu, A., et al. 2020, A&A, 642, A121
Lopez, E. D., & Fortney, J. J. 2014, ApJ, 792, 1
Lopez, E. D., & Rice, K. 2018, MNRAS, 479, 5303
Lovis, C., & Pepe, F. 2007, A&A, 468, 1115
Luque, R., Pallé, E., Kossakowski, D., et al. 2019, A&A, 628, A39
Luyten, W. J. 1974, IAU Symp., 61, 169
Madhusudhan, N., Nixon, M. C., Welbanks, L., Piette, A. A. A., & Booth, R. A. 2020, ApJ, 891, L7
Martinez, C. F., Cunha, K., Ghezzi, L., & Smith, V. V. 2019, ApJ, 875, 29
Mayor, M., Pepe, F., Queloz, D., et al. 2003, The Messenger, 114, 20
Molaverdikhani, K., Henning, T., & Mollière, P. 2019a, ApJ, 883, 194
Molaverdikhani, K., Henning, T., & Mollière, P. 2019b, ApJ, 873, 32
Molaverdikhani, K., Henning, T., & Mollière, P. 2020, ApJ, 899, 53
Mollière, P., Wardenier, J., van Boekel, R., et al. 2019, A&A, 627, A67
Montet, B. T., Morton, T. D., Foreman-Mackey, D., et al. 2015, ApJ, 809, 25
Mordasini, C. 2020, A&A, 638, A52
Morton, T. D. 2015, Isochrones: Stellar model grid package (USA: NASA)
Murdoch, K. A., Hearnshaw, J. B., & Clark, M. 1993, ApJ, 413, 349
Murray-Clay, R. A., Chiang, E. I., & Murray, N. 2009, ApJ, 693, 23
Nelson, B. E., Ford, E. B., Buchner, J., et al. 2020, AJ, 159, 73
Niraula, P., Redfield, S., Dai, F., et al. 2017, AJ, 154, 266
Nixon, M. C., & Madhusudhan, N. 2020, MNRAS, submitted
Nowak, G., Luque, R., Parviainen, H., et al. 2020, A&A, 642, A173
Osborn, H. P., Santerne, A., Barros, S. C. C., et al. 2017, A&A, 604, A19
Owen, J. E., & Campos Estrada, B. 2020, MNRAS, 491, 5287
Owen, J. E., & Jackson, A. P. 2012, MNRAS, 425, 2931
Owen, J. E., & Wu, Y. 2013, ApJ, 775, 105
Pojmanski, G. 2002, Acta Astron., 52, 397
Pollacco, D. L., Skillen, I., Collier Cameron, A., et al. 2006, PASP, 118, 1407
Reddy, B. E., Lambert, D. L., & Allende Prieto, C. 2006, MNRAS, 367, 1329
Rein, H., & Liu, S. F. 2012, A&A, 537, A128
Rein, H., & Spiegel, D. S. 2015, MNRAS, 446, 1424
Riess, A. G., Casertano, S., Yuan, W., et al. 2018, ApJ, 861, 126
Rowe, J. F., Bryson, S. T., Marcy, G. W., et al. 2014, ApJ, 784, 45
Rüdiger, G., Küker, M., & Tereshin, I. 2014, A&A, 572, L7
Salpeter, E. E., & Zapolsky, H. S. 1967, Phys. Rev., 158, 876
Sanz-Forcada, J., Micela, G., Ribas, I., et al. 2011, A&A, 532, A6
Schlichting, H. E., Sari, R., & Yalinewich, A. 2015, Icarus, 247, 81
Schweitzer, A., Passegger, V. M., Cifuentes, C., et al. 2019, A&A, 625, A68
Scott, N. J. 2019, AAS/Division for Extreme Solar Systems Abstracts, 15, 330.15
Seager, S., Kuchner, M., Hier-Majumder, C. A., & Militzer, B. 2007, ApJ, 669, 1279
Shuvalov, V. 2009, Meteorit. Planet. Sci., 44, 1095
Skrutskie, M. F., Cutri, R. M., Stiening, R., et al. 2006, AJ, 131, 1163
Smith, J. C., Stumpe, M. C., Van Cleve, J. E., et al. 2012, PASP, 124, 1000
Southworth, J. 2011, MNRAS, 417, 2166
Stassun, K. G., & Torres, G. 2018, ApJ, 862, 61
Stassun, K. G., Oelkers, R. J., Pepper, J., et al. 2018, AJ, 156, 102
Steffen, J. H., Fabrycky, D. C., Ford, E. B., et al. 2012, MNRAS, 421, 2342
Stumpe, M. C., Smith, J. C., Van Cleve, J. E., et al. 2012, PASP, 124, 985
Stumpe, M. C., Smith, J. C., Catanzarite, J. H., et al. 2014, PASP, 126, 100
Teske, J. K., Ciardi, D. R., Howell, S. B., Hirsch, L. A., & Johnson, R. A. 2018, AJ, 156, 292
Thomas, S. W., & Madhusudhan, N. 2016, MNRAS, 458, 1330
Tokovinin, A. 2018, PASP, 130, 035002
Trotta, R. 2008, Contemp. Phys., 49, 71
Tu, L., Johnstone, C. P., Güdel, M., & Lammer, H. 2015, A&A, 577, L3
Twicken, J. D., Catanzarite, J. H., Clarke, B. D., et al. 2018, PASP, 130, 064502
Van Eylen, V., & Albrecht, S. 2015, ApJ, 808, 126
Van Eylen, V., Agentoft, C., Lundkvist, M. S., et al. 2018, MNRAS, 479, 4786
Van Eylen, V., Albrecht, S., Huang, X., et al. 2019, AJ, 157, 61
Vinet, P., Rose, J. H., Ferrante, J., & Smith, J. R. 1989, J. Phys. Conden. Matter, 1, 1941
Wagner, W., & Pruß, A. 2002, J. Phys. Chem. Ref. Data, 31, 387
Wakeford, H. R., Sing, D. K., Kataria, T., et al. 2017, Science, 356, 628
Walter, F. M., Brown, A., Mathieu, R. D., Myers, P. C., & Vrba, F. J. 1988, AJ, 96, 297
Weiss, L. M., & Marcy, G. W. 2014, ApJ, 783, L6
Winn, J. N. 2010, Exoplanet Transits and Occultations (Tucson: University of Arizona Press), 55
Winn, J. N., Sanchis-Ojeda, R., Rogers, L., et al. 2017, AJ, 154, 60
Woźniak, P. R., Vestrand, W. T., Akerlof, C. W., et al. 2004, AJ, 127, 2436

Wu, Y. 2019, ApJ, 874, 91
Wyatt, M. C., Kral, Q., & Sinclair, C. A. 2020, MNRAS, 491, 782
Xie, J.-W., Dong, S., Zhu, Z., et al. 2016, Proc. Natl. Acad. Sci., 113, 11431
Yee, S. W., Petigura, E. A., & von Braun, K. 2017, ApJ, 836, 77
Zacharias, N., Finch, C. T., Girard, T. M., et al. 2013, AJ, 145, 44
Zechmeister, M., Kürster, M., & Endl, M. 2009, A&A, 505, 859
Zechmeister, M., Reiners, A., Amado, P. J., et al. 2018, A&A, 609, A12
Zeng, L., & Sasselov, D. 2013, PASP, 125, 227
Zeng, L., Sasselov, D. D., & Jacobsen, S. B. 2016, ApJ, 819, 127
Zeng, L., Jacobsen, S. B., Sasselov, D. D., et al. 2019, Proc. Natl. Acad. Sci., 116, 9723
Ziegler, C., Tokovinin, A., Briceño, C., et al. 2020, AJ, 159, 19
Zinn, J. C., Pinsonneault, M. H., Huber, D., & Stello, D. 2019, ApJ, 878, 136

[1] Instituto de Astrofísica de Canarias, 38205 La Laguna, Tenerife, Spain
e-mail: rluque@iac.es
[2] Departamento de Astrofísica, Universidad de La Laguna, 38206 La Laguna, Tenerife, Spain
[3] Dipartimento di Fisica, Università degli Studi di Torino, via Pietro Giuria 1, 10125 Torino, Italy
[4] Max-Planck-Institut für Astronomie, Königstuhl 17, 69117 Heidelberg, Germany
[5] Landessternwarte, Zentrum für Astronomie der Universität Heidelberg, Königstuhl 12, 69117 Heidelberg, Germany
[6] Institute of Astronomy, University of Cambridge, Madingley Road, Cambridge CB3 0HA, UK
[7] Department of Astronomy, University of Tokyo, 7-3-1 Hongo, Bunkyo-ky, Tokyo 113-0033, Japan
[8] Thüringer Landessternwarte Tautenburg, Sternwarte 5, 07778 Tautenburg, Germany
[9] Rheinisches Institut für Umweltforschung an der Universität zu Köln, Aachener Strasse 209, 50931 Köln, Germany
[10] Center for Planetary Systems Habitability and McDonald Observatory, The University of Texas at Austin, Austin, TX 78730, USA
[11] Department of Earth and Planetary Sciences, Tokyo Institute of Technology, 2-12-1 Ookayama, Meguro-ku, Tokyo 152-8551, Japan
[12] Stellar Astrophysics Centre, Department of Physics and Astronomy, Aarhus University, Ny Munkegade 120, 8000 Aarhus C, Denmark
[13] Sub-department of Astrophysics, Department of Physics, University of Oxford, Oxford, OX1 3RH, UK
[14] Cerro Tololo Inter-American Observatory/NSF's NOIRLab, Casilla 603, La Serena, Chile
[15] Deutsches Zentrum für Luft- und Raumfahrt, Institut für Planetenforschung, 12489 Berlin, Rutherfordstrasse 2., Germany
[16] Center for Astrophysics |Harvard & Smithsonian, 60 Garden Street, Cambridge, MA 02138, USA
[17] George Mason University, 4400 University Drive, Fairfax, VA 22030 USA
[18] Exoplanets and Stellar Astrophysics Laboratory, Mail Code 667, NASA Goddard Space Flight Center, 8800 Greenbelt Rd., Greenbelt MD 20771, USA
[19] Department of Physics and Astronomy, University of Kansas, Lawrence, KS, USA
[20] Division of Geological and Planetary Sciences, California Institute of Technology, 1200 East California Blvd, Pasadena, CA 91125, USA
[21] Leiden Observatory, Leiden University, 2333CA Leiden, The Netherlands
[22] Department of Space, Earth and Environment, Chalmers University of Technology, Onsala Space Observatory, 439 92 Onsala, Sweden
[23] Department of Earth, Atmospheric and Planetary Sciences, Massachusetts Institute of Technology, Cambridge, MA 02139, USA
[24] Department of Physics and Kavli Institute for Astrophysics and Space Research, Massachusetts Institute of Technology, Cambridge, MA 02139, USA
[25] Space Science & Astrobiology Division, NASA Ames Research Center, Moffett Field, CA 94035, USA
[26] Department of Physics & Astronomy, Swarthmore College, Swarthmore PA 19081, USA
[27] Astronomical Institute, Czech Academy of Sciences, Fričova 298, 25165 Ondřejov, Czech Republic
[28] Space Telescope Science Institute, Baltimore, MD, USA
[29] Department of Physics and Astronomy, University of Louisville, Louisville, KY 40292, USA
[30] Center for Astronomy and Astrophysics, Technical University Berlin, Hardenbergstr. 36, 10623 Berlin, Germany
[31] Department of Physics and Astronomy, The University of North Carolina at Chapel Hill, Chapel Hill, NC 27599-3255, USA
[32] Komaba Institute for Science, The University of Tokyo, 3-8-1 Komaba, Meguro, Tokyo 153-8902, Japan
[33] JST, PRESTO, 3-8-1 Komaba, Meguro, Tokyo 153-8902, Japan
[34] Astrobiology Center, 2-21-1 Osawa, Mitaka, Tokyo 181-8588, Japan
[35] Astronomy Department and Van Vleck Observatory, Wesleyan University, Middletown, CT 06459, USA
[36] European Southern Observatory (ESO), Alonso de Córdova 3107, Vitacura, Casilla 19001, Santiago de Chile, Chile
[37] Department of Aeronautics and Astronautics, Massachusetts Institute of Technology, 77 Massachusetts Avenue, Cambridge, MA 02139, USA
[38] Perth Exoplanet Survey Telescope, Perth, Western Australia
[39] Mullard Space Science Laboratory, University College London, Holmbury St. Mary, Dorking, Surrey, RH5 6NT, UK
[40] Department of Astrophysical Sciences, Princeton University, 4 Ivy Lane, Princeton, NJ 08544, USA
[41] Dunlap Institute for Astronomy and Astrophysics, University of Toronto, 50 St. George Street, Toronto, Ontario M5S 3H4, Canada

Appendix A: Joint fit priors

Table A.1. Priors used for the models presented in Sect. 5 using `juliet`.

Parameter name	Prior	Units	Description
		Stellar parameters	
$\rho_\star$	$\mathcal{N}(5300, 1500^2)$	kg m^{-3}	Stellar density
		Planet parameters	
P_b	$\mathcal{N}(8.24, 0.05^2)$	d	Period of planet b
P_c	$\mathcal{N}(15.65, 0.05^2)$	d	Period of planet c
$t_{0,b} - 2\,450\,000$	$\mathcal{N}(8571.41, 0.01^2)$	d	Transit-center time of planet b
$t_{0,c} - 2\,450\,000$	$\mathcal{N}(8572.60, 0.01^2)$	d	Transit-center time of planet c
$r_{1,b}$	$\mathcal{U}(0, 1)$	...	Parameterization for p and b of planet b
$r_{2,b}$	$\mathcal{U}(0, 1)$	...	Parameterization for p and b of planet b
$r_{1,c}$	$\mathcal{U}(0, 1)$	...	Parameterization for p and b of planet c
$r_{2,c}$	$\mathcal{U}(0, 1)$	...	Parameterization for p and b of planet c
K_b	$\mathcal{U}(0, 20)$	m s^{-1}	RV semi-amplitude of planet b
K_c	$\mathcal{U}(0, 20)$	m s^{-1}	RV semi-amplitude of planet c
e_b	$\mathcal{B}(1.52, 29)$	...	Eccentricity of planet b
e_c	$\mathcal{B}(1.52, 29)$	...	Eccentricity of planet c
ω_b	$\mathcal{U}(-180, 180)$	deg	Argument of periastron of planet b
ω_c	$\mathcal{U}(-180, 180)$	deg	Argument of periastron of planet c
		Photometry parameters	
σ_{TESS}	$\mathcal{J}(1, 1000)$	ppm	Extra jitter term for *TESS*
D_{TESS}	1.0 (fixed)	...	Dilution factor for *TESS*
M_{TESS}	0.0 (fixed)	ppm	Relative flux offset for *TESS*
$q_{1,TESS}$	$\mathcal{U}(0, 1)$	...	Quadratic limb darkening parameterization for *TESS*
$q_{2,TESS}$	$\mathcal{U}(0, 1)$	...	Quadratic limb darkening parameterization for *TESS*
$\sigma_{LCO\text{-}CTIO}$	$\mathcal{J}(10, 10^5)$	ppm	Extra jitter term for LCO-CTIO
$M_{LCO\text{-}CTIO}$	$\mathcal{N}(0, 0.01^2)$	ppm	Relative flux offset for LCO-CTIO
$\theta_{LCO\text{-}CTIO}$	$\mathcal{U}(-1.0, 1.0)$	...	Airmass regression coefficients for LCO-CTIO
$q_{1,LCO\text{-}CTIO}$	$\mathcal{U}(0, 1)$	...	Linear limb darkening parameterization for LCO-CTIO
$\sigma_{LCO\text{-}SAAO}$	$\mathcal{J}(10, 10^5)$	ppm	Extra jitter term for LCO-SAAO
$M_{LCO\text{-}SAAO}$	$\mathcal{N}(0, 0.01^2)$	ppm	Relative flux offset for LCO-SAAO
$\theta_{LCO\text{-}SAAO}$	$\mathcal{U}(-1.0, 1.0)$	...	Airmass regression coefficients for LCO-SAAO
$q_{1,LCO\text{-}SAAO}$	$\mathcal{U}(0, 1)$	...	Linear limb darkening parameterization for LCO-SAAO
$\sigma_{LCO\text{-}SSO}$	$\mathcal{J}(10, 10^5)$	ppm	Extra jitter term for LCO-SSO
$M_{LCO\text{-}SSO}$	$\mathcal{N}(0, 0.01^2)$	ppm	Relative flux offset for LCO-SSO
$\theta_{LCO\text{-}SSO}$	$\mathcal{U}(-1.0, 1.0)$	...	Airmass regression coefficients for LCO-SSO
$q_{1,LCO\text{-}SSO}$	$\mathcal{U}(0, 1)$	...	Linear limb darkening parameterization for LCO-SSO
σ_{MEarth}	$\mathcal{J}(10, 10^5)$	ppm	Extra jitter term for MEarth
M_{MEarth}	$\mathcal{N}(0, 0.01^2)$	ppm	Relative flux offset for MEarth
$q_{1,MEarth}$	$\mathcal{U}(0, 1)$	...	Linear limb darkening parameterization for MEarth
		RV parameters	
μ_{HARPS}	$\mathcal{U}(-100, 100)$	m s^{-1}	Systemic velocity for HARPS
σ_{HARPS}	$\mathcal{J}(0.1, 100)$	m s^{-1}	Extra jitter term for HARPS
		GP hyperparameters and additional sinusoid	
$\sigma_{GP,TESS}$	$\mathcal{J}(10^{-2}, 10^6)$	ppm	Amplitude of GP component for TESS
$T_{GP,TESS}$	$\mathcal{J}(10^{-6}, 10^4)$	d	Length scale of GP component for TESS
K	$\mathcal{U}(0, 20)$	m s^{-1}	RV semi-amplitude of the additional sinusoid
$t_0 - 2\,450\,000$	$\mathcal{U}(8575.0, 8655.0)$	d	Transit-center time of the additional sinusoid
P	$\mathcal{N}(35.0, 10.0^2)$	d	Period of the additional sinusoid

Notes. The prior labels of $\mathcal{N}$, $\mathcal{U}$, $\mathcal{B}$, and $\mathcal{J}$ represent normal, uniform, Beta, and Jeffrey's distributions. The parameterization for (p, b) using (r_1, r_2) (Espinoza 2018) and the linear (q_1) and quadratic (q_1, q_2) limb darkening parameterization (Kipping 2013) are both described in Sect. 5.2.1.

Appendix B: HARPS RV measurements and spectral line indicators

Table B.1. `Serval` extraction.

$BJD_{TBD} - 2\,457\,000$	RV ($m\,s^{-1}$)	σ_{RV} ($m\,s^{-1}$)	CRX ($m\,s^{-1}\,Np^{-1}$)	σ_{CRX} ($m\,s^{-1}\,Np^{-1}$)	dLW ($m^2\,s^{-2}$)	σ_{dLW} ($m^2\,s^{-2}$)
1884.75667	4.3	3.1	−4.0	26.4	−3.4	4.0
1886.88043	−0.2	1.6	−4.7	13.3	−15.1	2.0
1887.79526	2.2	1.9	10.9	15.8	−14.7	2.1
1888.83087	1.2	1.3	−12.3	10.7	−13.6	1.9
1889.79811	1.2	1.6	5.1	12.9	−12.1	2.5
1890.80821	7.3	2.4	−2.6	19.2	−15.0	3.0
1894.81627	−0.2	2.1	25.4	16.8	−23.2	2.9
1898.85272	4.5	1.4	−3.7	11.2	−26.8	1.5
1899.86392	9.3	1.5	14.7	12.0	−25.8	1.5
1900.84340	6.0	1.4	−12.9	11.0	−24.8	2.0
1902.80747	0.5	1.5	14.9	12.2	−24.4	1.9
1903.81551	0.2	2.0	−4.2	16.2	−27.4	1.7
1910.81439	5.0	1.3	−1.8	10.4	−15.2	1.8
1911.72654	8.3	1.5	8.6	12.4	−19.5	1.8
1912.77545	10.0	1.5	−7.8	11.8	−23.4	2.3
1914.81139	10.9	1.5	13.4	12.2	−20.5	2.0
1915.74379	7.6	1.2	0.3	9.7	−23.1	1.8
1916.69654	6.0	1.3	8.3	10.8	−25.2	1.4
1918.78064	−0.2	1.3	13.0	10.4	−19.5	1.6
1919.64336	3.2	1.4	−0.8	11.0	−7.3	1.8
1924.80573	0.4	1.4	5.0	11.2	−16.8	1.8
1925.68888	2.7	1.3	−13.1	10.6	−16.3	1.8
1925.83889	−0.5	1.5	−19.7	12.0	−20.7	1.8
1926.79127	0.4	1.3	3.8	10.7	−20.7	1.5
1927.83074	1.8	1.6	−14.7	12.8	−18.8	2.2
1928.78734	2.9	1.3	−2.8	10.3	−16.6	1.9
1929.76211	5.2	1.7	−18.0	13.5	−7.4	2.4
1930.83118	6.0	1.6	−10.0	13.2	−7.2	2.2
1931.76389	7.3	1.4	−17.5	11.4	−7.1	2.4

Table B.2. TERRA extraction.

$BJD_{TBD} - 2\,457\,000$	RV ($m\,s^{-1}$)	σ_{RV} ($m\,s^{-1}$)	H_α	S-index	$\sigma_{S-index}$	NaD_1	NaD_2
1884.75667	0.7	3.2	0.353	1.501	0.025	1.050	0.783
1886.88043	−3.1	1.8	0.345	1.555	0.018	1.056	0.800
1887.79526	−2.4	1.6	0.358	1.380	0.012	1.046	0.792
1888.83087	−3.5	1.4	0.357	1.391	0.012	1.044	0.795
1889.79811	−2.0	1.4	0.315	1.496	0.013	1.041	0.789
1890.80821	1.5	2.1	0.336	1.508	0.015	1.047	0.797
1894.81627	−5.6	1.8	0.346	1.407	0.016	1.057	0.787
1898.85272	1.3	1.4	0.361	1.356	0.014	1.055	0.797
1899.86392	5.7	1.5	0.350	1.399	0.016	1.060	0.798
1900.84340	2.6	1.6	0.364	1.336	0.015	1.057	0.799
1902.80747	−3.2	1.4	0.357	1.340	0.013	1.063	0.796
1903.81551	−4.0	1.2	0.366	1.342	0.018	1.060	0.799
1910.81439	3.6	1.2	0.339	1.445	0.014	1.053	0.799
1911.72654	5.3	1.5	0.349	1.394	0.013	1.049	0.800
1912.77545	5.6	1.4	0.315	1.559	0.015	1.054	0.790
1914.81139	6.5	1.6	0.341	1.460	0.018	1.056	0.796
1915.74379	4.6	1.0	0.324	1.462	0.013	1.056	0.792
1916.69654	2.8	1.1	0.348	1.368	0.011	1.059	0.801
1918.78064	−2.5	1.3	0.359	1.298	0.013	1.066	0.804
1919.64336	−0.3	1.2	0.356	1.338	0.012	1.061	0.794
1924.80573	−3.3	1.3	0.361	1.246	0.015	1.054	0.798
1925.68888	−2.1	1.2	0.375	1.286	0.012	1.059	0.805
1925.83889	−4.3	1.5	0.369	1.267	0.014	1.054	0.789
1926.79127	−2.5	1.2	0.365	1.231	0.014	1.054	0.797
1927.83074	0.0	1.8	0.347	1.275	0.018	1.046	0.798
1928.78734	−1.6	1.3	0.331	1.391	0.017	1.047	0.797
1929.76211	2.2	1.7	0.349	1.324	0.018	1.044	0.802
1930.83118	3.3	1.5	0.356	1.386	0.020	1.045	0.782
1931.76389	4.0	1.4	0.353	1.415	0.020	1.039	0.777

Appendix C: Corner plots

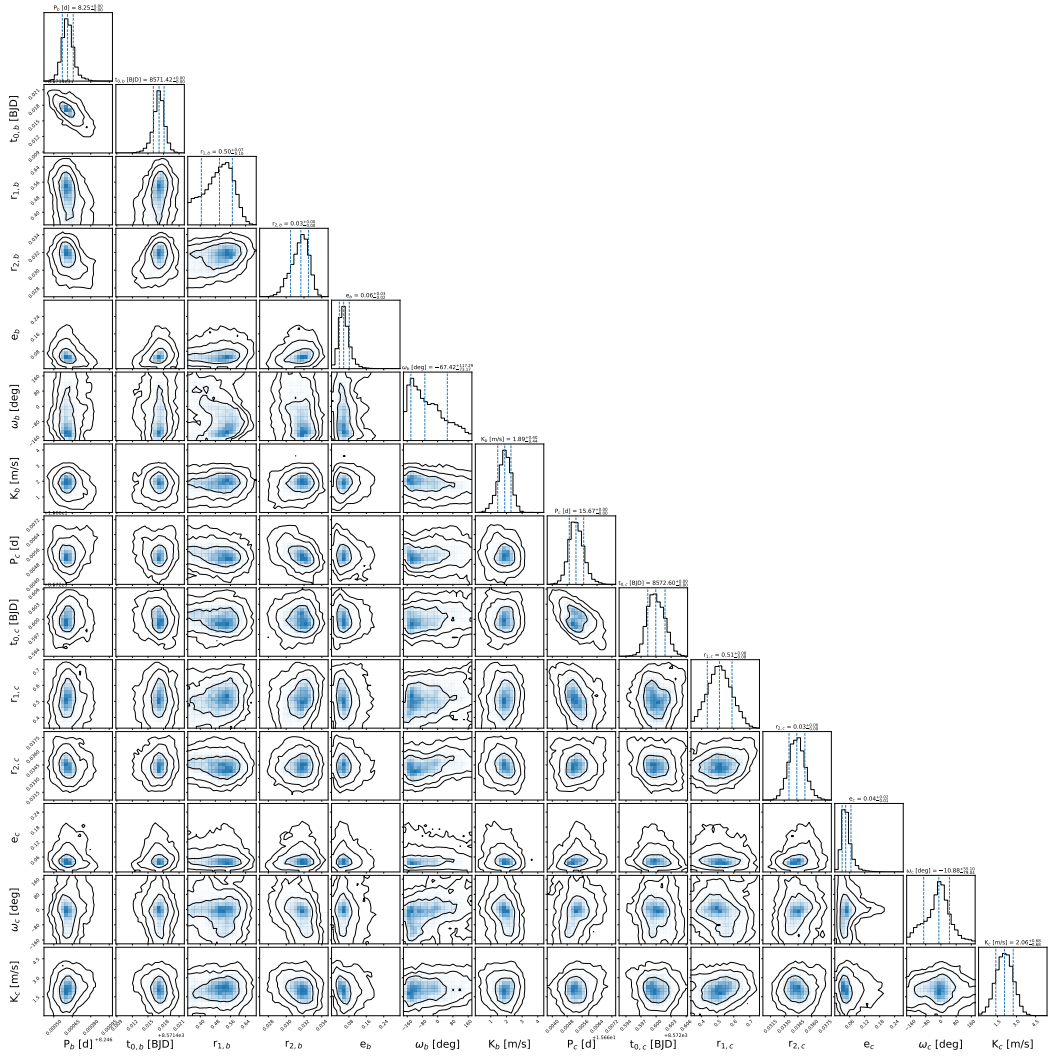

Fig. C.1. Posterior distributions of the orbital parameters of the TOI-776 system. Each panel contains ~220 000 samples. The top panels of the corner plot show the probability density distributions of each orbital parameter. The vertical dashed lines indicate the 16th, 50th, and the 84th percentiles of the samples. Contours are drawn to improve the visualization of the 2D histograms and indicate the 68.3, 95.5, and 99.7% confidence interval levels (i.e., 1σ, 2σ, and 3σ).

5

Discussion and conclusions

Caminante, son tus huellas
el camino y nada más;
Caminante, no hay camino,
se hace camino al andar.

Al andar se hace el camino,
y al volver la vista atrás
se ve la senda que nunca
se ha de volver a pisar.

Caminante no hay camino
sino estelas en la mar.

Antonio Machado (1912)

This thesis focuses on the study of planetary systems around M dwarfs using the radial velocity and transit techniques. Chapter 2 presents the discovery of two super-Earths using radial velocity observations from the CARMENES blind search for planets around M dwarfs. Chapters 3 and 4 describe the discovery of two multi-planetary systems transiting bright M dwarfs detected first with *TESS* and then followed-up with different instruments from ground. Seven new planets are detected and characterized as the main result of this PhD thesis. Here, I discuss the results from this work and summarize its conclusions.

Dedicated instrumentation and projects to capitalize on the "M dwarf opportunity" have advanced dramatically the field in a very short period of time. On the one hand, the CARMENES blind search for planets has contributed to more than 40% of the discoveries around M-dwarf hosts with masses below 0.2 $M_\odot$ since its commencement in

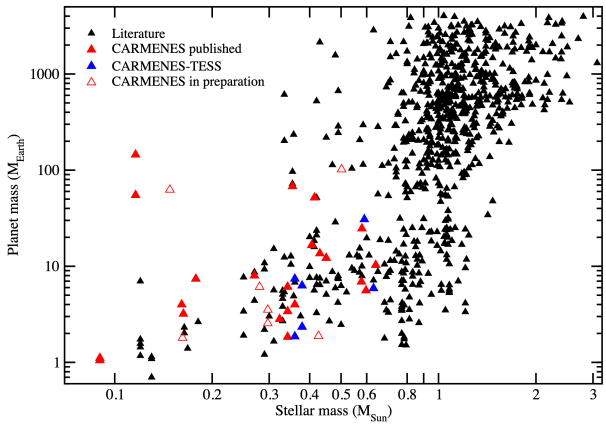

FIGURE 5.1— Planets discovered by the "blind" CARMENES survey (red) and from the CARMENES-TESS program (blue) in the context of all planets with dynamical masses determined with radial velocities. From Quirrenbach & Carmenes Consortium (2020).

2016 (Fig. 5.1). On the other hand, the shift to brighter target stars in transit surveys as in *K2* and *TESS* has opened a window to find planets suitable for a comprehensive characterization with current facilities. The change has been particularly relevant for M-dwarf planets. At the commencement of this thesis, in January 2018, only 12 planets orbiting M dwarfs had masses and radii constrained to better than 40% and 20%, respectively (Fig. 5.2, top). Three years later, the number has increased to 33, with more than a half of the new additions (11) belonging to the efforts of this thesis as leading or contributing author (Fig. 5.2, bottom). Appendix A contains the full list of publications that I have participated during this thesis.

New discoveries in this realm of the parameter space start to reveal interesting observational trends. As discussed in Chapter 2, one of these features is the absence of planets with masses between 2–5 $M_\oplus$ in close orbits orbiting mid- and late-type M dwarfs, with super-Earths frequently appearing in single systems and Earth-mass planets in multi-planetary ones. This "mass gap" was first presented in Luque et al. (2018) and has triggered some discussion in the literature about its origin. In one of these studies, Pinamonti et al. (2019) tested our hypothesis that the masses of single and multiple systems around M dwarfs should follow different distributions. Their results show that M-dwarf super-Earths are likely formed by aggregation of smaller planets, rather than appearing single because they prevent the formation of Earth-mass

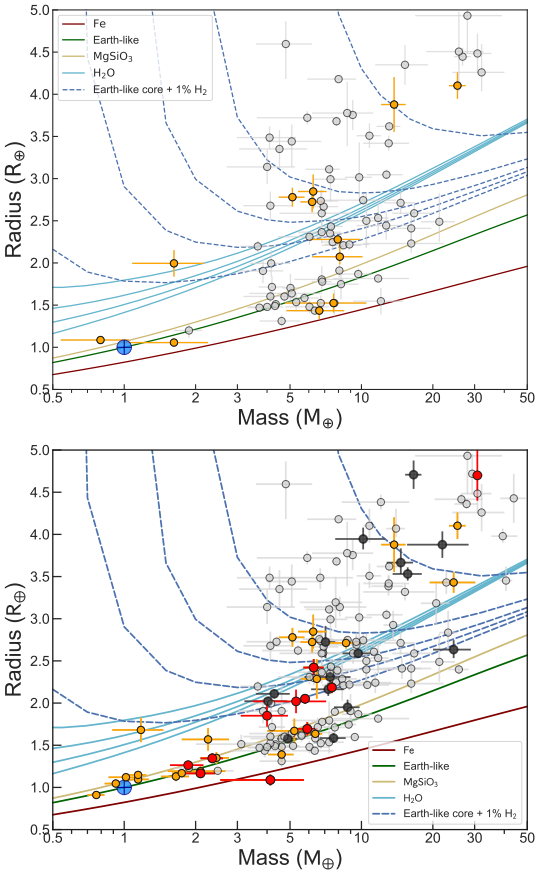

FIGURE 5.2— Mass-radius diagram of transiting exoplanets with masses and radii constrained to better than 40% and 20%, respectively, before (*top*, as of January 2018) and after this thesis (*bottom*, as of January 2021). Light gray points indicate planets orbiting solar-type stars, orange for planets around M dwarfs. Planet discoveries and/or mass measurements that I have participated in are indicated in black for solar-type planets and in red for M-dwarf planets. The location of the Earth is marked with a blue cross. The different curves show distinct internal composition models from Zeng et al. (2019) as in Fig 1.25.

planets within the same system. Additional discoveries from currently active radial velocity searches around M dwarfs from SPIRou (Artigau et al., 2014; Cloutier et al., 2018), HPF (e.g., Stefansson et al., 2020a,b; Mahadevan et al., 2021), and, in the near future, NIRPS (Bouchy et al., 2017) will probe if this trend is due to observational biases or an imprint of the formation and evolution of these systems.

Another interesting feature is the radius valley that separates close-in rocky super-Earths from gas-rich sub-Neptune planets around solar-type stars detected with *Kepler* (Fulton et al., 2017; Fulton & Petigura, 2018; Van Eylen et al., 2018). Now, for the first time, it is possible to study its dependency with stellar mass and orbital period for M dwarfs. The slope of the radius valley as a function of orbital period encodes information about the physical mechanism at the origins of this observational feature (Owen & Wu, 2017; Jin & Mordasini, 2018; Ginzburg et al., 2018; Gupta & Schlichting, 2019, 2020). For solar-type stars, the slope from different radius valley emergence models are all compatible with the observations within the uncertainties (Cloutier & Menou, 2020; Lee & Connors, 2020). However, the predictions from the models start to diverge towards lower mass hosts. As discussed in Chapter 4, multi-planetary systems inside or near the radius valley for M dwarfs are very valuable to infer the main formation and evolution pathway followed by small, close-in planets. Those with precise bulk density measurements located in the radius-period space where the models differ have the potential to pinpoint the stellar mass at which one or another mechanism at play becomes the dominant pathway for planet formation and evolution.

The synergy between *TESS* and high-precision velocimeters such as CARMENES allows us to measure the radius valley directly from the observations of individual, precisely-characterized systems; becoming an alternative to the statistical determination based on injection-recovery methods in the data from transit searches alone (e.g., Fulton et al., 2017; Cloutier & Menou, 2020). Thanks to the larger sample of precise masses and radii measurements of these systems in the last years, I could determine the presence and location of a radius valley for small planets around M dwarfs (Fig. 5.3). The valley is located at $R_p = m \log P + a$, with $m = -0.096 \pm 0.02$ and $a = 1.8 \pm 0.3$. This location is similar to the radius valley around solar-type stars, but at slightly smaller planet radii for the same orbital period, as predicted by thermally driven atmospheric mass loss models. The slope is of the same sign, but shallower, in between the predictions from photo-evaporation/core-powered mass loss models and gas-poor formation scenarios. Further, well-characterized discoveries in this region of the parameter space will help to narrow down the uncertainties in the slope in order to constrain the formation and evolution models responsible of this feature.

Finally, the ultimate goal of this thesis is to seize the "M dwarf opportunity" to find and fully characterize some of the best candidates for atmospheric characterization, particularly to carry out transmission spectroscopy studies with the *JWST*. Precise

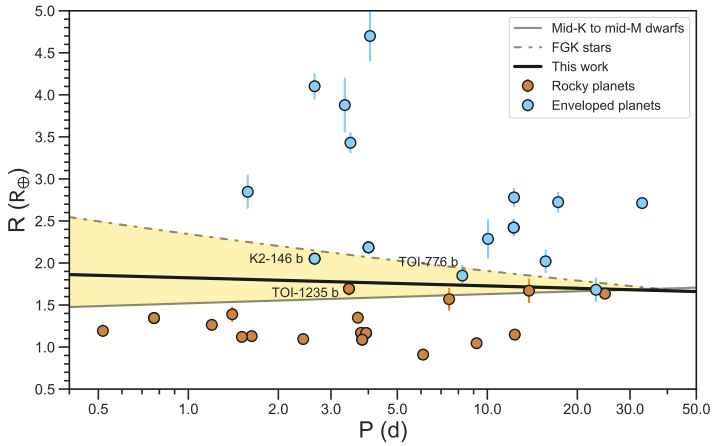

FIGURE 5.3— Period-radius diagram in Earth units of transiting exoplanets around M dwarfs with masses and radii constrained to better than 40% and 20%, respectively (orange and red circles in the bottom panel of Fig. 5.2). The dashed line represents the location of the radius valley measured for F-, G-, and K-type stars from Van Eylen et al. (2018), consistent with the predictions from photoevaporation and core-powered mass-loss models, while the solid line represents the location of the radius valley measured for mid-K and mid-M dwarfs from Cloutier & Menou (2020), consistent with gas-poor formation scenarios. The solid black line indicates the location of the radius valley obtained in this work that marks the transition between rocky (brown) and enveloped (blue) planets around M dwarfs. The shaded golden area is the region of the parameter space where radius valley emergence theories make different predictions. Planets in this region are labeled due to their importance in order to constrain the slope of the valley.

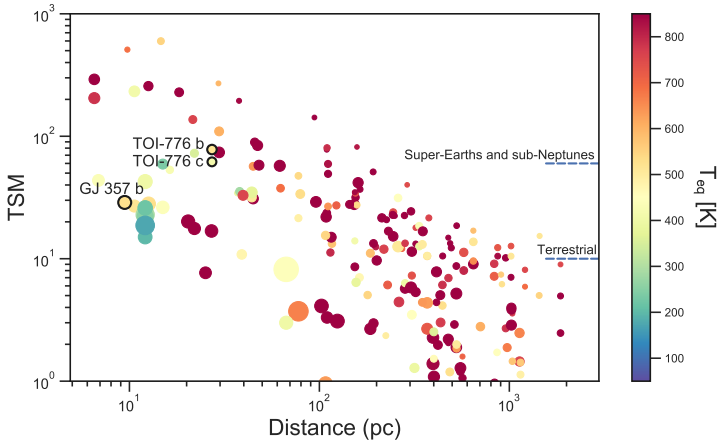

FIGURE 5.4— Transiting planets (as of January 2021) with radii smaller than 5 $R_\oplus$ and dynamical masses measured via transit timing variations or radial velocities as a function of distance from the Sun and the transmission spectroscopy metric (TSM) from Kempton et al. (2018). The color indicates the equilibrium temperature of the planet. Planets in the habitable zone have equilibrium temperatures ranging between 200 and 300 K and are depicted in turquoise. The circle size is inversely proportional to the radius of the planet; hence, bigger and smaller dots correspond to Earth-sized and Neptune-sized planets, respectively. The dashed lines on the right indicate the TSM threshold to select the most amenable targets for atmospheric characterization studies with the *JWST* for terrestrial ($R_p < 1.5\,R_\oplus$) and super-Earth/sub-Neptune ($1.5 < R_p < 2.8\,R_\oplus$) planets. The planet discoveries from Chapters 3 and 4 are indicated.

mass characterization for transiting candidates is not only important to infer the bulk density and estimate the internal composition of the planet, but also to obtain precise and reliable chemical abundances from follow-up atmospheric observations using retrieval codes. The M-dwarf multi-planetary systems GJ 357 and TOI-776 presented in Chapters 3 and 4, respectively, successfully meet this objective (Fig. 5.4).

The transiting planet GJ 357 b is, according to the transmission spectroscopy metric (TSM) derived by Kempton et al. (2018), one of the best Earth-like density planets amenable for a detailed atmospheric study with the *JWST*. Although they do not orbit inside the HZ of their host star, warm Earth analogs like GJ 357 b are interesting to study if terrestrial planets can retain an atmosphere despite receiving a higher stellar radiation, and if their composition are as diverse as the rocky bodies in the solar system. Besides, such planets may have experienced a similar evolution as their temperate Earth-analog counterparts and, thus, may possess similar atmospheric and interior

properties, while providing the advantage of a larger observational signal. For these reasons, GJ 357 b has been included in a sample of 15 exoplanets spanning the full available range of equilibrium temperatures and masses to be observed with the *JWST* during Guaranteed Time Observations (PI: Lafreniére). The project will answer fundamental issues such as the formation process and formation location of close-in planets, and place some constraints on the mean molecular weight of their atmospheres.

On the other hand, the two sub-Neptune planets transiting the star TOI-776 are also promising targets for atmospheric characterization. The high TSM of TOI-776 b and c places them among the top priority targets for atmospheric follow-up of small planets around nearby stars. This is not surprising, because TOI-776 is one of the brightest M dwarfs with known transiting planets. However, although multi-planetary systems of super-Earths and/or sub-Neptunes are common around early-type M dwarfs, TOI-776 is one of the few systems that have precise bulk density measurements, precise stellar parameters, and a host star bright enough for atmospheric characterization of *all* of its planets. Atmospheric observations are needed to break the degeneracy of internal models and to determine whether the two planets are water worlds or Earth-like cores with large envelopes rich in volatiles, which is impossible to determine from bulk density measurements only. Therefore, we have submitted a General Observer proposal for Cycle 1 *JWST* observations (PI: Luque) to carry out a comparative atmospheric study of the two planets in the same system using the NIRISS instrument. If successful, the different location of the planets with respect to the radius valley will allow us to test theories of small rocky planet atmospheres formation and evolution with time, and to break the degeneracies of internal composition models.

Although the main novelty of this work has been the discovery of planets around M dwarfs suitable for atmospheric studies, the methods to reduce and analyze the data in this thesis are also state-of-the-art. In particular, the assessment of the best model to explain the data comparing directly the Bayesian evidence rather than other statistical metrics is one of the strengths of this work. This model comparison scheme provides a robust answer so as to evaluate the veracity of the radial velocity signals and choose the best approach to account for and remove stellar variability in the data. Thanks to the versatility of new codes like `juliet` (Espinoza et al., 2019) — used in Chapters 3, 4, and the majority of the works from Appendix A — it is possible to perform a joint modeling of all the data in hand simultaneously, which improves considerably the reliability of the fitted parameters and their uncertainties, including realistic modeling of correlated noise using GPs within a reasonable computational time. I used these techniques not only to fit jointly the transit photometry and follow-up radial velocity data, but also to determine the rotational period of the host stars, key to deal with the effects of stellar activity, from long-term ground-based monitoring data using different instruments, passbands, and observing cadence. Only the flexibility and the possibility

to share hyperparameters between instruments in the GP kernels permit to carry out such analyses using all the available wide-ranging data at once.

The number of precisely characterized planets orbiting M dwarfs has increased dramatically in the last years, as seen in Figs. 5.1 and 5.2. Small planets seem to be ubiquitous in these stars, confirming the predictions from HARPS and *Kepler* studies, but appear divided in two distinct populations. Low-mass planets follow a trend in bulk densities consistent with the composition of the Earth: an iron-rich core surrounded by a mantle of silicates. There are very few low-mass planets ($M_p < 3\,M_\oplus$) with significant envelopes, despite their detectability advantages in transit searches. However, a mass measurement for such candidates is still challenging with current instrumentation and require a significant observing time investment and activity-quiet host stars. The situation will be reversed when sub meter-per-second dedicated radial velocity facilities such as EXPRES[1] (Jurgenson et al., 2016), NEID (Schwab et al., 2016), or HARPS3 (Thompson et al., 2016) join the efforts of ESPRESSO, which has an enormous telescope pressure. Along with allowing to measure the mass of small rocky planets even for solar-type stars, radial velocity searches with such high-precision instruments will extend the determination of occurrence rates toward terrestrial planets, allowing to infer the frequency of Earth-like companions in the habitable zone of their stars with higher precision thanks to their better sensitivity to longer orbital periods and sky-projected orientations compared to transit surveys.

Another remarkable observational inference is the large number of M-dwarf planets with low densities and substantial envelopes ($R_p > 2\,R_\oplus$). Such systems were difficult to conceive in the past due to the long pre-main sequence phase that exposes them to strong stellar irradiation and solar wind fluxes, and after, in the main sequence, still powerful flaring events and high energy luminosities. However, recent efforts to characterize the atmospheres of such planets — e.g., GJ 3470 b (Chen et al., 2017; Bourrier et al., 2018; Benneke et al., 2019; Palle et al., 2020), GJ 436 b (Ehrenreich et al., 2015; Bourrier et al., 2016) — hints toward a population of low-metallicity, hydrogen-dominated envelopes, indicating that these planets may form within the ice line of their hosts and rapidly accrete hydrogen from the circumstellar disk of gas and dust around the star before it dissipates. Observations with the *JWST* in the coming decade of the smaller planets from this population ($2 < R_p < 4\,R_\oplus$) will confirm if their lower sizes are simply a consequence of atmospheric erosion or a different formation and evolution mechanism is responsible of their properties altogether.

[1] **EX**treme **PRE**cision **S**pectrometer.

6

Future work

Si yo encontrara la estrella que me guiara,
Yo la metería muy dentro de mi pecho
Y la venerara.
Si encontrara la estrella
Que en el camino me alumbrara.

Enrique Morente (1977)

The work in this thesis gives room to a number of perspectives that I outline below.

- So far, the CARMENES data analyzed in this work have come from the optical arm of the instrument only. However, CARMENES observations are always performed simultaneously with the visual and near-infrared channels. Although the spectroscopic radial velocity information content for the M dwarfs analyzed in this work is higher in the optical than in the near-infrared (Reiners et al., 2018), half of our data has been discarded. The performance of the CARMENES near-infrared spectrograph has been studied in detail by Bauer et al. (2020), but the main limiting factor to reach an instrumental precision equal to the spectroscopic radial velocity information content (stellar astrophysical noise aside) is the active thermal stabilization system of the instrument. For the next three years, the CARMENES consortium has been granted an extension of its GTO survey with the aim to continue its search for planetary systems around M dwarfs, including an upgrade of the instrument to keep it at the technological forefront. The instrumental improvements will allow to push the detection limits of planetary systems around the latest spectral-type M dwarfs, which will increase the opportunities to detect Earth-like planets in the habitable zone of their hosts.

- To tackle this opportunity, it would be interesting to carry out a "secondary", deep survey of a handful of late-type M dwarfs in the solar neighborhood to collect hundreds of observations using CARMENES. A Bayesian model comparison framework like the one employed throughout this thesis is of utmost importance in this case, when signals of planetary or instrumental/astrophysical origin are at the level of the instrumental precision. The goal of such program would be to find the largest number of planets possible in these stars, which, given the physical parameters and the closeness of their hosts, would be prime targets for atmospheric characterization by means of direct imaging and/or transmission spectroscopy (if transiting) with planned and upcoming facilities. Besides, such study could set constraints in the occurrence rate of Earth-mass planets in the solar neighborhood and around the lowest mass stars, which have not been largely surveyed so far.

- On the other hand, the radial velocity detection of truly Earth-like planets orbiting Sun-like stars is at the frontier of our technological capabilities. Based upon the developments achieved for terrestrial M-dwarf planets in the last years, upcoming instruments must incorporate solutions at every step of the process such as allocated telescope time (lasting several years in order to be sensitive to planets in the habitable zone of hotter stars), long-term instrumental stability, accurate wavelength calibration (using laser combs), improved and larger detectors, radial velocity computation (GP-based, template-free approaches, forward-modeling techniques, line-by-line derivations, etc.), telluric contamination subtraction (space-based velocimeters, data-driven modeling, improved line lists from laboratory work), and collaboration between observers, instrument builders, stellar astrophysicists, heliophysicists, and statisticians. The Terra Hunting Experiment (Thompson et al., 2016), expected to start in early 2022, will be the first dedicated project to include such improvements and assess the potential capability to discover Earth-twins via daily observations for a 10–year program duration using a state-of-the-art radial velocity instrument like HARPS3.

- Stellar variability effects, nevertheless, are perhaps the most limiting factor in order to detect temperate Earth-like worlds. Non-parametric approaches to model correlated noise such as Gaussian Processes used in this thesis are valid when the information is scarce, but they limit the sensitivity towards small signals below the astrophysical noise level. An interesting approach would be to combine two methodologies that have been proven successful individually to detect terrestrial planets around M dwarfs: regular sampling (e.g., Anglada-Escudé et al., 2016) and simultaneous photometric monitoring (e.g., Oshagh et al., 2017). Uniform and regular sampling simplify the window function, making frequencies statisti-

cally independent of each other and allowing to disentangle between stationary planet signals and variable stellar activity in the time domain. On the other hand, simultaneous photometric monitoring is very valuable for the correct interpretation of radial velocity signals and, modeling this data to simulate the stellar surface with tools like `StarSim` (Rosich et al., 2020), it is possible to predict and correct the stellar effects imprinted in the spectral lines. Combining both strategies with datasets consisting of hundreds of measurements is a way to push the planet detection limits to the internal instrument precision and not to the astrophysical noise level.

- A novel alternative to these observationally expensive approaches is the use of machine learning algorithms. This technique does not require densely sampled observations, but a substantial training dataset. However, they have the potential to resolve the stellar activity challenge by identifying, and even predict, subtle changes to the average shape of spectral lines due to astrophysical effects. Recent studies have shown that neural networks trained on observations from the HARPS-N Solar Telescope (Dumusque et al., 2015) are able to recover planetary signals down to $30\,\mathrm{cm\,s^{-1}}$ and improve radial velocity scatter by a factor of 1.9 in real data (de Beurs et al., 2020). With the rapid improvement of machine learning and artificial intelligence algorithms this approach will play an important role on the radial velocity detection of habitable-zone Earth-mass exoplanets around Sun-like stars.

- By the end of its mission, *TESS* will have detected nearly all of the transiting planets in short orbits orbiting bright stars across the sky. It will be able to estimate the occurrence of Earth-sized planets around early- and mid-type M dwarfs, but its small aperture prevents it from surveying a large number of these stars and the estimates will have large uncertainties. A dedicated mission with a longer observing baseline and larger aperture is needed to infer $\eta_\oplus$ for M dwarfs and, certainly, for Sun-like stars. *PLATO*, with 26 telescopes of 20 cm class covering a field of view 10 000 times the area of the full Moon with at least 2-year long pointings, will allow the detection of Earth analogues transiting bright solar-type stars, a task that will not be covered by any other project in this decade. Furthermore, among its science objectives is the precise characterization of the planet host star, including its age, using asteroseismology, which will substantially improve the precision in the measured planet parameters of both known and new detections.

- The atmospheric study of the planets from Chapters 3 and 4 as well as any other Earth-sized candidate will be only possible with upcoming facilities. *JWST* observations are the decade's object of desire for any exoplanet researcher and will

certainly revolutionize, again, our understanding of the chemistry and composition of planetary systems. In particular, for planetary systems around M dwarfs, transiting Earth-sized planets will be within reach for the first time by means of transmission and/or eclipse spectroscopy and suitable candidates like the ones studied in this thesis are increasing steadily since the last years thanks to projects like *TESS* or SPECULOOS.

- On the other hand, ground-based astronomy in the next decade will be marked by the construction of giant segmented telescopes. The 3-fold improvement in angular resolution, 10-fold improvement in light-collecting capabilities, and 80-fold improvement in sensitivity to point sources provided by the next generation of ELTs will open up new windows of exoplanet exploration. Extremely sensitive direct imaging instruments coupled to high-dispersion spectrographs will enable the detection of biosignatures in temperate M-dwarf planets and assess their habitability. For the latter, the synergy of the ELTs (which could detect O_2 in the atmospheres of several temperate terrestrial M-dwarf planets) and *JWST* (which likely cannot detect O_2, but could detect other gases such as O_3, H_2O, CO_2, and CH_4, which are essential to evaluating whether the oxygen is biogenic) will be crucial.

- The concept of the habitable zone used in this thesis has provided a first-order proxy for identifying exoplanets that may be able to harbor life. A multi-parameter holistic approach to understand habitability is ultimately required for target selection for biosignature searches. Temperate rocky planets orbiting the closest small stars may be studied with facilities under construction, but the environment of M dwarfs requires a significant extrapolation of our knowledge of habitability in the solar system. A coronagraphic or starshade-based direct imaging space-based mission is the only path currently identified to detect and characterize Earth-sized planets in the habitable zones of a large sample of nearby Sun-like stars. Although extremely challenging, the exoplanet community must develop the tools to study such worlds. Mission concepts such as HabEx or LUVOIR will become a reality in the near future.

Bibliography

Aigrain, S., Pont, F., & Zucker, S. 2012, MNRAS, 419, 3147

Alonso, R., Brown, T. M., Torres, G., et al. 2004, ApJ, 613, L153

Alonso-Floriano, F. J., Morales, J. C., Caballero, J. A., et al. 2015, A&A, 577, A128

Alsubai, K. A., Parley, N. R., Bramich, D. M., et al. 2013, Acta Astron., 63, 465

Anglada-Escudé, G., Amado, P. J., Barnes, J., et al. 2016, Nature, 536, 437

Anglada-Escudé, G. & Butler, R. P. 2012, ApJS, 200, 15

Artigau, É., Kouach, D., Donati, J.-F., et al. 2014, in Society of Photo-Optical Instrumentation Engineers (SPIE) Conference Series, Vol. 9147, Ground-based and Airborne Instrumentation for Astronomy V, ed. S. K. Ramsay, I. S. McLean, & H. Takami, 914715

Astudillo-Defru, N., Delfosse, X., Bonfils, X., et al. 2017, A&A, 600, A13

Baglin, A., Auvergne, M., Boisnard, L., et al. 2006, in 36th COSPAR Scientific Assembly, Vol. 36, 3749

Bakos, G., Noyes, R. W., Kovács, G., et al. 2004, PASP, 116, 266

Bakos, G. Á., Csubry, Z., Penev, K., et al. 2013, PASP, 125, 154

Baliunas, S. L., Donahue, R. A., Soon, W. H., et al. 1995, ApJ, 438, 269

Baranne, A., Queloz, D., Mayor, M., et al. 1996, A&AS, 119, 373

Barclay, T., Pepper, J., & Quintana, E. V. 2018, ApJS, 239, 2

Barnes, S. A. 2003, ApJ, 586, 464

Barnes, S. A. 2007, ApJ, 669, 1167

Baroch, D., Morales, J. C., Ribas, I., et al. 2020, A&A, 641, A69

Batalha, N. E., Lewis, T., Fortney, J. J., et al. 2019, ApJ, 885, L25

Bauer, F. F., Zechmeister, M., Kaminski, A., et al. 2020, A&A, 640, A50

Bean, J. L., Seifahrt, A., Hartman, H., et al. 2010, ApJ, 713, 410

Beichman, C., Benneke, B., Knutson, H., et al. 2014, PASP, 126, 1134

Benneke, B., Knutson, H. A., Lothringer, J., et al. 2019, Nature Astronomy, 3, 813

Benz, A. O. & Güdel, M. 2010, ARA&A, 48, 241

Berdiñas, Z. M., Rodríguez-López, C., Amado, P. J., et al. 2017, MNRAS, 469, 4268

Berdyugina, S. V. 2005, Living Reviews in Solar Physics, 2, 8

Berta, Z. K., Irwin, J., & Charbonneau, D. 2013, ApJ, 775, 91

Bochanski, J. J., Hawley, S. L., Covey, K. R., et al. 2010, AJ, 139, 2679

Boisse, I., Bonfils, X., & Santos, N. C. 2012, A&A, 545, A109

Boisse, I., Bouchy, F., Hébrard, G., et al. 2011, A&A, 528, A4

Bonfils, X., Astudillo-Defru, N., Díaz, R., et al. 2018, A&A, 613, A25

Bonfils, X., Delfosse, X., Udry, S., et al. 2013, A&A, 549, A109

Bonfils, X., Mayor, M., Delfosse, X., et al. 2007, A&A, 474, 293

Borucki, W. J., Koch, D., Basri, G., et al. 2010, Science, 327, 977

Bouchy, F., Doyon, R., Artigau, É., et al. 2017, The Messenger, 169, 21

Bourrier, V., Lecavelier des Etangs, A., Ehrenreich, D., et al. 2018, A&A, 620, A147

Bourrier, V., Lecavelier des Etangs, A., Ehrenreich, D., Tanaka, Y. A., & Vidotto, A. A. 2016, A&A, 591, A121

Boyajian, T. S., von Braun, K., van Belle, G., et al. 2013, ApJ, 771, 40

Boyajian, T. S., von Braun, K., van Belle, G., et al. 2012, ApJ, 757, 112

Briot, D. & Schneider, J. 2018, Prehistory of Transit Searches, ed. H. J. Deeg & J. A. Belmonte, 169

Buchhave, L. A., Latham, D. W., Johansen, A., et al. 2012, Nature, 486, 375

Burke, C. J., Christiansen, J. L., Mullally, F., et al. 2015, ApJ, 809, 8

Burkert, A. & Ida, S. 2007, ApJ, 660, 845

Campbell, B., Walker, G. A. H., & Yang, S. 1988, ApJ, 331, 902

Casasayas-Barris, N., Palle, E., Stangret, M., et al. 2021, arXiv e-prints, arXiv:2101.04094

Casasayas-Barris, N., Pallé, E., Yan, F., et al. 2020, A&A, 635, A206

Cegla, H. 2019, Geosciences, 9, 114

Chabrier, G. & Baraffe, I. 1997, A&A, 327, 1039

Chaplin, W. J., Cegla, H. M., Watson, C. A., Davies, G. R., & Ball, W. H. 2019, AJ, 157, 163

Charbonneau, D., Brown, T. M., Latham, D. W., & Mayor, M. 2000, ApJ, 529, L45

Charbonneau, D., Brown, T. M., Noyes, R. W., & Gilliland, R. L. 2002, ApJ, 568, 377

Charbonneau, D. & Deming, D. 2007, arXiv e-prints, arXiv:0706.1047

Checlair, J. H., Olson, S. L., Jansen, M. F., & Abbot, D. S. 2019, ApJ, 884, L46

Chen, G., Guenther, E. W., Pallé, E., et al. 2017, A&A, 600, A138

Chen, G., Pallé, E., Welbanks, L., et al. 2018, A&A, 616, A145

Cifuentes, C., Caballero, J. A., Cortés-Contreras, M., et al. 2020, A&A, 642, A115

Cloutier, R., Artigau, É., Delfosse, X., et al. 2018, AJ, 155, 93

Cloutier, R. & Menou, K. 2020, AJ, 159, 211

Cosentino, R., Lovis, C., Pepe, F., et al. 2012, in Society of Photo-Optical Instrumentation Engineers (SPIE) Conference Series, Vol. 8446, Ground-based and Airborne Instrumentation for Astronomy IV, ed. I. S. McLean, S. K. Ramsay, & H. Takami, 84461V

Crane, J. D., Shectman, S. A., & Butler, R. P. 2006, in Society of Photo-Optical Instrumentation Engineers (SPIE) Conference Series, Vol. 6269, Society of Photo-Optical Instrumentation Engineers (SPIE) Conference Series, ed. I. S. McLean & M. Iye, 626931

Cretignier, M., Dumusque, X., Allart, R., Pepe, F., & Lovis, C. 2020, A&A, 633, A76

Crossfield, I. J. M. 2015, PASP, 127, 941

Cumming, A., Butler, R. P., Marcy, G. W., et al. 2008, PASP, 120, 531

Czesla, S., Huber, K. F., Wolter, U., Schröter, S., & Schmitt, J. H. M. M. 2009, A&A, 505, 1277

Dai, F., Winn, J. N., Gandolfi, D., et al. 2017, AJ, 154, 226

Dawson, R. I. & Murray-Clay, R. A. 2013, ApJ, 767, L24

de Beurs, Z. L., Vanderburg, A., Shallue, C. J., et al. 2020, arXiv e-prints, arXiv:2011.00003

de Kort, J. J. M. A. 1954, Ricerche Astronomiche, 3, 109

Dekker, H., D'Odorico, S., Kaufer, A., Delabre, B., & Kotzlowski, H. 2000, in Society of Photo-Optical Instrumentation Engineers (SPIE) Conference Series, Vol. 4008, Optical and IR Telescope Instrumentation and Detectors, ed. M. Iye & A. F. Moorwood, 534–545

Des Marais, D. J., Harwit, M. O., Jucks, K. W., et al. 2002, Astrobiology, 2, 153

Desort, M., Lagrange, A. M., Galland, F., Udry, S., & Mayor, M. 2007, A&A, 473, 983

Díez Alonso, E., Caballero, J. A., Montes, D., et al. 2019, A&A, 621, A126

Dong, C., Lingam, M., Ma, Y., & Cohen, O. 2017, ApJ, 837, L26

Dorn, C., Venturini, J., Khan, A., et al. 2017, A&A, 597, A37

Dravins, D. 1982, ARA&A, 20, 61

Dreizler, S., Jeffers, S. V., Rodríguez, E., et al. 2020, MNRAS, 493, 536

Dressing, C. D. & Charbonneau, D. 2013, ApJ, 767, 95

Dressing, C. D. & Charbonneau, D. 2015, ApJ, 807, 45

Dumusque, X. 2016, A&A, 593, A5

Dumusque, X. 2018, A&A, 620, A47

Dumusque, X., Boisse, I., & Santos, N. C. 2014, ApJ, 796, 132

Dumusque, X., Borsa, F., Damasso, M., et al. 2017, A&A, 598, A133

Dumusque, X., Glenday, A., Phillips, D. F., et al. 2015, ApJ, 814, L21

Dumusque, X., Lovis, C., Ségransan, D., et al. 2011a, A&A, 535, A55

Dumusque, X., Udry, S., Lovis, C., Santos, N. C., & Monteiro, M. J. P. F. G. 2011b, A&A, 525, A140

Duncan, D. K., Vaughan, A. H., Wilson, O. C., et al. 1991, ApJS, 76, 383

Eggenberger, A. & Udry, S. 2010, in EAS Publications Series, Vol. 41, EAS Publications Series, ed. T. Montmerle, D. Ehrenreich, & A. M. Lagrange, 27–75

Ehrenreich, D., Bourrier, V., Wheatley, P. J., et al. 2015, Nature, 522, 459

Ehrenreich, D., Lovis, C., Allart, R., et al. 2020, Nature, 580, 597

Endl, M., Cochran, W. D., Kürster, M., et al. 2006, ApJ, 649, 436

Espinoza, N. 2019, Research Notes of the American Astronomical Society, 3, 122

Espinoza, N., Kossakowski, D., & Brahm, R. 2019, MNRAS, 490, 2262

Esteves, L. J., De Mooij, E. J. W., & Jayawardhana, R. 2013, ApJ, 772, 51

Fabrycky, D. C., Lissauer, J. J., Ragozzine, D., et al. 2014, ApJ, 790, 146

Fauchez, T. J., Turbet, M., Villanueva, G. L., et al. 2019, ApJ, 887, 194

Fischer, D. A. & Valenti, J. 2005, ApJ, 622, 1102

Foreman-Mackey, D., Hogg, D. W., Lang, D., & Goodman, J. 2013, PASP, 125, 306

Fridlund, M., Gaidos, E., Barragán, O., et al. 2017, A&A, 604, A16

Frink, S., Mitchell, D. S., Quirrenbach, A., et al. 2002, ApJ, 576, 478

Fulton, B. J. & Petigura, E. A. 2018, AJ, 156, 264

Fulton, B. J., Petigura, E. A., Howard, A. W., et al. 2017, AJ, 154, 109

Gaia Collaboration, Brown, A. G. A., Vallenari, A., et al. 2018, A&A, 616, A1

Gaidos, E., Mann, A. W., Kraus, A. L., & Ireland, M. 2016, MNRAS, 457, 2877

Garcia-Sage, K., Glocer, A., Drake, J. J., Gronoff, G., & Cohen, O. 2017, ApJ, 844, L13

Gardner, J. P., Mather, J. C., Clampin, M., et al. 2006, Space Sci. Rev., 123, 485

Garhart, E., Deming, D., Mandell, A., et al. 2020, AJ, 159, 137

Gaudi, B. S., Seager, S., Mennesson, B., et al. 2020, arXiv e-prints, arXiv:2001.06683

Gillon, M., Jehin, E., Fumel, A., Magain, P., & Queloz, D. 2013, in European Physical Journal Web of Conferences, Vol. 47, European Physical Journal Web of Conferences, 03001

Gillon, M., Jehin, E., Lederer, S. M., et al. 2016, Nature, 533, 221

Gillon, M., Meadows, V., Agol, E., et al. 2020a, arXiv e-prints, arXiv:2002.04798

Gillon, M., Meadows, V., Agol, E., et al. 2020b, in Bulletin of the American Astronomical Society, Vol. 52, 0208

Gillon, M., Triaud, A. H. M. J., Demory, B.-O., et al. 2017, Nature, 542, 456

Ginzburg, S., Schlichting, H. E., & Sari, R. 2018, MNRAS, 476, 759

Gomes da Silva, J., Santos, N. C., Bonfils, X., et al. 2012, A&A, 541, A9

Gonzalez, G. 1997, MNRAS, 285, 403

Gray, D. F. 1992, The observation and analysis of stellar photospheres., Vol. 20

Greene, T. P., Line, M. R., Montero, C., et al. 2016, ApJ, 817, 17

Grunblatt, S. K., Howard, A. W., & Haywood, R. D. 2015, ApJ, 808, 127

Günther, M. N., Zhan, Z., Seager, S., et al. 2020a, AJ, 159, 60

Günther, M. N., Zhan, Z., Seager, S., et al. 2020b, AJ, 159, 60

Gupta, A. & Schlichting, H. E. 2019, MNRAS, 487, 24

Gupta, A. & Schlichting, H. E. 2020, MNRAS, 493, 792

Hardegree-Ullman, K. K., Cushing, M. C., Muirhead, P. S., & Christiansen, J. L. 2019, AJ, 158, 75

Hartmann, L. & Stauffer, J. R. 1989, AJ, 97, 873

Hatzes, A. P. 2014, A&A, 568, A84

Hatzes, A. P., Cochran, W. D., Endl, M., et al. 2003, ApJ, 599, 1383

Hatzes, A. P., Fridlund, M., Nachmani, G., et al. 2011, ApJ, 743, 75

Haywood, R. D., Collier Cameron, A., Queloz, D., et al. 2014, MNRAS, 443, 2517

Heller, R., Leconte, J., & Barnes, R. 2011, A&A, 528, A27

Hellier, C., Anderson, D. R., Collier Cameron, A., et al. 2015, AJ, 150, 18

Henry, G. W., Marcy, G., Butler, R. P., & Vogt, S. S. 1999, IAU Circular, 7307, 1

Henry, G. W., Marcy, G. W., Butler, R. P., & Vogt, S. S. 2000, ApJ, 529, L41

Herrero, E., Ribas, I., Jordi, C., et al. 2016, A&A, 586, A131

Hertzsprung, E. 1924, Bull. Astron. Inst. Netherlands, 2, 87

Howard, A. W., Marcy, G. W., Bryson, S. T., et al. 2012, ApJS, 201, 15

Howard, A. W., Marcy, G. W., Johnson, J. A., et al. 2010, Science, 330, 653

Howell, S. B., Sobeck, C., Haas, M., et al. 2014, PASP, 126, 398

Hsu, D. C., Ford, E. B., & Terrien, R. 2020, MNRAS, 498, 2249

Huélamo, N., Figueira, P., Bonfils, X., et al. 2008, A&A, 489, L9

Iben, Icko, J. 1967, ARA&A, 5, 571

Izidoro, A., Ogihara, M., Raymond, S. N., et al. 2017, MNRAS, 470, 1750

Jin, S. & Mordasini, C. 2018, ApJ, 853, 163

Johansen, A., Davies, M. B., Church, R. P., & Holmelin, V. 2012, ApJ, 758, 39

Johnson, M. C., Gandolfi, D., Fridlund, M., et al. 2016, AJ, 151, 171

Jurgenson, C., Fischer, D., McCracken, T., et al. 2016, in Society of Photo-Optical Instrumentation Engineers (SPIE) Conference Series, Vol. 9908, Ground-based and Airborne Instrumentation for Astronomy VI, ed. C. J. Evans, L. Simard, & H. Takami, 99086T

Kaltenegger, L., Madden, J., Lin, Z., et al. 2019, ApJ, 883, L40

Kasting, J. F., Whitmire, D. P., & Reynolds, R. T. 1993, Icarus, 101, 108

Kempton, E. M. R., Bean, J. L., Louie, D. R., et al. 2018, PASP, 130, 114401

Kjeldsen, H. & Bedding, T. R. 2011, A&A, 529, L8

Kjeldsen, H., Bedding, T. R., Butler, R. P., et al. 2005, ApJ, 635, 1281

Konacki, M., Torres, G., Jha, S., & Sasselov, D. D. 2003, Nature, 421, 507

Kopparapu, R. K. 2013, ApJ, 767, L8

Kopparapu, R. K., Ramirez, R., Kasting, J. F., et al. 2013, ApJ, 765, 131

Kopparapu, R. K., Ramirez, R. M., SchottelKotte, J., et al. 2014, ApJ, 787, L29

Kotani, T., Tamura, M., Suto, H., et al. 2014, in Society of Photo-Optical Instrumentation Engineers (SPIE) Conference Series, Vol. 9147, Ground-based and Airborne Instrumentation for Astronomy V, ed. S. K. Ramsay, I. S. McLean, & H. Takami, 914714

Kovács, G., Zucker, S., & Mazeh, T. 2002, A&A, 391, 369

Kürster, M., Endl, M., Rouesnel, F., et al. 2003, A&A, 403, 1077

Lafarga, M., Ribas, I., Lovis, C., et al. 2020, A&A, 636, A36

Lanza, A. F., Bonomo, A. S., Moutou, C., et al. 2010, A&A, 520, A53

Laughlin, G., Bodenheimer, P., & Adams, F. C. 1997, ApJ, 482, 420

Leconte, J., Wu, H., Menou, K., & Murray, N. 2015, Science, 347, 632

Lee, E. J. & Connors, N. J. 2020, arXiv e-prints, arXiv:2008.01105

Léger, A., Rouan, D., Schneider, J., et al. 2009, A&A, 506, 287

Lehmer, O. R., Catling, D. C., Parenteau, M. N., & Hoehler, T. M. 2018, ApJ, 859, 171

Lin, D. N. C., Bodenheimer, P., & Richardson, D. C. 1996, Nature, 380, 606

Lingam, M. & Loeb, A. 2018, International Journal of Astrobiology, 17, 116

Lissauer, J. J., Ragozzine, D., Fabrycky, D. C., et al. 2011, ApJS, 197, 8

Lovis, C., Snellen, I., Mouillet, D., et al. 2017, A&A, 599, A16

Luger, R. & Barnes, R. 2015, Astrobiology, 15, 119

Luque, R., Casasayas-Barris, N., Parviainen, H., et al. 2020, A&A, 642, A50

Luque, R., Nowak, G., Pallé, E., et al. 2019a, A&A, 623, A114

Luque, R., Nowak, G., Pallé, E., et al. 2018, A&A, 620, A171

Luque, R., Pallé, E., Kossakowski, D., et al. 2019b, A&A, 628, A39

Luque, R., Serrano, L. M., Molaverdikhani, K., et al. 2021, A&A, 645, A41

Luque, R., Trifonov, T., Reffert, S., et al. 2019c, A&A, 631, A136

Madhusudhan, N. 2019, ARA&A, 57, 617

Mahadevan, S., Ramsey, L., Bender, C., et al. 2012, in Society of Photo-Optical Instrumentation Engineers (SPIE) Conference Series, Vol. 8446, Ground-based and Airborne Instrumentation for Astronomy IV, ed. I. S. McLean, S. K. Ramsay, & H. Takami, 84461S

Mahadevan, S., Stefánsson, G., Robertson, P., et al. 2021, arXiv e-prints, arXiv:2102.02233

Makarov, V. V. 2010, ApJ, 715, 500

Mamajek, E. E. & Hillenbrand, L. A. 2008, ApJ, 687, 1264

Marcy, G. W. & Butler, R. P. 1992, PASP, 104, 270

Marcy, G. W. & Butler, R. P. 2000, PASP, 112, 137

Mayor, M., Marmier, M., Lovis, C., et al. 2011, arXiv e-prints, arXiv:1109.2497

Mayor, M., Pepe, F., Queloz, D., et al. 2003, The Messenger, 114, 20

Mayor, M. & Queloz, D. 1995, Nature, 378, 355

McCullough, P. R., Stys, J. E., Valenti, J. A., et al. 2005, PASP, 117, 783

McQuillan, A., Aigrain, S., & Mazeh, T. 2013, MNRAS, 432, 1203

Meadows, V. S. 2017, Astrobiology, 17, 1022

Meunier, N. & Lagrange, A. M. 2013, A&A, 551, A101

Meunier, N., Lagrange, A. M., Mbemba Kabuiku, L., et al. 2017, A&A, 597, A52

Moore, K. & Cowan, N. B. 2020, MNRAS, 496, 3786

Morley, C. V., Kreidberg, L., Rustamkulov, Z., Robinson, T., & Fortney, J. J. 2017, ApJ, 850, 121

Mullan, D. J. & Bais, H. P. 2018, ApJ, 865, 101

Murray, C. D. & Correia, A. C. M. 2010, Keplerian Orbits and Dynamics of Exoplanets, ed. S. Seager, 15–23

Narita, N., Fukui, A., Kusakabe, N., et al. 2019, Journal of Astronomical Telescopes, Instruments, and Systems, 5, 015001

Newton, E. R., Irwin, J., Charbonneau, D., Berta-Thompson, Z. K., & Dittmann, J. A. 2016a, ApJ, 821, L19

Newton, E. R., Irwin, J., Charbonneau, D., et al. 2016b, ApJ, 821, 93

Nortmann, L., Pallé, E., Salz, M., et al. 2018, Science, 362, 1388

Noyes, R. W., Weiss, N. O., & Vaughan, A. H. 1984, ApJ, 287, 769

Nutzman, P. & Charbonneau, D. 2008, PASP, 120, 317

O'Malley-James, J. T. & Kaltenegger, L. 2019, MNRAS, 485, 5598

Oshagh, M., Boué, G., Haghighipour, N., et al. 2012, A&A, 540, A62

Oshagh, M., Santos, N. C., Boisse, I., et al. 2013, A&A, 556, A19

Oshagh, M., Santos, N. C., Figueira, P., et al. 2017, A&A, 606, A107

Otegi, J. F., Dorn, C., Helled, R., et al. 2020, A&A, 640, A135

Owen, J. E. & Mohanty, S. 2016, MNRAS, 459, 4088

Owen, J. E. & Wu, Y. 2017, ApJ, 847, 29

Palle, E., Nortmann, L., Casasayas-Barris, N., et al. 2020, A&A, 638, A61

Passegger, V. M., Bello-García, A., Ordieres-Meré, J., et al. 2020, A&A, 642, A22

Passegger, V. M., Reiners, A., Jeffers, S. V., et al. 2018, A&A, 615, A6

Passegger, V. M., Wende-von Berg, S., & Reiners, A. 2016, A&A, 587, A19

Pepe, F. A., Cristiani, S., Rebolo Lopez, R., et al. 2010, in Society of Photo-Optical Instrumentation Engineers (SPIE) Conference Series, Vol. 7735, Ground-based and Airborne Instrumentation for Astronomy III, 77350F

Pepper, J., Pogge, R. W., DePoy, D. L., et al. 2007, PASP, 119, 923

Perryman, M. 2011, The Exoplanet Handbook

Pinamonti, M., Sozzetti, A., Giacobbe, P., et al. 2019, A&A, 625, A126

Pollacco, D. L., Skillen, I., Collier Cameron, A., et al. 2006, PASP, 118, 1407

Pont, F., Knutson, H., Gilliland, R. L., Moutou, C., & Charbonneau, D. 2008, MNRAS, 385, 109

Press, W. H., Teukolsky, S. A., Vetterling, W. T., & Flannery, B. P. 1992, Numerical recipes in FORTRAN. The art of scientific computing

Queloz, D., Henry, G. W., Sivan, J. P., et al. 2001, A&A, 379, 279

Quirrenbach, A., Amado, P. J., Caballero, J. A., et al. 2014, in Proc. SPIE, Vol. 9147, Ground-based and Airborne Instrumentation for Astronomy V, 91471F

Quirrenbach, A. & Carmenes Consortium. 2020, in Society of Photo-Optical Instrumentation Engineers (SPIE) Conference Series, Vol. 11447, Society of Photo-Optical Instrumentation Engineers (SPIE) Conference Series

Rabus, M., Alonso, R., Belmonte, J. A., et al. 2009, A&A, 494, 391

Rackham, B. V., Apai, D., & Giampapa, M. S. 2018, ApJ, 853, 122

Rajpaul, V., Aigrain, S., Osborne, M. A., Reece, S., & Roberts, S. 2015, MNRAS, 452, 2269

Rauer, H., Catala, C., Aerts, C., et al. 2014, Experimental Astronomy, 38, 249

Redfield, S., Endl, M., Cochran, W. D., & Koesterke, L. 2008, ApJ, 673, L87

Reffert, S., Bergmann, C., Quirrenbach, A., Trifonov, T., & Künstler, A. 2015, A&A, 574, A116

Reffert, S., Quirrenbach, A., Mitchell, D. S., et al. 2006, ApJ, 652, 661

Reid, I. N. & Gizis, J. E. 1997, AJ, 113, 2246

Reiners, A. 2009, A&A, 498, 853

Reiners, A., Bean, J. L., Huber, K. F., et al. 2010, ApJ, 710, 432

Reiners, A. & Zechmeister, M. 2020, ApJS, 247, 11

Reiners, A., Zechmeister, M., Caballero, J. A., et al. 2018, A&A, 612, A49

Ribas, I., Tuomi, M., Reiners, A., et al. 2018, Nature, 563, 365

Ricker, G. R., Winn, J. N., Vanderspek, R., et al. 2014, in Proc. SPIE, Vol. 9143, Space Telescopes and Instrumentation 2014: Optical, Infrared, and Millimeter Wave, 914320

Robertson, P., Endl, M., Cochran, W. D., & Dodson-Robinson, S. E. 2013, ApJ, 764, 3

Rodríguez, E., Rodríguez-López, C., López-González, M. J., et al. 2016, MNRAS, 457, 1851

Rodríguez-López, C., MacDonald, J., Amado, P. J., Moya, A., & Mullan, D. 2014, MNRAS, 438, 2371

Rodríguez-López, C., MacDonald, J., & Moya, A. 2012, MNRAS, 419, L44

Rosich, A., Herrero, E., Mallonn, M., et al. 2020, A&A, 641, A82

Saar, S. H. & Donahue, R. A. 1997, ApJ, 485, 319

Sanchis-Ojeda, R., Rappaport, S., Pallè, E., et al. 2015, ApJ, 812, 112

Sanchis-Ojeda, R. & Winn, J. N. 2011, ApJ, 743, 61

Sanchis-Ojeda, R., Winn, J. N., Holman, M. J., et al. 2011, ApJ, 733, 127

Santos, N. C., Gomes da Silva, J., Lovis, C., & Melo, C. 2010, A&A, 511, A54

Savanov, I. S. 2012, Astronomy Reports, 56, 716

Scalo, J., Kaltenegger, L., Segura, A. G., et al. 2007, Astrobiology, 7, 85

Schöfer, P., Jeffers, S. V., Reiners, A., et al. 2019, A&A, 623, A44

Schrijver, C. J. & Zwaan, C. 2000, Solar and Stellar Magnetic Activity

Schwab, C., Rakich, A., Gong, Q., et al. 2016, in Society of Photo-Optical Instrumentation Engineers (SPIE) Conference Series, Vol. 9908, Ground-based and Airborne Instrumentation for Astronomy VI, ed. C. J. Evans, L. Simard, & H. Takami, 99087H

Schweitzer, A., Passegger, V. M., & Béjar, V. J. S. 2018, A&A, to be submitted

Schwieterman, E. W., Kiang, N. Y., Parenteau, M. N., et al. 2018, Astrobiology, 18, 663

Seager, S. 2010, Exoplanets

Seager, S. 2018, International Journal of Astrobiology, 17, 294

Seager, S. & Mallén-Ornelas, G. 2003, ApJ, 585, 1038

Shields, A. L., Ballard, S., & Johnson, J. A. 2016, Phys. Rep., 663, 1

Shields, A. L., Meadows, V. S., Bitz, C. M., et al. 2013, Astrobiology, 13, 715

Sing, D. K., Fortney, J. J., Nikolov, N., et al. 2016, Nature, 529, 59

Skumanich, A. 1972, ApJ, 171, 565

Snellen, I., de Kok, R., Birkby, J. L., et al. 2015, A&A, 576, A59

Snellen, I. A. G., de Kok, R. J., de Mooij, E. J. W., & Albrecht, S. 2010, Nature, 465, 1049

Snellen, I. A. G., de Kok, R. J., le Poole, R., Brogi, M., & Birkby, J. 2013, ApJ, 764, 182

Sousa, S. G., Santos, N. C., Mayor, M., et al. 2008, A&A, 487, 373

Stefansson, G., Cañas, C., Wisniewski, J., et al. 2020a, AJ, 159, 100

Stefansson, G., Mahadevan, S., Maney, M., et al. 2020b, AJ, 160, 192

Suárez Mascareño, A., Faria, J. P., Figueira, P., et al. 2020, A&A, 639, A77

Suárez Mascareño, A., Rebolo, R., González Hernández, J. I., & Esposito, M. 2015, MNRAS, 452, 2745

Suárez Mascareño, A., Rebolo, R., González Hernández, J. I., & Esposito, M. 2017, MNRAS, 468, 4772

Tarter, J. C., Backus, P. R., Mancinelli, R. L., et al. 2007, Astrobiology, 7, 30

The LUVOIR Team. 2019, arXiv e-prints, arXiv:1912.06219

Thompson, S. J., Queloz, D., Baraffe, I., et al. 2016, in Society of Photo-Optical Instrumentation Engineers (SPIE) Conference Series, Vol. 9908, Ground-based and Airborne Instrumentation for Astronomy VI, ed. C. J. Evans, L. Simard, & H. Takami, 99086F

Tian, F. & Ida, S. 2015, Nature Geoscience, 8, 177

Tilley, M. A., Segura, A., Meadows, V., Hawley, S., & Davenport, J. 2019, Astrobiology, 19, 64

Toledo-Padrón, B., González Hernández, J. I., Rodríguez-López, C., et al. 2019, MNRAS, 488, 5145

Trifonov, T., Reffert, S., Tan, X., Lee, M. H., & Quirrenbach, A. 2014, A&A, 568, A64

Tsiaras, A., Waldmann, I. P., Zingales, T., et al. 2018, AJ, 155, 156

Van Eylen, V., Agentoft, C., Lundkvist, M. S., et al. 2018, MNRAS, 479, 4786

Van Eylen, V., Albrecht, S., Huang, X., et al. 2019, AJ, 157, 61

Vanderburg, A., Plavchan, P., Johnson, J. A., et al. 2016, MNRAS, 459, 3565

Vaughan, A. H., Baliunas, S. L., Middelkoop, F., et al. 1981, ApJ, 250, 276

Villaver, E. & Livio, M. 2009, ApJ, 705, L81

Villaver, E., Livio, M., Mustill, A. J., & Siess, L. 2014, ApJ, 794, 3

Vogt, S. S., Allen, S. L., Bigelow, B. C., et al. 1994, in Proc. SPIE, Vol. 2198, Instrumentation in Astronomy VIII, ed. D. L. Crawford & E. R. Craine, 362

Wandel, A. 2018, ApJ, 856, 165

Wang, J., Mawet, D., Ruane, G., Hu, R., & Benneke, B. 2017, AJ, 153, 183

Watson, F. T., Fletcher, L., & Marshall, S. 2011, A&A, 533, A14

Weiss, L. M., Marcy, G. W., Petigura, E. A., et al. 2018, AJ, 155, 48

Wheatley, P. J., Pollacco, D. L., Queloz, D., et al. 2013, in European Physical Journal Web of Conferences, Vol. 47, European Physical Journal Web of Conferences, 13002

Winn, J. N. 2010, Exoplanet Transits and Occultations, ed. S. Seager, 55–77

Wolszczan, A. & Frail, D. A. 1992, Nature, 355, 145

Wunderlich, F., Godolt, M., Grenfell, J. L., et al. 2019, A&A, 624, A49

Zechmeister, M., Dreizler, S., Ribas, I., et al. 2019, A&A, 627, A49

Zechmeister, M. & Kürster, M. 2009, A&A, 496, 577

Zechmeister, M., Kürster, M., & Endl, M. 2009, A&A, 505, 859

Zechmeister, M., Reiners, A., Amado, P. J., et al. 2018, A&A, 609, A12

Zeng, L., Jacobsen, S. B., Sasselov, D. D., et al. 2019, Proceedings of the National Academy of Science, 116, 9723

A

Additional publications

During this thesis I have investigated not only planetary systems around M dwarfs, but also several other aspects of exoplanet research. This Appendix summarizes first the projects that I have led contemporaneously to my work on M dwarfs. Then, I include the full list of publications to which I participated during this thesis since its start in January 2018.

A.1 Contemporaneous work

Follow-up of transiting planets orbiting main sequence stars.

The methodology employed in this thesis to discover and characterize extrasolar worlds is not only applicable to M dwarfs, but to a broad range of stellar hosts also. In the course of this thesis I have applied the data reduction and modeling techniques developed for M-dwarf planetary systems to analyze the data from transit space-based searches on stars of different spectral types. As part of the efforts of the KESPRINT consortium, I have contributed to several works devoted to the discovery and mass determination of transiting candidates observed with *K2* and *TESS*. The number of new transiting planets with precise bulk density measurements resulting from this project is more than 30 (references in Appendix A). Fifteen of them have radii smaller than 5 $R_\oplus$ and are depicted as black dots in the bottom panel of Fig. 5.2.

My role within the KESPRINT consortium and, in particular, my contributions to these works (a total of 19 refereed publications during the span of this thesis) include: i) obtaining telescope time to carry out high-precision radial velocity follow-up of transiting candidates with Spanish facilities such as CARMENES, HARPS-N, and FIES; ii) prioritizing and carrying out the observations of the most promising candidates; iii) computing the radial velocities and spectral line indicators from spectroscopic obser-

vations using template-matching algorithms; iv) frequency analyses; v) joint modeling of the light curves and radial velocities using, e.g., `juliet`; and vi) the discussion and interpretation of the results in terms of planet demographics, formation, evolution and prospects for atmospheric characterization. In addition to the work presented in Chapter 4, I have led another publication within KESPRINT, which is the discovery and mass determination of a rare ultra-dense sub-Neptune planet orbiting a star identical to the Sun using *K2* and CARMENES data (Luque et al., 2019a).

Atmospheric characterization of giant planets.

On the other hand, I have participated in several works related to the atmospheric characterization of giant planets within the Exoplanets & Astrobiology research group in the Instituto de Astrofísica de Canarias. In particular, during my thesis, I have led a novel analysis of the WASP-74 planetary system. WASP-74 b is a hot Jupiter discovered by Hellier et al. (2015) and re-observed by our group using the multi-band simultaneous imager MuSCAT2 (Narita et al., 2019) and the high-resolution spectrograph HARPS-N (PI: Casasayas-Barris). In this work, I learned and applied the techniques from spectrophotometry and high-dispersion spectroscopy to study the atmosphere of this giant planet and, in addition, modeled the Rossiter-McLaughlin effect in the radial velocity data obtained during the HARPS-N transit observations to measure the obliquity of the system for the first time. Although the S/N of the spectra obtained is not sufficiently high to claim the detection of any atomic or molecular feature, the low-resolution transmission spectrum built upon multi-color photometric observations indicates a low abundance of water and optical absorbers such as titanium and/or vanadium oxide in the atmosphere of the planet. The publication, Luque et al. (2020), represents a preparatory step to the atmospheric characterization of the planets presented in Chapters 3 and 4 in the future with the *JWST* and the ELTs.

Planets in giant stars.

The work of this thesis aims to improve the understanding of the properties of planetary systems orbiting low mass stars. However, to have a more complete picture about the formation and evolution of planetary systems is also necessary to probe the upper-end of the host stellar mass range. As discussed in Chapter 1, the detection of planets orbiting massive O-, A-, and F-type main sequence stars is very challenging for both the transit and radial velocity techniques. However, an alternative is to probe the high-mass end of the distribution targeting giant stars that evolved from main sequence solar-type stars. In parallel to my work about M dwarfs, I have been involved in two projects related to planets around giant stars.

A pioneer study using the radial velocity technique with this goal was the Lick survey (e.g., Frink et al., 2002; Reffert et al., 2006; Trifonov et al., 2014). With data

spanning more than 12 years of a sample of 373 G- and K-type giants, this project confirmed that the planet-metallicity correlation is also evident in giant stars and that the giant planet occurrence rate increases monotonously up to a host stellar mass of 2 $M_{\odot}$ and then decreases rapidly, implying that giant planet formation or inward migration is suppressed around higher mass stars (Reffert et al., 2015). As a member of this project, I led the discovery of a Jupiter-like planet in the 7 CMa system, a naked-eye giant star, trapped in a very rare mean-motion resonance with its inner Jupiter-mass companion (Luque et al., 2019c). In this work, due to the close orbits between the massive planets, the radial velocity data is modeled taking into account the effects that the gravitational interactions between the planets imprint to the host star. Besides, the fitted orbital solutions must be tested for long-term dynamical stability by integrating the orbits for several million years and check if any of the planets are ejected or experience a collision.

On the other hand, in collaboration with Dr. Jorge Lillo-Box from the Centro de Astrobiología in Madrid (Spain), I have started a project to find close-in planets around giant stars using photometry from *TESS*. Close-in planets around giant stars are very scarce, and the reason could be two-fold. On the one hand, it could be related to different migration mechanisms that prevents the formed planets from migrating to close-in orbits (Burkert & Ida, 2007). On the other hand, it could be an evidence for planet engulfment or disruption (Villaver & Livio, 2009; Villaver et al., 2014). However, these results are based in less than a dozen discoveries and the large size (shallow transit depths) and mass (low radial velocity amplitudes) of the host stars have prevented further detections. Our approach consists to detect such companions using the light curve phase modulations produced by the planet on the external layers of its host due to tidal effects (Esteves et al., 2013). This effect is maximized in close-in orbits to large stars due to their lower surface gravity and it does not need the planet to transit, hence becoming an alternative method to transits and RV searches. The enormous sample of stars observed by *TESS* and its high photometric precision is the perfect database to look for these rare systems. Since the beginning of 2019, we have analyzed hundreds of thousands of light curves from giant stars observed with *TESS* in both hemispheres and found hundreds of candidates exhibiting phase modulations compatible with planetary companions in short orbits. During the past two years we have applied and obtained telescope time with different high-resolution spectrographs in both hemispheres (HARPS, FIES, CAFE, HERMES, STELLA, and SONG) to confirm the most promising candidates with radial velocity observations and infer their masses and orbital properties. If bona-fide, these planets will massively populate the desert of close-in planets around giant stars, serving as benchmarks for studies on the coupling of the evolution of planetary systems as their host star ages.

A.2 Full list of publications

First author publications

6. *A planetary system with two transiting mini-Neptunes near the radius valley transition around the bright M dwarf TOI-776.*
R. Luque et al.
2021A&A...645A..41L — doi:10.1051/0004-6361/202039455.

5. *Obliquity measurement and atmospheric characterisation of the WASP-74 planetary system.*
R. Luque et al.
2020A&A...642A..50L — doi:10.1051/0004-6361/202038703.

4. *Precise radial velocities of giant stars - XIII: A second Jupiter orbiting in 4:3 resonance in the 7 CMa system.*
R. Luque et al.
2019A&A...631A.136L — doi:10.1051/0004-6361/201936464.

3. *Planetary system around the nearby M dwarf GJ 357 including a transiting, hot, Earth-sized planet optimal for atmospheric characterization.*
R. Luque et al.
2019A&A...628A..39L — doi:10.1051/0004-6361/201935801.

2. *Detection and characterization of an ultra-dense sub-Neptunian planet orbiting the Sun-like star K2-292.*
R. Luque et al.
2019A&A...623A.114L — doi:10.1051/0004-6361/201834952.

1. *The CARMENES search for exoplanets around M dwarfs: The warm super-Earths in twin orbits around the mid-type M dwarfs Ross 1020 and LP 819-052.*
R. Luque et al.
2018A&A...620A.171L — doi:10.1051/0004-6361/201833423.

Second and third author publications

4. *The CARMENES search for exoplanets around M dwarfs. Two planets on opposite sides of the radius gap transiting the nearby M dwarf LTT 3780.*
G. Nowak, **R. Luque**, et al.
2020A&A...642A.173N — doi:10.1051/0004-6361/202037867.

3. *TESS Reveals a Short-period Sub-Neptune Sibling (HD 86226c) to a Known Long-period Giant Planet.*
J. Teske, M. R. Díaz, **R. Luque**, et al.
2020AJ....160...96T — doi:10.3847/1538-3881/ab9f95.

2. *Precise mass and radius of a transiting super-Earth planet orbiting the M dwarf TOI-1235: a planet in the radius gap?.*
P. Bluhm, **R. Luque**, et al.
2020A&A...639A.132B — doi:10.1051/0004-6361/202038160.

1. *Detection and Doppler monitoring of K2-285 (EPIC 246471491), a system of four transiting planets smaller than Neptune.*
E. Pallé, G. Nowak, **R. Luque** et al.
2019A&A...623A..41P — doi:10.1051/0004-6361/201834001.

Co-author publications

38. *A nearby transiting rocky exoplanet that is suitable for atmospheric investigation*.
T. Trifonov et al. (including **R. Luque**).
2021Sci...371.6533T — doi:10.1126/science.abd7645.

37. *An ultra-short-period transiting super-Earth orbiting the M3 dwarf TOI-1685*.
P. Bluhm et al. (including **R. Luque**).
2021arXiv210301016B — arXiv:2103.01016.

36. *Masses and compositions of three small planets orbiting the nearby M dwarf L231-32 (TOI-270) and the M dwarf radius valley*.
V. Van Eylen et al. (including **R. Luque**).
2021arXiv210101593V — arXiv:2101.01593.

35. *An enhanced slope in the transmission spectrum of the hot Jupiter WASP-104b*.
G. Chen et al. (including **R. Luque**).
2021MNRAS.500.5420C — doi:10.1093/mnras/staa3555.

34. *TOI-519 b: a short-period substellar object around an M dwarf validated using multicolour photometry and phase curve analysis*.
H. Parviainen et al. (including **R. Luque**).
2021A&A...645A..16P — doi:10.1051/0004-6361/202038934.

33. *The CARMENES search for exoplanets around M dwarfs – LP 714-47 b (TOI 442.01): Populating the Neptune desert*.
S. Dreizler et al. (including **R. Luque**).
2020A&A...644A.127D — doi:10.1051/0004-6361/202038016.

32. *Transmission spectroscopy and Rossiter-McLaughlin measurements of the young Neptune orbiting AU Mic*.
E. Pallé et al. (including **R. Luque**).
2020A&A...643A..25P — doi:10.1051/0004-6361/202038583.

31. *Discovery of a hot, transiting, Earth-sized planet and a second temperate, non-transiting planet around the M4 dwarf GJ 3473 (TOI-488)*.
J. Kemmer et al. (including **R. Luque**).
2020A&A...642A.236K — doi:10.1051/0004-6361/202038967.

30. *Detection of Na in WASP-21b's lower and upper atmosphere*.
G. Chen et al. (including **R. Luque**).
2020A&A...642A..54C — doi:10.1051/0004-6361/202038661.

29. *The Multiplanet System TOI-421*.
I. Carleo et al. (including **R. Luque**).
2020AJ....160..114C — doi:10.3847/1538-3881/aba124.

28. *The TOI-763 system: sub-Neptunes orbiting a Sun-like star*.
M. Fridlund et al. (including **R. Luque**).
2020MNRAS.498.4503F — doi:10.1093/mnras/staa2502.

27. *K2-280b – a low density warm sub-Saturn around a mildly evolved star*.
G. Nowak et al. (including **R. Luque**).
2020MNRAS.497.4423N — doi:10.1093/mnras/staa2077.

26. *A multiple planet system of super-Earths orbiting the brightest red dwarf star GJ887*.
S. V. Jeffers et al. (including **R. Luque**).
2020Sci...368.6498J — doi:10.1126/science.aaz0795.

25. *LHS 1815b: The First Thick-disk Planet Detected by TESS*.
T. Gan et al. (including **R. Luque**).
2020AJ....159..160G — doi:10.3847/1538-3881/ab775a.

24. *TOI-503: The First Known Brown-dwarf Am-star Binary from the TESS Mission*.
J. Subjak et al. (including **R. Luque**).
2020AJ....159..151S — doi:10.3847/1538-3881/ab7245.

23. *Three planets transiting the evolved star EPIC 249893012: a hot 8.8-$M_\oplus$ super-Earth and two warm 14.7 and 10.2-$M_\oplus$ sub-Neptunes*.
D. Hidalgo et al. (including **R. Luque**).
2020A&A...636A..89H — doi:10.1051/0004-6361/201937080.

22. *Mass determinations of the three mini-Neptunes transiting TOI-125*.
L. Nielsen et al. (including **R. Luque**).
2020MNRAS.492.5399N — doi:10.1093/mnras/staa197.

21. *It Takes Two Planets in Resonance to Tango around K2-146*.
K.W.F. Lam et al. (including **R. Luque**).
2020AJ....159..120L — doi:10.3847/1538-3881/ab66c9.

20. *Is there Na I in the atmosphere of HD 209458b?. Effect of the centre-to-limb variation and Rossiter-McLaughlin effect in transmission spectroscopy studies*.
N. Casasayas-Barris et al. (including **R. Luque**).
2020A&A...635A.206C — doi:10.1051/0004-6361/201937221.

19. *MuSCAT2 multicolour validation of TESS candidates: an ultra-short-period substellar object around an M dwarf*.
H. Parviainen et al. (including **R. Luque**).
2020A&A...633A..28P — doi:10.1051/0004-6361/201935958.

18. *Radial velocity confirmation of K2-100b: a young, highly irradiated, and low-density transiting hot Neptune*.
O. Barragán et al. (including **R. Luque**).
2019MNRAS.490..698B — doi:10.1093/mnras/stz2569.

17. *Kojima-1Lb Is a Mildly Cold Neptune around the Brightest Microlensing Host Star*.
A. Fukui et al. (including **R. Luque**).
2019AJ....158..206F — doi:10.3847/1538-3881/ab487f.

16. *The Habitability of GJ 357 d : Possible Climates and Observability*.
L. Kaltenegger, J. Madden, Z. Lin, S. Rugheimer, A. Segura, **R. Luque**, E. Pallé, N. Espinoza.
2019ApJ...883L..40K — doi:10.3847/2041-8213/ab3d40.

15. *Multicolour photometry for exoplanet candidate validation*.
H. Parviainen et al. (including **R. Luque**).
2019A&A...630A..89P — doi:10.1051/0004-6361/201935709.

14. *A giant exoplanet orbiting a very-low-mass star challenges planet formation models*.
J. C. Morales et al. (including **R. Luque**).
2019Sci...365.1441M — doi:10.1126/science.aax3198.

13. *Greening of the brown-dwarf desert. EPIC 212036875b: a* 51 M_J *object in a 5-day orbit around an F7 V star*.
C. M. Persson et al. (including **R. Luque**).
2019A&A...628A..64P — doi:10.1051/0004-6361/201935505.

12. *The CARMENES search for exoplanets around M dwarfs: Two temperate Earth-mass planet candidates around Teegarden's Star*.
M. Zechmeister et al. (including **R. Luque**).
2019A&A...627A..49Z — doi:10.1051/0004-6361/201935460.

11. *The Transiting Multi-planet System HD15337: Two Nearly Equal-mass Planets Straddling the Radius Gap*.
D. Gandolfi et al. (including **R. Luque**).
2019ApJ...876L..24G — doi:10.3847/2041-8213/ab17d9.

10. *K2-290: a warm Jupiter and a mini-Neptune in a triple-star system*.
M. Hjorth et al. (including **R. Luque**).
2019MNRAS.484.3522H — doi:10.1093/mnras/stz139.

9. *HD 219666 b: a hot-Neptune from TESS Sector 1*.
M. Esposito et al. (including **R. Luque**).
2019A&A...623A.165E — doi:10.1051/0004-6361/201834853.

8. *MuSCAT2: four-color Simultaneous Camera for the 1.52-m Telescopio Carlos Sánchez*.
N. Narita et al. (including **R. Luque**).
2019JATIS...5a5001N — doi:10.1117/1.JATIS.5.1.015001.

7. *TESS's first planet: a super-Earth transiting the naked-eye star π Mensae*.
D. Gandolfi et al. (including **R. Luque**).
2018A&A...619L..10G — doi:10.1051/0004-6361/201834289.

6. *Mass determination of the 1:3:5 near-resonant planets transiting GJ 9827 (K2-135)*.
J. Prieto-Arranz et al. (including **R. Luque**).
2018A&A...618A.116P — doi:10.1051/0004-6361/201832872.

5. *The CARMENES search for exoplanets around M dwarfs: A Neptune-mass planet traversing the habitable zone around HD 180617*.
A. Kaminski et al. (including **R. Luque**).
2018A&A...618A.115K — doi:10.1051/0004-6361/201833354.

4. *CARMENES: high-resolution spectra and precise radial velocities in the red and infrared*.
A. Quirrenbach et al. (including **R. Luque**).
2018SPIE10702E..0WQ — doi:10.1117/12.2313689.

3. *The CARMENES search for exoplanets around M dwarfs: High-resolution optical and near-infrared spectroscopy of 324 survey stars*.
A. Reiners et al. (including **R. Luque**).
2018A&A...612A..49R — doi:10.1051/0004-6361/201732054.

2. *The CARMENES search for exoplanets around M dwarfs: First visual-channel radial-velocity measurements and orbital parameter updates of seven M-dwarf planetary systems*.
T. Trifonov et al. (including **R. Luque**).
2018A&A...609A.117T — doi:10.1051/0004-6361/201731442.

1. *The CARMENES search for exoplanets around M dwarfs: HD 147379b: A nearby Neptune in the temperate zone of an early-M dwarf*.
A. Reiners et al. (including **R. Luque**).
2018A&A...609L...5R — doi:10.1051/0004-6361/201732165.